

**QUANTUM THREE-BODY REACTION DYNAMICS INCLUDING
THE GEOMETRIC PHASE EFFECT**

Thesis by
Yi-Shuen Mark Wu

In Partial Fulfillment of the Requirements
for the Degree of
Doctor of Philosophy

Division of Chemistry and Chemical Engineering
California Institute of Technology
Pasadena, California

1992
(Defended February 14, 1992)

ACKNOWLEDGEMENTS

It is with great pleasure that I acknowledge the guidance of Prof. Aron Kuppermann, my advisor. Much of the work contained in this thesis resulted directly from his ideas and suggestions. I wish to thank him especially for his encouragement, patience and seemingly tireless dedication to his research group over the years.

Other members of the Kuppermann group, both past and present, have contributed to this thesis in many ways, and for this I would like to thank them all. I owe special thanks to Dr. Steve Cuccaro who was an inexhaustible source of information about reactive scattering in particular and computers in general, Prof. G. C. Fox and Dr. Paul Messina who initiated me into the world of parallel computing, and Dr. Bruno Lepetit who taught me about hyperspherical harmonics. I owe a special debt of gratitude to Maria Giorgi and Mary Rodgers for their friendship during my stay at Caltech. The innumerable discussions we had doubtless have had an impact on the work reported in this thesis, and perhaps on a few things as well. I also wish to thank the members of my committee, Prof. R. A. Marcus, Prof. H. B. Gray and Prof. B. V. McKoy for their interest in my work.

I would also like to thank the following Kuppermann group members: Paul Hipes, Tim Mattson, Joseph Wong, Zhengwei Peng, Jin Qiu, Diane Hood, Søren Padkjaer, N. Vaidehi, Amy Shaw and Sandor Kristyan for their invaluable stimulating scientific discussions as well as the sharing of their experiences. I am also grateful to Carrie Stroud who deserve enormous thanks for helping in the preparation of this thesis.

My wife, Porin, deserves much of the credit for this work. Her companionship, support and understanding were a constant source of strength for me, and for this I owe her a great deal. I would also like to thank my parents for all their support.

Finally, I would like to take this opportunity to thank all the members of the staff at Caltech. They have helped to make my stay very enjoyable because of the friendly and personal way they handle bussiness.

ABSTRACT

Accurate quantum mechanical reactive scattering calculations within the framework of symmetrized hyperspherical coordinate techniques are presented for several processes involving collisions of an electron with a hydrogen atom and an atom with a diatomic molecule in three-dimensional space, and the collinear collision of an atom with a diatomic molecule. In addition to the interest of the processes themselves, the results are compared with previous experimental and theoretical results in such a way as to provide tests of the general usefulness of the methods used.

The general theory for the calculation of accurate differential cross sections in the reactive collision of an atom with a diatomic molecule including the geometric phase effect in three-dimensional space is described. This methodology has permitted, for the first time, the calculation of integral and differential cross sections over a significantly larger range of collision energies (up to 2.6 eV total energy) than previously possible for the system $\text{H} + \text{H}_2$.

We present numerical solutions of the quantum mechanical streamlines of probability current density for collinear atom-diatom reactions. It is used to study the barrier height dependence of dynamics on the $\text{Cl} + \text{HCl}$ reaction

TABLE OF CONTENTS

Acknowledgements	ii
Abstract	iv
Table of Contents	v
Chapter I. Introduction	1
Chapter II. Quantum Mechanical Reactive Scattering for Three Body Systems Including the Geometric Phase Effect.	
Theory	5
Abstract	6
1. Introduction	7
2. Conical Intersection	10
3. Schrödinger Equation	15
4. Symmetrized Hyperspherical Coordinates	18
5. Expansion of Partial Waves in Terms of Pseudo Surface Functions	20
6. Asymptotic Analysis	29
7. Symmetry Considerations	33
8. Pauli Principle and Observable Cross Sections	39
9. Summary	42
References	43
Figure Captions	47
Tables	48
Figure	52
Chapter III. Effect of the Geometric Phase on Product Rotational State Distributions and Integral Cross Sections	53
Abstract	54

1. Introduction	55
2. Methodology	57
3. Numerical Parameters	60
4. Results of Scattering Calculations	62
5. Summary	66
References	67
Figure Captions	72
Figures	75

Chapter IV. Theoretical Calculation Of Experimentally

Observable Consequences of the Geometric Phase on

Chemical Reaction Cross Sections 81

Abstract 82

1. Introduction 83

2. Methodology 84

3. Numerical Parameters 89

4. Results and Discussion 90

5. Conclusions 95

Acknowledgement 95

References 97

Figure Captions 101

Table 102

Figures 103

Chapter V. Quantum Mechanical Reactive Scattering Using a

High-Performance Distributed-Memory Parallel Computer . . 106

Abstract 107

1. Introduction 108

2. Methodology	110
3. Parallel Algorithm	112
4. Results and Discussion	116
5. Summary	120
Acknowledgements	121
References	122
Figure Captions	126
Tables	128
Figures	132

Chapter VI. Quantum Chemical Reaction Dynamics on a

Highly Parallel Supercomputer 137

Abstract 138

1. Introduction 140

2. Quantum Chemical Dynamics 142

3. Parallel Algorithm 145

4. Results and Discussion 150

5. Summary 154

Acknowledgements 155

References 156

Figure Captions 160

Tables 161

Figures 165

Chapter VII. Three-Dimensional Quantum Mechanical

Electron-Hydrogen Scattering by Symmetrized

Hyperspherical Coordinate Method. Theory 167

Abstract 168

1. Introduction	169
2. The Space-fixed Schrödinger Equation	171
3. Symmetrized Hyperspherical Coordinates	172
4. Potential Energy Function	173
5. Partial Wave Expansion of the Wavefunction	175
6. Expansion of the Partial Waves in Terms of Surface Functions	176
7. Basis Set for Expansion of the Surface Function	178
8. Calculation of Potential Matrix Elements	182
9. Solution of Coupled Equations	184
10. Asymptotic Analysis - R and S matrices	185
11. Asymptotic Analysis - Differential and Integral Cross Sections	188
Summary	189
References	191
Figure Captions	193
Figure	194

Chapter VIII. Quantum Mechanical Streamlines of Probability

Current Density and Tunneling Fractions for Collinear

Atom-Diatom Reactions 196

Abstract 197

1. Introduction 198

2. Hyperspherical Coordinate in Quantum Mechanical Collinear

Reactive Scattering 200

3. Generating the Physical Wavefunction 202

4. Quantum Mechanical Streamlines and Tunneling Fraction 221

5. Method of Computation 204

6. Summary 210

Appendix A.	211
References	214
Figure Captions	216
Figures	217

Appendix A. Quantum Mechanical Study on the Barrier Height

Dependence of the Dynamics for the Collinear

Cl' + HCl → Cl'H + Cl Reaction	220
---	------------

Abstract	221
--------------------	-----

1. Introduction	222
---------------------------	-----

2. Potential Energy Surface	223
---------------------------------------	-----

3. Methodology	224
--------------------------	-----

4. Results and Discussion	225
-------------------------------------	-----

5. Summary	229
----------------------	-----

References	230
----------------------	-----

Figure Captions	232
---------------------------	-----

Table	236
-----------------	-----

Figures	237
-------------------	-----

Appendix B. Chemical Reaction Dynamics: Integration of Coupled

Sets of Ordinary Differential Equations on the Caltech

Hypercube	246
----------------------------	------------

Abstract	247
--------------------	-----

1. Introduction	248
---------------------------	-----

2. Methodology Based on Symmetrized Hyperspherical Coordinates	250
---	-----

3. Logarithmic Derivative Integrator	253
--	-----

4. Future Work	257
--------------------------	-----

Acknowledgement	258
References	259
Figure Caption	262
Figure	263

CHAPTER I

Introduction

Introduction

This thesis is composed of a series of papers in which different aspects of computational methodology and results are presented. Four of these papers are already in the literature. The focus of this thesis is the use of symmetrized hyperspherical coordinate technique to study reactive collision in three-dimensional space. Since each chapter is individual paper that contains its own background materials, they can be read more or less independently. This introduction will give only a summary for each chapter in order to bring a measure of coherence to the thesis as a whole.

Chapter two present a method for accurately solving the Schrödinger equation for the reactive collision of an atom with a diatomic molecule in three dimensions on a single Born-Oppenheimer potential energy surface including the geometric phase effect. The Schrödinger equation is first expressed in symmetrized principal-axis body-fixed hyperspherical coordinates. The formal expansion in a basis set, the local hyperspherical pseudo-surface functions, and the resulting coupled set of ordinary differential equations are discussed. Symmetry considerations that simplify the calculations are analyzed in detail. The formalism for the calculation of the differential and integral cross sections is given. This method permits a very complete description of the atom-diatom scattering processes.

Chapter three gives a numerical detail about the method of chapter two. We apply the method to the $\text{H} + \text{H}_2$ system to explore the behavior of the product rotational state distributions and the integral cross sections. Convergence test are performed and comparison are made to previous independent calculations and the agreements of the results are good, thus validating the method. The influences of the conical intersection and the associated geometric phase effect are also discussed.

Chapter four is a reprint of the publication presenting results from the first successful reactive scattering calculations that include the geometric phase effect. The calculations are for $\text{H} + \text{H}_2$ on the LSTH potential energy surface. Differential cross sections for ortho to ortho transition are shown both with and without the inclusion of the geometric phase effect. The calculations are extended to all total angular momenta needed to obtain converged integral and differential cross sections over the energy range from 0.7 eV to 1.2 eV.

Chapter five and six are reprint of publications that explore the three-dimensional quantum mechanical reactive scattering calculations on high-performance distributed-memory parallel computer. Parallel algorithm is presented for Caltech/JPL Mark IIIfp hypercube and $J = 2$ resonances for $\text{H} + \text{H}_2$ system are also analyzed.

Chapter seven presents a method that uses hyperspherical coordinates for accurately solving the Schrödinger equation for the scattering of an electron from a hydrogen atom in three dimensions.

Chapter eight describes the work of quantum mechanical streamlines of probability current density calculation. Both the formal and numerical aspects of the method are discussed in detail. The dynamics of the collinear $\text{Cl} + \text{HCl}$ reaction on a low and high barrier potential energy surface is investigated by the help of the quantum streamlines and the results are presented in Appendix A. It is found that the vibrational excitation leads to enhancement of the reaction rate on the high barrier surface but inhibition of reaction on the low barrier surface.

Appendix B is a reprint of a publication that describes work related to topic of three-dimensional reactive scattering, namely the logarithmic derivative propagator. Matrix inversion and multiplication are the necessary part of algorithms for propagating the coupled ordinary differential equations that results from the expansion of the scattering wave function in a surface function basis set.

The implementation on the hypercube concurrent processors and detailed tests of the performance of the parallel code are provided in this section.

Chapter II

Quantum Mechanical Reactive Scattering for Three Body Systems Including the Geometric Phase Effect. Theory

**Quantum Mechanical Reactive Scattering for Three Body
Systems Including the Geometric Phase Effect. Theory**

Yi-Shuen Mark Wu ^a and Aron Kuppermann

Arthur Amos Noyes Laboratory of Chemical Physics

Division of Chemistry and Chemical Engineering

California Institute of Technology

Pasadena, CA 91125, USA

Abstract

A method is present for accurately solving the Schrödinger equation for the reactive collision of an atom with a diatomic molecule in three dimensions on a single Born-Oppenheimer potential energy surface including the geometric phase effect. The Schrödinger equation is expressed in symmetrized principal-axis body-fixed hyperspherical coordinates. The formal expansion in a basis set, the local hyperspherical pseudo-surface functions, and the resulting coupled set of ordinary differential equations are discussed. We show how permutational symmetry of the total wave function with respect to the interchange of nuclei can be enforced both in the presence and the absence of the geometric phase effect. Expressions have been obtained for the integral and differential cross sections in helicity representation including two and three identical nuclei.

^a Work performed in partial fulfillment of the requirements for the Ph.D. degree in Chemistry at the California Institute of Technology.

1. Introduction

The reactive atom-diatom collision is the fundamental microscopic event that underlies the chemical reaction. The ability to describe this process from the knowledge of forces operating at the molecular level has long been the goal of the theoretical dynamicist. However, accurate quantum mechanical solutions for reactive atom-diatom scattering have proved to be difficult and computationally expensive to obtain[1]. In fact, only a few groups to date have published accurate integral and differential cross sections, and most of these calculations are based on the system $\text{H} + \text{H}_2$ [2-10].

The exchange reaction between a hydrogen atom and a hydrogen molecule is the prototype example of an elementary bimolecular reaction. This reaction provides the simplest case where, for neutral species, the fundamental kinetic process of bond breaking under the influence of new bond formation can be studied experimentally and theoretically. Most of the quantum theoretical calculations of experimentally observable reaction cross sections for the $\text{H} + \text{H}_2$ system performed so far have used the Born-Oppenheimer adiabatic approximation[2-21], and assumed the reaction occurs on the single ground electronic potential energy surface. This approximation is expected to be quite accurate below about 2.6 eV of total energy (with respect to the bottom of the H_2 potential well) since this is about 0.1 eV below the energy of the minimum of the first excited electronic potential.

However, a complication may arise in using the Born-Oppenheimer approximation when two electronic potential energy surfaces display a conical intersection. It has been shown[22] that in a triangular system of three hydrogen-like atoms the lowest doublet state is linked with an excited doublet state by a conical intersection even when all three atoms are dissimilar. The ground state Born-Oppenheimer

electronic wave function (considered as a function of the nuclear coordinates) must undergo a change in sign when one follows a closed path in nuclear configuration space around the curve along which two potential surfaces intersect conically[23-28]. There must be a compensating sign change on the part of the nuclear wave function if the full electronuclear wave function is to be continuous and single valued[22-26]. This sign change is a particular case of Berry's geometric phase[29] and is sometimes referred to as the molecular Aharonov-Bohm effect[30]. Berry's geometric phase is an example of *holonomy*, the phenomenon by which some variables change when other variables or parameters characterizing a system return to their initial values[31,32]. It is a purely geometric phenomenon that depends solely on the area and curvature of the surface enclosed by the circuit. This effect may have nonnegligible effects on the results for H + H₂ system and other cases where the potential energy hypersurface involves a conical intersection.

Mead and Truhlar[24] have shown formally for H + H₂ system that, if the condition that the wave function is zero in a certain region of nuclear configuration space separating different arrangement channels is fulfilled, the only effect of the geometric phase is to change the sign of the corresponding exchange scattering matrix elements and of the associated total scattering amplitude, while leaving the absolute value of their real and imaginary parts unchanged. This condition is likely to be satisfied for the para → ortho and ortho → para transition cross sections at low collision energies considered in the earlier quantum studies[2-21]. It has been recently shown however[27], that in the absence of coupling to the ground electronic state, the geometric phase completely modifies the energy spectrum and the permutation symmetry properties of the quasi-bound rovibrational states of the first electronically excited state of H₃. It has also been shown[28,33] that the integral and differential cross sections of para → para and ortho → ortho transitions

for this system are significantly changed by this effect. Therefore, to perform a numerical study including the geometric phase effect is necessary to find out if this condition remains valid at higher energy and accurately assess the magnitude of its effect on this system. In addition, it is even more important to develop a general methodology for a system composed of three atoms, which may be dissimilar, that can take the geometric phase effect into account in the absence and the presence of conical intersections.

In this paper and the subsequent papers to follow, we present a method for accurately solving the Schrödinger equation for the reactive collision of an atom with a diatomic molecule in three dimensions on a single Born-Oppenheimer potential energy surface including the geometric phase effect. This method is developed within the framework of the symmetrized hyperspherical coordinate technique[27,28,33-35]. It easily allow inclusion of the full permutation symmetries of the three body system and permits inclusion of the effect of the conical intersection on the phase of the nuclear wave function.

Section 2 will describe a general formalism for the conical intersection and associated geometric phase effect. Section 3 presents the various Jacobi coordinates and the corresponding Schrödinger equation. Section 4 introduces the symmetrized hyperspherical coordinates and associated pseudo surface functions. Section 5 has a discussion of the diabatic coupled channel expansion and the propagation equation from the expansion of the wave function in terms of pseudo surface functions. The formalism for the propagation of general triatomic systems will be given. Section 6 introduces the asymptotic boundary conditions and the determination of the \mathbf{R} and \mathbf{S} matrices of the system. The formalism for determination of the cross sections from the \mathbf{S} matrix is developed. In section 7, the symmetry properties of the system are discussed. Section 8 presents the construction of physically observable cross

sections from irreducible representation scattering amplitudes. A summary of the main points are provided in section 9.

2. Conical Intersection

Geometric phase is known to appear in problems involving the Born-Oppenheimer approximation, in which electronic and nuclear degrees of freedom are separated. This separation of electronic and nuclear motion provides a widely used framework for interpreting molecular energy levels and collision processes. As we recall, in this approximation the electronic problem is solved for each configuration of the nuclei; the positions of the nuclei define a slowly varying environment, which the electrons "follow" adiabatically[36]. Surprisingly, this well-understood procedure gives rise to apparently anomalous results, especially near electronic degeneracies. One such example is the $E \otimes e$ Jahn-Teller effect[37] which involves the vibronic interaction of a doubly degenerate electronic state (E) with a doubly degenerate vibrational mode (e). The nuclear motion lifts the electronic degeneracy and distorts nuclear configurations of lower energy than the symmetric state. The two surfaces diverge linearly from one another at the origin, at a point called the *conical intersection*. Of course, near the origin the adiabatic approximation breaks down, and this point is a singularity of the Born-Oppenheimer procedure. The conical intersection at the degeneracy is the source of geometric phase for the evolution of adiabatic states. The simplest molecules subject to this effect are trimers, with an electronic degeneracy at the symmetric D_{3h} configuration of the nuclei.

In this section, we consider a system of three atoms, not necessarily identical. Following Mead and Truhlers' analysis, in the Born-Oppenheimer approximation

the electronuclear wave function corresponding to the i th electronic state can be written as

$$\Psi(\mathbf{r}; \mathbf{R}) = \psi(\mathbf{R}) | \psi_{ie}(\mathbf{r}; \mathbf{R}) \rangle \quad (2.1)$$

where \mathbf{r} and \mathbf{R} represents the electronic and nuclear coordinates respectively. $| \psi_{ie}(\mathbf{r}; \mathbf{R}) \rangle$ is the i th member of the set of orthonormal eigenstates of the electronic Hamiltonian $\hat{H}_e(\mathbf{r}; \mathbf{R})$, such that

$$\hat{H}_e(\mathbf{r}; \mathbf{R}) | \psi_{ie}(\mathbf{r}; \mathbf{R}) \rangle = U_i(\mathbf{R}) | \psi_{ie}(\mathbf{r}; \mathbf{R}) \rangle. \quad (2.2)$$

To obtain the equation for the nuclear wave function we retain all derivatives of the electronic wave function with respect to nuclear coordinates. By this we mean simply that all coupling to other electronic states is neglected. If we choose a scaled coordinate system such that the effective mass of every nucleus is M , the total nuclear kinetic energy operator becomes

$$\hat{T}_N = -\frac{\hbar^2}{2M} \nabla_{\mathbf{R}'}^2, \quad (2.3)$$

where \mathbf{R}' is a 3N-dimensional vector formed by 3N nuclear coordinates. In these mass-scaled coordinates, the nuclear wave function $\Psi(\mathbf{R}')$ satisfies

$$\left\{ -\frac{\hbar^2}{2M} \nabla_{\mathbf{R}'}^2 + U_i(\mathbf{R}') - \frac{\hbar^2}{M} \mathbf{F}(\mathbf{R}') \cdot \nabla_{\mathbf{R}'} - \frac{\hbar^2}{2M} \mathbf{G}(\mathbf{R}') \right\} \Psi(\mathbf{R}') = E \Psi(\mathbf{R}') \quad (2.4)$$

where

$$\begin{aligned} \mathbf{F}(\mathbf{R}') &= \langle \psi_{ie}(\mathbf{R}') | \nabla_{\mathbf{R}'} | \psi_{ie}(\mathbf{R}') \rangle \\ \mathbf{G}(\mathbf{R}') &= \langle \psi_{ie}(\mathbf{R}') | \nabla_{\mathbf{R}'}^2 | \psi_{ie}(\mathbf{R}') \rangle \end{aligned} \quad (2.5)$$

In general, $\mathbf{F}(\mathbf{R}')$ must vanish if $\psi_{ie}(\mathbf{R}')$ is chosen to be real. Even if it does not vanish, we can multiply the electronic wave function by a phase factor $e^{if(\mathbf{R}')}$ for which $i\nabla_{\mathbf{R}'} f(\mathbf{R}')$ equal to $-\mathbf{F}(\mathbf{R}')$ in order to cancel out the $\mathbf{F}(\mathbf{R}')$ term.

However, if $\mathbf{F}(\mathbf{R}')$ has non-zero curl, it cannot be made to vanish everywhere by a phase factor with the single-valued function $f(\mathbf{R}')$. The phase factor can still

be determined along any path to make $\mathbf{F}(\mathbf{R}')$ vanish, but there may be a net change in the phase of $\psi_{ie}(\mathbf{R}')$ on traversing a closed path, which means that $\psi_{ie}(\mathbf{R}')$ is no longer a single-valued function of the nuclear configuration \mathbf{R}' .

Consider a case[22] in which one may neglect the spin terms in the electronic Hamiltonian, so that the electronic wave function may always be taken in real form. We can examine the behavior of the electronic wave function near the vicinity of the conical intersection. We imagine, that all but two of the electronic wave functions have been found, and that φ_1 and φ_2 are any two functions which, together with the found solutions, constitute a complete orthonormal set. These functions are assumed independent to the nuclear configuration. It is then possible to express each of the two electronic eigenfunction in the form

$$\psi_e = c_1\varphi_1 + c_2\varphi_2. \quad (2.6)$$

The matrix elements of the electronic Hamiltonian \hat{H}_e are expressed as

$$\begin{aligned} H_{11} &= \langle \varphi_1 | \hat{H}_e | \varphi_1 \rangle \\ H_{22} &= \langle \varphi_2 | \hat{H}_e | \varphi_2 \rangle \\ H_{12} &= H_{21} = \langle \varphi_1 | \hat{H}_e | \varphi_2 \rangle \end{aligned} \quad (2.7)$$

where, the following secular equation must be satisfied

$$\begin{pmatrix} H_{11} - E & H_{12} \\ H_{21} & H_{22} - E \end{pmatrix} \begin{pmatrix} c_1 \\ c_2 \end{pmatrix} = 0 \quad (2.8)$$

All quantities in this equation are real.

In order for equation (2.8) to have degenerate solutions, it is necessary to satisfy two independent conditions, namely,

$$H_{11} = H_{22}, \quad H_{12} = H_{21} = 0 \quad (2.9)$$

and this requires the existence of at least two independently variable nuclear coordinates. We denote a local (x, y, z) coordinate system where the conical intersection happens at $x = y = 0$ with any fixed z . The secular equations may be cast in the following form without any loss of generality:

$$\begin{pmatrix} W + h_1 x - E & ly \\ ly & W + h_2 x - E \end{pmatrix} \begin{pmatrix} c_1 \\ c_2 \end{pmatrix} = 0 \quad (2.10)$$

The eigenvalues are

$$E = W + mx \pm \sqrt{(k^2 x^2 + l^2 y^2)} \quad (2.11)$$

where $m = \frac{1}{2}(h_1 + h_2)$, and $k = \frac{1}{2}(h_1 - h_2)$. It is easy to see that this equation corresponds a double cone with vertex at the origin, as the two potential energy surfaces would form around the conical intersection.

If we define an angle ϕ by the equations

$$kx = d\cos\phi, \quad ly = d\sin\phi \quad (2.12)$$

where

$$d = \sqrt{(k^2 x^2 + l^2 y^2)} > 0 \quad (2.13)$$

The eigenvalues and eigenfunctions are then expressed as

$$E_{\pm} = W + d(\cos\phi \pm 1) \quad (2.14)$$

and

$$|\psi^+\rangle = \sin\frac{\phi}{2} |\varphi_1\rangle + \cos\frac{\phi}{2} |\varphi_2\rangle \quad (2.15)$$

$$|\psi^-\rangle = \cos\frac{\phi}{2} |\varphi_1\rangle - \sin\frac{\phi}{2} |\varphi_2\rangle \quad (2.16)$$

The choice of phase factor in equations (2.15) and (2.16) comes from convention alone, since one can easily verifies that

$$\frac{\partial}{\partial\phi} |\psi^+\rangle = \frac{1}{2} |\psi^-\rangle \quad \frac{\partial}{\partial\phi} |\psi^-\rangle = \frac{1}{2} |\psi^+\rangle \quad (2.17)$$

so that

$$\langle \psi^+ | \frac{\partial}{\partial \phi} | \psi^+ \rangle = \langle \psi^- | \frac{\partial}{\partial \phi} | \psi^- \rangle = 0 \quad (2.18)$$

When one traverses a closed path around the conical intersection, the angle ϕ , increases by 2π , so both eigenfunctions ψ^+ and ψ^- undergo a change of sign (phase change of π). This sign-change is a particular case of Berry's geometric phase[29] which holds not only in the vicinity of the conical intersection point but for any closed path enclosing the conical intersection.

In order to make the electronic wave function single valued, one must draw a cut to the conical intersection point, and have the function change sign on going through the cut. Since the full wave function must be continuous, this would require a compensating discontinuity in the nuclear function. Alternatively, one can add extra complex phase factors to the electronic and nuclear parts of the wave function to enforce the continuity and single-valuedness of each of them. These extra phases add to the nuclear Schrödinger equation a term formally similar to a vector potential associated to a delta-function magnetic field located on the conical intersection line[24,25].

The case of three identical hydrogen atoms near the vertices of an equilateral triangle is shown in the center of Figure 1. According to both the valence-bond and molecular orbital theories, the ground state is of species ${}^2E'$ in the D_{3h} configuration. Let φ_A be the valence-bond wave function for a situation in which the electron on A has spin up and the electrons on B and C are spin-paired; let φ_B and φ_C be similarly defined, so that

$$\varphi_A + \varphi_B + \varphi_C = 0. \quad (2.19)$$

We now take the system around a series of continuous loops in the nuclear geometry configuration of the H_3 system in an equilateral triangle configuration. If we require

the electronic wave function to be real, this cyclic set of deformations changes the sign of that wave function, which as a result is not single-valued. Since the total electronuclear wave function is continuous and single-valued, there has to be a compensating sign change in the nuclear part of the wave function.

3. Schrödinger Equation

In this section, the Schrödinger equation in Jacobi coordinates and in the mass-scaled coordinates of Delves for a three particle system is examined. This discussion is entirely general with regard to the nature of the particles.

We begin with a system of three atoms A_λ , A_ν and A_κ with masses m_λ , m_ν and m_κ , respectively. Let λ, ν, κ be an arbitrary cyclic permutation of α, β, γ . There are three sets of body-fixed Jacobi coordinates, $(\mathbf{R}'_\lambda, \mathbf{r}'_\lambda)$, for this system, where \mathbf{r}'_λ is the vector from atom A_ν to atom A_κ and \mathbf{R}'_λ is the vector from the center of mass of $\{A_\nu, A_\kappa\}$ to the atom A_λ . The index λ can be any of the values α, β or γ . In the present calculations, we neglect all spin-orbit and spin-spin interactions. Under conditions of validity of the Born-Oppenheimer approximation, the electronuclear wave function can be written as a product of the electronic part ψ_e , which we chose to be real, and the nuclear part. The latter can be factored into a nuclear spin part and a spacial part $\psi^{JM\Pi\Gamma}$. J is the total angular momentum quantum number, M its projection onto a laboratory-fixed axis, Π the parity with respect to inversion of the nuclei through the system's center of mass and Γ the irreducible representation of the nuclear permutation group (P_3 for the H_3 system) to which $\Psi^{JM\Pi\Gamma}$, the electro-nuclear wave function excluding the nuclear spin part, belongs:

$$\Psi^{JM\Pi\Gamma} = \psi^{JM\Pi\Gamma}(\mathbf{R}'_\lambda, \mathbf{r}'_\lambda)\psi_e(q_e; \mathbf{R}'_\lambda, \mathbf{r}'_\lambda). \quad (3.1)$$

Here q_e refers to the set of all, spacial and spin, electronic coordinates. $\psi^{JM\Pi\Pi}$ is an eigenfunction of the nuclear motion hamiltonian[11-13] which is required to be single-valued, continuous and differentiable. The Hamiltonian for the three particles in this Jacobi, center of mass coordinate system is

$$\hat{H}_\lambda = \frac{-\hbar^2}{2\mu_{\lambda,\nu\kappa}} \nabla_{\mathbf{R}'_\lambda}^2 - \frac{\hbar^2}{2\mu_{\nu\kappa}} \nabla_{\mathbf{r}'_\lambda}^2 + V'_\lambda(R'_\lambda, r'_\lambda, \gamma_\lambda) \quad (3.2)$$

in which the reduced masses are

$$\mu_{\lambda,\nu\kappa} = \frac{m_\lambda(m_\nu + m_\kappa)}{m_\lambda + m_\nu + m_\kappa}; \quad \mu_{\nu\kappa} = \frac{m_\nu m_\kappa}{m_\nu + m_\kappa}. \quad (3.3)$$

The Born-Oppenheimer potential energy surface V'_λ depends on the interatomic distances R'_λ and r'_λ and on the angle $\gamma_\lambda = \arccos \frac{(\mathbf{R}'_\lambda \cdot \mathbf{r}'_\lambda)}{R'_\lambda r'_\lambda}$.

The Hamiltonian can be put in a simpler form by the introduction of Delves' mass-scaled coordinates[38,39], defined as

$$\mathbf{R}_\lambda = \left(\frac{\mu_{\lambda,\nu\kappa}}{\mu} \right)^{\frac{1}{2}} \mathbf{R}'_\lambda; \quad \mathbf{r}_\lambda = \left(\frac{\mu_{\nu\kappa}}{\mu} \right)^{\frac{1}{2}} \mathbf{r}'_\lambda \quad (3.4)$$

where

$$\mu = \left(\frac{m_\lambda m_\nu m_\kappa}{m_\lambda + m_\nu + m_\kappa} \right)^{\frac{1}{2}} = \left(\frac{m_\alpha m_\beta m_\gamma}{m_\alpha + m_\beta + m_\gamma} \right)^{\frac{1}{2}} \quad (3.5)$$

The Hamiltonian in this mass-scaled, center of mass coordinates is

$$\hat{H}_\lambda = \frac{-\hbar^2}{2\mu} (\nabla_{\mathbf{R}_\lambda}^2 + \nabla_{\mathbf{r}_\lambda}^2) + V_\lambda(R_\lambda, r_\lambda, \gamma_\lambda). \quad (3.6)$$

A change of coordinates, $\lambda \rightarrow \nu$, is a simple orthogonal transformation in the six-dimensional configuration space spanned by $(\mathbf{R}_\lambda, \mathbf{r}_\lambda)$ when the mass scaled coordinates are used. The mass-scaled Schrödinger equation has the same form as that for a single particle of mass μ in a six dimensional space.

The complete symmetry group of the Hamiltonian is the set of all operators which commute with the Hamiltonian and is organized into operator subgroups

which follow naturally from the character of the symmetry operations. Rotational invariance of the Hamiltonian permits us to choose the spatial wave function to belong to an irreducible representation of the subgroup $SO(3)$ of the complete symmetry group of the Hamiltonian. Therefore, the wave function can be chosen to transform as an irreducible representation of $SO(3)$ and it is a simultaneous eigenfunction of \hat{J}^2 and \hat{J}_z .

The discrete symmetry subgroups of the symmetry group of the Hamiltonian are the inversion group, the time-reversal group, and the group of permutations of the identical particles among the system. The inversion group consists of two operators \hat{I} and \hat{E} , where \hat{E} denotes the identity and \hat{I} inverts the spatial coordinates of all the particles through the center of mass. The inversion group has two irreducible representations labelled $\Pi = \pm$. The time reversal subgroup permits us to choose the time-independent wave function to be real function which leads to a symmetric scattering matrix. The final symmetry group is the set of all possible permutations of identical particles. For the H_3 system, it belongs to the P_3 permutation group. It has irreducible representations labelled by $\Gamma \in (A_1, A_2, E)$ and is isomorphic with the point group C_{3v} . The E representation is doubly degenerate while A_1 and A_2 are nondegenerate. In the asymptotic regions of configuration space, the spatial solutions which transform as $A_1(A_2)$ are composed of even (odd) rotational states of the diatomic molecules while those that transform as E contain both even and odd rotational diatomic states.

The existence of symmetry in a physical system leads to the ability to construct solutions to the Schrödinger equation which transform under the symmetry operations as irreducible representations of the operator groups. We will show later how permutational symmetry of the total electronuclear wave function with respect to interchange of nuclei can be enforced in the Born-Oppenheimer approximation

both in the presence and the absence of conical intersections. The treatment of nuclear motion wave functions in the presence of conical intersections and the treatment of nuclear interchange symmetry in general both require careful consideration of the phases of the electronic and nuclear motion wave functions, and this will be discussed in detail later.

4. Symmetrized Hyperspherical Coordinates

It has been proposed[34,35] and validated[11-14,17] that symmetrized hyperspherical coordinates which are derived from the $\mathbf{R}_\lambda, \mathbf{r}_\lambda, \gamma_\lambda$ coordinates are well suited for three dimensional reactive atom-diatom scattering. There is more than one possible set of hyperspherical coordinates[40-45] which may be used for the calculations. All these coordinates share the same spirit to treat all three arrangement channels in equivalent ways.

We use a set of principal-axis body-fixed hyperspherical coordinates closely related to the modified Whitten-Smith coordinates[41,42,46]. Three of the 5 hyperangles are the Euler angles ($\alpha\beta\gamma$) which specify the orientation of the body frame in space. The other two are the symmetrized hyperangles (θ, ϕ_λ) obtained by a rotation of the internal configuration space axis described previously[34] through Euler angles ($\frac{\pi}{2}, \frac{\pi}{2}, \pi$). The angle θ is in the $[0, \frac{\pi}{2}]$ range and ϕ_λ in the $[0, 2\pi)$ range. These two angles describe the shape of the molecular triangle, such that $\theta = \pi/2$ corresponds to linear configurations and $\theta = 0$ to symmetric top configurations. The quantization axis Z for the internal motion is chosen to be the axis of least inertia and the Y axis is associated to the axis of maximum inertia, perpendicular to the molecular plane. This choice enables one to minimize coupling due to rotation of the body frame at linear or near-linear configurations[17,46].

The cartesian components of r_λ and R_λ in this body-fixed frame are given by

$$r_{\lambda X} = -\rho \sin(\pi/4 - \theta/2) \cos(\phi_\lambda/2); \quad (4.1a)$$

$$r_{\lambda Y} = 0; \quad (4.1b)$$

$$r_{\lambda Z} = \rho \cos(\pi/4 - \theta/2) \sin(\phi_\lambda/2); \quad (4.1c)$$

$$R_{\lambda X} = \rho \sin(\pi/4 - \theta/2) \sin(\phi_\lambda/2); \quad (4.1d)$$

$$R_{\lambda Y} = 0; \quad (4.1e)$$

$$R_{\lambda Z} = \rho \cos(\pi/4 - \theta/2) \cos(\phi_\lambda/2). \quad (4.1f)$$

The corresponding Hamiltonian is expressed as

$$\hat{H}_\lambda = \hat{T}(\rho) + \hat{h}_\lambda(\zeta_\lambda; \rho) \quad (4.2)$$

where we have defined the quantity ζ_λ to represent all five hyperangles in the λ arrangement channel: $\alpha, \beta, \gamma, \theta, \phi_\lambda$. The hyperradial kinetic energy operator $\hat{T}(\rho)$ has the form

$$\hat{T}(\rho) = -\frac{\hbar^2}{2\mu} \rho^{-5} \frac{\partial}{\partial \rho} \rho^5 \frac{\partial}{\partial \rho} = -\frac{\hbar^2}{2\mu} \rho^{-\frac{5}{2}} \frac{\partial^2}{\partial \rho^2} \rho^{\frac{5}{2}} + \frac{15\hbar^2}{8\mu\rho^2} \quad (4.3)$$

and the surface hamiltonian $\hat{h}_\lambda(\zeta_\lambda; \rho)$ is

$$\hat{h}_\lambda(\zeta_\lambda; \rho) = \frac{\hat{\Lambda}^2(\zeta_\lambda)}{2\mu\rho^2} + V(\rho, \theta, \phi_\lambda). \quad (4.3)$$

The square of the grand canonical angular momentum operator $\hat{\Lambda}^2$ can be expressed in terms of these angles as

$$\hat{\Lambda}^2 = \hat{\Lambda}_\circ^2 + \frac{4\hat{J}_Z^2}{\cos^2\theta} + \hat{R} \quad (4.4)$$

where $\hat{\Lambda}_\circ^2$ and \hat{R} are given by

$$\hat{\Lambda}_\circ^2 = -4\hbar^2 \left[\frac{1}{\sin 2\theta} \frac{\partial}{\partial \theta} \sin 2\theta \frac{\partial}{\partial \theta} + \frac{1}{\sin^2 \theta} \frac{\partial^2}{\partial \phi_\lambda^2} \right] \quad (4.5)$$

$$\hat{R} = \frac{1}{\cos^2(\frac{\pi}{4} - \frac{\theta}{2})} \left[\frac{\hat{J}^2 - \hat{J}_Z^2}{2} + \frac{\hat{J}_+^2 + \hat{J}_-^2}{4} - \hat{J}_Z^2 + \frac{1}{\sin^2\theta} \left[\frac{\hat{J}^2 - \hat{J}_Z^2}{2} - \frac{\hat{J}_+^2 + \hat{J}_-^2}{4} \right] \right] - 2\hbar \frac{\cos\theta}{\sin^2\theta} (\hat{J}_+ + \hat{J}_-) \frac{\partial}{\partial\phi_\lambda} \quad (4.6)$$

\hat{J}_Z being the body-fixed Z component of the total angular momentum \hat{J} , and $\hat{J}_\pm = \hat{J}_X \pm i\hat{J}_Y$.

This principal-axis hyperspherical formalism has an attractive feature in which the quantization axis for the internal motion is the axis of lowest inertia where the Coriolis coupling remains minimal in that frame. Calculations[17,47] neglecting them still yield good results for low partial waves at low energy, while strongly coupled states are notably reduced.

5. Expansion of the Partial Waves in terms of Pseudo Surface Functions

Since the Hamiltonian operator (4.2) commutes with \hat{J}^2 , \hat{J}_z , \hat{I} and permutation operator \hat{P} , we can expand the wave function of the system in terms of their simultaneous eigenfunctions $\Psi^{JM\Pi\Gamma k}(\rho, \zeta_\lambda)$:

$$\Psi(\rho, \zeta_\lambda) = \sum_{J=0}^{\infty} \sum_{M=-J}^J C_\lambda^{JM} \sum_{\Pi=0}^1 \sum_{\Gamma} \sum_{k=1}^{n_\Gamma} \Psi^{JM\Pi\Gamma k}(\rho, \zeta_\lambda). \quad (5.1)$$

The partial wave functions $\Psi^{JM\Pi\Gamma k}(\rho, \zeta_\lambda)$ simultaneously satisfy the equations

$$\hat{H}_\lambda(\rho, \zeta_\lambda) \Psi^{JM\Pi\Gamma k}(\rho, \zeta_\lambda) = E \Psi^{JM\Pi\Gamma k}(\rho, \zeta_\lambda) \quad (5.2)$$

$$\hat{J}^2(\theta_\lambda, \phi_\lambda, \psi_\lambda) \Psi^{JM\Pi\Gamma k}(\rho, \zeta_\lambda) = \hbar^2 J(J+1) \Psi^{JM\Pi\Gamma k}(\rho, \zeta_\lambda) \quad (5.3)$$

$$\hat{J}_z(\phi_\lambda) \Psi^{JM\Pi\Gamma k}(\rho, \zeta_\lambda) = \hbar M \Psi^{JM\Pi\Gamma k}(\rho, \zeta_\lambda) \quad (5.4)$$

$$\hat{I}(\theta_\lambda, \phi_\lambda, \psi_\lambda) \Psi^{JM\Pi\Gamma k}(\rho, \zeta_\lambda) = (-1)^\Pi \Psi^{JM\Pi\Gamma k}(\rho, \zeta_\lambda) \quad (5.5)$$

$$\hat{P}_{ii}^{\Gamma'}(\zeta_\lambda) \Psi^{JM\Pi\Gamma k}(\rho, \zeta_\lambda) = \delta_\Gamma^{\Gamma'} \delta_i^k \Psi^{JM\Pi\Gamma k}(\rho, \zeta_\lambda). \quad (5.6)$$

We now define a set of five-dimensional pseudo surface functions $\Phi_{n\Omega}^{JM\Pi\Pi}$ at the hyperradius $\bar{\rho}$ for the expansion of the six dimensional scattering wave function $\Psi^{JM\Pi\Pi^*}(\rho, \zeta_\lambda)$ by

$$\Phi_{n\Omega}^{JM\Pi\Pi}(\alpha, \beta, \gamma, \theta, \phi_\lambda; \bar{\rho}) = \varphi_n^{\Omega\Pi\Pi}(\theta, \phi_\lambda; \bar{\rho}) N_\Omega^{JM\Pi}(\alpha, \beta, \gamma) \quad (5.7)$$

The functions $N_\Omega^{JM\Pi}$ are linear combinations of Wigner rotation matrices with definite parity $\Pi = \pm 1$ [17,48].

$$N_\Omega^{JM\Pi} = \sqrt{\frac{2J+1}{16\Pi^2(1+\delta_{\Omega 0})}} [D_{M\Omega}^{J*}(\alpha, \beta, \gamma) + (-1)^{\Pi+J+\Omega} D_{M,-\Omega}^{J*}(\alpha, \beta, \gamma)] \quad (5.8)$$

where $\Omega \geq 0$ is the absolute magnitude of the quantum number for the projection of the total angular momentum onto the body-fixed Z axis.

The $\varphi_n^{\Omega\Pi\Pi}$ are Ω - and $\bar{\rho}$ -dependent eigenfunctions of the hamiltonian

$$\hat{H}^\Omega(\theta, \phi_\lambda; \bar{\rho}) = \frac{1}{2\mu\bar{\rho}^2} (\hat{\Lambda}_\circ^2 + \frac{4\Omega^2}{\cos^2\theta}) + V(\theta, \phi_\lambda; \bar{\rho}). \quad (5.9)$$

These eigenfunctions are obtained variationally by expanding them in a body-fixed basis $\chi_{n_\theta n_\phi}^{\Pi\Pi\Omega}$ built from products of simple analytical functions[17]:

$$\chi_{n_\theta n_\phi}^{\Pi\Pi\Omega}(\theta, \phi_\lambda) = f_{n_\theta}^\Omega(\theta) g_{n_\phi}^{\Pi\Pi\Omega}(\phi_\lambda) \quad (5.10)$$

where n_θ and n_ϕ are integers or half-odd integers, and $f_{n_\theta}^\Omega(\theta)$ and $g_{n_\phi}^{\Pi\Pi\Omega}(\phi_\lambda)$ are simple linear combinations of trigonometric functions.

The functions $f_{n_\theta}^\Omega(\theta)$ can be chosen as the functions $\cos(n_\theta\theta)$ or $\sin(n_\theta\theta)$, with n_θ integer or half-odd integer, in terms of which the hyperspherical harmonics can be written as polynomials in $\cos\theta$ [7,49-51]. Table 1 indicates how to choose the functions of $g_{n_\phi}^{\Pi\Pi\Omega}(\phi_\lambda)$ to obtain electronuclear wavefunctions with correct P_3 permutation symmetries, with and without the effect of the geometric phase.

We now focus our attention on the special case of three identical nuclei and describe how to build electronuclear wave function $\Psi^{JM\Pi\Gamma}$ which are bases for the irreducible representation of the P_3 permutation group of the three identical nuclei. The operations of this group correspond to simple changes in ϕ_λ (which are related to the isomorphism between P_3 and C_{3v}) as indicated in Table II.

If there is no conical intersection between electronic states, a non-degenerate electronic wave function $\psi_e(q_e; \rho\xi)$ belongs to a one-dimensional representation of the nuclear permutation group (A_1 for symmetric with respect to pairwise permutation of nuclei, or A_2 for antisymmetric with respect to pairwise permutation of nuclei), and is also single-valued with respect to the nuclear configuration. For this reason, the nuclear wave function also needs to be single-valued, which subsequently means that $|n_\phi|$ has to be an integer.

For even parity, even Ω quantum number, with $|n_\phi| = 3m$, basis functions defined in Table I will give $\sin(3m\phi_\lambda)$ (an A_2 -type function) or $\cos(3m\phi_\lambda)$ (an A_1 -type function). For even parity, even Ω quantum number, with $|n_\phi| = 3m \pm 1$, pairs of basis functions of the form $\begin{pmatrix} \sin(3m \pm 1) \\ \cos(3m \pm 1) \end{pmatrix}$ with m integer can be easily proven to form an E irreducible representation of the P_3 permutation group.

If there is a conical intersection between two electronic states for the equilateral triangular configuration of the nuclei and if the geometric phase effect is taken into account, in the vicinity of the conical intersection ($\phi_\lambda = 0$) the ϕ_λ dependence of those two non-degenerate Born-Oppenheimer electronic wave function is given by (2.15) and (2.16)

$$|\psi_e^-\rangle = \cos\frac{\phi_\lambda}{2} |\psi_e^{E_1}\rangle - \sin\frac{\phi_\lambda}{2} |\psi_e^{E_2}\rangle \quad (\text{lower energy}) \quad (5.11)$$

$$|\psi_e^+\rangle = \cos\frac{\phi_\lambda}{2} |\psi_e^{E_2}\rangle + \sin\frac{\phi_\lambda}{2} |\psi_e^{E_1}\rangle \quad (\text{higher energy}) \quad (5.12)$$

where $\psi_e^{E_1}$, $\psi_e^{E_2}$ are two degenerate ρ -dependent but ϕ_λ independent states at $\phi_\lambda = 0$ which form a basis for the E irreducible representation of P_3 ($\psi_e^{E_1}$ being symmetric for the pairwise permutation of nuclei and $\psi_e^{E_2}$ being antisymmetric for the pairwise permutation of nuclei). Under the permutation operation of the P_3 permutation group, although $\psi_e^{E_1}$ and $\psi_e^{E_2}$ do not depend on ϕ_λ explicitly, the permutation operation does change the internal coordinate system in which $\psi_e^{E_1}$ and $\psi_e^{E_2}$ are described. If we take the active view of those symmetric operations, then $\psi_e^{E_1}$ and $\psi_e^{E_2}$ would behave like a pair of unit vectors under the C_{3v} point group operations, except that the rotation angles are -120° and -240° instead of 120° and 240° as described in Table II.

As mentioned before, ψ_e^- and ψ_e^+ are both singlet (non-degenerate) electronic states with their phase factors to be chosen in such a way as make both of them real functions. Their behavior under the operation of the P_3 nuclear permutation is also listed in Table II. It can be seen that although permutation of the nuclei can only change the sign of ψ_e^+ and ψ_e^- , these Born-Oppenheimer electronic wave functions do not belong to any one-dimensional irreducible representation of P_3 and they are discontinuous in the internal configuration space when crossing the plane of $\phi_\lambda = 0$.

However, we can build continuous electronuclear wave functions that do form irreducible representation of P_3 by using the new set of n_ϕ values as indicated in Table I. For example, with even parity, even Ω quantum number, and with the choice of $n_\phi = 3m + \frac{3}{2}$, we can form basis functions $\sin(3m + \frac{3}{2})\phi_\lambda$ and $\cos(3m + \frac{3}{2})\phi_\lambda$ which behave as

$$\sin(3m + \frac{3}{2})\phi_\lambda | \psi_e^- \rangle \rightarrow A_1 \quad ? \quad (5.13)$$

and

$$\cos(3m + \frac{3}{2})\phi_\lambda | \psi_e^+ \rangle \rightarrow A_2. \quad \checkmark \quad (5.14)$$

It can also be proven that for even parity, even Ω quantum number, the pairs of functions

$$\begin{pmatrix} \sin(3m \pm \frac{1}{2}) | \psi_e^+ \rangle \\ \cos(3m \pm \frac{1}{2}) | \psi_e^+ \rangle \end{pmatrix} \quad (5.15)$$

and

$$\begin{pmatrix} \sin(3m \pm \frac{1}{2}) | \psi_e^- \rangle \\ \cos(3m \pm \frac{1}{2}) | \psi_e^- \rangle \end{pmatrix} \quad (5.16)$$

form E irreducible representation of P_3 nuclear permutation group.

The pseudo surface functions $\Phi_{n\Omega}^{JM\Pi\Gamma}$, in addition to being discrete, span the three arrangement channels and provide an effective basis set in which to expand the scattering wave function. We expand the six-dimensional scattering wave functions as

$$\psi^{JM\Pi\Gamma}(\alpha, \beta, \gamma, \theta, \phi_\lambda, \rho) = \frac{1}{\rho^{5/2}} \sum_{n\Omega} b_{n\Omega}^{JM\Pi\Gamma}(\rho; \bar{\rho}) \Phi_{n\Omega}^{JM\Pi\Gamma}(\alpha, \beta, \gamma, \theta, \phi_\lambda; \bar{\rho}) \quad (5.17)$$

where the pseudo surface functions are calculated at $\bar{\rho}$. This is an efficient expansion when ρ is near $\bar{\rho}$. In this sense we say that the pseudo surface function basis set is a local basis set. In addition, due to the factorization of pseudo surface functions into an internal part $\varphi_n^{\Omega\Pi\Gamma}$, which is independent of total angular momentum J , and an external part $N_\Omega^{JM\Pi}$, the evaluation of matrix elements from the expansion become easy. As a result of the isotropicity of space and the indistinguishability of the particles, it can be shown that the coefficients in the expansion are independent of M , so these labels do not appear in the differential equation for the coefficients. Since the parameter rb is considered to be fixed in any given expansion, the pseudo surface function basis set is diabatic in ρ .

The expansion in pseudo surface functions yields the following set of coupled ordinary differential equations in the variable ρ :

$$\left[-\frac{\hbar^2}{2\mu} \frac{d^2}{d\rho^2} + \frac{15\hbar^2}{8\mu\rho^2} + \frac{\bar{\rho}^2}{\rho^2} \epsilon_n^{\Gamma\Omega}(\bar{\rho}) - E \right] b_{n\Omega}^{JM\Pi\Gamma}(\rho; \bar{\rho}) + \sum_{n'} U_{nn'}^{\Pi\Gamma\Omega}(\rho; \bar{\rho}) b_{n'\Omega}^{JM\Pi\Gamma}(\rho; \bar{\rho})$$

$$\begin{aligned}
& + \frac{\hbar^2}{2\mu\rho^2} \sum_{n'} W_{nn'}^{\Pi\Gamma\Omega}(\rho; \bar{\rho}) b_{n',\Omega}^{J\Pi\Gamma}(\rho; \bar{\rho}) + \frac{\hbar^2}{\mu\rho^2} \sum_{n'} X_{nn',\Omega\pm 1}^{\Pi\Gamma,\Omega}(\rho; \bar{\rho}) b_{n',\Omega\pm 1}^{J\Pi\Gamma}(\rho; \bar{\rho}) \\
& + \frac{\hbar^2}{4\mu\rho^2} \sum_{n'} Y_{nn',\Omega\pm 2}^{\Pi\Gamma,\Omega}(\rho; \bar{\rho}) b_{n',\Omega\pm 2}^{J\Pi\Gamma}(\rho; \bar{\rho}) = 0
\end{aligned} \tag{5.18}$$

where

$$\Omega = \begin{cases} 0, 1, 2, \dots, J & \text{for } J + \Pi \text{ even;} \\ 1, 2, 3, \dots, J & \text{for } J + \Pi \text{ odd;} \end{cases}$$

with coupling matrix elements given by

$$U_{nn'}^{\Pi\Gamma\Omega}(\rho; \bar{\rho}) = \langle \varphi_n^{\Pi\Gamma\Omega} | V(\theta, \phi_\lambda, \rho) - \frac{\bar{\rho}^2}{\rho^2} V(\theta, \phi_\lambda; \bar{\rho}) | \varphi_{n'}^{\Pi\Gamma\Omega} \rangle \tag{5.19a}$$

$$\begin{aligned}
W_{nn'}^{\Pi\Gamma\Omega}(\rho; \bar{\rho}) &= [J(J+1)] \langle \varphi_n^{\Pi\Gamma\Omega} | \frac{1}{1+\sin\theta} + \frac{1}{2\sin^2\theta} | \varphi_{n'}^{\Pi\Gamma\Omega} \rangle \\
-\Omega^2 \langle \varphi_n^{\Pi\Gamma\Omega} | \frac{3}{1+\sin\theta} + \frac{1}{2\sin^2\theta} | \varphi_{n'}^{\Pi\Gamma\Omega} \rangle &
\end{aligned} \tag{5.19b}$$

$$\begin{aligned}
X_{nn',\Omega\pm 1}^{\Pi\Gamma,\Omega} &= -\xi_+(J, \Omega) \frac{\eta_{J,\Omega+1}}{\eta_{J,\Omega}} \langle \varphi_n^{\Pi\Gamma\Omega} | \frac{\cos\theta}{\sin^2\theta} | \frac{\partial \varphi_{n'}^{\Pi\Gamma,\Omega+1}}{\partial \phi_\lambda} \rangle \\
&+ \xi_-(J, \Omega) \frac{\eta_{J,\Omega-1}}{\eta_{J,\Omega}} \langle \varphi_n^{\Pi\Gamma\Omega} | \frac{\cos\theta}{\sin^2\theta} | \frac{\partial \varphi_{n'}^{\Pi\Gamma,\Omega-1}}{\partial \phi_\lambda} \rangle
\end{aligned} \tag{5.19c}$$

$$\begin{aligned}
Y_{nn',\Omega\pm 2}^{\Pi\Gamma\Omega} &= \xi_+(J, \Omega) \xi_+(J, \Omega+1) \frac{\eta_{J,\Omega+2}}{\eta_{J,\Omega}} \langle \varphi_n^{\Pi\Gamma\Omega} | \frac{1}{1+\sin\theta} - \frac{1}{2\sin^2\theta} | \varphi_{n'}^{\Pi\Gamma,\Omega+2} \rangle \\
&+ \xi_-(J, \Omega) \xi_-(J, \Omega-1) \frac{\eta_{J,\Omega-2}}{\eta_{J,\Omega}} \langle \varphi_n^{\Pi\Gamma\Omega} | \frac{1}{1+\sin\theta} - \frac{1}{2\sin^2\theta} | \varphi_{n'}^{\Pi\Gamma,\Omega-2} \rangle
\end{aligned} \tag{5.19d}$$

where $\eta_{J,\Omega}$, $\eta_{J,\Omega\pm 1}$, $\eta_{J,\Omega\pm 2}$ are normalization constants for $N_\Omega^{JM\Pi}(\alpha, \beta, \gamma)$, $N_{\Omega\pm 1}^{JM\Pi}(\alpha, \beta, \gamma)$ and $N_{\Omega\pm 2}^{JM\Pi}(\alpha, \beta, \gamma)$ functions. The coupling constants $\xi_\pm(i, k)$ are defined as

$$\xi_\pm(i, k) = [i(i+1) - k(k\pm 1)]^{1/2}. \tag{5.20}$$

The coupling matrix is penta-diagonal in Ω and can be evaluated efficiently by 2D-numerical quadratures. The potential energy coupling matrix \mathbf{U} is independent of J and connects states with the same Ω which only needs to be calculated at the boundaries and the middle of each sector. For the coupling matrix elements

W, X, Y , the integrals over $\theta\phi_\lambda$ are independent of J , the J dependence arising from the analytically known matrix elements of the total angular momentum body-fixed frame components.

Pseudo surface functions at single rb are not efficient for expanding the wave function for all values of ρ . The strategy is to calculate a set of pseudo surface functions at each of a family of values of the hyperradius $\bar{\rho}_i$, $i = 0, 1, 2, 3\dots$ For each value of $\bar{\rho}_i$, the system of ordinary differential equations is integrated as an initial value problem. The range of ρ over which a single pseudo surface function set is used is called a sector. With the exception of the very first sector beginning at ρ_0 , the initial conditions follow from continuity of the wave function and its ρ derivative between sectors. This is accomplished by imposing the conditions

$$b_n^{J\Pi\Pi}(\rho_{i,i+1}; \bar{\rho}_{i+1}) = \sum_{n'} b_{n'}^{J\Pi\Pi}(\rho_{i,i+1}; \bar{\rho}_i) [\mathcal{O}^{J\Pi\Pi}]_n^{n'}(\bar{\rho}_{i+1}, \bar{\rho}_i); \quad (5.21)$$

$$\left(\frac{\partial b_n^{J\Pi\Pi}(\rho; \bar{\rho}_{i+1})}{\partial \rho} \right)_{\rho \rightarrow \rho_{i,i+1}^{(+)}} = \sum_{n'} \left(\frac{\partial b_{n'}^{J\Pi\Pi}(\rho; \bar{\rho}_i)}{\partial \rho} \right)_{\rho \rightarrow \rho_{i,i+1}^{(-)}} [\mathcal{O}^{J\Pi\Pi}]_n^{n'}(\bar{\rho}_{i+1}, \bar{\rho}_i); \quad (5.22)$$

in which the overlap matrices $\mathcal{O}^{J\Pi\Pi}$ are defined by

$$[\mathcal{O}^{J\Pi\Pi}]_n^{n'}(\bar{\rho}_{i+1}, \bar{\rho}_i) = \left\langle \Phi_n^{JM\Pi\Pi k}(\zeta_\lambda; \bar{\rho}_{i+1}) \left| \Phi_{n'}^{JM\Pi\Pi k}(\zeta_\lambda; \bar{\rho}_i) \right. \right\rangle. \quad (5.23)$$

These matrices are also independent of M .

For small values of the hyperradius for which the three atoms interact strongly, simple trigonometric basis functions proved to form an efficient set in which to expand the electronuclear wavefunctions $\Psi^{JM\Pi\Pi}$. However, for large values of the hyperradius for which the system has nearly separated into an atom and a diatom, the nuclear wavefunction is highly localized in each arrangement channel. This localization makes the trigonometric basis set inefficient and suggests the use of a basis set based on the previously defined symmetrized hyperspherical coordinates

$\omega_\lambda, \gamma_\lambda$ [34,35] defined by $\omega_\lambda = 2\arctan(r_\lambda/R_\lambda)$ and $\gamma_\lambda = \arccos(\mathbf{R}_\lambda \cdot \mathbf{r}_\lambda/R_\lambda r_\lambda)$, instead. These are related to θ, ϕ_λ by the transformation

$$\sin\theta\cos\theta = \cos\omega_\lambda; \quad (5.24a)$$

$$\sin\theta\sin\phi_\lambda = \sin\omega_\lambda\cos\gamma_\lambda; \quad (5.24b)$$

$$\cos\theta = \sin\omega_\lambda\sin\gamma_\lambda. \quad (5.24c)$$

The basis set based on ω_λ and γ_λ for large values of ρ has previously been shown to be very efficient[13]. The pseudo surface functions are now expanded in a product basis[13] of Legendre polynomials in $\cos\gamma_\lambda$ and vibrational type functions in ω_λ . Since product bases associated to different arrangement channels do not overlap for large values of ρ , the pseudo surface functions which include the geometric phase differ from the ones which exclude it only by simple changes in the signs of the pieces of the wave function within each arrangement channel. The geometric phase can be included straightforwardly in this region since it does not change the overlap and potential coupling matrices.

Equation (5.18) for the ρ -dependent part of the wavefunction has as many linearly independent solutions as there are pseudo surface functions in the expansion. We may write (5.18) in matrix form as

$$\ddot{\mathbf{b}}^{J\Pi\Gamma}(\rho; \bar{\rho}_i) = \mathbf{K}(\rho, \bar{\rho}_i)\mathbf{b}^{J\Pi\Gamma}(\rho; \bar{\rho}_i) \quad (5.25)$$

where

$$\mathbf{K} = \frac{2\mu}{\hbar^2}\mathbf{U} + \frac{1}{\rho^2}\mathbf{W} + \frac{2}{\rho^2}\mathbf{X} + \frac{1}{2\rho^2}\mathbf{Y} - \mathbf{k}^2 \quad (5.26)$$

in which

$$[\mathbf{k}^2(\rho, \bar{\rho}_i)]_n^{n'} = \frac{2\mu}{\hbar^2}\delta_n^{n'} \left(E - \frac{15\hbar^2}{8\mu\rho^2} - \left(\frac{\bar{\rho}_i}{\rho} \right)^2 \epsilon_n^{\Gamma\Omega}(\bar{\rho}_i) \right). \quad (5.27)$$

If we define the logarithmic derivative[52] of the $\mathbf{b}^{J\Pi\Gamma}$ matrix of coefficients to be

$$\mathcal{Y}^{J\Pi\Gamma}(\rho; \bar{\rho}_i) = \dot{\mathbf{b}}^{J\Pi\Gamma}(\rho, \bar{\rho}_i) (\mathbf{b}^{J\Pi\Gamma}(\rho, \bar{\rho}_i))^{-1} \quad (5.28)$$

we find by differentiation of (5.28) and using (5.25) that \mathcal{Y} satisfies the matrix Ricatti-Bessel equation

$$\dot{\mathcal{Y}}^{\text{JIII}}(\rho; \bar{\rho}_i) = \mathbf{K}(\rho, \bar{\rho}_i) - \left(\mathcal{Y}^{\text{JIII}}(\rho; \bar{\rho}_i) \right)^2. \quad (5.29)$$

We have used a version of Johnson's logarithmic derivative integrator[52], modified to include the improvements suggested by Manolopoulos[53], for integrating the matrix Ricatti-Bessel equation. In this method, the initial log derivative matrix is set to correspond to a wavefunction with very small amplitude, and the matrix is propagated according to the rules

$$\mathbf{Z}_0 = \mathbf{P} + \Delta\rho \mathcal{Y}(\rho_0) + \mathbf{V}_0$$

$$\mathbf{Z}_i = 2\mathbf{P} + \mathbf{V}_i + \mathbf{Q}[\mathbf{Z}_{i-1}]^{-1}\mathbf{Q}; \quad i = 1, N_I - 1 \quad (5.30)$$

$$\mathcal{Y}(\rho_{N_I}) = (\mathbf{P} + \mathbf{V}_{N_I} + \mathbf{Q}[\mathbf{Z}_{N_I-1}]^{-1}\mathbf{Q})/\Delta\rho$$

where

$$[\mathbf{P}]_n^{n'} = \delta_n^{n'} \begin{cases} \Delta\rho p_n \coth(\Delta\rho p_n) & p_n^2 \geq 0 \\ \Delta\rho |p_n| \cot(\Delta\rho |p_n|) & p_n^2 < 0 \end{cases} \quad (5.31)$$

$$[\mathbf{Q}]_n^{n'} = \delta_n^{n'} \begin{cases} \Delta\rho p_n / \sinh(\Delta\rho p_n) & p_n^2 \geq 0 \\ \Delta\rho |p_n| / \sin(\Delta\rho |p_n|) & p_n^2 < 0 \end{cases} \quad (5.32)$$

and there are N_I steps of size $\Delta\rho = (\rho_{N_I} - \rho_0)/N_I$ between calculations of the log derivative \mathcal{Y} . The potential terms \mathbf{V}_i are given by

$$\mathbf{V}_i = \begin{cases} \frac{\Delta\rho}{3} \mathbf{U}_i & i = 0, N_I \\ \frac{2\Delta\rho}{3} \mathbf{U}_i & i = 2, 4, 6, \dots, N_I - 2 \\ 8\mathbf{I} - 8 \left[\mathbf{I} - \frac{\Delta\rho^2}{6} \mathbf{U}_i \right]^{-1} & i = 1, 3, 5, \dots, N_I - 1 \end{cases} \quad (5.33)$$

with the matrix \mathbf{U} defined as

$$\mathbf{U} = \mathbf{K} - \mathbf{K}_{\text{ref}} \quad (5.34)$$

where

$$\begin{aligned} [\mathbf{K}_{\text{ref}}]_n^{n'} &= \delta_n^{n'} [\mathbf{K}_{\frac{N}{2}}]_n^n \\ &= \delta_n^{n'} p_n^2 \end{aligned} \quad (5.35)$$

with $K_{\frac{N}{2}}$ being the value of K at the center of the interval between calculations of \mathcal{Y} .

Because U is independent of E , this version of the logarithmic derivative integrator[53] can effectively eliminate $\frac{1}{3}$ of operations and computer time necessary for the second and subsequent energies. In addition, it allows one to start the integration at a larger value of $\bar{\rho}$ than the previous version would permit.

6. Asymptotic Analysis

In this section, the asymptotic boundary conditions are considered. To obtain differential and integral cross sections, it is necessary to use an asymptotic form which corresponds to the physical conditions of a scattering process. The numerical solutions to the Schrödinger equation are labelled by J, II , and Γ whereas the asymptotic boundary conditions which represent a scattering experiment have no such labels. Therefore, construct the P_3 irreducible representation space-fixed scattering wave function first and then transforming it to the helicity form will be a most straightforward procedure

An asymptotic form which describes a scattering experiment has an incident plane wave multiplying the initial state wave function of the diatomic molecule and outgoing spherical waves multiplying each energetically accessible diatom state. One possible form for the asymptotic scattering spatial wave function arises if we assume the particles are distinguishable. The coordinates and diatom rotational angular momentum projection quantum numbers are referred to the laboratory-fixed axes. The boundary conditions for energies significantly below the dissociation

energy are given as:

$$\begin{aligned} \Psi_{\bar{\lambda}}^{\lambda' \nu' j'_{\lambda'} m'_{\lambda'}} \underset{R_{\bar{\lambda}} \rightarrow \infty}{\sim} \sum_{\lambda} \sum_{\nu_{\lambda} j_{\lambda} m_{\lambda}} \left[e^{i \mathbf{k}_{\lambda \nu_{\lambda} j_{\lambda}} \cdot \mathbf{R}_{\lambda}} \delta_{\lambda \nu_{\lambda} j_{\lambda} m_{\lambda}}^{\lambda' \nu' j'_{\lambda'} m'_{\lambda'}} \right. \\ \left. + \hat{f}_{\lambda \nu_{\lambda} j_{\lambda} m_{\lambda}}^{\lambda' \nu' j'_{\lambda'} m'_{\lambda'}}(\theta_{\lambda}, \phi_{\lambda}) \frac{e^{i k_{\lambda \nu_{\lambda} j_{\lambda}} R_{\lambda}}}{R_{\lambda}} \right] \varphi_{\lambda \nu_{\lambda} j_{\lambda} m_{\lambda}}^{\text{sf}}(\mathbf{r}_{\lambda}) \end{aligned} \quad (6.1)$$

where $\{\lambda', \nu', \kappa'\}$ is a cyclic permutation of the arrangement channel indices $\{\alpha, \beta, \gamma\}$ and $\bar{\lambda}$ is a fixed but otherwise arbitrary channel index which corresponds to the asymptotic arrangement channel under examination. The coefficients $\hat{f}_{\lambda \nu_{\lambda} j_{\lambda} m_{\lambda}}^{\lambda' \nu' j'_{\lambda'} m'_{\lambda'}}$ are the space-fixed scattering amplitudes and contain the information needed for the cross section determination. The diatomic wavefunction $\varphi_{\lambda \nu_{\lambda} j_{\lambda} m_{\lambda}}^{\text{sf}}$ is given in space-fixed coordinates by

$$\varphi_{\lambda \nu_{\lambda} j_{\lambda} m_{\lambda}}^{\text{sf}}(\mathbf{r}_{\lambda}) = Y_{j_{\lambda}}^{m_{\lambda}}(\theta_{\mathbf{r}_{\lambda}}, \phi_{\mathbf{r}_{\lambda}}) \frac{\phi_{\lambda \nu_{\lambda} j_{\lambda}}(r_{\lambda})}{r_{\lambda}} \quad (6.2)$$

where $\theta_{\mathbf{r}_{\lambda}}$ and $\phi_{\mathbf{r}_{\lambda}}$ are the polar coordinates of \mathbf{r}_{λ} with respect to the space-fixed \mathbf{Z} axis. The quantum number ν_{λ} labels the vibrational levels for a given j_{λ} where $j_{\lambda}(j_{\lambda} + 1)\hbar^2$ is the square of the diatom rotational angular momentum. The projection of the diatom rotational angular momentum onto the space-fixed \mathbf{Z} axis is $m_{\lambda}\hbar$. The quantum numbers ν_{λ} , j_{λ} and m_{λ} are labeled with the subscript λ to differentiate between the states of distinguishable diatomic molecules.

The corresponding boundary conditions for the body-fixed helicity representation are given by[2]

$$\begin{aligned} \Psi_{\bar{\lambda}}^{\lambda' \nu' j'_{\lambda'} m'_{\lambda'}} \underset{R_{\bar{\lambda}} \rightarrow \infty}{\sim} e^{i \mathbf{k}_{\lambda' \nu' j'_{\lambda'}} \cdot \mathbf{R}_{\lambda'}} \varphi_{\lambda' \nu' j'_{\lambda'} m'_{\lambda'}}^{\text{sf}}(\mathbf{r}_{\lambda'}) \\ + \sum_{\lambda} \sum_{\nu_{\lambda} j_{\lambda} \Omega_{\lambda}} f_{\lambda \nu_{\lambda} j_{\lambda} \Omega_{\lambda}}^{\lambda' \nu' j'_{\lambda'} m'_{\lambda'}}(\theta_{\lambda}, \phi_{\lambda}) \frac{e^{i k_{\lambda \nu_{\lambda} j_{\lambda}} R_{\lambda}}}{R_{\lambda}} \varphi_{\lambda \nu_{\lambda} j_{\lambda} \Omega_{\lambda}}^{\text{bf}}(\mathbf{r}_{\lambda}) \end{aligned} \quad (6.3)$$

where the body-fixed expression for the diatomic wavefunction is given by

$$\varphi_{\lambda \nu_{\lambda} j_{\lambda} \Omega_{\lambda}}^{\text{bf}}(\mathbf{r}_{\lambda}) = Y_{j_{\lambda}}^{\Omega_{\lambda}}(\gamma_{\lambda}, \psi_{\lambda}) \frac{\phi_{\lambda \nu_{\lambda} j_{\lambda}}(r_{\lambda})}{r_{\lambda}} \quad (6.4)$$

and the quantum number Ω_λ labels the orientation of the diatom with respect to the body-fixed \mathbf{z}_λ axis so that the projection of the diatomic angular momentum on the \mathbf{z}_λ axis is $\Omega_\lambda \hbar$.

The transformation of the final diatom projection quantum number to the corresponding helicity quantum number is accomplished by using the definition of the Wigner rotation matrices[54]:

$$Y_j^m(\theta_{\mathbf{r}_\lambda}, \phi_{\mathbf{r}_\lambda}) = \sum_{\Omega=-j}^j D_{m\Omega}^j(\phi_\lambda, \theta_\lambda, 0) Y_j^\Omega(\gamma_\lambda, \psi_\lambda) \quad (6.5)$$

Combining equations (6.5), (6.2), (6.1) and (6.3), yields the relation

$$\hat{f}_{\lambda v_\lambda j_\lambda m_\lambda}^{\lambda' v'_\lambda j'_\lambda m'_\lambda}(\theta_\lambda, \phi_\lambda) = \sum_{\Omega_\lambda} D_{m_\lambda \Omega_\lambda}^j(\phi_\lambda, \theta_\lambda, 0) f_{\lambda v_\lambda j_\lambda \Omega_\lambda}^{\lambda' v'_\lambda j'_\lambda m'_\lambda}(\theta_\lambda, \phi_\lambda) \quad (6.6)$$

Since the Hamiltonian commutes with the operators of SO(3), so any solution to the Schrödinger equation can be written as a linear combination of solutions which separately transform as irreducible representation of SO(3). If the decomposition is done using body-fixed coordinates, then the partial wave series is given in terms of the Wigner rotation matrices. Here we define the asymptotic form for a partial wave body-fixed solution to the Schrödinger equation for an atom-diatom collision at energies below dissociation of the diatom to be

$$\Psi_\lambda^{JM, n'} \underset{R_\lambda \rightarrow \infty}{\sim} \sum_{\Omega_\lambda=-J}^J \sum_{j_\lambda=|\Omega_\lambda|}^{j_\lambda^{max}} \mathcal{D}_{j_\lambda \Omega_\lambda}^{JM}(\theta_\lambda, \phi_\lambda, \gamma_\lambda, \psi_\lambda) \sum_{v_\lambda=0}^{v_\lambda^{max}} \frac{\phi_{\lambda v_\lambda j_\lambda}(r_\lambda)}{r_\lambda R_\lambda} G_{\lambda v_\lambda j_\lambda \Omega_\lambda}^{J, n'}(R_\lambda) \quad (6.7)$$

where the function $\mathcal{D}_{j\Omega}^{JM}$ is defined as

$$\mathcal{D}_{j\Omega}^{JM} = \left(\frac{2J+1}{8\pi^2} \right)^{\frac{1}{2}} D_{M\Omega}^J(\phi_\lambda, \theta_\lambda, \psi_\lambda) \mathcal{P}_j^\Omega(\cos \gamma_\lambda). \quad (6.8)$$

with Wigner rotation functions[54] $D_{M\Omega}^J$ and normalized[2] associated Legendre functions \mathcal{P}_j^Ω . The coefficients $G_{\bar{\lambda}\Omega}^{J,n'}(R_\lambda)$ are given by[2]

$$G_{\bar{\lambda}\Omega}^{J,n'}(R_\lambda) = |v_{\bar{\lambda}}|^{-\frac{1}{2}} \sum_{\Omega''=-J}^J [\mathcal{S}_{\bar{\lambda}\Omega}^{J,\Omega''}(R_\lambda) A_{\bar{\lambda}\Omega''}^{J,n'} + \mathcal{C}_{\bar{\lambda}\Omega}^{J,\Omega''}(R_\lambda) B_{\bar{\lambda}\Omega''}^{J,n'}] \quad (6.9)$$

where the term $v_{\bar{\lambda}}$ is the channel velocity, defined by

$$v_{\bar{\lambda}} = \frac{\hbar}{\mu} k_{\bar{\lambda}}; \quad k_{\bar{\lambda}}^2 = \frac{2\mu}{\hbar^2} (E - e_{\bar{\lambda}}). \quad (6.10)$$

For open states, *i.e.*, those states with $E > e_{\bar{\lambda}}$, the resulting wavenumber is real and positive; for closed states ($E < e_{\bar{\lambda}}$) the wavenumber is positive imaginary, so that the parts of the wavefunction in equation (6.7) which are associated to closed states of the system decay exponentially. The sum over the diatomic quantum numbers in equation (6.7) is over all open and closed states for the system.

The preceding scattering asymptotic boundary conditions involve plane waves and spherical waves because these are familiar boundary conditions for a scattering wave function; however it is most convenient for numerical purposes to calculate solutions to the Schrödinger equation which are real functions. These are the well known reactance matrix formalism given by

$$\bar{\mathcal{S}}_{\bar{\lambda}}^{J,\ell}(R_\lambda) = \begin{cases} j_\ell(k_{\bar{\lambda}} R_\lambda) \cos \left[\frac{\pi}{2} (J+j-\ell) \right] + \eta_\ell(k_{\bar{\lambda}} R_\lambda) \sin \left[\frac{\pi}{2} (J+j-\ell) \right] & \text{open} \\ 2i_\ell(|k_{\bar{\lambda}}| R_\lambda) & \text{closed} \end{cases} \quad (6.11)$$

$$\bar{\mathcal{C}}_{\bar{\lambda}}^{J,\ell}(R_\lambda) = \begin{cases} j_\ell(k_{\bar{\lambda}} R_\lambda) \sin \left[\frac{\pi}{2} (J+j-\ell) \right] - \eta_\ell(k_{\bar{\lambda}} R_\lambda) \cos \left[\frac{\pi}{2} (J+j-\ell) \right] & \text{open} \\ \frac{2}{\pi} \kappa_\ell(|k_{\bar{\lambda}}| R_\lambda) & \text{closed} \end{cases}$$

in which j_ℓ and η_ℓ are spherical Bessel functions of the first and second kind, respectively[55]. At sufficiently large R_λ the spherical Bessel functions reduce to

trigonometric functions, and we can write,

$$G_{\bar{\lambda}\Omega}^{J,n'}(R_\lambda) = |v_{\bar{\lambda}}|^{-\frac{1}{2}} \begin{cases} \left\{ \begin{aligned} &\sin\left(k_{\bar{\lambda}}R_\lambda - \frac{\pi}{2}(J+j)\right) A_{\bar{\lambda}\Omega}^{J,n'} \\ &+ \cos\left(k_{\bar{\lambda}}R_\lambda - \frac{\pi}{2}(J+j)\right) B_{\bar{\lambda}\Omega}^{J,n'} \end{aligned} \right\} & \text{open} \\ \left\{ e^{i k_{\bar{\lambda}} R_\lambda} A_{\bar{\lambda}\Omega}^{J,n'} + e^{-i k_{\bar{\lambda}} R_\lambda} B_{\bar{\lambda}\Omega}^{J,n'} \right\} & \text{closed} \end{cases} \quad (6.12)$$

From the matrices \mathbf{A}^J and \mathbf{B}^J , we obtain the reactance matrix by using the expression

$$\mathbf{R}^J = \mathbf{B}^J (\mathbf{A}^J)^{-1}. \quad (6.13)$$

The reactance matrix is unique, real, and the open part ${}^o\mathbf{R}$ is symmetric[56].

The relationship between the open-channel parts of the scattering and reactance matrices is also well known[56]. For a fixed collision energy, the number of open initial states and final states is equal. It is simple to show that

$${}^o\mathbf{S}^J = \left(\mathbf{I} + i {}^o\mathbf{R}^J \right) \left(\mathbf{I} - i {}^o\mathbf{R}^J \right)^{-1} \quad (6.13)$$

where the left hand superscript o indicates that we are referring to the open parts of the corresponding matrices. Physical quantities such as reaction cross sections can be easily related to the scattering matrix.

7. Symmetry Considerations

There are three possible permutation groups for three particles, depending on the number of these particles which are indistinguishable, and the number of operators needed in each case differs. These three permutation groups are: P_1 , which corresponds to a system in which all three particles A, B and C are distinguishable, and the only permutation operation under which the hamiltonian is invariant is the identity; P_2 , for a system that has two indistinguishable particles

(the AB_2 system), and for which the hamiltonian is invariant under the identity and one two-particle permutation; and P_3 , for a system with three indistinguishable particles (the A_3 system), with six permutations under which the hamiltonian is invariant, the identity, two three-particle permutations and three two-particle permutations.

The distinguishable atom representation asymptotic form, $\Psi_{\lambda}^{\lambda' v' j' m'}$, does not transform according to any irreducible representation of permutation group. To find spatial asymptotic forms that do transform as irreducible representations of permutation group, the distinguishable atom asymptotic form is multiplied by the appropriate group theoretic projection operator[57]. This projection operator is given by

$$\hat{P}_{i,i'}^{\Gamma} = \frac{l_{\Gamma}}{h} \sum_{\hat{R}} M_{i,i'}^{\Gamma*}(\hat{R})\hat{R} \quad (7.1)$$

where Γ is the irreducible representation, i, i' are the row and column of the representation, l_{Γ} is the dimensionality of the representation, h is the order of the group and $M_{i,i'}^{\Gamma}(\hat{R})$ is the i, i' element of the matrix representing the operator \hat{R} for the Γ irreducible representation. The sum is over all of the operators in the group. The transformations \hat{R} and the permutations which generate them are defined in Table III.

We want a scattering wave function corresponding to equation (6.3) which transforms as an irreducible representation of permutation group. Such an irreducible asymptotic wave function is derived by applying the projection operator (7.1) to the asymptotic form (6.3) followed by normalization of the resulting wave

function. With this information, the irreducible asymptotic form is

$$\begin{aligned} \Psi_{\vec{\lambda}}^{JM\Gamma_k, \tau' v'_\tau, j'_\tau, \Omega'_\tau} \underset{R_{\vec{\lambda}} \rightarrow \infty}{\sim} \sum_{\tau} \sum_{\lambda} \sum_{\Omega_\tau = -J}^J \sum_{j_\tau = |\Omega_\tau|}^{j_\tau^{max}} c_{\tau\lambda j_\tau}^{\Gamma_k} \mathcal{D}_{j_\tau \Omega_\tau}^{JM}(\theta_\lambda, \phi_\lambda, \gamma_\lambda, \psi_\lambda) \sum_{v_\tau=0}^{v_\tau^{max}} \times \\ |v_{\vec{\tau}}|^{-\frac{1}{2}} \frac{\phi_{\vec{\tau}}(r_\lambda)}{r_\lambda R_\lambda} \sum_{\Omega''_\tau = -J}^J \left(\mathcal{S}_{\vec{\tau}\Omega_\tau}^{J, \Omega''_\tau}(R_\lambda) \delta_{\tau v_\tau j_\tau \Omega''_\tau}^{\tau' v'_\tau, j'_\tau, \Omega'_\tau} + \mathcal{C}_{\vec{\tau}\Omega_\tau}^{J, \Omega''_\tau}(R_\lambda) W_{\tau v_\tau j_\tau \Omega''_\tau}^{J\Gamma \tau' v'_\tau, j'_\tau, -\Omega'_\tau} \right) \end{aligned} \quad (7.2)$$

where \mathbf{W} may stand for either \mathbf{R} or \mathbf{S} matrix. Since the arrangement channels of type τ are all identical, the form of the functions in these arrangement channels must all be the same, and therefore we may replace the label λ in these functions with the label τ . The composite index $\vec{\tau}$ is defined similarly to $\vec{\lambda}$, *i.e.*, $\vec{\tau} \equiv \{\tau v_\tau j_\tau\}$. The coefficients $c_{\tau\lambda j_\tau}^{\Gamma_k}$ are easily determined from the transformation matrices from Table III and are given in Table IV; they are defined so that a summation over λ will result in non-zero contributions from all channels of type τ and zero contributions from channels of types $\tau' \neq \tau$, and a summation over both λ and τ will result in a single term from each arrangement channel. The irreducible representation asymptotic form (7.2) has a interesting characteristic that the matrix \mathbf{W} has the same functional form in all arrangement channels.

By taking the appropriate projection for the P_1 group, the irreducible asymptotic wave functions are

$$\left. \begin{aligned} \Psi_{\alpha}^{JM\{\Gamma_k=A\}, n'} &= \Psi_{\alpha}^{JM, n'} \\ \Psi_{\beta}^{JM\{\Gamma_k=A\}, n'} &= \Psi_{\beta}^{JM, n'} \\ \Psi_{\gamma}^{JM\{\Gamma_k=A\}, n'} &= \Psi_{\gamma}^{JM, n'} \end{aligned} \right\} P_1 \quad (7.3)$$

which in this case are the same functions defined in each arrangement channel. For the P_2 permutation group, we have

$$\left. \begin{aligned} \Psi_{\alpha}^{JM\{\Gamma_k=A'\}, n'} &= \hat{P}^{A'} \Psi_{\alpha}^{JM, n'} \\ \Psi_{\alpha}^{JM\{\Gamma_k=A''\}, n'} &= \hat{P}^{A''} \Psi_{\alpha}^{JM, n'} \\ \Psi_{\beta}^{JM\{\Gamma_k=A'\}, n'} &= \hat{P}^{A'} \Psi_{\beta}^{JM, n'} \\ \Psi_{\beta}^{JM\{\Gamma_k=A''\}, n'} &= \hat{P}^{A''} \Psi_{\beta}^{JM, n'} \end{aligned} \right\} P_2 \quad (7.4)$$

If the three particles are identical, all three arrangement channels are indistinguishable, giving

$$\left. \begin{aligned} \Psi_{\alpha}^{JM\{\Gamma_k=A_1\},n'} &= \hat{P}^{A_1} \Psi_{\beta}^{JM,n'} \\ \Psi_{\alpha}^{JM\{\Gamma_k=A_2\},n'} &= \hat{P}^{A_2} \Psi_{\beta}^{JM,n'} \\ \Psi_{\alpha}^{JM\{\Gamma_k=E_k\},n'} &= \hat{P}_{kk}^E \Psi_{\beta}^{JM,n'} \end{aligned} \right\} P_3 \quad (7.5)$$

We can apply the permutation operators (shown in Table III) to the equation (7.3), and take group theoretic projections which leads to expressions between the irreducible representation **R** and **S** matrices and the corresponding distinguishable particle matrices. The P_2 permutation group can be expressed as

$$\begin{aligned} W_{\alpha\nu_{\alpha}j_{\alpha}\Omega_{\alpha}}^{A'\alpha\nu'_{\alpha}j'_{\alpha}\Omega'_{\alpha}} &= \begin{cases} W_{\alpha\nu_{\alpha}j_{\alpha}\Omega_{\alpha}}^{\alpha\nu'_{\alpha}j'_{\alpha}\Omega'_{\alpha}} & j_{\alpha} \text{ and } j'_{\alpha} \text{ even} \\ 0 & j_{\alpha} \text{ or } j'_{\alpha} \text{ odd} \end{cases} \\ W_{\alpha\nu_{\alpha}j_{\alpha}\Omega_{\alpha}}^{A''\alpha\nu'_{\alpha}j'_{\alpha}\Omega'_{\alpha}} &= \begin{cases} W_{\alpha\nu_{\alpha}j_{\alpha}\Omega_{\alpha}}^{\alpha\nu'_{\alpha}j'_{\alpha}\Omega'_{\alpha}} & j_{\alpha} \text{ and } j'_{\alpha} \text{ odd} \\ 0 & j_{\alpha} \text{ or } j'_{\alpha} \text{ even} \end{cases} \end{aligned} \quad (7.6)$$

$$\begin{aligned} W_{\beta\nu_{\beta}j_{\beta}\Omega_{\beta}}^{A'\alpha\nu'_{\alpha}j'_{\alpha}\Omega'_{\alpha}} &= \begin{cases} \sqrt{2}W_{\beta\nu_{\beta}j_{\beta}\Omega_{\beta}}^{\alpha\nu'_{\alpha}j'_{\alpha}\Omega'_{\alpha}} & j'_{\alpha} \text{ even} \\ 0 & j'_{\alpha} \text{ odd} \end{cases} \\ W_{\beta\nu_{\beta}j_{\beta}\Omega_{\beta}}^{A''\alpha\nu'_{\alpha}j'_{\alpha}\Omega'_{\alpha}} &= \begin{cases} \sqrt{2}W_{\beta\nu_{\beta}j_{\beta}\Omega_{\beta}}^{\alpha\nu'_{\alpha}j'_{\alpha}\Omega'_{\alpha}} & j'_{\alpha} \text{ odd} \\ 0 & j'_{\alpha} \text{ even} \end{cases} \\ W_{\alpha\nu_{\alpha}j_{\alpha}\Omega_{\alpha}}^{A'\beta\nu'_{\beta}j'_{\beta}\Omega'_{\beta}} &= \begin{cases} \sqrt{2}W_{\alpha\nu_{\alpha}j_{\alpha}\Omega_{\alpha}}^{\beta\nu'_{\beta}j'_{\beta}\Omega'_{\beta}} & j_{\alpha} \text{ even} \\ 0 & j_{\alpha} \text{ odd} \end{cases} \\ W_{\alpha\nu_{\alpha}j_{\alpha}\Omega_{\alpha}}^{A''\beta\nu'_{\beta}j'_{\beta}\Omega'_{\beta}} &= \begin{cases} \sqrt{2}W_{\alpha\nu_{\alpha}j_{\alpha}\Omega_{\alpha}}^{\beta\nu'_{\beta}j'_{\beta}\Omega'_{\beta}} & j_{\alpha} \text{ odd} \\ 0 & j_{\alpha} \text{ even} \end{cases} \end{aligned} \quad (7.7)$$

$$\begin{aligned} W_{\beta\nu_{\beta}j_{\beta}\Omega_{\beta}}^{A'\beta\nu'_{\beta}j'_{\beta}\Omega'_{\beta}} &= W_{\beta\nu_{\beta}j_{\beta}\Omega_{\beta}}^{\beta\nu'_{\beta}j'_{\beta}\Omega'_{\beta}} + (-1)^{j'} W_{\beta\nu_{\beta}j_{\beta}\Omega_{\beta}}^{\gamma\nu'_{\beta}j'_{\beta}\Omega'_{\beta}} \\ W_{\beta\nu_{\beta}j_{\beta}\Omega_{\beta}}^{A''\beta\nu'_{\beta}j'_{\beta}\Omega'_{\beta}} &= W_{\beta\nu_{\beta}j_{\beta}\Omega_{\beta}}^{\beta\nu'_{\beta}j'_{\beta}\Omega'_{\beta}} - (-1)^{j'} W_{\beta\nu_{\beta}j_{\beta}\Omega_{\beta}}^{\gamma\nu'_{\beta}j'_{\beta}\Omega'_{\beta}} \end{aligned} \quad (7.8)$$

The inverse of these relations is

$$\begin{aligned}
W_{\alpha\nu\alpha j\alpha\Omega\alpha}^{\alpha\nu'\alpha j'\Omega'\alpha} &= W_{\alpha\nu\alpha j\alpha\Omega\alpha}^{A'\alpha\nu'\alpha j'\Omega'\alpha} + W_{\alpha\nu\alpha j\alpha\Omega}^{A''\alpha\nu'\alpha j'\Omega'\alpha} \\
W_{\beta\nu\beta j\beta\Omega\beta}^{\beta\nu'\beta j'\Omega'\beta} &= \frac{1}{2} \left(W_{\beta\nu\beta j\beta\Omega\beta}^{A'\beta\nu'\beta j'\Omega'\beta} + W_{\beta\nu\beta j\beta\Omega\beta}^{A''\beta\nu'\beta j'\Omega'\beta} \right) \\
W_{\beta\nu\beta j\beta\Omega\beta}^{\alpha\nu' j'\Omega'} &= \frac{1}{\sqrt{2}} \left(W_{\beta\nu\beta j\beta\Omega\beta}^{A'\alpha\nu' j'\Omega'} + W_{\beta\nu\beta j\beta\Omega\beta}^{A''\alpha\nu' j'\Omega'} \right) \\
W_{\alpha\nu\alpha j\alpha\Omega\alpha}^{\beta\nu' j'\Omega'\beta} &= \frac{1}{\sqrt{2}} \left(W_{\alpha\nu\alpha j\alpha\Omega\alpha}^{A'\beta\nu' j'\Omega'\beta} + W_{\alpha\nu\alpha j\alpha\Omega\alpha}^{A''\beta\nu' j'\Omega'\beta} \right) \\
W_{\gamma\nu\gamma j\gamma\Omega\gamma}^{\beta\nu' j'\Omega'\beta} &= \frac{(-1)^{j\beta}}{2} \left(W_{\beta\nu\beta j\beta\Omega\beta}^{A'\beta\nu' j'\Omega'\beta} - W_{\beta\nu\beta j\beta\Omega\beta}^{A''\beta\nu' j'\Omega'\beta} \right)
\end{aligned} \tag{7.9}$$

For the three identical particles (P_3), we can derive the set of relation between \mathbf{R} and \mathbf{S} matrices for the irreducible representation and those for distinguishable particles:

$$\begin{aligned}
W_{vj\Omega}^{A_1\nu' j'\Omega'} &= \begin{cases} W_{\lambda\nu j\Omega}^{\lambda\nu' j'\Omega'} + 2W_{\lambda\nu j\Omega}^{\nu\nu' j'\Omega'} & j \text{ and } j' \text{ even} \\ 0 & j \text{ or } j' \text{ odd} \end{cases} \\
W_{vj\Omega}^{A_2\nu' j'\Omega'} &= \begin{cases} W_{\lambda\nu j\Omega}^{\lambda\nu' j'\Omega'} + 2W_{\lambda\nu j\Omega}^{\nu\nu' j'\Omega'} & j \text{ and } j' \text{ odd} \\ 0 & j \text{ or } j' \text{ even} \end{cases} \\
W_{vj\Omega}^{E\nu' j'\Omega'} &= \begin{cases} W_{\lambda\nu j\Omega}^{\lambda\nu' j'\Omega'} - W_{\lambda\nu j\Omega}^{\nu\nu' j'\Omega'} & j + j' \text{ even} \\ \sqrt{3}W_{\lambda\nu j\Omega}^{\nu\nu' j'\Omega'} & j \text{ even, } j' \text{ odd} \\ -\sqrt{3}W_{\lambda\nu j\Omega}^{\nu\nu' j'\Omega'} & j \text{ odd, } j' \text{ even} \end{cases}
\end{aligned} \tag{7.10}$$

The inverses of these relations are:

$$\begin{aligned}
W_{\lambda\nu j\Omega}^{\lambda\nu' j'\Omega'} &= \begin{cases} \frac{1}{3}W_{vj\Omega}^{A_1\nu' j'\Omega'} + \frac{2}{3}W_{vj\Omega}^{E\nu' j'\Omega'} & j \text{ and } j' \text{ even} \\ \frac{1}{3}W_{vj\Omega}^{A_2\nu' j'\Omega'} + \frac{2}{3}W_{vj\Omega}^{E\nu' j'\Omega'} & j \text{ and } j' \text{ odd} \\ 0 & j + j' \text{ odd} \end{cases} \\
W_{\lambda\nu j\Omega}^{\nu\nu' j'\Omega'} &= \begin{cases} \frac{1}{3}W_{vj\Omega}^{A_1\nu' j'\Omega'} - \frac{1}{3}W_{vj\Omega}^{E\nu' j'\Omega'} & j \text{ and } j' \text{ even} \\ \frac{1}{3}W_{vj\Omega}^{A_2\nu' j'\Omega'} - \frac{1}{3}W_{vj\Omega}^{E\nu' j'\Omega'} & j \text{ and } j' \text{ odd} \\ \frac{1}{\sqrt{3}}W_{vj\Omega}^{E\nu' j'\Omega'} & j \text{ even, } j' \text{ odd} \\ -\frac{1}{\sqrt{3}}W_{vj\Omega}^{E\nu' j'\Omega'} & j \text{ odd, } j' \text{ even} \end{cases}
\end{aligned} \tag{7.11}$$

The parity label has not appeared in the foregoing analysis but is a label for the numerical solutions, so it is desirable to have the asymptotic form expanded in the corresponding parity components. The parity labeled components have a simple phase change when the sign of the final state index changes sign.

Multiplying by the parity projection operators, which are special cases of equation (7.1), we can find the parity components of the asymptotic form and express the asymptotic form as an expansion in the parity components. Since the inversion parity operator acts only on the generalized Wigner rotation function as $\hat{I}\mathcal{D}_{j\Omega}^{JM} = (-1)^J \mathcal{D}_{j,-\Omega}^{JM}$, we get from (7.2) that

$$\begin{aligned} \Psi_{\tau}^{JM\Pi\Gamma k, \tau' v'_{\tau}, j'_{\tau}, \Omega'_{\tau}} \underset{R_{\bar{\lambda}} \rightarrow \infty}{\sim} \sum_{\tau} \sum_{\lambda} \sum_{\Omega_{\tau} = -J}^J \sum_{j_{\tau} = |\Omega_{\tau}|}^{j_{\tau}^{max}} c_{\tau\lambda j_{\tau}}^{\Gamma k} \mathcal{D}_{j_{\tau}\Omega_{\tau}}^{JM\Pi}(\theta_{\lambda}, \phi_{\lambda}, \gamma_{\lambda}, \psi_{\lambda}) \sum_{v_{\tau}=0}^{v_{\tau}^{max}} \times \\ \frac{\phi_{\bar{\tau}}(r_{\lambda})}{r_{\lambda} R_{\lambda}} |v_{\bar{\tau}}|^{-\frac{1}{2}} \sum_{\Omega''_{\tau} = -J}^J \left(\mathcal{S}_{\bar{\tau}\Omega_{\tau}}^{J, \Omega''_{\tau}}(R_{\lambda}) \delta_{\tau v_{\tau} j_{\tau} \Omega''_{\tau}}^{\tau' v'_{\tau}, j'_{\tau}, \Omega'_{\tau}} + C_{\bar{\tau}\Omega_{\tau}}^{J, \Omega''_{\tau}}(R_{\lambda}) W_{\tau v_{\tau} j_{\tau} \Omega''_{\tau}}^{J\Gamma \tau' v'_{\tau}, j'_{\tau}, -\Omega'_{\tau'}} \right) \end{aligned} \quad (7.12)$$

where the function $\mathcal{D}_{j\Omega}^{JM\Pi}$ is defined by

$$\mathcal{D}_{j\Omega}^{JM\Pi}(\theta_{\lambda}, \phi_{\lambda}, \gamma_{\lambda}, \psi_{\lambda}) = D_{M\Omega}^{J\Pi}(\phi_{\lambda}, \theta_{\lambda}, \psi_{\lambda}) \mathcal{P}_j^{\Omega}(\cos \gamma_{\lambda}) \quad (7.13)$$

With some manipulation this can be reorganized into the form

$$\begin{aligned} \Psi_{\bar{\lambda}}^{JM\Pi\Gamma k, \tau' v'_{\tau}, j'_{\tau}, \Omega'_{\tau}} \underset{R_{\bar{\lambda}} \rightarrow \infty}{\sim} \sum_{\tau} \sum_{\lambda} \sum_{\Omega_{\tau}=0}^J \sum_{j_{\tau}=|\Omega_{\tau}|}^{j_{\tau}^{max}} c_{\tau\lambda j_{\tau}}^{\Gamma k} \mathcal{D}_{j_{\tau}\Omega_{\tau}}^{JM\Pi}(\theta_{\lambda}, \phi_{\lambda}, \gamma_{\lambda}, \psi_{\lambda}) \times \\ \sum_{v_{\tau}=0}^{v_{\tau}^{max}} \frac{\phi_{\bar{\tau}}(r_{\lambda})}{r_{\lambda} R_{\lambda}} |v_{\bar{\tau}}|^{-\frac{1}{2}} \left(\frac{1 + \delta_{\Omega'_{\tau'}}^0}{1 + \delta_{\Omega_{\tau}}^0} \right)^{\frac{1}{2}} \sum_{\Omega''_{\tau}=0}^J \\ \left(\mathcal{S}_{\bar{\tau}\Omega_{\tau}}^{J\Pi, \Omega''_{\tau}}(R_{\lambda}) E_{\tau v_{\tau} j_{\tau} \Omega''_{\tau}}^{J\Pi \tau' v'_{\tau}, j'_{\tau}, \Omega'_{\tau'}} + C_{\bar{\tau}\Omega_{\tau}}^{J\Pi, \Omega''_{\tau}}(R_{\lambda}) W_{\tau v_{\tau} j_{\tau} \Omega''_{\tau}}^{J\Pi\Gamma \tau' v'_{\tau}, j'_{\tau}, -\Omega'_{\tau'}} \right) \end{aligned} \quad (7.14)$$

in which both indices Ω_{τ} and Ω''_{τ} are greater than or equal to zero. Furthermore,

$$(E^{J\Pi})_{\tau v_{\tau} j_{\tau}, \Omega_{\tau}=0}^{\tau' v'_{\tau}, j'_{\tau}, \Omega'_{\tau'}} = (E^{J\Pi})_{\tau v_{\tau} j_{\tau} \Omega_{\tau}}^{\tau' v'_{\tau}, j'_{\tau}, \Omega'_{\tau'}, 0} = \frac{1}{2} [1 + (-1)^{J+\Pi}] \delta_{\tau v_{\tau} j_{\tau} \Omega'_{\tau}}^{\tau' v'_{\tau}, j'_{\tau}, \Omega'_{\tau'}} \quad (7.15)$$

$$\begin{aligned} (W^{J\Pi\Gamma})_{\tau v_{\tau} j_{\tau}, \Omega_{\tau}=0}^{\tau' v'_{\tau}, j'_{\tau}, \Omega'_{\tau'}} &= \frac{1}{2} [1 + (-1)^{J+\Pi}] (W^{J\Pi\Gamma})_{\tau v_{\tau} j_{\tau} \Omega_{\tau}=0}^{\tau' v'_{\tau}, j'_{\tau}, \Omega'_{\tau'}} \\ (W^{J\Pi\Gamma})_{\tau v_{\tau} j_{\tau} \Omega_{\tau}}^{\tau' v'_{\tau}, j'_{\tau}, \Omega'_{\tau'}, 0} &= \frac{1}{2} [1 + (-1)^{J+\Pi}] (W^{J\Pi\Gamma})_{\tau v_{\tau} j_{\tau} \Omega_{\tau}}^{\tau' v'_{\tau}, j'_{\tau}, \Omega'_{\tau'}, 0} \end{aligned} \quad (7.16)$$

As a result, $(W^{J\Pi\Gamma})_{\tau v_\tau j_\tau, \Omega_\tau}^{\tau' v'_\tau j'_\tau, \Omega'_\tau}$ has the symmetry property

$$(W^{J\Pi\Gamma})_{\tau v_\tau j_\tau, -\Omega_\tau}^{\tau' v'_\tau j'_\tau, \Omega'_\tau} = \Pi(-1)^J (W^{J\Pi\Gamma})_{\tau v_\tau j_\tau, \Omega_\tau}^{\tau' v'_\tau j'_\tau, \Omega'_\tau} \quad (7.17)$$

so if the parity labelled scattering matrix elements with $\Omega \geq 0$ are calculated, then the elements with $\Omega < 0$ are known by equation (7.17).

8. Pauli Principle and Observable Cross Sections

The differential cross section is defined as the outgoing flux into a unit solid angle for some final state of the diatomic molecule divided by the total incident flux. Before writing down this expression in terms of the helicity scattering amplitude, it is necessary to undo the effects of mass-scaling on the latter.

The use of mass scaled coordinates affects the normalization of the diatomic molecule wave functions, the wave vectors, and the spherical wave terms of the asymptotic form. First, consider the diatomic molecule normalization.

$$\int_0^{r_\lambda^{max}} |\phi_{\bar{\tau}}(r_\lambda)|^2 dr_\lambda = 1 = a_\tau^{-1} \int_0^{r'_\lambda^{max}} |\phi_{\bar{\tau}}(r'_\lambda)|^2 dr'_\lambda \quad (8.1)$$

If the diatomic molecule wave functions in unscaled Jacobi coordinates are defined to have normalization

$$\int_0^{r'_\lambda^{max}} |\phi'_{\bar{\tau}}(r'_\lambda)|^2 dr'_\lambda = 1 \quad (8.2)$$

then the following relationship exists between the mass-scaled and unscaled diatomic wave functions:

$$\phi_{\bar{\tau}}(r'_\lambda) = a_\tau^{1/2} \phi'_{\bar{\tau}}(r'_\lambda) \quad (8.3)$$

where we have defined

$$a_\lambda = \left(\frac{\mu_{\lambda, \nu\kappa}}{\mu} \right)^{\frac{1}{2}} = \left(\frac{\mu}{\mu_{\nu\kappa}} \right)^{\frac{1}{2}} = \left(\frac{\mu_{\lambda, \nu\kappa}}{\mu_{\nu\kappa}} \right)^{\frac{1}{4}} \quad (8.4)$$

Also, the wave vector corresponding to unscaled coordinates is

$$\mathbf{k}'_{\tau v j} = a_{\tau} \mathbf{k}_{\tau v j} \quad (8.5)$$

which implies that

$$\begin{aligned} \mathbf{k}'_{\tau v j} \cdot \mathbf{R}'_{\lambda} &= \mathbf{k}_{\tau v j} \cdot \mathbf{R}_{\lambda} \\ k'_{\lambda v j} R'_{\lambda} &= k_{\lambda v j} R_{\lambda} \end{aligned} \quad (8.6)$$

The unscaled scattering amplitude can be related to scaled scattering amplitude by

$$f'_{\tau v j \Omega}{}^{\Gamma \tau' v' j' m'}(\theta_{\lambda}, \phi_{\lambda}) = \left(\frac{a_{\tau}}{a_{\tau'}^3} \right)^{\frac{1}{2}} f_{\tau v j \Omega}{}^{\Gamma \tau' v' j' m'}(\theta_{\lambda}, \phi_{\lambda}) \quad (8.7)$$

From the scaled helicity scattering amplitude, the irreducible representation differential cross section can be defined

$$\sigma_{\tau v j \Omega}{}^{\Gamma \tau' v' j' m'}(\theta_{\lambda}, \phi_{\lambda}) = a_{\tau'}^{-2} \frac{v_{\tau v j}}{v_{\tau' v' j'}} \left| f_{\tau v j \Omega}{}^{\Gamma \tau' v' j' m'}(\theta_{\lambda}, \phi_{\lambda}) \right|^2 \quad (8.8)$$

which can be rewritten as[2]

$$\sigma_{\tau v j \Omega}{}^{\Gamma \tau' v' j' m'}(\theta_{\lambda}) = \frac{1}{4k'^2_{\tau' v' j'}} \left| \sum_{J=0}^{\infty} (2J+1) d_{m' \Omega}^J(\theta_{\lambda}) [T^{J\Gamma}]_{\tau v j \Omega}{}^{\tau' v' j' m'} \right|^2 \quad (8.9)$$

where

$$\mathbf{T}^{J\Gamma} = \mathbf{I} - \mathbf{S}^{J\Gamma} \quad (8.10)$$

The integral cross section $Q_{\tau v j m}{}^{\Gamma \tau' v' j' m'}$ is obtained by integration of (8.10) over θ_{λ} and ϕ_{λ} and using the orthonormality property of the d^J functions giving

$$Q_{\tau v j \Omega}{}^{\Gamma \tau' v' j' m'} = \frac{\pi}{k'^2_{\tau' v' j'}} \sum_{J=0}^{\infty} (2J+1) \left| [T^{J\Gamma}]_{\tau v j \Omega}{}^{\tau' v' j' m'} \right|^2 \quad (8.11)$$

When the three-particle system under consideration has P_2 or P_3 permutation symmetry, the nuclear spin of the identical particles must be taken into account. The Hamiltonian considered so far does not include spin dependent terms;

therefore, the complete wave function can be written as a direct product of a spatial wave function, which satisfies the Schrödinger equation, and a spin wave function for the three particles. In earlier sections we have discussed the explicit construction of the spatial part of the scattering wave function. From the direct product of the spatial and spin functions, differential cross sections for appropriately antisymmetrized scattering wave functions can be extracted. The existence of nuclear spin does not affect the previous sections and becomes important here in connection with the Pauli principle.

Rotational invariance implies conservation of the spin total angular momenta squared and one of its space-fixed components. The spin functions that we will use are chosen to be eigenfunctions of \hat{S}^2 , the square of the total spin angular momentum operator and \hat{S}_Z , its space-fixed Z component.

The permutation operators also affect the spin functions. Since the operators of permutation group all commute with those of SO(3), the spin functions just chosen form irreducible representations of permutation groups. For example, the direct product for the P_3 representations are (spin \otimes spatial)

$$\begin{aligned}
 A_1 \otimes A_1 &= A_2 \otimes A_2 = A_1 \\
 A_2 \otimes A_1 &= A_1 \otimes A_2 = A_2 \\
 E \otimes A_1 &= A_1 \otimes E = E \\
 E \otimes A_2 &= A_2 \otimes E = E \\
 E \otimes E &= A_1 \oplus A_2 \oplus E
 \end{aligned} \tag{8.12}$$

It is seen that in the case of fermions the only irreducible representation spatial solutions that contribute to nature are A_2 and E . When the Pauli principle is satisfied, we associate the quartet nuclear spin state with the A_2 spatial scattering amplitude and the doublet nuclear spin state with the E spatial scattering amplitude for spin $\frac{1}{2}$ nuclei like hydrogen. It is easily seen that bosons require

spatial solutions that transforms as A_1 and E . If the initial rotational state of the diatomic j is even (para-hydrogen), then the corresponding spatial wave function must belong to the E irreducible representation because A_2 solutions contain no even rotational states. The explicit form for the observable cross sections in this case is

$$P_{3, s = 1/2} : \sigma_{vj\Omega}^{v'j'm'} = \begin{cases} \sigma_{vj\Omega}^{Ev'j'm'} & j \text{ and } j' \text{ even} \\ \frac{2}{3}\sigma_{vj\Omega}^{A_2v'j'm'} + \frac{1}{3}\sigma_{vj\Omega}^{Ev'j'm'} & j \text{ and } j' \text{ odd} \\ \frac{1}{3}\sigma_{vj\Omega}^{Ev'j'm'} & j \text{ even, } j' \text{ odd} \\ \sigma_{vj\Omega}^{Ev'j'm'} & j \text{ odd, } j' \text{ even} \end{cases} \quad (8.13)$$

Summing up for this example, all differential cross sections are composed solely of E differential cross sections except the ortho to ortho ones which are simple linear combination of the E and A_2 differential cross sections.

9. Summary

We have presented in detail a methodology for performing accurate quantum mechanical reactive scattering calculations based on symmetrized principal-axis moment inertia hyperspherical coordinates. The formalism includes the expansion of the wave function in terms of local hyperspherical pseudo surface functions which are independent of total angular momentum. The geometric phase effect due to the conical intersections requires careful consideration of the phases of the electronic and nuclear wave functions.

References

- [1] D. G. Truhlar and R. E. Wyatt, *Ann. Rev. Phys. Chem.* **27** 1 (1976);
G. C. Schatz, in: *Theory of Chemical Reaction Dynamics*, ed. by D. C. Clary,
Proceeding of NATO Workshop, Orsay, France, 1988, p.1;
B. C. Garrett and D. G. Truhlar, *Ann. Rev. Phys. Chem.* **35** 159 (1984);
J. M. Bowman, *Adv. Chem. Phys.* **61** 115 (1985).
- [2] A. Kuppermann and G. C. Schatz, *J. Chem. Phys.* **62**, 2502 (1975).
- [3] G. C. Schatz and A. Kuppermann, *J. Chem. Phys.* **65**, 4642,4668 (1976).
- [4] A. B. Elkowitz and R. E. Wyatt, *J. Chem. Phys.* **62**, 2504 (1975).
- [5] A. B. Elkowitz and R. E. Wyatt, *J. Chem. Phys.* **63**, 702 (1975).
- [6] R. B. Walker, E. B. Stechel and J. C. Light, *J. Chem. Phys.* **69**, 2922 (1978).
- [7] D. E. Manolopoulos and R. E. Wyatt, *Chem. Phys. Lett.* **159**, 123 (1989).
- [8] J. Z. H. Zhang and W. H. Miller, *J. Chem. Phys.* **91**, 1528 (1989); **92**, 1811 (1990).
- [9] J. Z. H. Zhang and W. H. Miller, *J. Chem. Phys.* **88**, 4549 (1988); **90**, 7610 (1989); *Chem. Phys. Lett.* **159**, 130 (1989).
- [10] M. Zhao, D. G. Truhlar, D. W. Schwenke and D. J. Kouri, *J. Phys. Chem.* **94**, 7074 (1990).
11. P. Siegbahn and B. Liu, *J. Chem. Phys.* **68**, 2457 (1978); D. G. Truhlar and C. J. Horowitz, *J. Chem. Phys.* **68**, 2466 (1978); **71**, 1514E (1979).
- [11] A. Kuppermann and P. G. Hipes, *J. Chem. Phys.* **84**, 5962 (1986).
- [12] P. G. Hipes and A. Kuppermann, *Chem. Phys. Lett.* **133**, 1 (1987).
- [13] S. A. Cuccaro, P. G. Hipes and A. Kuppermann, *Chem. Phys. Lett.* **154**, 155 (1989); **157**, 440 (1989).
- [14] Y. M. Wu, S. A. Cuccaro, P. G. Hipes and A. Kuppermann, *Chem. Phys. Lett.* **168**, 429 (1990).

- [15] G. C. Schatz, *Chem. Phys. Lett.* **150**, 92 (1988).
- [16] J. Linderberg, *Int. J. Quant. Chem. Symp.* **19**, 467 (1986); J. Linderberg and B. Vessal, *Int. J. Quant. Chem.* **31**, 65 (1987); J. Linderberg, S. B. Padkjaer, Y. Öhrn and B. Vessal, *J. Chem. Phys.* **90**, 6254 (1989).
- [17] J. M. Launay and M. Le Dorneuf, *Chem. Phys. Lett.* **163**, 178 (1989).
- [18] R. T. Pack and G. A. Parker, *J. Chem. Phys.* **87**, 3888 (1987); **90**, 3511 (1989).
- [19] M. Mladenovic, M. Zhao, D. G. Truhlar, D. W. Schwenke, Y. Sun and D. J. Kouri, *Chem. Phys. Lett.* **146**, 358 (1988).
- [20] M. Mladenovic, M. Zhao, D. G. Truhlar, D. W. Schwenke, Y. Sun and D. J. Kouri, *J. Phys. Chem.* **92**, 7035 (1988).
- [21] J. Z. H. Zhang, D. J. Kouri, K. Haug, D. W. Schwenke, Y. Shima and D. G. Truhlar, *J. Chem. Phys.* **88**, 2492 (1988).
- [22] G. Herzberg and H. C. Longuet-Higgins, *Discussions Faraday Soc.* **35** 77 (1963); H. C. Longuet-Higgins, *Proc. Roy. Soc. Lond. A* **344** 147 (1975).
- [23] H. C. Longuet-Higgins, *Advan. Spectry.* **2** 429 (1961).
H. C. Longuet-Higgins, U. Öpik, M. H. L. Pryce and R. A. Sack, *Proc. Roy. Soc. Lond. A* **244** 1 (1958).
- [24] C. A. Mead and D. G. Truhlar, *J. Chem. Phys.* **70** 2284 (1979).
- [25] C. A. Mead, *Chem. Phys.* **49** 23 (1980).
- [26] C. A. Mead, *J. Chem. Phys.* **72** 3839 (1980).
- [27] B. Lepetit, Z. Peng and A. Kuppermann, *Chem. Phys. Letters* **166** 572 (1990).
- [28] B. Lepetit and A. Kuppermann, *Chem. Phys. Letters* **166** 581 (1990).
- [29] M. V. Berry, *Proc. Roy. Soc. A* **392** 45 (1984).
- [30] Y. Aharonov and D. Bohm, *Phys. Rev.* **115** 485 (1959).

- [31] N. Nash, S. Sen, *Topology and Geometry for Physicists*. Academic, London 1983.
- [32] A. Shapere, F. Wilczek, *Geometric Phases in Physics*. World Scientific, Singapore 1989.
- [33] Y. M. Wu, A. Kuppermann and B. Lepetit, *Chem Phys. Lett.*, **186** 319 (1991).
- [34] A. Kuppermann, *Chem. Phys. Lett.* **32**, 374 (1975).
- [35] R. T. Ling and A. Kuppermann, in: **Electronic and Atomic Collisions, Abstracts of Papers of the 9th International Conference on the Physics of Electronic and Atomic Collisions**, Seattle, Washington, 24–30 July, 1975, Vol. 1, eds. J. Risley and R. Geballe (Univ. Washington Press, Seattle, 1975) pp. 353, 354.
- [36] H. Köppel, W. Domcke, L. S. Cederbaum, *Adv. Chem. Phys.* **57** 246 (1984).
- [37] H. A. Jahn, E. Teller, *Proc. Roy. Soc. London Ser A*, **161** 220 (1937).
- [38] L. M. Delves, *Nucl. Phys.* **9**, 391 (1958); **20**, 275 (1960).
- [39] A. Kuppermann, in: **Theoretical chemistry — Theory of scattering: papers in honor of Henry Eyring**, ed. D. Henderson (Academic Press, New York, 1981) Vol. 6, part A, chapter 2, pp. 79–164.
- [40] G. C. Schatz, *Chem. Phys. Lett.* **151**, 409 (1988); *J. Chem. Phys.* **90**, 3582 (1989).
- [41] F. T. Smith, *J. Math. Phys.* **3**, 735 (1962); *J. Chem. Phys.* **38**, 1304 (1963); R. C. Whitten and F. T. Smith, *J. Math. Phys.* **9**, 1103 (1968).
- [42] B. R. Johnson, *J. Chem. Phys.* **73**, 5051 (1980).
- [43] C. A. Mead, *Chem. Phys.* **49**, 23 (1980); *J. Chem. Phys.* **72**, 3839 (1980).
- [44] J. D. Kress, Z. Bačić, G. A. Parker and R. T. Pack, *Chem. Phys. Lett.* **157**, 585 (1989); **170**, 306 (1990).

- [45] Z. Bačić, J. D. Kress, G. A. Parker and R. T. Pack, *J. Chem. Phys.* **92**, 2344 (1990).
- [46] R. T. Pack and G. A. Parker, *J. Chem. Phys.* **87** 3888 (1987).
- [47] B. Lepetit and J. M. Launay, *Chem. Phys. Lett.* **151** 287 (1988).
- [48] A. Messiah, *Quantum Mechanics*, Vol 2 (Dunod, Paris, 1964).
- [49] W. Zickendraht, *Ann. Phys.* **35** 18 (1965).
- [50] H. Mayer, *J. Phys. A* **8** 1562 (1975).
- [51] L. Wolniewicz, *J. Chem. Phys.* **90** 371 (1989).
- [52] B. R. Johnson, *J. Comp. Phys.* **12**, 445 (1973); *J. Chem. Phys.* **67**, 4086 (1977).
- [53] D. E. Manolopoulos, *J. Chem. Phys.* **85**, 6425 (1986).
- [54] A. S. Davydov, **Quantum Mechanics**, 2nd edition (Pergamon Press, Oxford, 1976), pp. 167, 178.
- [55] AMS 55, **Handbook of Mathematical Functions**, eds. M. Abramowitz and I. A. Stegun, (National Bureau of Standards, Washington, D. C., 1972) pp. 437,443.
- [56] A. M. Lane and R. G. Thomas, *Rev. Mod. Phys.* **30**, 257 (1958).
- [57] M. Hammermesh, **Group Theory**, (Addison-Wesley, Reading, Mass., 1962) p.113.

FIGURE CAPTIONS

Figure 1. Diagram displaying a pseudo-rotation in the H_3 system. The electronic degeneracy occurs at the symmetric configuration, shown as the equilateral triangle in the center. As one round a series of continuous loop in the space of nuclear coordinates, this cyclic evolution as a result changes the sign of the electronic wave function.

Table I: Choice of $g_{n\phi}^{\Pi\Gamma\Omega}$ for each Π , Ω and Γ for nuclear permutation group P_3

Π	even Ω		Π	odd Ω	
	Γ^c	$g_{n\phi}^{\Pi\Gamma\Omega}$		Γ^c	$g_{n\phi}^{\Pi\Gamma\Omega}$
even, without phase ^a	A ₁ A ₂ E	$\cos(3m\phi_\lambda)^d$ $\sin(3m\phi_\lambda)^d$ $\cos[(3n\pm 1)\phi_\lambda]^e$	even, without phase ^a	A ₁ A ₂ E	$\sin(3m\phi_\lambda)^d$ $\cos(3m\phi_\lambda)^d$ $\sin[(3n\pm 1)\phi_\lambda]^e$
even, with phase ^b	A ₁ A ₂ E	$\cos[(3m+\frac{3}{2})\phi_\lambda]^d$ $\sin[(3m+\frac{3}{2})\phi_\lambda]^d$ $\cos[(3n\pm\frac{1}{2})\phi_\lambda]^e$	even, with phase ^b	A ₁ A ₂ E	$\sin[(3m+\frac{3}{2})\phi_\lambda]^d$ $\cos[(3m+\frac{3}{2})\phi_\lambda]^d$ $\sin[(3n\pm\frac{1}{2})\phi_\lambda]^e$
odd, without phase ^a	A ₁ A ₂ E	$\cos[(3m+\frac{3}{2})\phi_\lambda]^d$ $\sin[(3m+\frac{3}{2})\phi_\lambda]^d$ $\cos[(3n\pm\frac{1}{2})\phi_\lambda]^e$	odd, without phase ^a	A ₁ A ₂ E	$\sin[(3m+\frac{3}{2})\phi_\lambda]^d$ $\cos[(3m+\frac{3}{2})\phi_\lambda]^d$ $\sin[(3n\pm\frac{1}{2})\phi_\lambda]^e$
odd, with phase ^b	A ₁ A ₂ E	$\cos(3m\phi_\lambda)^d$ $\sin(3m\phi_\lambda)^d$ $\cos[(3n\pm 1)\phi_\lambda]^e$	odd, with phase ^b	A ₁ A ₂ E	$\sin(3m\phi_\lambda)^d$ $\cos(3m\phi_\lambda)^d$ $\sin[(3n\pm 1)\phi_\lambda]^e$

- a. Without consideration of the geometric phase due to the conical intersection.
- b. With consideration of the geometric phase due to the conical intersection.
- c. Γ is the irreducible representation of P_3 to which $\Phi^{JM\Pi\Gamma}$ belongs.
- d. m is a non-negative integer.
- e. n is a positive integer.

Table II: Effect of permutation of the nuclei on the angle ϕ_λ .

Permutation	$P_{\lambda\nu\kappa}^a$	$P_{\nu\kappa\lambda}^b$	$P_{\kappa\lambda\nu}^c$	$P_{\nu\kappa}^d$	$P_{\lambda\nu}^d$	$P_{\lambda\kappa}^d$
Value of ϕ_λ^e	ϕ_λ	$\phi_\lambda + \frac{2\pi}{3}$	$\phi_\lambda + \frac{4\pi}{3}$	$2\pi - \phi_\lambda$	$\frac{2\pi}{3} - \phi_\lambda$	$\frac{4\pi}{3} - \phi_\lambda$
$\sin(3m + \frac{3}{2})\phi_\lambda$	1	-1	1	1	1	-1
$\cos(3m + \frac{3}{2})\phi_\lambda$	1	-1	1	-1	-1	1
ψ_e^+	1	-1	1	-1	-1	1
ψ_e^-	1	-1	1	1	1	-1

a. $P_{\lambda\nu\kappa}$ is the identity permutation.

b. $P_{\nu\kappa\lambda}$ refers to the cyclic permutation $\lambda\nu\kappa \rightarrow \nu\kappa\lambda$.

c. $P_{\kappa\lambda\nu}$ refers to the cyclic permutation $\lambda\nu\kappa \rightarrow \kappa\lambda\nu$.

d. P_{ij} refers to the pairwise permutation of nuclei i and j .

e. The change in ϕ_λ are true modulo 2π since ϕ_λ must remain in the range $[0, 2\pi]$.

Table III: Operations and irreducible representations for P_p

P_1

Operation	Permutation	\mathbf{d}^A
\hat{O}_E	$\begin{pmatrix} \alpha & \beta & \gamma \\ \alpha & \beta & \gamma \end{pmatrix}$	1

P_2

Operation	Permutation	\mathbf{d}^{A_1}	\mathbf{d}^{A_2}
\hat{O}_E	$\begin{pmatrix} \alpha & \beta & \gamma \\ \alpha & \beta & \gamma \end{pmatrix}$	1	1
\hat{O}_A	$\begin{pmatrix} \alpha & \beta & \gamma \\ \alpha & \gamma & \beta \end{pmatrix}$	1	-1

P_3

	Operation	Permutation	\mathbf{d}^{A_1}	\mathbf{d}^{A_2}	\mathbf{d}^E
E	\hat{O}_E	$\begin{pmatrix} \alpha & \beta & \gamma \\ \alpha & \beta & \gamma \end{pmatrix}$	1	1	$\begin{pmatrix} 1 & 0 \\ 0 & 1 \end{pmatrix}$
$\sigma_v(xz)$	\hat{O}_A	$\begin{pmatrix} \alpha & \beta & \gamma \\ \alpha & \gamma & \beta \end{pmatrix}$	1	-1	$\begin{pmatrix} 1 & 0 \\ 0 & -1 \end{pmatrix}$
σ_v'	\hat{O}_B	$\begin{pmatrix} \alpha & \beta & \gamma \\ \gamma & \beta & \alpha \end{pmatrix}$	1	-1	$\begin{pmatrix} -\frac{1}{2} & \frac{\sqrt{3}}{2} \\ \frac{\sqrt{3}}{2} & \frac{1}{2} \end{pmatrix}$
σ_v''	\hat{O}_C	$\begin{pmatrix} \alpha & \beta & \gamma \\ \beta & \alpha & \gamma \end{pmatrix}$	1	-1	$\begin{pmatrix} -\frac{1}{2} & -\frac{\sqrt{3}}{2} \\ -\frac{\sqrt{3}}{2} & \frac{1}{2} \end{pmatrix}$
C_3^2	\hat{O}_D	$\begin{pmatrix} \alpha & \beta & \gamma \\ \gamma & \alpha & \beta \end{pmatrix}$	1	1	$\begin{pmatrix} -\frac{1}{2} & \frac{\sqrt{3}}{2} \\ -\frac{\sqrt{3}}{2} & -\frac{1}{2} \end{pmatrix}$
C_3	\hat{O}_F	$\begin{pmatrix} \alpha & \beta & \gamma \\ \beta & \gamma & \alpha \end{pmatrix}$	1	1	$\begin{pmatrix} -\frac{1}{2} & -\frac{\sqrt{3}}{2} \\ \frac{\sqrt{3}}{2} & -\frac{1}{2} \end{pmatrix}$

Table IV: Symmetry coefficients $c_{\tau\lambda_j}^{\Gamma_{kk}}$ for P_p

P_1

Γ_{kk}	τ	λ		
		α	β	γ
A	A	1	0	0
	B	0	1	0
	C	0	0	1

P_2

Γ_{kk}	τ	λ		
		α	β	γ
A'	A	$\frac{1+(-1)^j}{2}$	0	0
	B	0	$\frac{1}{\sqrt{2}}$	$\frac{(-1)^j}{\sqrt{2}}$
A''	A	$\frac{1-(-1)^j}{2}$	0	0
	B	0	$\frac{1}{\sqrt{2}}$	$-\frac{(-1)^j}{\sqrt{2}}$

P_3

Γ_{kk}	τ	λ		
		α	β	γ
A_1	A	$\frac{1+(-1)^j}{2\sqrt{3}}$	$\frac{1+(-1)^j}{2\sqrt{3}}$	$\frac{1+(-1)^j}{2\sqrt{3}}$
A_2	A	$\frac{1-(-1)^j}{2\sqrt{3}}$	$\frac{1-(-1)^j}{2\sqrt{3}}$	$\frac{1-(-1)^j}{2\sqrt{3}}$
E_{kk}	A	$\frac{c_1}{\sqrt{6}}$	$-\frac{c_1}{2\sqrt{6}} + \frac{c_2}{2\sqrt{2}}$	$-\frac{c_1}{2\sqrt{6}} - \frac{c_2}{2\sqrt{2}}$

$$c_1 = [1 - (-1)^{j+k}] \quad c_2 = [(-1)^k + (-1)^j]$$

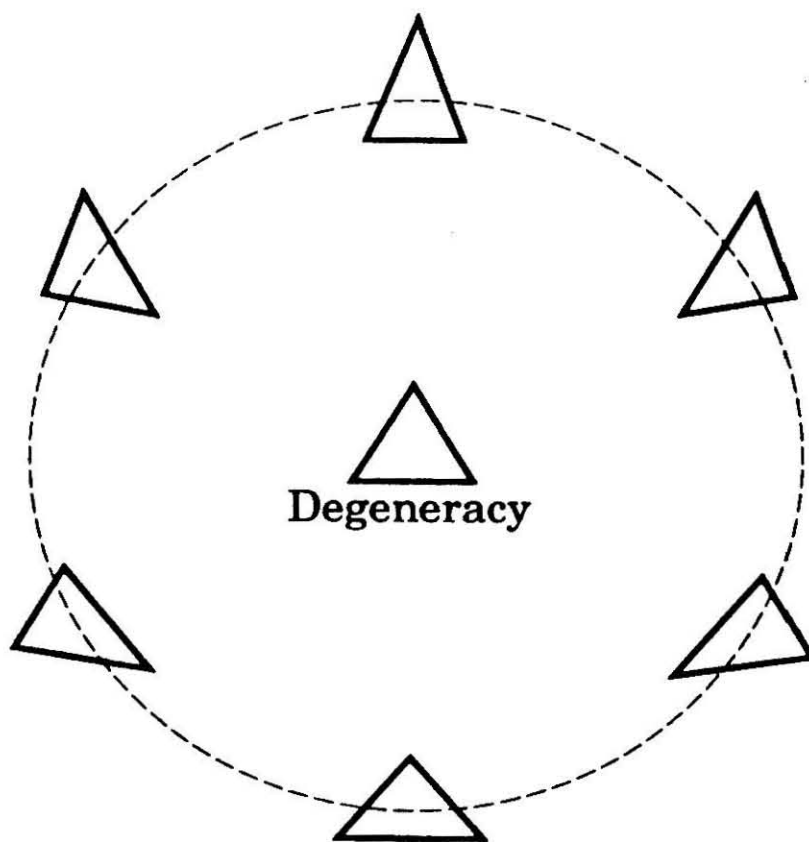


Figure 1.

CHAPTER III

Effect of the Geometric Phase on Product Rotational State Distributions and Integral Cross Sections

**Effect of the Geometric Phase on Product Rotational
State Distributions and Integral Cross Sections**

Yi-Shuen Mark Wu and Aron Kuppermann

Arthur Amos Noyes Laboratory of Chemical Physics

Division of Chemistry and Chemical Engineering^a

California Institute of Technology

Pasadena, CA 91125, USA

Abstract

The effect of the geometric phase induced by the conical intersection between the two lowest electronic states for the $\text{H} + \text{H}_2$ system on product rotational state distributions and integral cross sections is investigated by an accurate quantum mechanical calculation with total collision energies up to 2.6 eV above the bottom of the ground state H_2 electronic well. Inclusion of the effect of the geometric phase is shown to change significantly the rotational state distributions and para-to-ortho integral cross sections for energies higher than 1.8 eV. These results are in excellent qualitative agreement with the experimentally measured distributions for the $\text{D} + \text{H}_2$ reaction, and strongly suggest that under appropriate conditions the geometric phase effect may be significant in the many systems that display conical intersections.

^a Contribution number 8603.

1. Introduction

The H+H₂ reaction and its isotopic variations, such as the D+H₂ reaction, play a special role in chemical kinetics[1]. They are the simplest and most fundamental of the gas-phase exchange reactions for which the processes of concurrent bond breaking and bond formation can be studied in detail both experimentally and theoretically. Early three-dimensional quantum cross section calculations for the H + H₂ reaction were carried out about 17 years ago[2-6] at energies below the opening of the first vibrationally excited state of H₂. The methods used have proven computationally too expensive to extend to higher energies[1].

As a result of the current development of efficient methodologies and increased access to supercomputers, beginning in 1986 with the publication of $J = 0$ partial wave results for the H + H₂ reaction up to energies of 1.6 eV above threshold using symmetrized hyperspherical coordinates[7,8], there has been a remarkable surge of activity in this field[9-51]. These calculations are of three basic types: the propagation methods of Kuppermann *et al.*[7-12], Pack *et al.*[13-17], Schatz[18,19], Linderberg *et al.*[20], and Launay *et al.* [21-23], all involving some form of hyperspherical coordinates; the variational methods of the Truhlar and Kouri groups[24-38], Miller *et al.*[39-43], and Manolopoulos, Wyatt *et al.*[44-49], using Jacobi coordinates; and the recent work of Webster and Light[50-51] using a natural collision coordinate[52] method related to earlier approaches[2-6].

Most of the above calculations for reactive scattering implicitly assume that the Born-Oppenheimer approximation is valid and that the reaction occurs on the ground state electronically adiabatic potential energy surface. Since the minimum of the first excited electronic state surface is 2.7 eV above the minimum of the ground state surface (which is the bottom of the isolated H₂ diatom potential well), it would seem that this is a very good approximation for the energy range of

the previous calculations (0.3-1.6 eV). However, a complication arises in using the Born-Oppenheimer approximation when two electronic potential energy surfaces exhibit a conical intersection. It has been shown[53] that in a system of three atoms each having only one valence electron of the s-type (such as hydrogen atom isotopes or alkali atoms), the lowest electronic doublet state displays a conical intersection even when all three atoms are dissimilar. If one traces a path in nuclear configuration space which encircles the line of the conical intersections and returns to the original configuration, the electronic wavefunction, if forced to be real, changes sign. Since the total wavefunction including electronic and nuclear parts must be single-valued and continuous, there must be a compensating sign change in the nuclear wavefunction. This is known as the molecular Aharonov-Bohm effect[54-57] and is a special case of Berry's geometric phase[58].

Recently, Kliner, Zare *et al.*[59-60] have reported resonance-enhanced multi-photon ionization and time-of-flight mass spectroscopic measurements of product rotational state distributions for the $D + H_2$ reaction in which the H_2 reagent was either thermal ($v=0, j$) or prepared in the level ($v=1, j=1$) by stimulated Raman pumping. Previous quantum calculations[37,41] are in perfect agreement with the measured distribution[59] for the $D + H_2(v = 0, j) \rightarrow HD(v' = 1, j') + H$ reaction at center-of-mass collision energy $E_{tr} = 1.05$ eV. However, quantum calculations of the $D + H_2(v = 1, j = 1) \rightarrow HD(v' = 1, j') + H$ distribution at $E_{tr} = 1.02$ eV[37,38] do not agree with experiment[60]. Specifically, the calculated distribution is 2-3 quanta hotter than the experimental one. It has been suggested[12] that for the $D + H_2$ reaction the influence of the geometric phase on integral and differential cross sections is apt to manifest itself at total energies above 1.8 eV. Since only exchange processes contribute to this reaction (as opposed to the contribution of both direct and exchange processes in the $H + H_2$ reaction), the influence of the

geometric phase on $D + H_2$ should be qualitatively similar to that on the para \rightarrow ortho and ortho \rightarrow para transitions for $H + H_2$.

In this letter, we present accurate numerical results for $H + H_2$ including and excluding the geometric phase in order to assess the magnitude of its effect on the product rotational state distributions and on para \rightarrow ortho and ortho \rightarrow para integral cross sections. We performed these calculations for energies up to 2.6 eV (about 0.1 eV below the minimum of the first electronically excited potential energy surface) and to all total angular momenta needed to obtain converged cross sections. In section 2 we provide an overview of the methodology based on a hyperspherical coordinate formalism[12]. The numerical details of the calculations are discussed in section 3. In section 4 results of the scattering calculations for the $H + H_2$ with and without the geometric phase effect are presented. We focus attention on the influence of the geometric phase on the product rotational state distributions and on the para \rightarrow ortho and ortho \rightarrow para integral cross sections. In section 5 we summarize the main points of this letter.

2. Methodology

The calculations were carried out using a symmetrized hyperspherical coordinate formalism, as described elsewhere[12]. In particular, we use symmetrized hyperspherical coordinates[61,62] and local hyperspherical pseudo surface functions[12] to solve the three-dimensional Schrödinger equation including the geometric phase effect. This approach has several attractive features. First, it can be incorporated into a body-fixed formalism[14,21], in which the body frame is tied to the instantaneous principal axes of moment inertia, and in which a reference

hamiltonian is used which omits some centrifugal couplings terms[12,21]. The resulting pseudo surface functions can be calculated very economically and provide a very efficient basis set for expansion of the six-variable wave function.

In the Born-Oppenheimer approximation, the total wave function is expressed as a product of an electronic wave function ψ_e , which we choose to be real, and a nuclear wave function. The latter is a product of the nuclear space wave function $\psi^{JM\Pi\Gamma}$ and a nuclear spin wavefunction. The electronuclear wave function $\Psi^{JM\Pi\Gamma}$ excluding the nuclear spin part is expressed as

$$\Psi^{JM\Pi\Gamma} = \psi^{JM\Pi\Gamma}(\rho, \xi)\psi_e(q_e; \rho, \xi) \quad (1)$$

which is chosen to belong to an irreducible representation Γ of the nuclear permutation group (P_3) of H_3 . Here q_e refers to the set of all spacial and spin electronic coordinates. The symbol ρ designates the system's hyperradius and ξ an appropriately chosen set of five symmetrized hyperangles. It is also labelled by the total spatial nuclear angular momentum quantum number J , its component M along a laboratory-fixed axis and the spatial nuclear parity Π . In the absence of the geometric phase, we make the electronic wave function belong to the A_1 irreducible representation of the nuclear permutation group. In this case, the spatial part $\psi^{JM\Pi\Gamma}$ of the nuclear wave function belongs to the same irreducible representation Γ as $\Psi^{JM\Pi\Gamma}$. In the presence of the geometric phase, although $\Psi^{JM\Pi\Gamma}$ still belongs to the irreducible representation Γ of P_3 , the spatial part of the nuclear wave function and the electronic wave function do not.

The details of the methodology have been described previously[11,12,63] and will not be repeated here.

For $H + H_2$ reaction, in the P_3 permutation group, only two independent scattering amplitude matrices between a given initial state vjm and final state $v'j'm'$ need be considered, which may be represented as \mathbf{f}^N (the non-reactive one)

and \mathbf{f}^R (the reactive one). For the purposes of the present paper it is convenient to relate these matrices to those corresponding to the irreducible representations A_1, A_2 and E . In the helicity representation these relations are[64]:

$$f_{vjm}^{Nv'j'm'} = \begin{cases} \frac{1}{3}f_{vjm}^{A_1v'j'm'} + \frac{2}{3}f_{vjm}^{Ev'j'm'} & j \text{ and } j' \text{ even} \\ \frac{1}{3}f_{vjm}^{A_2v'j'm'} + \frac{2}{3}f_{vjm}^{Ev'j'm'} & j \text{ and } j' \text{ odd} \\ 0 & j + j' \text{ odd} \end{cases}$$

$$f_{vjm}^{Rv'j'm'} = \begin{cases} \frac{1}{3}f_{vjm}^{A_1v'j'm'} - \frac{1}{3}f_{vjm}^{Ev'j'm'} & j \text{ and } j' \text{ even} \\ \frac{1}{3}f_{vjm}^{A_2v'j'm'} - \frac{1}{3}f_{vjm}^{Ev'j'm'} & j \text{ and } j' \text{ odd} \\ \frac{1}{\sqrt{3}}f_{vjm}^{Ev'j'm'} & j \text{ even, } j' \text{ odd} \\ -\frac{1}{\sqrt{3}}f_{vjm}^{Ev'j'm'} & j \text{ odd, } j' \text{ even} \end{cases} \quad (2)$$

To convert these distinguishable-atom scattering amplitudes into Pauli-antisymmetrized differential cross sections one may use the relations[3]:

(a) para \rightarrow para (j, j' even)

$$\sigma_{vjm}^{v'j'm'} = \frac{V_{v'j'}}{V_{vj}} |f_{vjm}^{Nv'j'm'} - f_{vjm}^{Rv'j'm'}|^2 \quad (3)$$

(b) para \rightarrow ortho (j even, j' odd)

$$\sigma_{vjm}^{v'j'm'} = 3 \frac{V_{v'j'}}{V_{vj}} |f_{vjm}^{Rv'j'm'}|^2 \quad (4)$$

(c) ortho \rightarrow para (j odd, j' even)

$$\sigma_{vjm}^{v'j'm'} = \frac{V_{v'j'}}{V_{vj}} |f_{vjm}^{Rv'j'm'}|^2 \quad (5)$$

(d) ortho \rightarrow ortho (j, j' odd)

$$\sigma_{vjm}^{v'j'm'} = \frac{V_{v'j'}}{V_{vj}} (|f_{vjm}^{Nv'j'm'} + f_{vjm}^{Rv'j'm'}|^2 + 2 |f_{vjm}^{Rv'j'm'}|^2) \quad (6)$$

where V_{vj} and $V_{v'j'}$ stand for initial and final relative velocities respectively. In addition, for comparison with the $D + H_2 \rightarrow DH + H$ reaction one may treat the $H + H_2$ reaction as having the P_2 permutation group and derive the

following relations between the helicity scattering amplitudes for the P_2 irreducible representations (A' and A'') and those for distinguishable particles:

$$\begin{aligned} f_{vjm}^{A'v'j'm'} &= \begin{cases} \sqrt{2}f_{vjm}^{Rv'j'm'} & j \text{ even} \\ 0 & j \text{ odd} \end{cases} \\ f_{vjm}^{A''v'j'm'} &= \begin{cases} \sqrt{2}f_{vjm}^{Rv'j'm'} & j \text{ odd} \\ 0 & j \text{ even} \end{cases} \end{aligned} \quad (7)$$

The explicit form for the Pauli-antisymmetrized reactive differential cross section is given by the simple expression

$$\sigma_{vjm}^{Rv'j'm'} = \begin{cases} \frac{1}{4}\sigma_{vjm}^{A'v'j'm'} & j \text{ even} \\ \frac{3}{4}\sigma_{vjm}^{A''v'j'm'} & j \text{ odd} \end{cases} \quad (8)$$

The corresponding state-to-state, $Q_{vjm}^{Rv'j'm'}$, and degeneracy-averaged, $Q_{vj}^{Rv'j'}$, integral cross sections can be obtained by analytical integration of the expressions above over the scattering angle and are easily expressed in terms of the absolute values of associated transition matrices[3].

3. Numerical Parameters

The pseudo surface function and propagation matrix element calculations were carried out on the Cray-2/4-256 supercomputer at the NASA Ames Supercomputer Center. The integrations of the coupled-channel equations and the final asymptotic analysis tasks were carried out on two Cray Y-MP/864s, one at the San Diego Supercomputer Center and the other at NASA Ames Supercomputer Center.

The LSTH Born-Oppenheimer electronic potential energy surface[65] has been used throughout the calculations covering the energy range between 0.3 eV to 2.6 eV measured with respect to the bottom of the H_2 well.

Pseudo surface functions were computed at 20 values of the hyperradius ρ between 2 and 6 bohr and at 31 values of ρ between 6 and 12 bohr. The results described in this paper were obtained by using 10000 products of trigonometric functions (100 for each of the two hyperangular coordinates θ and ϕ_λ [12]) for ρ between 2 and 6 bohr and 4000 asymptotic rovibrational states in the hyperangular coordinates ω_λ and γ_λ [12] for ρ between 6 and 12 bohr. 2500 pseudo surface functions were kept for the integration of the coupled-channel equations. This number of basis functions was found to be enough to produce sufficiently converged results over the energy range of these calculations, as described below. The boundary at which we change from the principal-axis moment of inertia frame to the body-fixed Jacobi frame[15] was set at $\rho_c = 6$ bohr. This value was used for all J , since the change-over distance is determined mainly by the ρ -dependence of the potential energy function V . For the present converged calculations, the results do not change as ρ_c is further increased.

The largest value of the angular momentum quantum number Ω along the smallest principal axis of inertia was determined by checking the convergence and the unitarity of the scattering matrix with respect to this quantity. A value of $\Omega_{max} = 26$ sufficed and as a result the size of the basis set increases with J for $J = 0 - 26$ and then remains the same for $J = 26 - 52$. For total energies E up to 2.6 eV values of J up to 52 were needed. Calculations were performed with a uniform energy grid of 0.01 eV.

Two important overall measurements of the accuracy of a scattering calculation are the conservation of flux and symmetry of the scattering matrix. For all energies below 2.0 eV, the deviations from flux conservation are 2.5 % or less. Over the same energy range, the scattering matrix is symmetric to within 8 % for elements with squared modulus greater than 0.01. If all elements of the

open part of the matrix was considered, the maximum deviation of the phases of the scattering matrix elements is found to be 9.2° . Limiting the comparison of elements with modulus greater than 0.01 reduces this figure to about 2.3° . For energies between 2.0 eV to 2.6 eV, the maximum deviations from flux conservation are between 5.0 % and 12 % while the scattering matrix is symmetric to within 10 % - 16 % for elements with squared modulus greater than 0.01. The corresponding maximum deviation of the phases of the scattering matrix elements was found to be within 8° . These are the worse cases and at lower collision energies, the scattering matrix unitarity and symmetry are much better. The flux conservation of the results given in the figures is better than 4% and the maximum deviation of the symmetry of the scattering matrix elements is within 5%.

4. Results of Scattering Calculations

We have performed the calculations of product rotational state distributions and for para \rightarrow ortho and ortho \rightarrow para integral cross sections of the $\text{H} + \text{H}_2$ reaction both with and without inclusion of the geometric phase effect for total energies below 2.6 eV (measured with respect to the bottom of the isolated H_2 well).

4.1 Rotational State Distributions

Experimental measurements of these distributions for the $\text{D} + \text{H}_2$ reaction have been made recently[59,60]. Since many aspects of this reaction are similar to those of the $\text{H} + \text{H}_2$ reaction, we will compare the current calculations with the experimental and theoretical results for the $\text{D} + \text{H}_2$ reaction in order to assess the importance of the geometric phase effect for the latter. Figure 1(a) shows a comparison of the theoretical results of Mielke *et al.*[38] (using the

DMBE[66] potential energy surface), and of Zhang and Miller[41] (using the LSTH potential energy surface[65]) with the experimental measurements of Kliner, Rinnen and Zare[59] on the integral cross section for the $D + H_2(v = 0, j = 0, 1) \rightarrow DH(v' = 1, j') + H$ reaction at a relative translational energy E_{tr} of 1.05 eV. The theoretical values are appropriately weighted averages over the initial rotational states $j = 0, 1$ according to their respective populations at $T = 294 \text{ K}^\circ$. The experimental distributions are normalized such that the sum of the cross sections for $j' = 0 - 9$ is the same as for the theoretical results. The absolute cross sections are also displayed on the figure. The two quantum calculations are in excellent agreement with the experimental results. The slight differences between the two calculations are consistent with the differences between the DMBE and LSTH potential energy surfaces. Figure 1(b) shows the corresponding cross sections of the $H + H_2(v = 0, j = 0, 1) \rightarrow H_2(v' = 1, j') + H$ reaction treated as having the P_2 symmetry and weighted by the $j = 0$ and $j = 1$ contributions according to their respective populations at $T = 294 \text{ K}^\circ$, as a function of final rotational states. The inclusion of the geometric phase produces no detectable difference to about three significant digits. The qualitative feature of the $H + H_2$ product rotational state distribution is similar to that for the $D + H_2$ reaction. This lack of influence of the geometric phase is in agreement with the semi-classical argument of Mead[56] and with the previous quantum calculations[12].

More recently, Kliner, Rinnen and Zare[60] have determined the product rotational state distribution for the reaction $D + H_2(v = 1, j = 1)$ in which the H_2 reagent was vibrationally excited. These results are shown in Figure 2(a). Also shown here are the results of converged 3D quantum calculations by S. L. Mielke *et al.*[38]. The calculations qualitatively reproduce the experimental results, but there are significant differences between them which are outside of the experimental

uncertainty. The theoretical distribution peaks at $j' = 10$ whereas the measured distribution peaks at $j' = 7$ and the predicted enhancement in the $v' = 1$ rate with reagent vibrational excitation is a factor of 4.2 ± 0.3 whereas the calculated one is 6.4, *i.e.* 52 % higher than the experimental one. Since the calculations are well converged and use an accurate *ab initio* potential energy surface and the experimental measurements are carefully checked, the discrepancy shown in Figure 2(a) is unlikely to be either attributed to the experimental uncertainty or the accuracy of the calculations. However, when we plot the corresponding converged quantum calculation of the product rotational states distributions for the $\text{H} + \text{H}_2$ reaction in Figure 2(b), inclusion of the geometric phase effect results in significant differences. Without inclusion of this phase the calculated rotational state distribution is similar to the theoretical $\text{D} + \text{H}_2$ results obtained previously (also without inclusion of this phase). When the geometric phase effect is included in our $\text{H} + \text{H}_2$ calculations, the results are much closer to the experimental ones. It has been suggested[12] that at the energies of these $\text{D} + \text{H}_2(v = 1, j = 1)$ experiments the influence of the geometric phase on $\text{D} + \text{H}_2$ should be qualitatively similar to those for the para \rightarrow ortho and ortho \rightarrow para transitions in $\text{H} + \text{H}_2$ because only exchange processes contribute both to the latter and to $\text{D} + \text{H}_2$ as opposed to the contribution of both direct and exchange processes for para \rightarrow para and ortho \rightarrow ortho transitions in $\text{H} + \text{H}_2$. When the geometric phase effect is included in the calculation, vibrational excitation of the H_2 reagent results in substantial rotational excitation of the $\text{H}_2(v' = 1)$ product and increase the reaction rate into $v' = 1$ by about a factor of 4.

Figure 3 shows a similar relation between the experimental $\text{D} + \text{H}_2$ rotational states distributions at $E_{\text{tr}} = 1.4$ eV and the present theoretical results for $\text{H} + \text{H}_2$. Theoretical results for $\text{D} + \text{H}_2$ are not available for comparison with the experiment

at this energy. The present calculations strongly suggest that the discrepancy between theory and experiment for the $D + H_2$ system is due to the geometric phase effect. For reactions involving dissimilar hydrogen atoms, such as $D + H_2$, it will become necessary to include this effect in the high energy regime.

4.2 Para \rightarrow ortho and ortho \rightarrow para Integral Cross Sections

In Figures 4 and 5 we display the integral cross sections as a function of energy for the $H + H_2(v = 0, j = 0, 1) \rightarrow H_2(v' = 1, j' = 0, 1) + H$ reaction treated as having the P_2 symmetry, summed over the angular momentum projection quantum number of the molecular product. Each of these figures displays three curves, one for the case in which the geometric phase effect is not included, Q^{NGP} , and the one for which it is included, Q^{GP} , and their difference. As can be seen, both figures display differences for energies higher than about 1.8 eV.

It is expected that as the system's energy increases towards the lowest conical intersection energy (2.7 eV), there should be two kinds of semi-classical paths which contribute to the exchange scattering amplitude, that which encircles the conical intersection and that which does not[11,12,56]. Figure 6 depicts these two kinds of semi-classical paths. For energies lower than 1.8 eV the semi-classical path does not encircle the conical intersection, it is expected that the phase of the scattering matrix elements and of the scattering amplitude should change by π as a result of the inclusion of the geometric phase effect. For energies higher than 1.8 eV, it is expected that both semi-classical paths will contribute to the reaction. As a result inclusion of the geometric phase effect will affect the phases of the corresponding contributions to the scattering matrix differently, and the net effect will result in a more complicated behavior. For sufficiently high energies it will be

necessary to include the nonadiabatic effects of coupling to the upper sheet of the potential energy surface.

5. Summary

We have investigated the effect of the geometric phase on the product rotational state distributions and on para \rightarrow ortho and ortho \rightarrow para integral cross sections for the $\text{H} + \text{H}_2$ system at total collision energies up to 2.6 eV above the bottom of the ground state H_2 electronic potential well. Inclusion of the effect of the geometric phase is shown to significantly change the distributions and integral cross sections for energies higher than 1.8 eV. The results for the $\text{H} + \text{H}_2$ reaction that include the effect of the geometric phase are in qualitative agreement with the measured distributions for the $\text{D} + \text{H}_2$ reaction. Our results strongly suggest that the geometric phase effect is very significant in the $\text{D} + \text{H}_2$ system at these energies. It may also be significant in other systems displaying conical intersections, under conditions for which paths in configuration space encircle the line representing such intersections.

References

- [1] D. G. Truhlar, R. E. Wyatt, *Annu. Rev. Phys. Chem.* **27** 1 (1976).
- [2] A. Kuppermann and G. C. Schatz, *J. Chem. Phys.* **62**, 2502 (1975).
- [3] G. C. Schatz and A. Kuppermann, *J. Chem. Phys.* **65**, 4642,4668 (1976).
- [4] A. B. Elkowitz and R. E. Wyatt, *J. Chem. Phys.* **62**, 2504 (1975).
- [5] A. B. Elkowitz and R. E. Wyatt, *J. Chem. Phys.* **63**, 702 (1975).
- [6] R. B. Walker, E. B. Stechel and J. C. Light, *J. Chem. Phys.* **69**, 2922 (1978).
- [7] A. Kuppermann and P. G. Hipes, *J. Chem. Phys.* **84**, 5962 (1986).
- [8] P. G. Hipes and A. Kuppermann, *Chem. Phys. Lett.* **133**, 1 (1987).
- [9] S. A. Cuccaro, P. G. Hipes and A. Kuppermann, *Chem. Phys. Lett.* **154**, 155 (1989); **157**, 440 (1989).
- [10] Y. M. Wu, S. A. Cuccaro, P. G. Hipes and A. Kuppermann, *Chem. Phys. Lett.* **168**, 429 (1990).
- [11] B. Lepetit and A. Kuppermann, *Chem. Phys. Lett.* **166** 581 (1990).
- [12] Y.S.M. Wu, B. Lepetit and A. Kuppermann, *Chem. Phys. Lett.* **186** 319 (1991).
- [13] G. A. Parker, R. T. Pack, B. J. Archer and R. B. Walker, *Chem. Phys. Lett.* **137**, 564 (1987).
- [14] R. T. Pack and G. A. Parker, *J. Chem. Phys.* **87**, 3888 (1987); **90**, 3511 (1989).
- [15] J. D. Kress, Z. Bačić, G. A. Parker and R. T. Pack, *Chem. Phys. Lett.* **157**, 585 (1989); **170**, 306 (1990).
- [16] Z. Bačić, J. D. Kress, G. A. Parker and R. T. Pack, *J. Chem. Phys.* **92**, 2344 (1990).
- [17] T. J. Park and J. C. Light, *J. Chem. Phys.* **91**, 974 (1989).
- [18] G. C. Schatz, *Chem. Phys. Lett.* **150**, 92 (1988).

- [19] G. C. Schatz, *Chem. Phys. Lett.* **151**, 409 (1988); *J. Chem. Phys.* **90**, 3582 (1989).
- [20] J. Linderberg, *Int. J. Quant. Chem. Symp.* **19**, 467 (1986); J. Linderberg and B. Vessal, *Int. J. Quant. Chem.* **31**, 65 (1987); J. Linderberg, S. B. Padkjaer, Y. Öhrn and B. Vessal, *J. Chem. Phys.* **90**, 6254 (1989).
- [21] J. M. Launay and M. Le Dorneuf, *Chem. Phys. Lett.* **163**, 178 (1989).
- [22] J. M. Launay and *Theor. Chim. Acta* **79** 183 (1991).
- [23] S. B. Padkjaer and J. M. Launay and *Chem. Phys. Lett.* **181** 95 (1991).
- [24] K. Haug, D. W. Schwenke, Y. Shima, D. G. Truhlar, J. Z. H. Zhang and K. J. Kouri, *J. Phys. Chem.* **90**, 6757 (1986).
- [25] J. Z. H. Zhang, D. J. Kouri, K. Haug, D. W. Schwenke, Y. Shima and D. G. Truhlar, *J. Chem. Phys.* **88**, 2492 (1988).
-
- [26] M. Mladenovic, M. Zhao, D. G. Truhlar, D. W. Schwenke, Y. Sun and D. J. Kouri, *Chem. Phys. Lett.* **146**, 358 (1988).
- [27] M. Mladenovic, M. Zhao, D. G. Truhlar, D. W. Schwenke, Y. Sun and D. J. Kouri, *J. Phys. Chem.* **92**, 7035 (1988).
- [28] M. Zhao, M. Mladenovic, D. G. Truhlar, D. W. Schwenke, Y. Sun, D. J. Kouri and N. C. Blais, *J. Am. Chem. Soc.* **111**, 852 (1989).
- [29] M. Zhao, M. Mladenovic, D. G. Truhlar, D. W. Schwenke, O. Sharafeddin, Y. Sun and D. J. Kouri, *J. Chem. Phys.* **91**, 5302 (1989).
- [30] M. Zhao, D. G. Truhlar, Y. Sun, D. J. Kouri and D. W. Schwenke, *Chem. Phys. Lett.* **156**, 281 (1989).
- [31] N. C. Blais, M. Zhao, M. Mladenovic, D. G. Truhlar, D. W. Schwenke, Y. Sun and D. J. Kouri, *J. Chem. Phys.* **91**, 1038 (1989).
- [32] C. Yu, D. J. Kouri, M. Zhao, D. G. Truhlar and D. W. Schwenke, *Chem. Phys. Lett.* **157**, 491 (1989).

- [33] C. Yu, Y. Sun, D. J. Kouri, P. Halvick, D. G. Truhlar and D. W. Schwenke, *J. Chem. Phys.* **90**, 7608 (1989).
- [34] C. Yu, D. J. Kouri, M. Zhao, D. G. Truhlar and D. W. Schwenke, *Int. J. Quant. Chem. Symp.* **23**, 45 (1989).
- [35] M. Zhao, D. G. Truhlar, D. W. Schwenke, C. H. Yu and D. J. Kouri, *J. Phys. Chem.* **94**, 7062 (1990).
- [36] M. Zhao, D. G. Truhlar, D. W. Schwenke and D. J. Kouri, *J. Phys. Chem.* **94**, 7074 (1990).
- [37] N. C. Blais, M. Zhao, D. G. Truhlar, D. W. Schwenke and D. J. Kouri, *Chem. Phys. Lett.* **166** 11 (1990).
- [38] S. L. Mielke, R. S. Friedman, D. G. Truhlar and D. W. Schwenke, *Chem. Phys. Lett.* **188** 359 (1992).
- [39] J. Z. H. Zhang and W. H. Miller, *Chem. Phys. Lett.* **140**, 329 (1987); **153**, 465 (1988); **159**, 130 (1989).
- [40] J. Z. H. Zhang and W. H. Miller, *J. Chem. Phys.* **88**, 4549 (1988); **90**, 7610 (1989); *Chem. Phys. Lett.* **159**, 130 (1989).
- [41] J. Z. H. Zhang and W. H. Miller, *J. Chem. Phys.* **91** 1528 (1989).
- [42] J. Z. H. Zhang and W. H. Miller, *J. Chem. Phys.* **91**, 1528 (1989); **92**, 1811 (1990).
- [43] S. M. Auerbach, J. Z. H. Zhang and W. H. Miller, *J. Chem. S. F.* **86**, 1701 (1990).
- [44] D. E. Manolopoulos and R. E. Wyatt, *Chem. Phys. Lett.* **159**, 123 (1989).
- [45] D. E. Manolopoulos and R. E. Wyatt, *Chem. Phys. Lett.* **152**, 23 (1988).
- [46] D. E. Manolopoulos and R. E. Wyatt, *J. Chem. Phys.* **92**, 810 (1990).
- [47] D. E. Manolopoulos, M. D'Mello and R. E. Wyatt, *J. Chem. Phys.* **93**, 403 (1990).

- [48] M. D'Mello, D. E. Manolopoulos and R. E. Wyatt, *Chem. Phys. Lett.* **168**, 113 (1990).
- [49] D. E. Manolopoulos, M. D'Mello, R. E. Wyatt and R. B. Walker, *Chem. Phys. Lett.* **169**, 482 (1990).
- [50] F. Webster and J. C. Light, *J. Chem. Phys.* **90**, 265 (1989).
- [51] F. Webster and J. C. Light, *J. Chem. Phys.* **90**, 300 (1989).
- [52] R. A. Marcus, *J. Chem. Phys.* **45**, 4493 (1966).
- [53] H. C. Longuet-Higgins, U. Öpik, M. H. L. Pryce and R. A. Sack, *Proc. Roy. Soc. A* **244**, 1 (1958); G. Herzberg and H. C. Longuet-Higgins, *Discuss. Faraday Soc.* **35**, 77 (1963); H. C. Longuet-Higgins, *Adv. Spec.* **2**, 429 (1961).
- [54] C. A. Mead and D. G. Truhlar, *J. Chem. Phys.* **70**, 2284 (1979).
- [55] C. A. Mead, *Chem. Phys.* **49**, 23 (1980).
- [56] C. A. Mead, *J. Chem. Phys.* **72**, 3839 (1980).
- [57] Y. Aharonov and D. Bohm, *Phys. Rev.* **115**, 485 (1959).
- [58] M. V. Berry, *Proc. Roy. Soc. A* **392**, 45 (1984).
- [59] D. A. V. Kliner, K.-D. Rinnen and R. N. Zare, *Chem. Phys. Lett.* **166** 107 (1990).
- [60] D. A. V. Kliner, D. E. Adelman and R. N. Zare, *J. Chem. Phys.* **95** 1648 (1991).
- [61] A. Kuppermann, *Chem. Phys. Lett.* **32** 374 (1974); R. T. Ling and A. Kuppermann, in: *Electronic and Atomic Collisions*, Abstracts of papers of the 9th International Conference on the Physics of Electronic and Atomic Collisions, Seattle, Washington, 24-30 July 1975, Vol. I. eds. J. S. Ridley and R. Geballe (Univ. Washington Press, Seattle, 1975) pp. 353, 354.

- [62] A. Kuppermann, Accurate Quantum calculations of Reactive Systems. In Theoretical Chemistry - Theory of Scattering: Papers in Honor of Henry Eyring; ed. D. Henderson (Academic Press, New York, 1981) pp. 127, 128.
- [63] B. Lepetit, Z. Peng and A. Kuppermann, *Chem. Phys. Lett.* **166** 572 (1990).
- [64] P. Hipes, Ph. D. Thesis, California Institute of Technology, pp.
- [65] P. Siegbahn and B. Liu, *J. Chem. Phys.* **68**, 2457 (1978); D. G. Truhlar and C. J. Horowitz, *J. Chem. Phys.* **68**, 2466 (1978); **71**, 1514E (1979).
- [66] A. J. Varandas, F. B. Brown, C. A. Mead, D. G. Truhlar and N. C. Blais, *J. Chem. Phys.* **86** 6258 (1987).

Figure Captions

Figure 1. (a) Comparison of theoretical and experimental integral cross sections as a function of the product rotational state quantum number j' for $D + H_2(v = 0, j = 0, 1) \rightarrow DH(v' = 1, j') + H$ at $E_{tr} = 1.05\text{eV}$. The circles connected by solid lines represent the experimental results of ref.[59]. Error bars represent one standard deviation. The squares connected by solid lines are the theoretical values of ref. [41] (using the LSTH surface), and the triangles connected by solid lines are the theoretical values of ref. [38] (using the DMBE surface). The experimental results are normalized such that the sum of the cross sections for $j' = 0 - 9$ is the same as for the theoretical results. (b) The present calculations of integral cross sections for $H + H_2(v = 0, j = 0, 1) \rightarrow H_2(v' = 1, j') + H$ reaction, treated as having the P_2 symmetry, as a function of the product rotational state j' at $E_{tr} = 1.05\text{eV}$. The cross sections have been weighted for the $j = 0$ and $j = 1$ contributions according to their respective populations at $T = 294\text{K}^\circ$. The open circles (squares) correspond to the case in which the geometric phase is included (is not included).

Figure 2. (a) Comparison of theoretical and experimental integral cross sections as a function of the product rotational state quantum number j' for $D + H_2(v = 1, j = 1) \rightarrow DH(v' = 1, j') + H$ at $E_{tr} = 1.0\text{eV}$. The circles connected by solid line represent the experimental results of ref.[60]. Error bars represent one standard deviation. The squares connected by solid lines are the theoretical values of ref. [38] (using the DMBE surface). The experimental results are normalized such that the sum of the cross sections for $j' = 0 - 12$ is the same as for the theoretical results. (b) The present calculations of integral cross sections for $H + H_2(v = 1, j = 1) \rightarrow H_2(v' = 1, j') + H$ reaction, treated as having the P_2 symmetry, as a function of the product rotational state quantum number j' at E_{tr}

= 1.0 eV. The open circles (squares) correspond to the case in which the geometric phase is included (is not included).

Figure 3. (a) The experimental integral cross sections from ref.[60] as a function of the product rotational state quantum number j' for $D + H_2(v = 1, j = 1) \rightarrow DH(v' = 1, j') + H$ at $E_{tr} = 1.4\text{eV}$. Error bars represent one standard deviation. (b) The present calculations of integral cross sections for $H + H_2(v = 1, j = 1) \rightarrow H_2(v' = 1, j') + H$ reaction, treated as having P_2 symmetry, as a function of the product rotational state quantum number j' at $E_{tr} = 1.4\text{ eV}$. The open circles (squares) correspond to the case in which the geometric phase is included (is not included).

Figure 4. Degeneracy-averaged integral cross sections for the $H + H_2(v = 0, j = 0) \rightarrow H_2(v' = 0, j' = 1) + H$ reaction, treated as having the P_2 symmetry, as a function of total energy. The open circles (squares) correspond to the case in which the geometric phase is included (is not included). Also plotted is the difference (represented by triangle) between those two curves which were multiplied by a scaling factor of 25 before being plotted.

Figure 5. Degeneracy-averaged integral cross sections for the $H + H_2(v = 0, j = 1) \rightarrow H_2(v' = 1, j' = 0) + H$ reaction, treated as having the P_2 symmetry, as a function of total energy. The open circles (squares) correspond to the case in which the geometric phase is included (is not included). Also plotted is the difference (represented by triangle) between those two curves which were multiplied by a scaling factor of 25 before being plotted.

Figure 6. This figure depicts two kinds of semi-classical path which contribute to the exchange scattering amplitude, that which encircles (represented by dash

line) the conical intersection and that which does not (represented by solid line). The motion of the approaching reagent molecules is represented by a point moving in from above at the gap between the two nearly vertical tubes displayed at the top of the figure. The motion of the product molecules receding from each other is represented by a point moving outward in the gap between the tubes pointing toward the bottom of the figure.

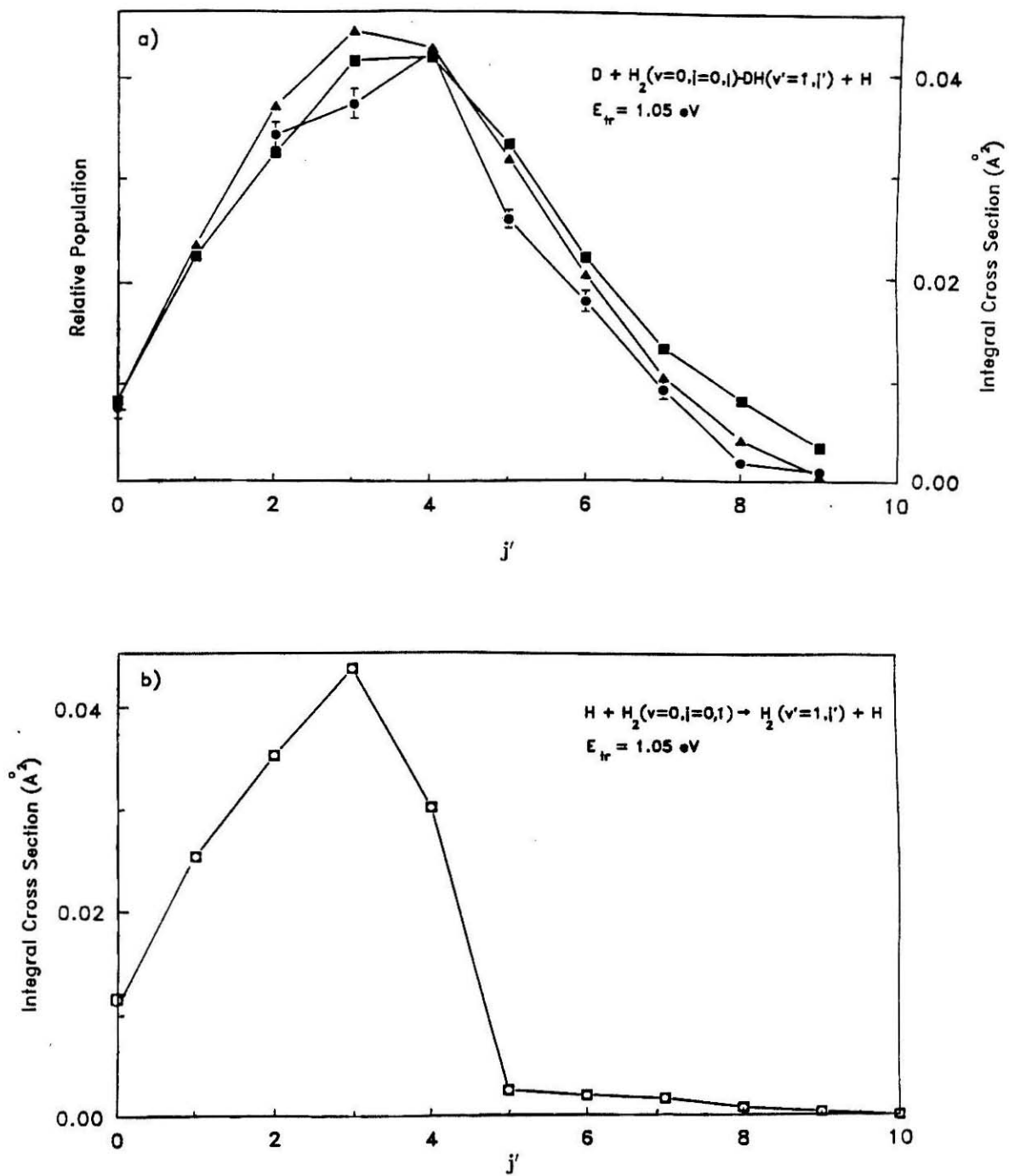


Figure 1

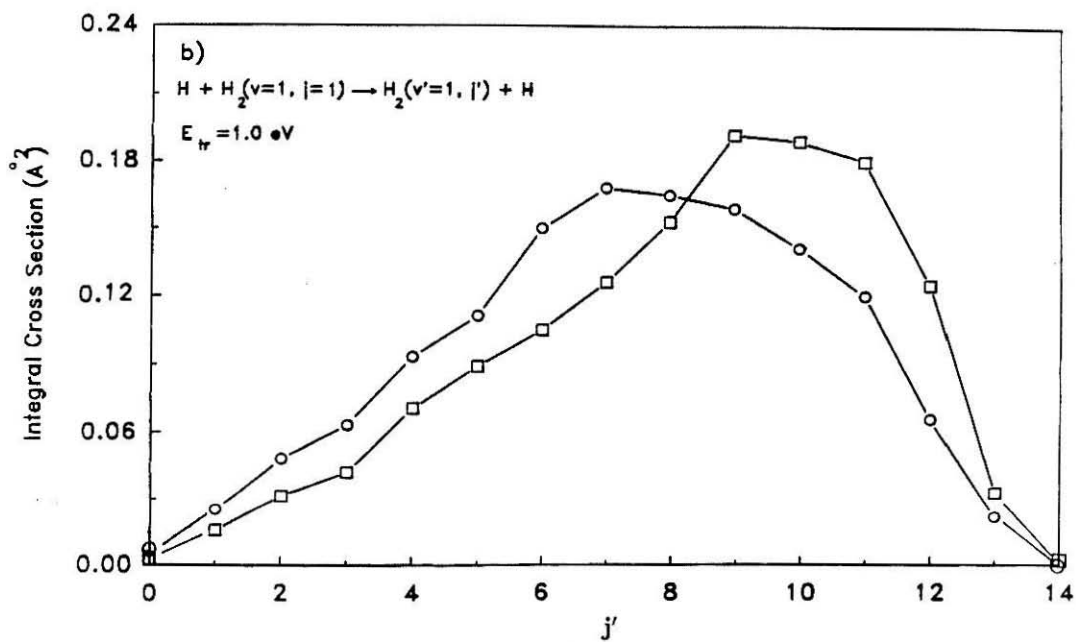
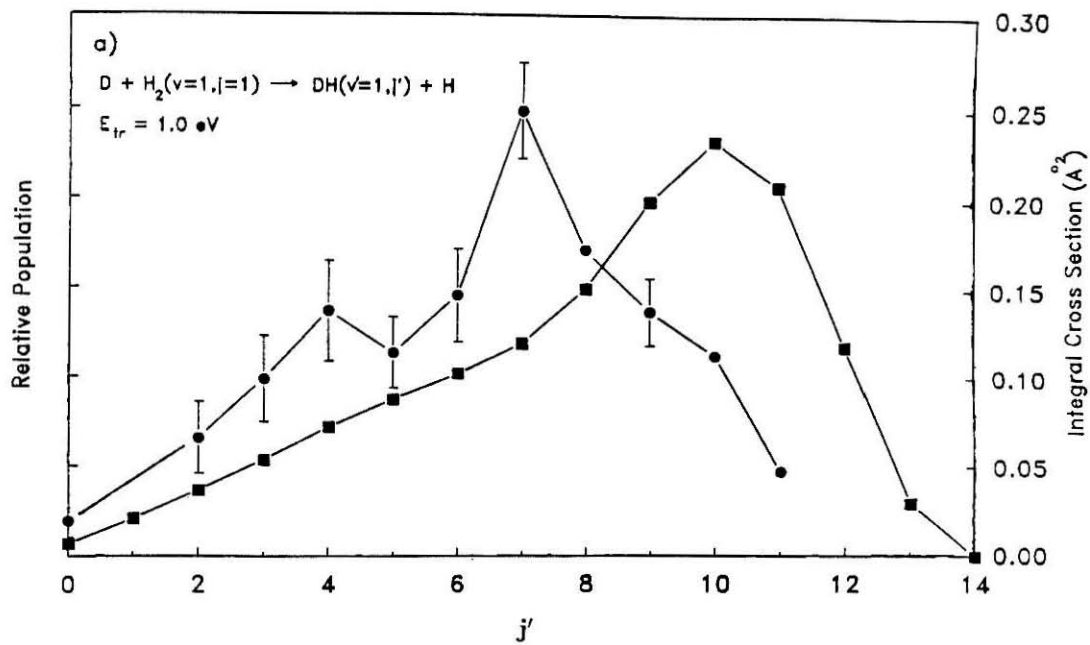


Figure 2

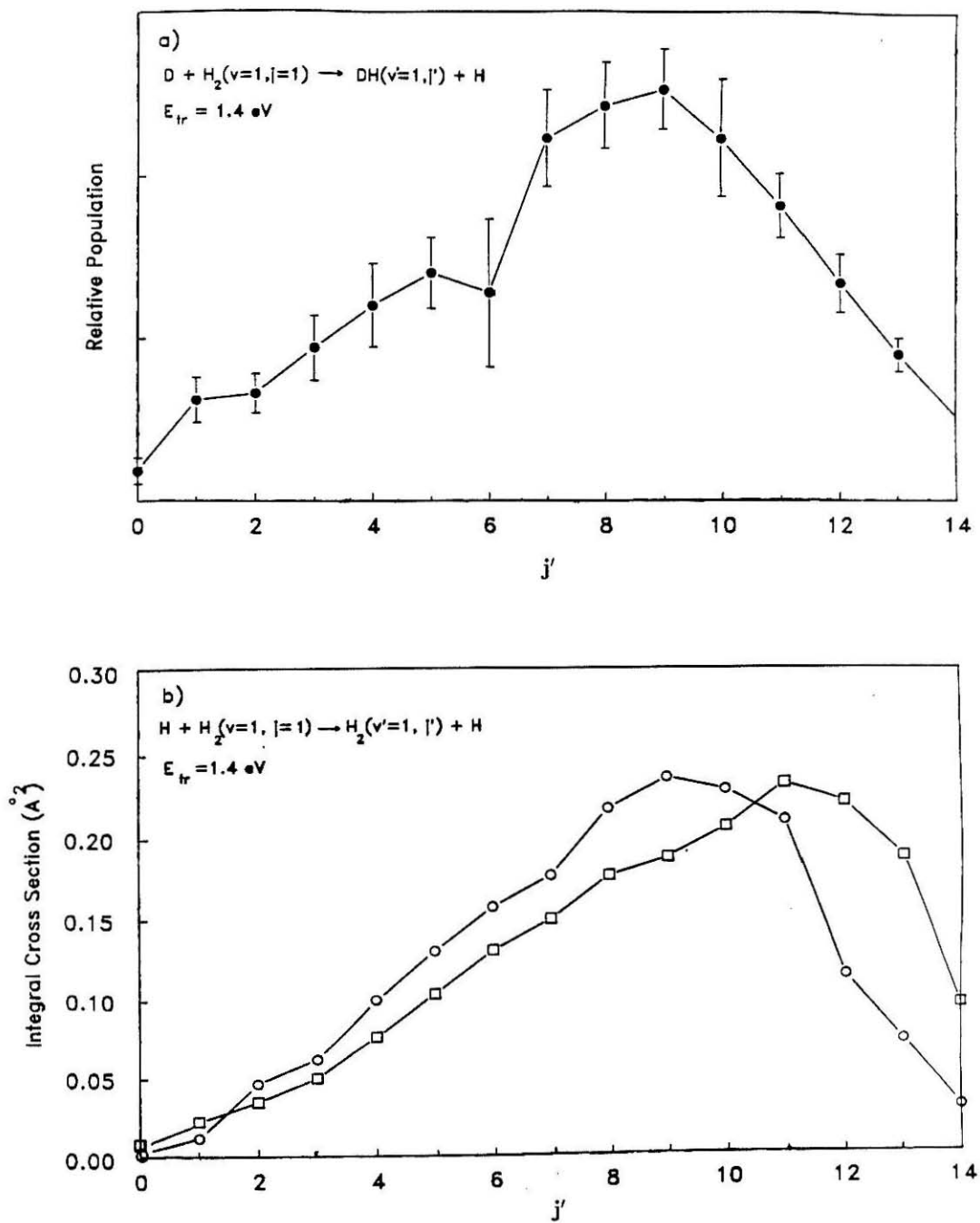
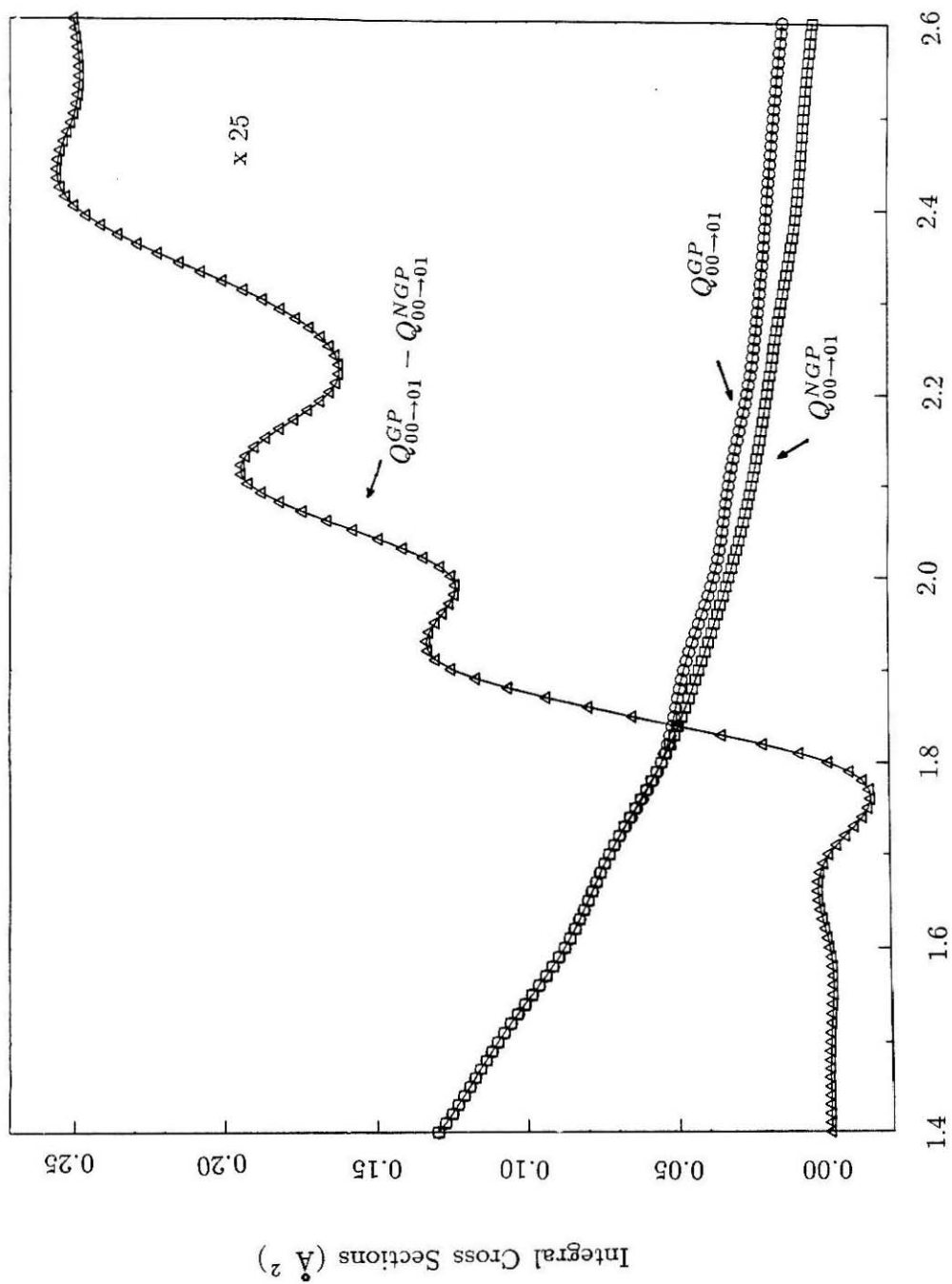
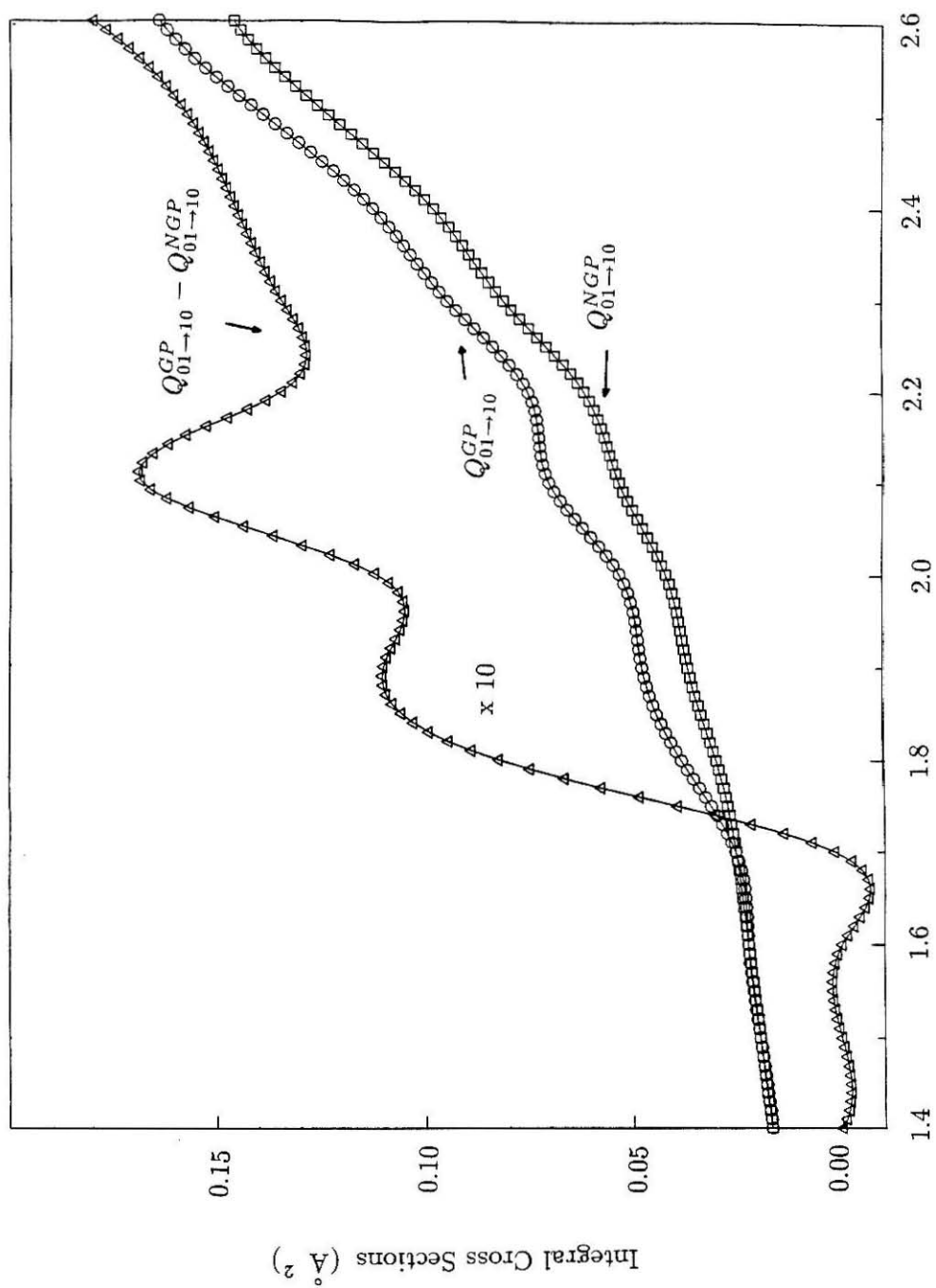


Figure 3



$E_{\text{total}}(\text{eV})$

Figure 4



$E_{\text{total}}(\text{eV})$

Figure 5

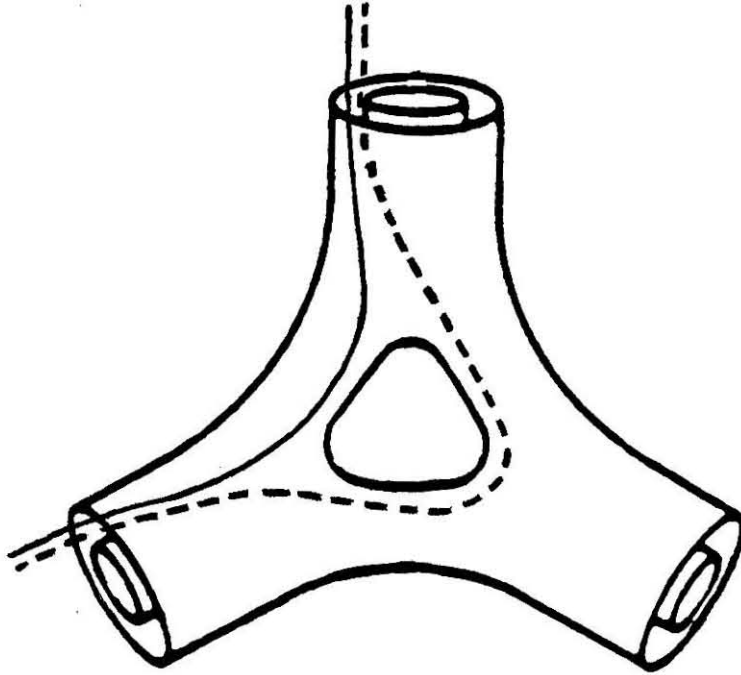


Figure 6

CHAPTER IV

Theoretical Calculation of Experimentally Observable Consequences of the geometric Phase on Chemical Reaction Cross Sections

† This paper appeared in *J. Chem. Phys.* **186**, 319 (1991).

THEORETICAL CALCULATION OF EXPERIMENTALLY OBSERVABLE
CONSEQUENCES OF THE GEOMETRIC PHASE ON
CHEMICAL REACTION CROSS SECTIONS

Yi-Shuen Mark Wu ¹, Aron Kuppermann and B. Lepetit ²

Arthur Amos Noyes Laboratory of Chemical Physics

Division of Chemistry and Chemical Engineering ³

California Institute of Technology

Pasadena, CA 91125, USA

(Received September 1991)

ABSTRACT

Any system composed of three similar or dissimilar atoms whose ground states are 2S , displays a conical intersection, as well as a corresponding geometric phase effect. We report for the first time the results of accurate quantum mechanical calculations including this effect. Integral and differential cross sections for the simple $H + H_2$ system over the energy range 0.7 eV to 1.2 eV are presented. For para \rightarrow para and ortho \rightarrow ortho transitions they are changed significantly, whereas for para \rightarrow ortho and ortho \rightarrow para transitions they are not. These results are verifiable experimentally.

¹ Work performed in partial fulfillment of the requirements for the Ph.D. degree in Chemistry at the California Institute of Technology.

² Current address: 111 Rue Olivier De Serres, 75015 Paris, France

³ Contribution number 8512

1. INTRODUCTION

It has been shown[1] that a system composed of three atoms, which may be dissimilar, but which have 2S ground states, displays a conical intersection between its two lowest electronically adiabatic potential energy surfaces. As one follows a closed path in nuclear configuration space around the line along which these two surfaces conically intersect, the ground state Born-Oppenheimer electronic wave function changes sign if it is required to real[1-7]. This sign change is a special case of Berry's geometric phase[8], and is sometimes referred to as the molecular Aharonov-Bohm effect[9]. Particular systems which display this sign change effect are those composed of three alkali atoms, be they identical or dissimilar, and of three isotopic hydrogen atoms, identical or dissimilar. For the isotopic H_3 system, the two lowest electronic states belong to the $^2E'$ irreducible representation of the D_{3h} point symmetry group at equilateral triangular geometries of the three nuclei, whether these are identical or not, *i.e.*, the geometry of the conical intersection is that of an equilateral triangle.

Mead and Truhlar[3] have shown that the change in sign associated with such conical intersections has consequences for the corresponding nuclear motion. A corollary of that change in sign is that the nuclear wavefunction must also change sign when taken through such closed path, to make the total product wavefunction single-valued. Berry's geometric phase is an example of holonomy, the phenomenon by which some variables change when other variables or parameters characterizing a system return to their initial values[10,11]. The origin of this additional phase are anholonomic, that is, they depend only on the geometry of the parameter space and the circuit traversed rather than on other aspects of the hamiltonian. Notably lacking are accurate quantitative predictions or experimental observations on real chemical reactions demonstrating the magnitude of this effect.

All quantum mechanical calculations of experimentally observable reaction cross sections for the $\text{H} + \text{H}_2$ system performed so far have assumed that the reaction occurs on the single ground electronic potential energy surface[12-28]. It has been recently shown however[6] that, in the absence of coupling to the ground electronic state, the geometric phase completely modifies the energy spectrum and the permutation symmetry properties of the quasi-bound rovibrational states of the first electronically excited state of H_3 . In addition, it has also been shown that the $J = 0$ total angular momentum partial cross sections of para \rightarrow para and ortho \rightarrow ortho transitions for this system is significantly changed by this effect[7]. In this letter, we report results obtained by extending these calculations to all total angular momenta needed to obtain converged integral and differential cross sections over an energy range from 0.7 eV to 1.2 eV. By performing these calculations including and excluding the geometric phase, we have been able to accurately assess the magnitude of its effect on this reaction.

We divide this paper into four additional sections. In Section 2 we provide an overview of the methodology based on a hyperspherical coordinate formalism. The numerical details of the calculations are discussed in Section 3. In Section 4 results of scattering calculations for the $\text{H} + \text{H}_2$ performed with and without the geometric phase are presented. Section 5 contains some concluding remarks.

2. METHODOLOGY

In the present calculations, we neglect all spin-orbit and spin-spin interactions. Under conditions of validity of the Born-Oppenheimer approximation, the electronuclear wave function can be written as a product of the electronic part ψ_e , which we chose to be real, and the nuclear part. The latter can be factored into a nuclear spin part and a spacial part $\psi^{JM\Pi\Gamma}$. J is the total angular momentum

quantum number, M its projection onto laboratory-fixed axis, Π the parity with respect to inversion of the nuclei through the system's center of mass and Γ the irreducible representation of the nuclear permutation group (P_3 for the H_3 system) to which $\Psi^{JM\Pi\Gamma}$, the electro-nuclear wave function excluding the nuclear spin part, belongs:

$$\Psi^{JM\Pi\Gamma} = \psi^{JM\Pi\Gamma}(\rho, \xi) \psi_e(q_e; \rho, \xi) \quad (1)$$

Here q_e refers to the set of all, spacial and spin, electronic coordinates. The symbol ρ designates the system's hyperradius and ξ an appropriately chosen set of 5 symmetrized hyperangles. $\psi^{JM\Pi\Gamma}$ is an eigenfunction of the nuclear motion hamiltonian[15-17]

$$\hat{H} = -\frac{\hbar^2}{2\mu\rho^5} \frac{\partial}{\partial\rho} \rho^5 \frac{\partial}{\partial\rho} + \frac{\hat{\Lambda}^2}{2\mu\rho^2} + V(\rho, \xi) \quad (2)$$

where μ is the three-body reduced mass. $\hat{\Lambda}$ the grand canonical angular momentum operator and V the Born-Openheimer electronic potential energy function.

We use a set of principal-axis body-fixed hyperspherical coordinates closely related to the modified Whitten-Smith coordinates[27,29,30]. Three of the 5 hyperangles are the Euler angles ($\alpha\beta\gamma$) which specify the orientation of the body frame in space. The other two are the symmetrized hyperangles (θ, ϕ_λ) obtained by a rotation of the internal configuration space axis described previously[31] through Euler angles ($\frac{\pi}{2}, \frac{\pi}{2}, \pi$). The angle θ is in the $[0, \frac{\pi}{2}]$ range and ϕ_λ in the $[0, 2\pi)$ range. These two angles describe the shape of the molecular triangle, such that $\theta = \pi/2$ corresponds to linear configurations and $\theta = 0$ to symmetric top configurations. The quantization axis Z for the internal motion is chosen to be the axis of least inertia and the Y axis is associated to the axis of maximum inertia, perpendicular to the molecular plane. This choice enables one to minimise coupling due to rotation of the body frame at linear or near-linear configurations[27,28]. Let r_λ and R_λ be

respectively the mass scaled vectors from A_ν to A_κ and from the center of mass of $A_\nu A_\kappa$ to A_λ , where the three nuclei are labelled $A_\alpha A_\beta$ and A_γ and $\lambda\nu\kappa$ is a cyclic permutation of $\alpha\beta\gamma$. The cartesian components of r_λ and R_λ in this body-fixed frame are given by

$$r_{\lambda X} = -\rho \sin(\pi/4 - \theta/2) \cos(\phi_\lambda/2); \quad (3a)$$

$$r_{\lambda Y} = 0; \quad (3b)$$

$$r_{\lambda Z} = \rho \cos(\pi/4 - \theta/2) \sin(\phi_\lambda/2); \quad (3c)$$

$$R_{\lambda X} = \rho \sin(\pi/4 - \theta/2) \sin(\phi_\lambda/2); \quad (3d)$$

$$R_{\lambda Y} = 0; \quad (3e)$$

$$R_{\lambda Z} = \rho \cos(\pi/4 - \theta/2) \cos(\phi_\lambda/2). \quad (3f)$$

The square of the grand canonical angular momentum operator $\hat{\Lambda}^2$ can be expressed in terms of these angles as

$$\hat{\Lambda}^2 = \hat{\Lambda}_\circ^2 + \frac{4\hat{J}_Z^2}{\cos^2\theta} + \hat{R} \quad (4)$$

where $\hat{\Lambda}_\circ^2$ and \hat{R} are given by

$$\hat{\Lambda}_\circ^2 = -4\hbar^2 \left[\frac{1}{\sin 2\theta} \frac{\partial}{\partial \theta} \sin 2\theta \frac{\partial}{\partial \theta} + \frac{1}{\sin^2 \theta} \frac{\partial^2}{\partial \phi_\lambda^2} \right] \quad (5a)$$

$$\begin{aligned} \hat{R} = \frac{1}{\cos^2(\frac{\pi}{4} - \frac{\theta}{2})} & \left[\frac{\hat{J}^2 - \hat{J}_Z^2}{2} + \frac{\hat{J}_+^2 + \hat{J}_-^2}{4} - \hat{J}_Z^2 + \frac{1}{\sin^2 \theta} \left[\frac{\hat{J}^2 - \hat{J}_Z^2}{2} \right. \right. \\ & \left. \left. - \frac{\hat{J}_+^2 + \hat{J}_-^2}{4} \right] \right] - 2\hbar \frac{\cos \theta}{\sin^2 \theta} (\hat{J}_+ + \hat{J}_-) \frac{\partial}{\partial \phi_\lambda} \end{aligned} \quad (5b)$$

\hat{J}_Z being the body-fixed Z component of the total angular momentum \hat{J} , and $\hat{J}_\pm = \hat{J}_X \pm i\hat{J}_Y$.

We define a set of five-dimensional pseudo surface functions $\Phi_{n\Omega}^{JM\Pi\Pi}$ at the hyperradius $\bar{\rho}$ by

$$\Phi_{n\Omega}^{JM\Pi\Pi}(\alpha, \beta, \gamma, \theta, \phi_\lambda; \bar{\rho}) = \varphi_n^{\Omega\Pi\Pi}(\theta, \phi_\lambda; \bar{\rho}) N_\Omega^{JM\Pi}(\alpha, \beta, \gamma) \quad (6)$$

The functions $N_{\Omega}^{JM\Pi}$ are linear combinations of Wigner rotation matrices with definite parity $\Pi = \pm 1$ [28,32].

$$N_{\Omega}^{JM\Pi} = \sqrt{\frac{2J+1}{16\Pi^2(1+\delta_{\Omega 0})}} [D_{M\Omega}^{J*}(\alpha, \beta, \gamma) + (-1)^{\Pi+J+\Omega} D_{M,-\Omega}^{J*}(\alpha, \beta, \gamma)] \quad (7)$$

where $\Omega \geq 0$ is the absolute magnitude of the quantum number for the projection of the total angular momentum onto the body-fixed Z axis.

The $\varphi_n^{\Omega\Pi\Gamma}$ are Ω - and $\bar{\rho}$ -dependent eigenfunctions of the hamiltonian

$$\hat{H}^{\Omega}(\theta, \phi_{\lambda}; \bar{\rho}) = \frac{1}{2\mu\bar{\rho}^2}(\hat{\Lambda}_o^2 + \frac{4\Omega^2}{\cos^2\theta}) + V(\theta, \phi_{\lambda}; \bar{\rho}) \quad (8)$$

These eigenfunctions are obtained variationally by expanding them in a body-fixed basis $\chi_{n_{\theta}n_{\phi}}^{\Pi\Gamma\Omega}$ built from products of simple analytical functions[28]:

$$\chi_{n_{\theta}n_{\phi}}^{\Pi\Gamma\Omega}(\theta, \phi_{\lambda}) = f_{n_{\theta}}^{\Omega}(\theta)g_{n_{\phi}}^{\Pi\Gamma\Omega}(\phi_{\lambda}) \quad (9)$$

n_{θ} and n_{ϕ} are integers or half-odd integers, and $f_{n_{\theta}}^{\Omega}(\theta)$ and $g_{n_{\phi}}^{\Pi\Gamma\Omega}(\phi_{\lambda})$ are simple linear combinations of trigonometric functions.

The functions $f_{n_{\theta}}^{\Omega}(\theta)$ can be chosen as the functions $\cos(n_{\theta}\theta)$ or $\sin(n_{\theta}\theta)$, with n_{θ} integer or half-odd integer, in terms of which the hyperspherical harmonics can be written as polynomials in $\cos\theta$ [6,33-35]. Table 1 indicates how to choose the functions of $g_{n_{\phi}}^{\Pi\Gamma\Omega}(\phi_{\lambda})$ to obtain electronuclear wavefunctions with correct permutation symmetries, with and without the effect of the geometric phase.

The complete six-dimensional scattering wavefunction is solved by expanding it over spherical sectors centered around the value of $\bar{\rho}$ in terms of the corresponding five-dimensional pseudo surface functions

$$\psi^{JM\Pi\Gamma}(\alpha, \beta, \gamma, \theta, \phi_{\lambda}, \rho) = \frac{1}{\rho^{5/2}} \sum_{n\Omega} b_{n\Omega}^{JM\Pi\Gamma}(\rho; \bar{\rho}) \Phi_{n\Omega}^{JM\Pi\Gamma}(\alpha, \beta, \gamma, \theta, \phi_{\lambda}; \bar{\rho}) \quad (10)$$

The $\Phi_{n\Omega}^{JM\Pi\Pi}$ are determined at a set of discrete values of $\bar{\rho}$. The hyperradial functions $b_{n\Omega}^{J\Pi\Pi}$ are solutions of the set of coupled second-order differential equations

$$\begin{aligned} & \left[-\frac{\hbar^2}{2\mu} \frac{d^2}{d\rho^2} + \frac{15\hbar^2}{8\mu\rho^2} + \frac{\bar{\rho}^2}{\rho^2} \epsilon_n^{\Gamma\Omega}(\bar{\rho}) - E \right] b_{n\Omega}^{J\Pi\Pi}(\rho; \bar{\rho}) + \sum_{n'} U_{nn'}^{\Pi\Pi\Omega}(\rho; \bar{\rho}) b_{n'\Omega}^{J\Pi\Pi}(\rho; \bar{\rho}) \\ & + \frac{\hbar^2}{2\mu\rho^2} \sum_{n'} W_{nn'}^{\Pi\Pi\Omega}(\rho; \bar{\rho}) b_{n'\Omega}^{J\Pi\Pi}(\rho; \bar{\rho}) + \frac{\hbar^2}{\mu\rho^2} \sum_{n'} X_{nn',\Omega\pm 1}^{\Pi\Pi,\Omega}(\rho; \bar{\rho}) b_{n',\Omega\pm 1}^{J\Pi\Pi}(\rho; \bar{\rho}) \\ & + \frac{\hbar^2}{4\mu\rho^2} \sum_{n'} Y_{nn',\Omega\pm 2}^{\Pi\Pi,\Omega}(\rho; \bar{\rho}) b_{n',\Omega\pm 2}^{J\Pi\Pi}(\rho; \bar{\rho}) = 0 \end{aligned} \quad (11)$$

where

$$\Omega = \begin{cases} 0, 1, 2, \dots, J & \text{for } J + \Pi \text{ even;} \\ 1, 2, 3, \dots, J & \text{for } J + \Pi \text{ odd;} \end{cases}$$

with coupling matrix elements given by

$$U_{nn'}^{\Pi\Pi\Omega}(\rho; \bar{\rho}) = \langle \varphi_n^{\Pi\Pi\Omega} | V(\theta, \phi_\lambda, \rho) - \frac{\bar{\rho}^2}{\rho^2} V(\theta, \phi_\lambda; \bar{\rho}) | \varphi_{n'}^{\Pi\Pi\Omega} \rangle \quad (12a)$$

$$\begin{aligned} W_{nn'}^{\Pi\Pi\Omega}(\rho; \bar{\rho}) &= [J(J+1)] \langle \varphi_n^{\Pi\Pi\Omega} | \frac{1}{1+\sin\theta} + \frac{1}{2\sin^2\theta} | \varphi_{n'}^{\Pi\Pi\Omega} \rangle \\ &- \Omega^2 \langle \varphi_n^{\Pi\Pi\Omega} | \frac{3}{1+\sin\theta} + \frac{1}{2\sin^2\theta} | \varphi_{n'}^{\Pi\Pi\Omega} \rangle \end{aligned} \quad (12b)$$

$$\begin{aligned} X_{nn',\Omega\pm 1}^{\Pi\Pi,\Omega} &= -\xi_+(J, \Omega) \frac{\eta_{J,\Omega+1}}{\eta_{J,\Omega}} \langle \varphi_n^{\Pi\Pi\Omega} | \frac{\cos\theta}{\sin^2\theta} | \frac{\partial \varphi_{n'}^{\Pi\Pi,\Omega+1}}{\partial \phi_\lambda} \rangle \\ &+ \xi_-(J, \Omega) \frac{\eta_{J,\Omega-1}}{\eta_{J,\Omega}} \langle \varphi_n^{\Pi\Pi\Omega} | \frac{\cos\theta}{\sin^2\theta} | \frac{\partial \varphi_{n'}^{\Pi\Pi,\Omega-1}}{\partial \phi_\lambda} \rangle \end{aligned} \quad (12c)$$

$$\begin{aligned} Y_{nn',\Omega\pm 2}^{\Pi\Pi,\Omega} &= \xi_+(J, \Omega) \xi_+(J, \Omega+1) \frac{\eta_{J,\Omega+2}}{\eta_{J,\Omega}} \langle \varphi_n^{\Pi\Pi\Omega} | \frac{1}{1+\sin\theta} - \frac{1}{2\sin^2\theta} | \varphi_{n'}^{\Pi\Pi,\Omega+2} \rangle \\ &+ \xi_-(J, \Omega) \xi_-(J, \Omega-1) \frac{\eta_{J,\Omega-2}}{\eta_{J,\Omega}} \langle \varphi_n^{\Pi\Pi\Omega} | \frac{1}{1+\sin\theta} - \frac{1}{2\sin^2\theta} | \varphi_{n'}^{\Pi\Pi,\Omega-2} \rangle \end{aligned} \quad (12d)$$

$\eta_{J,\Omega}$, $\eta_{J,\Omega\pm 1}$, $\eta_{J,\Omega\pm 2}$ are normalization constants for $N_\Omega^{JM\Pi}(\alpha, \beta, \gamma)$, $N_{\Omega\pm 1}^{JM\Pi}(\alpha, \beta, \gamma)$ and $N_{\Omega\pm 2}^{JM\Pi}(\alpha, \beta, \gamma)$ functions. The coupling constants $\xi_\pm(i, k)$ are defined as

$$\xi_\pm(i, k) = [i(i+1) - k(k\pm 1)]^{1/2} \quad (13)$$

The coupling matrix is penta-diagonal in Ω and can be evaluated efficiently by 2D-numerial quadratures. The matrix \mathbf{U} is independent of J and only needs to be calculated at the boundaries and the middle of each sector.

For small values of the hyperradius for which the three atoms interact strongly, simple trigonometric basis functions proved to be an efficient set in which to expand the electronuclear wavefunctions $\Psi^{JM\Pi\Gamma}$. However, for large values of the hyperradius for which the system has nearly separated into an atom and a diatom, the nuclear wavefunction is highly localized in each arrangement channels. This localization makes the trigonometric basis set inefficient and suggests the use of a basis set based on the previously defined symmetrized hyperspherical coordinates $\omega_\lambda, \gamma_\lambda$ [15,31] instead. These are related to θ, ϕ_λ by

$$\sin\theta\cos\theta = \cos\omega_\lambda; \tag{14a}$$

$$\sin\theta\sin\phi_\lambda = \sin\omega_\lambda\cos\gamma_\lambda; \tag{14b}$$

$$\cos\theta = \sin\omega_\lambda\sin\gamma_\lambda. \tag{14c}$$

The basis set based on $\omega_\lambda, \gamma_\lambda$ for large values of ρ has previously been shown to be very efficient[18].

Eq.(11) is integrated over each sector as an initial value problem by using a log-derivative algorithm[36,37], and by imposing continuity conditions of the 6D wave function and its first derivative with respect to ρ at the separations between consecutive spherical sectors. For the first sector the initial value of ρ is chosen to be sufficiently small for the WKB solution to be applicable. All aspects of the physics can be extracted from the solutions at large ρ by a constant ρ projection[17,18].

3. NUMERICAL PARAMETERS

The LSTH Born-Oppenheimer electronic potential energy surface[38,39] was used throughout the calculations. The boundary at which we change from the principal-axis moment of inertia frame to the body-fixed Jacobi frame[17,18] was set at $\rho_c = 6$ bohr. This value was used for all J, since the change-over distance is determined mainly by the ρ -dependence of the potential energy function V . For the present converged calculations, the results do not change as ρ_c is further increased. Pseudo surface functions are computed at 20 values of ρ between 2 and 6 bohr and 31 values of ρ between 6 and 12 bohr. One of the most important parameters for these calculations is the number of basis functions used to expand the pseudo surface functions. The results described in this paper were obtained by using 2500 product functions (50 for each of the two angular coordinates θ and ϕ_λ) for ρ between 2 and 6 bohr and 800 asymptotic rovibrational states for 6 to 12 bohr. The maximum value of Ω used was determined by checking the convergence and the unitarity of the scattering matrix with respect to this quantity. A value of $\Omega_{max} = 10$ sufficed. In the present study, all total angular momenta up to $J = 34$ were needed for the convergence of ortho \rightarrow ortho and para \rightarrow para differential cross sections for total energies E up to 1.2 eV. The unitarity of the resulting scattering matrix was always better than 1% for $J \leq 15$ and 3.5% for $J > 15$. For each parity and each irreducible representation the computation of pseudo surface functions for all values of $\bar{\rho}$ took about 24 minutes on a single CPU of a CRAY Y-MP. The logarithmic-derivative integrations for each parity and each irreducible representation for total angular momentum up to 34 took about 15 minutes for each energy. The results for para \rightarrow ortho transitions were in very good agreement with those published previously[22,23,28].

4. RESULTS AND DISCUSSION

We have performed converged calculations of integral and differential cross sections for the $\text{H} + \text{H}_2$ system over the total energy range (measured with respect to the bottom of the isolated H_2 potential energy curve) of 0.7 eV to 1.2 eV. These calculations were performed both with and without inclusion of the geometric phase effect, for a large variety of different transitions. Preliminary results were published elsewhere[40].

For para \rightarrow ortho and ortho \rightarrow para transitions the only effect of the inclusion of the geometric phase was to change the sign of the corresponding scattering matrix elements and of the associated total scattering amplitudes, while leaving the absolute value of their real and imaginary parts unchanged to about 3 significant digits. This sign change leaves both the differential and integral cross sections of the corresponding transitions unchanged. These results are in complete agreement with the semi-classical predictions of Mead[5], since at the energies considered semi-classical paths do not encircle the conical intersection[7]. As a result it is expected that the phase of the scattering matrix elements and of the scattering amplitude should change by π as a result of the inclusion of the geometric phase effect. At higher energies, closer to the lowest conical intersection energy (~ 2.7 eV) it is expected that semi-classical paths which encircle the conical intersection, as well as those which do not, will contribute to these transitions. For these two kinds of paths, inclusion of the geometric phase effect will affect the phases of the corresponding contributions to the scattering matrix differently, and the net results will be much more complicated. We are currently extending our calculations to higher energies, in an attempt to penetrate into this intersecting high energy regime. Eventually, coupling with the upper sheet of the potential energy surface must be included in such calculations.

For para→para and ortho→ortho transitions, inclusion of the geometric phase effect over the energy range considered affects both the differential and integral cross sections very significantly, in a manner accessible to experimental verification. In Figures 1 through 3 we display the results of converged calculations of differential cross sections as a function of scattering angle for the $v = 0, j = 0 \rightarrow v' = 0, j' = 2$ para-to-para process, summed over the angular momentum projection quantum number of the molecular product. These calculations were performed at total energies of 0.7 eV, 0.9 eV and 1.2 eV. Each of these 3 figures displays two curves, one for the case in which the geometric phase effect is not included and one for which it is included. As can be seen, all these curves display pronounced oscillations which, at each energy, are out of phase with each other. For all 3 figures, the first extremum in these curves is a minimum for the case for which the geometric phase effect is included and a maximum for the case in which it is not. As a logical exercise let us assume that the curves obtained including the geometric phase effect are experimental. If we were trying to fit these results by using the reasonably accurate LSTH potential energy surface but performing calculations which ignored the geometric phase effect, we would obtain a strong disagreement between theory and experiment. We might try to decrease this disagreement by iteratively changing the potential energy surface, but this procedure would result in a worse rather than a better surface. Without additional calculations, it is not known at present whether reasonable agreement could ever be obtained. However, the present results obviate the need for such calculations, since the necessity of including the geometric phase has hereby been strongly demonstrated. It would nevertheless be very interesting to make measurements of the H + H₂ differential cross sections under conditions corresponding as closely as possible to Figures 1 through 3. If such measurements were done, further theoretical calculations

would be necessary for comparison purposes. This could lead to a more accurate potential energy surface for this important system. The interesting point is that measurements of para→para and ortho→ortho differential cross sections would be much more informative, at these energies, than of para→ortho or ortho→para cross sections. The former are larger than the latter and because of the interference between direct and exchange processes described, the effect of the exchange part is magnified by the large direct one. The origin of the difference in the phases of the oscillations between the differential cross sections obtained including the geometric phase effect and excluding it can be understood on the basis of the same semi-classical argument given above[5] for the cross sections for the para→ortho and ortho→para transitions. That argument indicates that at the energies considered, inclusion of the geometric phase effect should not affect the direct scattering amplitude but should change the phase of the exchange scattering amplitude by π . We have performed our calculations by decomposing the wave function into its irreducible representation contributions and calculating the latter. However, in order to test the validity of the Mead's argument, we used these irreducible representation components to then calculate the direct and exchange scattering amplitudes. We found that Mead's predictions were quite accurate, up to the maximum energy of 1.2 eV for which these calculations were made. Since, for para→para processes, the collision cross section is proportional to the square of the absolute value of the difference between the direct and exchange scattering amplitudes[12], inclusion of the geometric phase effect should indeed produce oscillations of the differential cross sections as a function of angle which are out of phase with those obtained when this effect is neglected.

As for the para→ortho and ortho→para processes, it is expected that as the system's energy increases towards the lowest conical intersection energy, there

should be two kinds of semi-classical paths which contribute to the exchange scattering amplitude, that which encircles the conical intersection and that which does not. As a result, inclusion of the geometric phase effect in the calculations will result in a more complicated behavior. Furthermore, at sufficiently high energies it will also become necessary to include the effect of coupling to the upper sheet of the potential energy surface.

As a result of the contributions of both direct and exchange processes to para→para and ortho→ortho transitions, the geometric phase effect influences significantly the corresponding integral cross sections also. For example, at a total energy of 1.2 eV, the ratio of the summed and averaged $v = 0, j = 0 \rightarrow v' = 1, j' = 2$ cross section including the geometric phase effect to that excluding it is 1.28. This indicates that the angular integration performed over the differential cross sections to obtain integral ones does not totally cancel the effect of the opposite phases in the oscillations of those cross sections with scattering angle. Calculations are currently under way to determine the energy dependence of these integral cross sections over a finer energy grid.

For isotopic variations of $H + H_2$, such as the $D + H_2 \rightarrow DH + H$ reaction, the influence of the geometric phase on integral and differential cross sections is apt to manifest itself only at higher energies. The obvious reason is that only exchange processes contribute to this reaction, as opposed to the contribution of both direct and exchange processes to para→para and ortho→ortho transitions in $H + H_2$. In other words, the influence of the geometric phase on $D + H_2$ should be qualitatively similar to that on para→ortho and ortho→para transitions in $H + H_2$. This means that as one approaches the lowest conical intersection energy of ~ 2.7 eV, the influence of the geometric phase on reactive processes on systems such as $D + H_2$ should manifest itself through the interference of contributions from reaction paths

which encircle the conical intersection with those that do not. Differential cross section measurements for this system in the energy range 1.3 eV to 1.8 eV[41,42] are in reasonably good agreement with theory[43,44] but integral cross sections of the product rotational state distribution measurements at the relatively high energy of 2.1 eV[45] are not. It is worth investigating whether this discrepancy is or is not due to the geometric phase effect.

5. CONCLUSIONS

For para→para and ortho→ortho transitions in H_3 , the geometric phase strongly influences differential cross sections and to a lesser extent, integral cross sections, even at total energies of 1.2 eV and below. This effect is therefore experimentally measurable, and such measurements would be strongly desirable. For para→ortho and ortho→para transitions measurable effects should only occur at substantially higher energies, in the vicinity of 2.2 eV or above, and calculations in this energy regime are currently underway. For reactions involving dissimilar hydrogen atoms, such as $D + H_2 \rightarrow DH + H$, measurable effects of the geometric phase will also require such higher energies and it is worth pursuing experiments and calculations in this energy regime. In addition, triatomic systems composed of alkali atoms, whether dissimilar or not, may also manifest experimentally detectable consequences of the geometric phase. Finally, transitions involving electronically excited states of molecules displaying conical intersections, such as photodissociation or predissociation of appropriate states of C_2H [46,47], NH_2 [48] and NO_2 [48] are worthy of consideration from the point of view of the geometric phase effect.

ACKNOWLEDGEMENT

This work has been supported in part by the NSF/DARPA/CNRI CASA Gigabit Testbed Network Project. The quantum calculations were performed on the CRAY Y-MP/864 at the NSF San Diego Supercomputing Center and on the CRAY 2 at the NASA Ames Research Center. We thank those institutions for their help.

REFERENCES

- [1] G. Herzberg and H. C. Longuet-Higgins, *Discussions Faraday Soc.* 35 (1963) 77; H. C. Longuet-Higgins, *Proc. Roy. Soc. Lond. A* 344 (1975) 147.
- [2] H. C. Longuet-Higgins, *Advan. Spectry.* 2 (1961) 429.
H. C. Longuet-Higgins, U. Öpik, M. H. L. Pryce and R. A. Sack, *Proc. Roy. Soc. Lond. A* 244 (1958) 1.
- [3] C. A. Mead and D. G. Truhlar, *J. Chem. Phys.* 70 (1979) 2284.
- [4] C. A. Mead, *Chem. Phys.* 49 (1980) 23.
- [5] C. A. Mead, *J. Chem. Phys.* 72 (1980) 3839.
- [6] B. Lepetit, Z. Peng and A. Kuppermann, *Chem. Phys. Letters* 166 (1990) 572.
- [7] B. Lepetit and A. Kuppermann, *Chem. Phys. Letters* 166 (1990) 581.
- [8] M. V. Berry, *Proc. Roy. Soc. A* 392 (1984) 45.
- [9] Y. Aharonov and D. Bohm, *Phys. Rev.* 115 (1959) 485.
- [10] N. Nash, S. Sen, *Topology and Geometry for Physicists.* Academic, London 1983.
- [11] A. Shapere, F. Wilczek, *Geometric Phases in Physics.* World Scientific, Singapore 1989.
- [12] A. Kuppermann and G. C. Schatz, *J. Chem. Phys.* 62 (1975) 2502;
G. C. Schatz and A. Kuppermann, *J. Chem. Phys.* 65 (1976) 4642.
- [13] A. B. Elkowitz and R. E. Wyatt, *J. Chem. Phys.* 62 (1975) 2504; 63 (1975) 702.
- [14] R. B. Walker, E. B. Stechel and J. C. Light, *J. Chem. Phys.* 69 (1978) 2922.
- [15] R. T. Ling and A. Kuppermann, in: *Electronic and Atomic Collisions, Abstract of the 9th International Conference on the Physics of Electronic and*

- Atomic Collisions, Seattle, Washington, 24-30 July 1975, Vol. 1, eds. J. S. Risley and R. Geballe (Univ. Washington Press, Seattle, 1975) pp. 353, 354.
- [16] A. Kuppermann and P. G. Hipes, *J. Chem. Phys.* 84 (1986) 5962.
- [17] P. G. Hipes and A. Kuppermann, *Chem. Phys. Letters* 133 (1987) 1.
- [18] S. A. Cuccaro, P. G. Hipes and A. Kuppermann, *Chem. Phys. Letters* 154 (1989) 155; 157 (1989) 440.
- [19] Y. M. Wu, S. A. Cuccaro, P. G. Hipes and A. Kuppermann, *Chem. Phys. Letters* 168 (1990) 429.
- [20] Y. M. Wu, S. A. Cuccaro, P. G. Hipes and A. Kuppermann, *Theor. Chim. Acta.* 79 (1991) 225.
- [21] G. C. Schatz, *Chem. Phys. Letters* 150 (1988) 92.
- [22] J. Z. H. Zhang and W. H. Miller, *Chem. Phys. Letters* 153 (1988) 465; 159 (1989) 130.
- [23] D. E. Manopoulos and R. E. Wyatt, *Chem. Phys. Letters* 159 (1989) 123.
- [24] F. Webster and J. C. Light, *J. Chem. Phys.* 90 (1989) 300.
- [25] M. Mladenovic, M. Zhao, D. G. Truhlar, D. W. Schwenke, Y. Sun and D. J. Kouri, *Chem. Phys. Letters* 146 (1988) 358; *J. Phys. Chem.* 92 (1988) 7035.
- [26] J. Linderberg, S. Padkjaer, Y. Öhrn and B. Vessal, *J. Chem. Phys.* 90 (1989) 6254.
- [27] R. T. Pack and G. A. Parker, *J. Chem. Phys.* 87 (1987) 3888.
- [28] J. M. Launay and M. Le Dourneuf, *Chem. Phys. Letters* 163 (1989) 178.
- [29] B. R. Johnson, *J. Chem. Phys.* 73 (1980) 5051; 79 (1983) 1906; 1916.
- [30] R. C. Whitten and F. T. Smith, *J. Math. Phys.* 9 (1968) 1103.
- [31] A. Kuppermann, *Chem. Phys. Letters* 32 (1975) 374.
- [32] A. Messiah, *Quantum Mechanics*, Vol 2 (Dunod, Paris, 1964).
- [33] W. Zickendraht, *Ann. Phys.* 35 (1965) 18.

- [34] H. Mayer, *J. Phys. A* 8 (1975) 1562.
- [35] L. Wolniewicz, *J. Chem. Phys.* 90 (1989) 371.
- [36] B. R. Johnson, *J. Comp. Phys.* 13 (1973) 445; *J. Chem. Phys.* 67 (1977) 4086; NRCC Workshop, Lawrence Berkeley Laboratory, Report No. LBL 9501 (1979)
- [37] D. E. Manolopoulos, *J. Chem. Phys.* 85 (1986) 6425.
- [38] B. Liu, *J. Chem. Phys.* 58 (1973) 1925;
P. Siegbahn and B. Liu, *J. Chem. Phys.* 68 (1978) 2457.
- [39] D. G. Truhlar and C. J. Horowitz, *J. Chem. Phys.* 68 (1978) 2468; 71 (1979) 1514(E).
- [40] Y. M. Wu, A. Kuppermann and B. Lepetit, in *Seventeenth International Conference on the Physics of Electronic and Atomic Collisions, Brisbane, Australia, 10-16 July 1991, Abstracts of Contributed Paper*, eds. I. E. McCarthy, W. R. MacGillivray and M. C. Standage (Griffith University, Brisbane, 1991) p. 676.
- [41] R. E. Continetti, B. A. Balko and Y. T. Lee, *J. Chem. Phys.* 93 (1990) 5719.
- [42] S. A. Buntin, C. F. Giese and W. R. Gentry, *J. Chem. Phys.* 87 (1987) 1443.
- [43] N. C. Blais, M. Zhao, D. G. Truhlar, D. W. Schwenke and D. J. Kouri, *Chem. Phys. Letters* 166 (1990) 11.
- [44] J. Z. H. Zhang and W. H. Miller, *J. Chem. Phys.* 91 (1989) 1528.
- [45] D. A. V. Kliner, D. E. Adelman and R. N. Zare, *J. Chem. Phys.* 95 (1991) 1648.
- [46] P. G. Carrick, A. J. Merer and R. F. Curl, *J. Chem. Phys.* 78 (1983) 3652.
- [47] W. B. Yan, J. L. Hall, J. W. Stephens, M. L. Richnow and R. F. Curl, *J. Chem. Phys.* 86 (1986) 1657.
- [48] C. Petrongolo, G. Hirsch and R. J. Buenker, *Mol. Phys.* 70 (1990) 825.

[49] K. K. Lehmann and S. C. Coy, *Ber. Bunsenges. Phys. Chem.* 92 (1988) 306.

FIGURE CAPTIONS

Figure 1. Degeneracy-summed differential cross sections for the $v = 0, j = 0 \rightarrow v' = 0, j' = 2$ cross sections, at a total energy of 0.7 eV, as a function of scattering angle. The squares (circles) correspond to the case in which the geometric phase is included (is not included).

Figure 2. Degeneracy-summed differential cross sections for the $v = 0, j = 0 \rightarrow v' = 0, j' = 2$ cross sections, at a total energy of 0.9 eV, as a function of scattering angle. The squares (circles) correspond to the case in which the geometric phase is included (is not included).

Figure 3. Degeneracy-summed differential cross sections for the $v = 0, j = 0 \rightarrow v' = 0, j' = 2$ cross sections, at a total energy of 1.2 eV, as a function of scattering angle. The squares (circles) correspond to the case in which the geometric phase is included (is not included).

Table I: Choice of $g_{n\phi}^{\Pi\Gamma\Omega}$ for each Π , Ω and Γ for nuclear permutation group P_3

Π	even Ω		Π	odd Ω	
	Γ^c	$g_{n\phi}^{\Pi\Gamma\Omega}$		Γ^c	$g_{n\phi}^{\Pi\Gamma\Omega}$
even, without phase ^a	A ₁ A ₂ E	$\cos(3m\phi_\lambda)^d$ $\sin(3m\phi_\lambda)^d$ $\cos[(3n\pm 1)\phi_\lambda]^e$	even, without phase ^a	A ₁ A ₂ E	$\sin(3m\phi_\lambda)^d$ $\cos(3m\phi_\lambda)^d$ $\sin[(3n\pm 1)\phi_\lambda]^e$
even, with phase ^b	A ₁ A ₂ E	$\cos[(3m+\frac{3}{2})\phi_\lambda]^d$ $\sin[(3m+\frac{3}{2})\phi_\lambda]^d$ $\cos[(3n\pm\frac{1}{2})\phi_\lambda]^e$	even, with phase ^b	A ₁ A ₂ E	$\sin[(3m+\frac{3}{2})\phi_\lambda]^d$ $\cos[(3m+\frac{3}{2})\phi_\lambda]^d$ $\sin[(3n\pm\frac{1}{2})\phi_\lambda]^e$
odd, without phase ^a	A ₁ A ₂ E	$\cos[(3m+\frac{3}{2})\phi_\lambda]^d$ $\sin[(3m+\frac{3}{2})\phi_\lambda]^d$ $\cos[(3n\pm\frac{1}{2})\phi_\lambda]^e$	odd, without phase ^a	A ₁ A ₂ E	$\sin[(3m+\frac{3}{2})\phi_\lambda]^d$ $\cos[(3m+\frac{3}{2})\phi_\lambda]^d$ $\sin[(3n\pm\frac{1}{2})\phi_\lambda]^e$
odd, with phase ^b	A ₁ A ₂ E	$\cos(3m\phi_\lambda)^d$ $\sin(3m\phi_\lambda)^d$ $\cos[(3n\pm 1)\phi_\lambda]^e$	odd, with phase ^b	A ₁ A ₂ E	$\sin(3m\phi_\lambda)^d$ $\cos(3m\phi_\lambda)^d$ $\sin[(3n\pm 1)\phi_\lambda]^e$

- a. Without consideration of the geometric phase due to the conical intersection.
- b. With consideration of the geometric phase due to the conical intersection.
- c. Γ is the irreducible representation of P_3 to which $\Phi^{JM\Pi\Gamma}$ belongs.
- d. m is a non-negative integer.
- e. n is a positive integer.

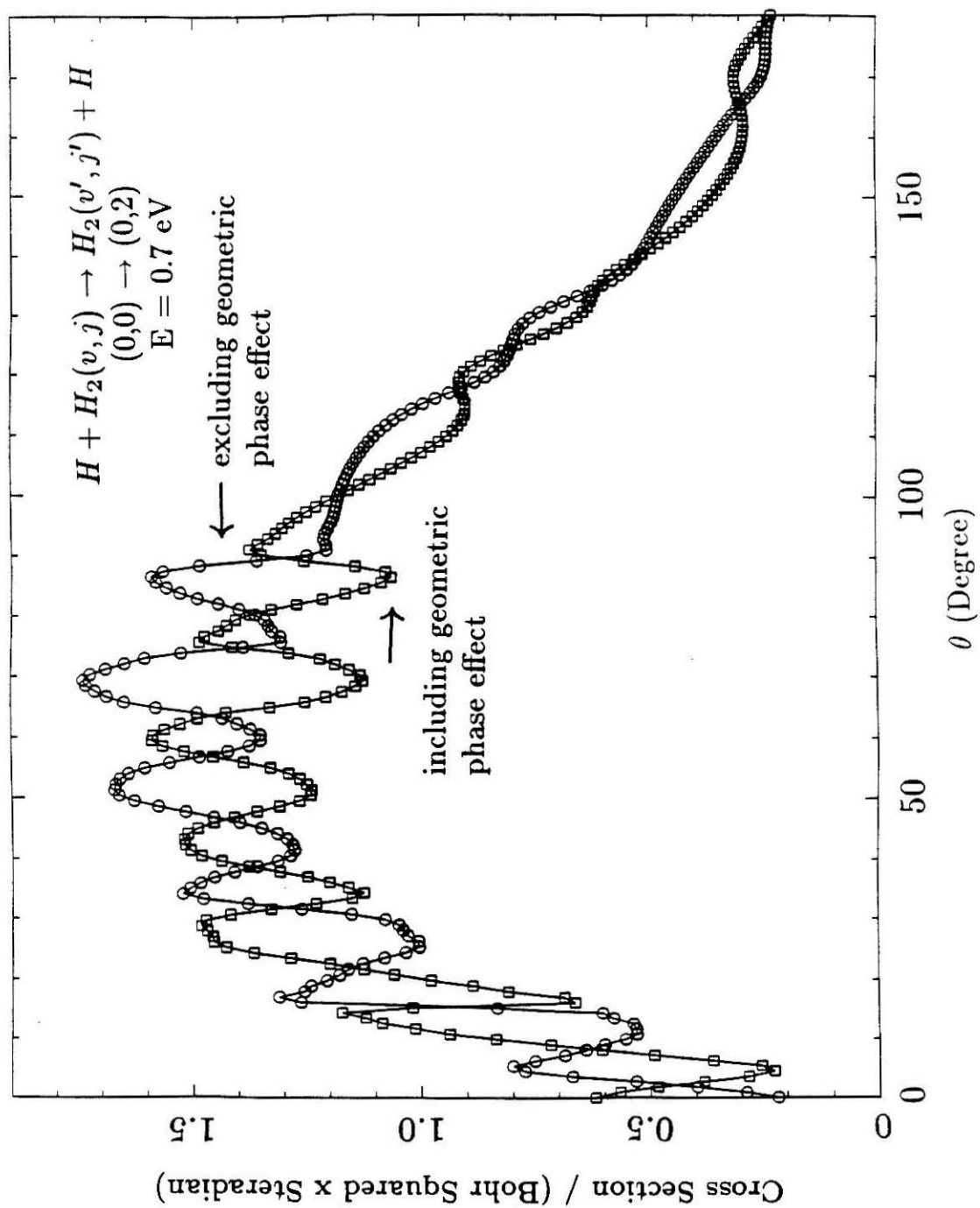


Figure 1

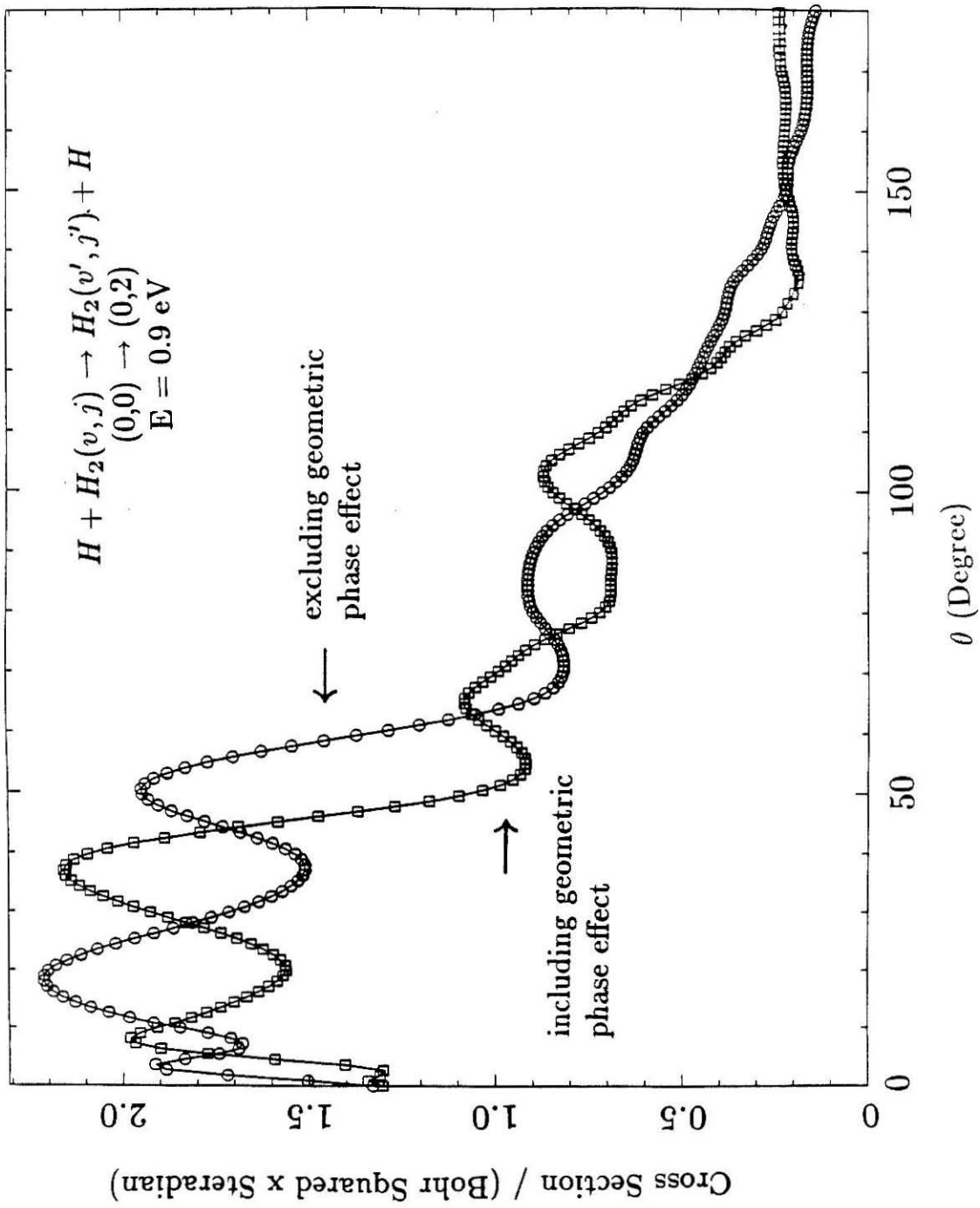


Figure 2

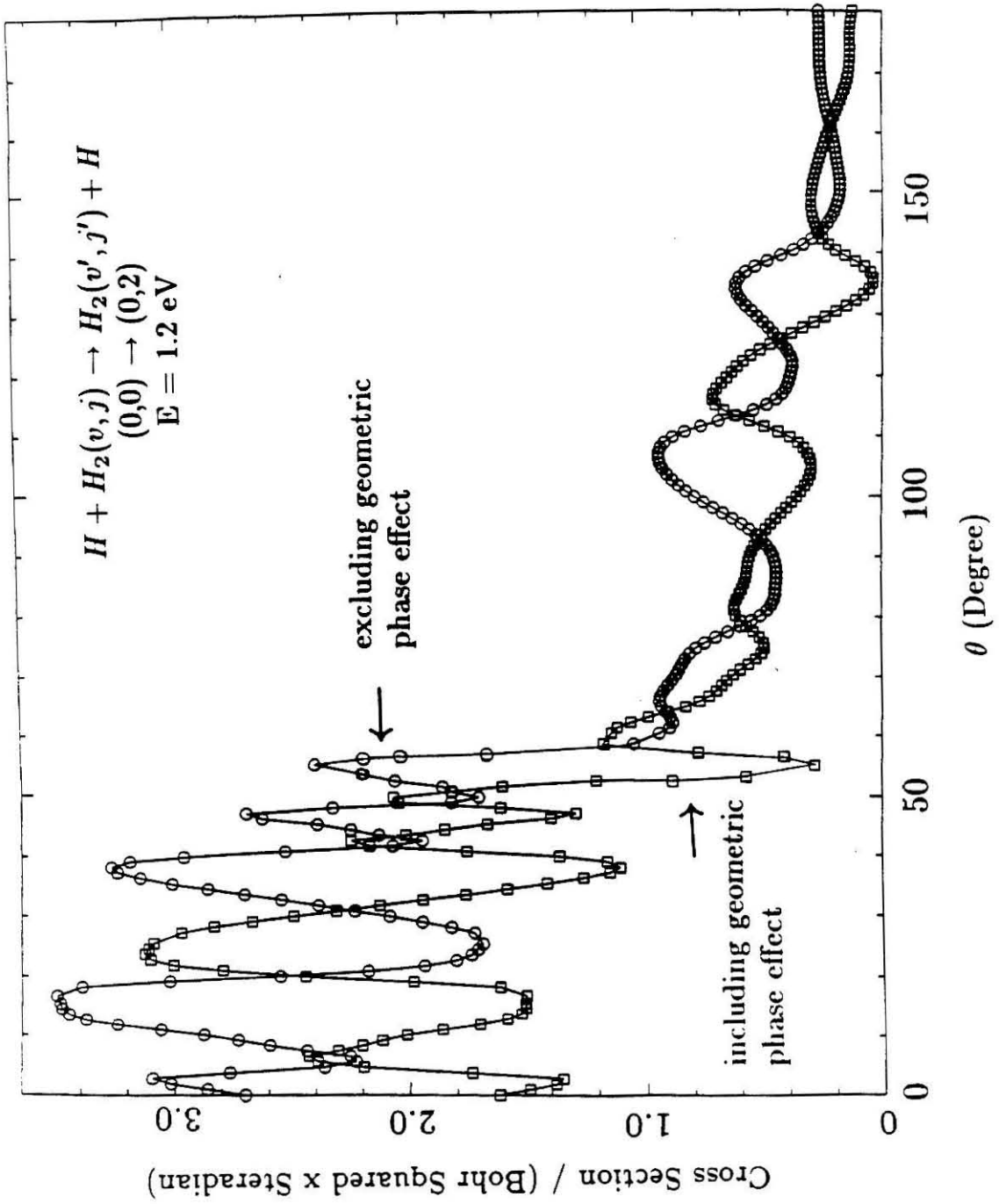


Figure 3

CHAPTER V

Quantum Mechanical Reactive Scattering Using a High-Performance Distributed-Memory Parallel Computer

† This paper appeared in *Chem. Phys. Lett.* **168**, 429 (1990)

QUANTUM MECHANICAL REACTIVE SCATTERING USING
A HIGH-PERFORMANCE DISTRIBUTED-MEMORY
PARALLEL COMPUTER

Yi-Shuen Mark Wu ¹ , Steven A. Cuccaro, Paul G. Hipes ² and Aron Kuppermann

Arthur Amos Noyes Laboratory of Chemical Physics

Division of Chemistry and Chemical Engineering ³

California Institute of Technology

Pasadena, CA 91125, USA

(Received January 1990)

ABSTRACT

We have performed accurate three-dimensional quantum mechanical reactive scattering calculations for the $H + H_2$ system on the Caltech/JPL Mark IIIfp 64 processor hypercube, using the method of symmetrized hyperspherical coordinates and local hyperspherical surface functions. The results and timing obtained demonstrate that such distributed memory parallel architectures are competitive with the CRAY X-MP, CRAY 2 and CRAY Y-MP supercomputers and should allow the study of larger, more complicated chemical systems. In addition, we show that a selection rule for scattering resonances developed previously and tested for $J = 0, 1$ resonances is also satisfied by the $J = 2$ resonances obtained in the present calculations.

¹ Work performed in partial fulfillment of the requirements for the Ph.D. degree in Chemistry at the California Institute of Technology.

² Current address: 2338 Redwood Road, Scotch Plains, NJ 07076.

³ Contribution number 8068

1. INTRODUCTION

There is considerable current interest in performing accurate quantum mechanical three-dimensional reactive scattering cross section calculations. Accurate solutions have until recently proved to be difficult and computationally expensive to obtain, in large part due to the lack of sufficiently powerful computers[1-7]. Prior to the advent of supercomputers, one could only solve the equations of motion for model systems or for sufficiently light atom-diatom systems at low energy[1-4]. As a result of the current development of efficient methodologies and increased access to supercomputers, there has been a remarkable surge of activity in this field[8-19]. The use of symmetrized hyperspherical coordinates[20] and of the local hyperspherical surface function formalism[21,8,9] has proven to be a successful approach to solve the three-dimensional Schrödinger equation[8,9,15,16]. However, even for modest reactive scattering calculations the memory and CPU demands are so great that CRAY-type supercomputers will soon be limiting progress.

Although there has been a steady improvement in the necessary technologies of the basic logic speeds of computers, there is little prospect of substantially faster single processor designs in the near future. Concurrent supercomputers are a natural next step in meeting the need for both increased memory and faster CPU. Individual processors, although slower than a single sequential supercomputer processor, can be connected together in sufficient number to make a powerful supercomputer. Such architectures offer the potential to obtain large increases in computing speed by simply increasing the number of processors. The actual speed-up depends on the nature of the algorithm, the characteristics of the processors, and the particular way these communicate with each other. The algorithms used and the codes developed on sequential machines should be replaced by codes optimized for parallel machines.

The essential property a calculation must have to be efficiently done on a highly parallel computer is that it be decomposable in such a way that in performing it almost all processors should be computing efficiently almost all of the time, and that the communication time between the processors should represent a small fraction of the computation time. In the present paper we show how quantum mechanical reactive scattering calculations can be structured so as to fulfil these criteria.

The hypercube architecture is a leading design for MIMD-type (Multiple Instruction Multiple Data) distributed memory parallel architectures based on message passing. The first such machine was developed by Charles Seitz[22] and used by Geoffrey Fox[23,24], both at Caltech. We have created efficient codes to solve the quantum mechanical equation of motion for reactive collisions of an atom with a diatomic molecule using a hypercube computer of this type. Very similar codes should be appropriate for other MIMD distributed memory parallel architectures.

In this paper, we present a concurrent algorithm for calculating local hyperspherical surface functions (LHSF) and use a parallelized version[25] of Johnson's logarithmic derivative method[26], modified to include the improvements suggested by Manolopoulos[27], for integrating the resulting coupled channel reactive scattering equations. We review the formalism briefly in section 2. In section 3 we discuss the parallel algorithms and in section 4 we compare the results of scattering calculations on the Caltech/JPL Mark IIIfp 64 processor hypercube for the $H + H_2$ system $J=0,1,2$ partial waves on the LSTH[28,29] potential energy surface with those of calculations done on a CRAY X-MP/48 and a CRAY-2. Both accuracy and performance are discussed, and speed estimates are made for the Mark IIIfp 128 processor hypercube soon to become available and the San

Diego Supercomputer Center CRAY Y-MP/864 machine which has just been put into operation. We summarize the conclusions in section 5.

2. METHODOLOGY

The detailed formulation of reactive scattering based on hyperspherical coordinates and local variational hyperspherical surface functions (LHSF) is discussed elsewhere[8,9,15]. We present a very brief review to facilitate the explanation of the parallel algorithms.

For a triatomic system, we label the three atoms A_α , A_β and A_γ . Let (λ, ν, κ) be any cyclic permutation of the indices (α, β, γ) . We define the λ coordinates, the mass-scaled[30] internuclear vector \mathbf{r}_λ from A_ν to A_κ , and the mass-scaled position vector \mathbf{R}_λ of A_λ with respect to the center of mass of $A_\nu A_\kappa$ diatom. The symmetrized hyperspherical coordinates[20] are the hyper-radius $\rho = (R_\lambda^2 + r_\lambda^2)^{1/2}$, and a set of 5 angles $\omega_\lambda, \gamma_\lambda, \theta_\lambda, \phi_\lambda$ and ψ_λ , denoted collectively as ζ_λ . The first two of these are in the range 0 to π and are respectively $2 \arctan \frac{r_\lambda}{R_\lambda}$ and the angle between \mathbf{R}_λ and \mathbf{r}_λ . The angles $\theta_\lambda, \phi_\lambda$ are the polar angles of \mathbf{R}_λ in a space-fixed frame and ψ_λ is the tumbling angle of the $\mathbf{R}_\lambda, \mathbf{r}_\lambda$ half-plane around its edge \mathbf{R}_λ . The hamiltonian \hat{H}_λ is the sum of a radial kinetic energy operator term in ρ , and the surface hamiltonian \hat{h}_λ , which contains all differential operators in ζ_λ and the electronically adiabatic potential $V(\rho, \omega_\lambda, \gamma_\lambda)$. \hat{h}_λ depends on ρ parametrically and is therefore the "frozen" hyperradius part of \hat{H}_λ .

The scattering wave function $\Psi^{JM\Pi\Gamma}$ is labelled by the total angular momentum J , its projection M on the laboratory-fixed Z axis, the inversion parity Π with respect to the center of mass of the system and the irreducible representation Γ of the permutation group of the system (P_3 for $H + H_2$) to which the electronuclear wave function, excluding the nuclear spin part[31,32], belongs.

It can be expanded in terms of the LHSF $\Phi^{JM\Pi\Pi}$, defined below, and calculated at the values $\bar{\rho}_q$ of ρ :

$$\Psi_i^{JM\Pi\Pi}(\rho, \zeta_\lambda) = \sum_n b_{ni}^{JM\Pi\Pi}(\rho; \bar{\rho}_q) \Phi_n^{JM\Pi\Pi}(\zeta_\lambda; \bar{\rho}_q) \quad (1)$$

The index i is introduced to permit consideration of a set of many linearly independent solutions of the Schrödinger equation corresponding to distinct initial conditions which are needed to obtain the appropriate scattering matrices.

The LHSF $\Phi_n^{JM\Pi\Pi}(\zeta_\lambda; \bar{\rho}_q)$ and associated energies $\epsilon_n^{JM\Pi\Pi}(\bar{\rho}_q)$ are respectively the eigenfunctions and eigenvalues of the surface hamiltonian \hat{h}_λ . They are obtained using a variational approach[15]. The variational basis set consists of products of Wigner rotation matrices $D_{M\Omega}^J(\phi_\lambda, \theta_\lambda, \psi_\lambda)$, associated Legendre functions of γ_λ and functions of ω_λ which depend parametically on $\bar{\rho}_q$ and are obtained from the numerical solution of one-dimensional eigenvalue-eigenfunction differential equations in ω_λ involving a potential related to $V(\bar{\rho}, \omega_\lambda, \gamma_\lambda)$.

The variational method leads to an eigenvalue problem with coefficient and overlap matrices $h^{JM\Pi\Pi}(\bar{\rho}_q)$ and $s^{JM\Pi\Pi}(\bar{\rho}_q)$ and whose elements are 5-dimensional integrals involving the variational basis functions.

The coefficients $b_{ni}^{JM\Pi\Pi}(\rho; \bar{\rho}_q)$ defined by equation (1) satisfy a coupled set of second order differential equations involving an interaction matrix $\mathcal{I}^{JM\Pi\Pi}(\rho; \bar{\rho}_q)$ whose elements are defined by

$$[\mathcal{I}^{JM\Pi\Pi}(\rho; \bar{\rho}_q)]_n^{n'} = \left\langle \Phi_n^{JM\Pi\Pi}(\zeta_\lambda; \bar{\rho}_q) \left| V(\rho, \omega_\lambda, \gamma_\lambda) - (\bar{\rho}_q/\rho)^2 V(\bar{\rho}_q, \omega_\lambda, \gamma_\lambda) \right| \Phi_{n'}^{JM\Pi\Pi}(\zeta_\lambda; \bar{\rho}_q) \right\rangle \quad (2)$$

The configuration space ρ, ζ_λ is divided in a set of Q hyperspherical shells $\rho_q \leq \rho \leq \rho_{q+1}$ ($q = 1, 2, \dots, Q$) within each of which we choose a value $\bar{\rho}_q$ used in expansion (1).

When changing from the LHSF set at $\bar{\rho}_q$ to the one at $\bar{\rho}_{q+1}$ neither $\Psi_i^{JM\Pi\Pi}$ nor its derivative with respect to ρ should change. This imposes continuity conditions on the $b_{ni}^{JM\Pi\Pi}$ and their ρ -derivatives at $\rho = \rho_{q+1}$, involving the overlap matrix $\mathcal{O}^{JM\Pi\Pi}(\bar{\rho}_{q+1}, \bar{\rho}_q)$ between the LHSF evaluated at $\bar{\rho}_q$ and $\bar{\rho}_{q+1}$

$$[\mathcal{O}^{JM\Pi\Pi}(\bar{\rho}_{q+1}, \bar{\rho}_q)]_n^{n'} = \left\langle \Phi_n^{JM\Pi\Pi}(\zeta_\lambda; \bar{\rho}_{q+1}) \left| \Phi_{n'}^{JM\Pi\Pi}(\zeta_\lambda; \bar{\rho}_q) \right. \right\rangle \quad (3)$$

The 5-dimensional integrals required to evaluate the elements of $h^{JM\Pi\Pi}$, $s^{JM\Pi\Pi}$, $\mathcal{I}^{JM\Pi\Pi}$ and $\mathcal{O}^{JM\Pi\Pi}$ are performed analytically over ϕ_λ , θ_λ and ψ_λ and by two-dimensional numerical quadratures over γ_λ and ω_λ . These quadratures account for 90% of the total time needed to calculate the LHSF $\Phi_n^{JM\Pi\Pi}$ and the matrices $\mathcal{I}^{JM\Pi\Pi}$ and $\mathcal{O}^{JM\Pi\Pi}$.

The system of second-order ordinary differential equations in the $b_{ni}^{JM\Pi\Pi}$ is integrated as an initial value problem from small values of ρ to large values using Manolopoulos' logarithmic derivative propagator[27]. Matrix inversions account for more than 90% of the time used by this propagator. All aspects of the physics can be extracted from the solutions at large ρ by a constant ρ projection[8,9,33].

3. PARALLEL ALGORITHM

The computer used for this work is a 64-processor Mark IIIfp hypercube. Each node consists of two independent Motorola 68020 microprocessors, one for computation and one for I/O, and four megabytes of dynamic memory. The computation microprocessor has a Motorola 68882 floating-point arithmetic coprocessor and 128 kilobytes of static private memory. The I/O microprocessor has 64 kilobytes of static private memory. An additional daughter board with a pipe-lined 32-bit floating point unit based on the Weitek XL series of chips is attached to each node and has a nominal peak speed of 16 Mflops. The Crystalline

Operating System(CrOS)-channel-addressed synchronous communication provides the library routines to handle communications between nodes[24,34,35]. Program development is done on a Motorola 68020-based Counterpoint workstation that runs on UNIX. The programs are written in C programming language except for the time-consuming two-dimensional quadratures and matrix inversions, which are optimized in assembly language.

The hypercube is configured as a two dimensional array of processors. The mapping is done using binary Gray codes[24,36] which gives the Cartesian coordinates in processor space and communication channel tags for a processor's nearest neighbors. With a distributed-memory machine like the hypercube, the elements of a large matrix of data must be distributed across the memory of all the processors. This makes it possible to fully utilize the large memory available and facilitates the load-balancing task of keeping most of the processors busy doing useful arithmetic most of the time. The parallelization of scientific codes is frequently based on a large grain size decomposition of the task. A method of distributing the global matrix among the processors is the first choice that must be made and it is closely related to the parallel algorithm chosen.

We mapped the matrices into processor space by local decomposition. Let N_r and N_c be the number of processors in the rows and columns of the hypercube configuration, respectively. Element $A(i, j)$ of an $M \times M$ matrix is placed in processor row $P_r = \text{int}(\frac{i \times N_r}{M})$ and column $P_c = \text{int}(\frac{j \times N_c}{M})$, where $\text{int } x$ means the integer part of x .

The parallel code implemented on the hypercube consists of five major steps. Step one constructs, for each value of $\bar{\rho}_q$, a primitive basis set composed of the product of Wigner rotation matrices, associated Legendre functions, and the numerical one-dimensional functions in ω_λ mentioned in Section 2 and obtained

by solving the corresponding one-dimensional eigenvalue-eigenvector differential equation using a finite difference method. This requires that a subset of the eigenvalues and eigenvectors of a tridiagonal matrix be found.

A bisection method[37] which accomplishes the eigenvalue computation using the TRIDIB routine from EISPACK[38] was ported to the Mark IIIfp. This implementation of the bisection method allows computation of any number of consecutive eigenvalues specified by their indices. Eigenvectors are obtained using the EISPACK inverse iteration routine TINVIT with modified Gram-Schmidt orthogonalization. Each processor solves independent tridiagonal eigenproblems since the number of eigenvalues desired from each tridiagonal system is small but there are a large number of distinct tridiagonal systems. To achieve load balancing, we distributed subsets of the primitive functions among the processors in such a way that no processor computes greater than one eigenvalue and eigenvector more than any other. These large grain tasks are most easily implemented on MIMD machines; SIMD (Single Instruction Multiple Data) machines would require more extensive modifications and would be less efficient because of the sequential nature of effective eigenvalue iteration procedures. The one-dimensional bases obtained are then broadcast to all the other nodes.

In step two a large number of two-dimensional quadratures involving the primitive basis functions which are needed for the variational procedure are evaluated. These quadratures are highly parallel procedures requiring no communication overhead once each processor has the necessary subset of functions. Each processor calculates a subset of integrals independently.

Step three assembles these integrals into the real symmetric dense matrices $s^{J\Pi\Pi}(\bar{\rho}_q)$ and $h^{J\Pi\Pi}(\bar{\rho}_q)$ which are distributed over processor space. The entire spectrum of eigenvalues and eigenvectors for the associated variational problem

is sought. With the parallel implementation of the Householder method[39], this generalized eigensystem is tridiagonalized and the resulting single tridiagonal matrix is solved in each processor completely with the QR algorithm[40]. The QR implementation is purely sequential since each processor obtains the entire solution to the eigensystem. However, only different subsets of the solution are kept in different processors for the evaluation of the interaction and overlap matrices in step four. This part of the algorithm is not time-consuming and the straightforward sequential approach was chosen. It has the further effect that the resulting solutions are fully distributed, so no communication is required.

Step four evaluates the two-dimensional quadratures needed for the interaction $\mathcal{I}^{J\Pi\Pi}(\rho; \bar{\rho}_q)$ and overlap $\mathcal{O}^{J\Pi\Pi}(\bar{\rho}_{q+1}; \bar{\rho}_q)$ matrices. The same type of algorithms are used as were used in step two. By far, the most expensive part of the sequential version of the surface function calculation is the calculation of the large number of two-dimensional numerical integrals required by steps 2 and 4. These steps are however highly parallel and well suited for the hypercube.

Step five uses Manolopoulos'[27] algorithm to integrate the coupled linear ordinary differential equations. The parallel implementation of this algorithm is discussed elsewhere[25]. The algorithm is dominated by parallel Gauss-Jordan matrix inversion and is I/O intensive, requiring the input of one interaction matrix per integration step. To reduce the I/O overhead a second source of parallelism is exploited. The entire interaction matrix (at all ρ) and overlap matrix (at all $\bar{\rho}_q$) data sets are loaded across the processors and many collision energies are calculated simultaneously. This strategy works because the same set of data is used for each collision energy and because enough main memory is available. Calculation of scattering matrices from the final logarithmic derivative matrices is not computationally intensive, and is done sequentially.

The program steps were all run on the Weitek coprocessor which only supports 32-bit arithmetic. Experimentation has shown that this precision is sufficient for the work reported below. The 64-bit arithmetic hardware needed for larger calculations was installed after the present calculations were completed.

4. RESULTS AND DISCUSSION

Accuracy:

Calculations were performed for the $H+H_2$ system on the LSTH surface[28,29] for partial waves with total angular momentum $J = 0, 1, 2$ and energies up to 1.6 eV. Flux is conserved to better than 1% for $J = 0$, 2.3% for $J = 1$ and 3.6% for $J = 2$ for all open channels over the entire energy range considered.

To illustrate the accuracy of the 32-bit arithmetic calculations, the scattering results from the Mark IIIfp with 64 processors are shown in figures 1, 2, and 3 for $J = 0, 1, 2$, respectively, in which some transition probabilities as a function of the total collision energy E are plotted. Also shown are the differences between these results and those obtained using a CRAY X-MP/48 and a CRAY-2. These differences do not exceed 0.004 in absolute value over the energy range investigated. The effect of the geometric phase associated with the conical intersection between the two lowest electronic potential energy surface of H_3 [32] is not included in these results. Much of the structure in the transition probability curves is due to the underlying resonances[1,9,16] and are discussed below. The two sets of data in each figure are virtually indistinguishable on the scale of the plots.

Analysis of $J = 2$ resonances:

Table I contains a list of the $J = 2$ resonance energies detected from the maxima in the lifetime versus energy curves, calculated as described previously[9,16], as well as their quantum number assignments, permutation and

inversion symmetry labels, and lifetimes. The permutation symmetries are given with and without the inclusion of the effect of the geometrical phase (GP) associated with the conical intersection between the two lowest electronic state potential energy surfaces[31,32]. The energy of these resonances is consistent with the physical model for the selection rule previously developed[16] and tested with the $J = 0, 1$ resonances. The results of Table I adds additional credence to the generality of that rule. According to it, if GP effects are ignored, a necessary (but not sufficient) condition for resonances to occur in $A_1(A_2)$ partial waves is that $(-1)^{l+K}$ be equal to $1(-1)$, where K is the vibrational angular momentum quantum number, whereas they are permitted in E partial waves for all K . To include the GP effect, it suffices to interchange A_1 and A_2 in this selection rule[32]. In agreement with this picture, not all higher energy $J = 2$ resonances which are allowed by this rule were detected.

Timing and parallel efficiency:

In Tables II and III we present the timing data on the 64 processor Mark IIIfp, a CRAY X-MP/48 and a CRAY 2, for both the surface function code (including calculation of the overlap $\mathcal{O}^{J_{III}}$ and interaction $\mathcal{I}^{J_{III}}$ matrices) and the logarithmic derivative propagation code. For the surface function code, the speeds on the first two machines is about the same. The CRAY 2 is 1.43 times faster than the Mark IIIfp and 1.51 times faster than the CRAY X-MP/48 for this code. The reason is that this program is dominated by matrix-vector multiplications which are done in optimized assembly code in all 3 machines. For this particular operation the CRAY-2 is 2.03 times faster than the CRAY X-MP/48 whereas for more memory-intensive operations the CRAY 2 is slower than the CRAY X-MP/48[41]. A slightly larger primitive basis set is required on the Mark IIIfp in order to obtain surface function energies of an accuracy equivalent to that obtained with the CRAY machines. This

is due to the lower accuracy of the 32-bit arithmetic of the former with respect to the 64-bit arithmetic of the latter.

The absolute times presented in Table II and III are apt to decrease as the codes are improved and the numerical parameters are further tuned. As a result, they are not well suited for an appropriate comparison of the relative effectiveness of different reactive scattering methodologies[8-19]. The relevant information in those tables is, instead, the relative times among different machines as given by the corresponding speeds. These are indicative of the relative effectiveness of these machines for performing the reactive scattering calculations described in this paper.

The efficiency (ε) of the parallel LHSF code was determined using the definition $\varepsilon = \frac{T_1}{(N \times T_N)}$ where T_1 and T_N are respectively the implementation times using a single processor and N processors. The single processor times are obtained from runs performed after removing the overhead of the parallel code, *i.e.*, after removing the communication calls and some logical statements. Perfect efficiency ($\varepsilon = 1.0$) implies that the N -processor hypercube is N times faster than a single processor. In figure 4 efficiencies for the surface function code (including the calculation of the overlap and interaction matrices) as a function of the size of the primitive basis set are plotted for 2, 4, 8, 16, 32 and 64 processor configurations of the hypercube. The global dimensions of the matrices used are chosen to be integer multiples of the number of processor rows and columns in order to insure load balancing among the processors. Because of the limited size of a single processor memory, the efficiency determination is limited to 32 primitives. As shown in figure 4, the efficiencies increase monotonically and approach unity asymptotically as the size of the calculation increases. Converged results require large enough primitive basis sets so that the efficiency of the surface function code is estimated to be about 0.95 or greater.

The data for the logarithmic derivative code given in Table III for a 245 channel (*i.e.*, LHSF) example show that the Mark IIIfp has a speed about 62% to that of the CRAY 2 but only about 31% of that of the CRAY X-MP/48. This code is dominated by matrix inversions, which are done in optimized assembly code in all three machines. The reason for the slowness of the hypercube with respect to the CRAYs is that the efficiency of the parallel logarithmic derivative code is 0.52. This relatively low value is due to the fact that matrix inversions require a significant amount of inter-processor communication. Figure 5 displays efficiencies of the logarithmic derivative code as a function of the number of channels propagated for different processor configurations, as done previously for the Mark III[25,42] hypercubes. The data can be fit well by an operations count formula developed previously for the matrix inversion part of the code[43]; this formula can be used to extrapolate the data to larger numbers of processors or larger numbers of channels. It can be seen that for an 8 processor configuration, the code runs with an efficiency of 0.81. This observation suggested that we divide the Mark IIIfp into 8 clusters of 8 processors each and perform calculations for different energies in different clusters. The corresponding timing information is also given in Table III. As can be seen from the last row of this table, the speed of the logarithmic derivative code using this configuration of the 64 processor Mark IIIfp is 48.5 Mflops, which is about 44% of that of the CRAY X-MP/48 and 88% of that of the CRAY 2. As the number of channels increases, the number of processors per cluster may be made larger in order to increase the amount of memory available in each cluster. The corresponding efficiency should continue to be adequate due to the larger matrix dimensions involved.

In the near future, the number of processors of the Mark IIIfp will be increased to 128 and the I/O system will be replaced by high performance CIO

(concurrent I/O) hardware. The new Weitek coprocessors installed since the present calculations were done perform 64 bit floating point arithmetic at about the same nominal peak speed as the 32 bit boards. From the data in the present paper it is possible to predict with good reliability the performance of this upgraded version of the Mark IIIfp. A CRAY Y-MP/864 has just been installed at the San Diego Supercomputer Center. Initial speed measurements show that it is 2 times faster than the CRAY X-MP/48 for the surface function code and 1.7 times faster for the logarithmic derivative code. In Table IV, we summarize the available or predicted speed information for the present codes for the current 64 processor and near future 128 processor Mark IIIfp as well as the CRAY X-MP/48, CRAY 2 and CRAY Y-MP/864 supercomputers. It can be seen that Mark IIIfp machines are competitive with all of the currently available CRAYs (operating as single processor machines).

5. SUMMARY

We performed quantum mechanical reactive scattering calculations on the Mark IIIfp hypercube parallel computer. The results obtained for the $H + H_2$ system $J = 0, 1, 2$ partial waves agree well with those from a CRAY X-MP/48 and a CRAY-2. The resonance structure in the $J = 2$ calculations is consistent with a selection rule developed previously[9,16]. The high degree of parallelism of the most time-consuming step of the surface function calculation (the evaluation of two-dimensional numerical quadratures) leads to a high efficiency for that calculation. As a result, the speed of the 64 processor Mark IIIfp for the surface function calculation is about the same as that of the CRAY X-MP/48 and about 0.7 of that of the CRAY 2. When configuring the Mark IIIfp into 8 clusters of 8 processors each, the logarithmic derivative code is about 56% slower than the CRAY X-MP/48

and 12% slower than the CRAY 2. The speed of the 128 processor Mark IIIfp soon to become available should exceed, both for the surface function calculation and the logarithmic derivative calculation, those of the CRAY X-MP/48 and CRAY 2; however, although still comparable to the CRAY Y-MP/864 for the surface function code, it will be 32% slower for the logarithmic derivative code (the CRAYs operating as single processor machines). These results demonstrate the feasibility of performing reactive scattering calculations with high efficiency in parallel fashion. As the number of processors continues to increase, such parallel calculations in systems of greater complexity will become practical in the not too distant future.

ACKNOWLEDGEMENTS

The work described in this paper was supported in part by DOE grant DE-AS03-83ER and Air Force Astronautics Laboratory contract F04611-86-K-0067. The calculations were performed on the 64 processor Mark IIIfp Caltech/JPL hypercube, the CRAY X-MP/48 and CRAY Y-MP/864 at the NSF San Diego Supercomputing Center and the CRAY-2 at the Air Force Weapons Laboratory and we thank those institutions for their help. We also thank Dr. B. Lepetit and Prof. Geoffrey Fox for useful discussions.

REFERENCES

- [1] G. C. Schatz and A. Kuppermann, *J. Chem. Phys.* 62 (1975) 2502; 65(1976) 4642; 65 (1976) 4668.
- [2] A. B. Elkowitz and R. E. Wyatt, *J. Chem. Phys.* 62 (1975) 2504; 63 (1975) 702.
- [3] R. B. Walker, E. B. Stechel and J. C. Light, *J. Chem. Phys.* 69 (1978) 2922.
- [4] R. B. Bernstein, ed.: *Atom-Molecule Collision Theory*; Plenum: New York, 1979.
- [5] G.C. Schatz, in: *Theory of Chemical Reaction Dynamics*, ed. by D. C. Clary, Proceedings of NATO workshop, Orsay, France, 1986, pp. 1.
- [6] B. C. Garrett and D. G. Truhlar, *Ann. Rev. Phys. Chem.* 35 (1984) 159.
- [7] J. M. Bowman, *Adv. Chem. Phys.* 61 (1985) 115.
- [8] A. Kuppermann and P. G. Hipes, *J. Chem. Phys.* 84 (1986) 5962.
- [9] P. G. Hipes and A. Kuppermann, *Chem. Phys. Lett.* 133 (1987) 1.
- [10] G. A. Parker, R. T Pack, B. J. Archer and R. B. Walker, *Chem. Phys. Lett.* 137 (1987) 564;
R. T Pack and G. A. Parker, *J. Chem. Phys.* 87 (1987) 3888.
- [11] J. Z. H. Zhang and W. H. Miller, *Chem. Phys. Lett.* 140 (1987) 329; 153 (1988) 465; 159 (1989) 130.
- [12] G. C. Schatz, *Chem. Phys. Lett.* 150 (1988) 92.
- [13] J. Z. H. Zhang, D. J. Kouri, K. Haug, D. W. Schwenke, Y. Shima and D. G. Truhlar, *J. Chem. Phys.* 88 (1988) 2492.
- [14] M. Mladenovic, M. Zhao, D. G. Truhlar, D. W. Schwenke, Y. Sun and D. J. Kouri, *Chem. Phys. Lett.* 146 (1988) 358;
C. H. Yu, D. J. Kouri, M. Zhao and D. G. Truhlar, *Chem. Phys. Lett.* 157 (1989) 491.

- [15] S. A. Cuccharo, P. G. Hipes and A. Kuppermann, *Chem. Phys. Lett.* 154 (1989) 155.
- [16] S. A. Cuccharo, P. G. Hipes and A. Kuppermann, *Chem. Phys. Lett.* 157 (1989) 440.
- [17] F. Webster and J. C. Light, *J. Chem. Phys.* 90 (1989) 300.
- [18] J. Linderberg, S. Padkjaer, Y. Öhrn and B. Vessal, *J. Chem. Phys.* 90 (1989) 6254.
- [19] D. E. Manolopoulos and R. E. Wyatt, *Chem. Phys. Lett.* 159 (1989) 123.
- [20] A. Kuppermann, *Chem. Phys. Lett.* 32 (1975) 374.
- [21] R. T. Ling and A. Kuppermann, in: *Electronic and Atomic Collisions, Abstracts of papers of the 9th International Conference on the Physics of Electronic and Atomic Collisions, Seattle, Washington, 24-30 July 1975, Vol. 1*, J. S. Rusley and R. Geballe, eds. (Univ. Washington Press, Seattle, 1975) pp. 353, 354.
- [22] C. L. Seitz and J. Matisoo, *Phys. Today* 37(5) (1984) 38;
C. L. Seitz, *Comm. of the ACM* 28(1) (1985) 22.
- [23] G. C. Fox and S. W. Otto, *Phys. Today* 37(5) (1984) 50.
- [24] G. C. Fox, M. A. Johnson, G. A. Cyzenga, S. W. Otto, J. K. Salmon and D. W. Walker in: *Solving Problems in Concurrent Processors*; Prentice Hall, New Jersey, 1988.
- [25] P. G. Hipes, T. Mattson, Y-S. Mark Wu and A. Kuppermann, *Proceedings of the Third Conference on Hypercube Concurrent Computers and Applications, Pasadena, 1988* (ACM, New York, 1988) pp. 1051-1061.
- [26] B. R. Johnson, *J. Compl. Phys.* 13 (1973) 445; *J. Chem. Phys.* 67(1977) 4086; NRCC Workshop, Lawrence Berkeley Laboratory, Report No. LBL 9501, 1979.

- [27] D. E. Manolopoulos, *J. Chem. Phys.* 85 (1986) 6425.
- [28] B. Liu, *J. Chem. Phys.* 58 (1973) 1925;
P. Siegbahn and B. Liu, *J. Chem. Phys.* 68 (1978) 2457.
- [29] D. G. Truhlar and C. J. Horowitz, *J. Chem. Phys.* 68 (1978) 2468; 71 (1979) 1514 (E).
- [30] L. M. Delves, *Nucl. Phys.* 9 (1959) 391; 20 (1960) 275.
- [31] B. Lepetit, Z. Peng and A. Kuppermann, "Calculation of Bound Rovibrational States on the First Electronically Excited State of the H_3 System", *Chem. Phys. Lett.*, in press.
- [32] B. Lepetit and A. Kuppermann, "Numerical Study of the Geometric Phase in the $H + H_2$ Reaction", *Chem. Phys. Lett.*, in press.
- [33] D. M. Hood and A. Kuppermann, in: *Theory of Chemical Reaction Dynamics*, ed. D. C. Clary (Reidel, Dordrecht, 1986) pp. 193-214.
- [34] G. C. Fox, editor, Caltech JPL concurrent computation project Annual report 1983-1984, February 1985.
- [35] G. C. Fox, G. Lyzenga, D. Rogstad and S. Otto, The Caltech concurrent computation program-Project description, Proc. 1985 ASME International Computers in Engineering Conference (1985).
- [36] E. N. Gilbert, *Bell System Technical Journal* 37 (1958) 815;
J. Salmon, Caltech Concurrent Computation Project Report C³P-51, 1984.
- [37] Ilse C. F. Ipsen and E. R. Jessup, *Proceeding of the Second Conference on Hypercube Multiprocessors*, Knoxville, Tennessee, 1987;
Ilse C. F. Ipsen and E. R. Jessup, Yale internal report: YALEU/DCS/RB-548;
G. C. Fox, Caltech Concurrent Computation Project Report C³P-95, 1984.
- [38] B. T. Smith, *Matrix Eigensystem Routine- EISPACK Guide*, 2nd ed., Vol. 6 of *Lecture Notes in Computer Science* (New York: Springer-Verlag) 1976.

- [39] G. C. Fox, Caltech Concurrent Computation Project Report C^3P -98, 1984;
J. Patterson, Caltech Concurrent Computation Project Report C^3P -56.58,
1986.
- [40] J. H. Wilkinson and C. Reinsch, in: Linear Algebra, vol.II of Handbook for
Automatic Computation (New York: Springer- Verlag) 1971 pp. 227-240.
- [41] W. Pfeiffer, A. Alagar, A. Kamrath, R. H. Leary and J. Rogers, Benchmarking
and Optimization of Scientific Codes on the CRAY X-MP, CRAY 2, and
SCS-40 Vector Computers, November 1988, San Diego Supercomputer Center
Report GA-A19478.
- [42] P. Messina, C. F. Baillie, E. W. Felten, P. G. Hipes, D. W. Walker,
R. D. Williams, W. Pfeiffer, A. Alagar, A. Kamrath, R. H. Leary
and J. Rogers, Benchmarking Advanced Architecture Computers, Caltech
Concurrent Computation Project Report C^3P -712, 1988.
- [43] P. G. Hipes and A. Kuppermann, Gauss-Jordan Inversion with Pivoting on
the Caltech Mark II Hypercube, in Proceeding of the Third Conference on
Hypercube Multiprocessors, Pasadena CA., 19-20 January 1988, edited by
G. C. Fox, Vol II-Applications (California Institute of Technology, Mail Stop
206-49, Pasadena, CA, 1988) pp. 1621-1634.

FIGURE CAPTIONS

Figure 1 Probabilities (a) and probability differences (b) as a function of total energy E (lower abscissa) and initial relative translational energy E_{00} (upper abscissa) for the $J=0$ $(0,0,0) \rightarrow (0,0,0)$ A_1 symmetry transition in $H + H_2$ collisions on the LSTH potential energy surface. The symbol (v, j, Ω) labels an asymptotic state of the $H + H_2$ system in which v , j , and Ω are the quantum numbers of the initial or final H_2 states. The vertical arrows on the upper abscissa denote the energies at which the corresponding $H_2(v, j)$ states open up. The length of those arrows decreases as v spans the values 0, 1 and 2, and the numbers 0, 5, and 10 associated with the arrows define a labelling for the value of j . (a) the results from the Mark IIIfp hypercube; (b) differences between these and those from the CRAY X-MP/48. The number of LHSF used was 36 and the number of primitives used to calculate these surface functions was 80.

Figure 2 Same as for fig. 1 except for $J=1$, A_1 , odd parity ($\Pi = 1$), $(0,0,0) \rightarrow (0,0,2)$ transitions. The number of LHSF used was 74 and the number of primitives used to calculate these surface functions was 152.

Figure 3 Same as for fig. 1 except for $J=2$, A_1 , odd parity ($\Pi = 1$), $(0,2,1) \rightarrow (0,2,1)$ transition. The differences plotted in (b) are between the Mark IIIfp hypercube and the CRAY-2 results. The number of LHSF used was 65 and the number of primitives used to calculate these surface functions was 136.

Figure 4 Efficiency of the surface function code (including the calculation of the overlap and interaction matrices) as a function of the global matrix dimension (*i.e.*, the size of the primitive basis set) for 2, 4, 8, 16, 32, and 64 processors. The solid curves are straight line segments connecting the data points for a fixed number of processors and are provided as an aid to examine the trends.

Figure 5 Efficiency of logarithmic derivative code as a function of the global matrix dimension (*i.e.*, the number of channels or LHSF) for 8, 16, 32, and 64 processors. The solid curves are straight line segments connecting the data points for a fixed number of processors and are provided as an aid to examine the trends.

Table I : $J = 2$ resonances and their characteristics for H_3

Assignment	Permutation Symmetry ^a		Inversion Symmetry Π^c	E(eV)	Lifetime(fs)
	Without GP ^b	With GP ^b			
(0,0 ⁰ ,0)	A_1, E	A_2, E	0	0.65	11
(0,1 ¹ ,0)	A_2, A_1, E	A_1, A_2, E	0,1	0.77	9
(0,2 ⁰ ,0)	A_1, E	A_2, E	0	0.88	10
(0,2 ² ,0)	A_1, A_2, E	A_2, A_1, E	0,1	0.90	10
(1,0 ⁰ ,0)	A_1, E	A_2, E	0	0.98	28
(0,3 ¹ ,0)	A_2, A_1, E	A_1, A_2, E	0,1	1.00	8
(1,1 ¹ ,0)	A_2, A_1, E	A_1, A_2, E	0,1	1.09	29
(0,4 ⁰ ,0)	A_1, E	A_2, E	0	1.10	5
(0,4 ² ,0)	A_1, A_2, E	A_2, A_1, E	0,1	1.12	5
(1,2 ² ,0)	A_1, A_2, E	A_2, A_1, E	0,1	1.22	8
(0,5 ¹ ,0)	A_2, A_1, E	A_1, A_2, E	0,1	1.22	6
(2,1 ¹ ,0)	A_2, A_1, E	A_1, A_2, E	0,1	1.45	38

- a. This refers to the irreducible representation of the F_3 permutation group to which the electronic wave function, excluding the nuclear spin part, belongs[31,32].
- b. With(out) GP refers to the case in which the effect of the geometrical phase associated to conical intersection between the two lowest electronic state potential energy surface is(not) included[31,32].
- c. When two values of Π are indicated, the first(second) one is associated with the first(second) permutation symmetry.

Table II: Performance of the surface function code^a

<i>J</i>	Mark IIIfp ^b 64 processors		CRAY X-MP/48		CRAY 2	
	Time (hr)	Speed (Mflops)	Time (hr)	Speed (Mflops)	Time (hr)	Speed (Mflops)
0	0.71 ^c	100 ^d	0.74 ^e	96 ^f	0.49 ^g	145 ^h
1	2.88 ⁱ	112 ^d	3.04 ^j	106 ^f	2.01 ^k	160 ^h
2	5.60 ^l	124 ^d	5.94 ^m	117 ⁿ	3.96 ^o	176 ^k

- a. This code calculates the surface functions at the 51 values of $\bar{\rho}$ from 2.0 bohr to 12.0 bohr in steps of 0.2 bohr, the corresponding overlap matrices between consecutive values of $\bar{\rho}$ and the propagation matrices in ρ steps of 0.1 bohr. The number of primitives used for each *J* and described in the remaining footnotes permits us to generate enough LHSF to achieve the accuracy described in the text.
- b. 64 single precision processors.
- c. For 80A₁, 80A₂ and 160E primitives. This basis is larger than the one described in e. below and is needed to generate the same number of linearly independent surface functions as in e. The reason for this difference is the 32-bit arithmetic of the Mark IIIfp compared to the 64-bit arithmetic of the CRAY X-MP/48.
- d. Estimated on the basis of the absolute measured speed on the CRAY X-MP/48 and the measured relative speeds of the Mark IIIfp with respect to the CRAY X-MP/48.
- e. For 76A₁, 76A₂ and 152E primitives.
- f. Measured using the hardware-performance monitor of the PERFMON and PERFPRT subroutines.
- g. This time, for the same primitives as described in e. was estimated on the basis of the relative speeds of the CRAY 2 and CRAY X-MP/48 measured for a set of 5 values of $\bar{\rho}$. It is smaller than the time in e. for the reason given in h.
- h. Estimated on the basis of the relative speed of the CRAY 2 with respect to the CRAY X-MP/48 described in g. The reason this speed is 2/3 of the corresponding CRAY X-MP/48 speed is that the dominant parts of the calculation are optimized assembly code matrix-vector multiplications for which the CRAY 2 is 50 % faster than the CRAY X-MP/48. Otherwise, the CRAY 2 is slightly slower than CRAY X-MP/48. See Text.
- i. For 72A₁, 80A₂ and 152E primitives of even parity and 152A₁, 160A₂ and 312E primitives of odd parity. These numbers of primitives are larger than the ones given in j. for the reason given in c.
- j. For 64A₁, 76A₂ and 140E primitives of even parity and 140A₁, 152A₂ and 292E primitives of odd parity.
- k. Estimated on the basis of the relative speeds of the CRAY X-MP/48 and CRAY 2 and the measured CRAY X-MP/48 times or speeds.
- l. For 216A₁, 232A₂ and 448E primitives of even parity and 136A₁, 152A₂ and 288E primitives of odd parity. These numbers are larger than those in o. for the reason given in c.
- m. This time is estimated as in k., since the calculation cannot be done on the CRAY X-MP/48 because of insufficient memory.
- n. Estimated to be the same as in f. since the calculation cannot be done on the CRAY X-MP/48 for the reason given in m.
- o. For 204A₁, 216A₂ and 420E primitives of even parity and 128A₁, 140A₂ and 268E primitives of odd parity.

Table III : Performance of the logarithmic derivative code^a

	Mark IIIfp ^b		CRAY X-MP/48	CRAY 2
	64 processor global configuration ^c	8 clusters of 8 processors ^d		
Total time(hrs)	4.8 ^e	3.4 ^{f,g}	1.5	2.9 ^h
Time for 1 energy(min)	2.2 ⁱ	1.6 ⁱ	0.7	1.3
Efficiency	0.52	0.81	—	—
Speed ^j (Mflops)	34.4 ^k	48.5 ^k	110	55.4

- a. Based on a calculation using 245 surface functions and 131 energies, and a logarithmic derivative integration step of 0.01 bohr.
- b. 64 single precision processors.
- c. The calculation for each energy was distributed among all 64 processors.
- d. The hypercube was configured into 8 clusters of 8 processors each. Each cluster did full calculations for 16 energies, for a total of 128 energies. The times reported were multiplied by 131/128 for normalization purposes. All 8 clusters operated simultaneously.
- e. This includes 1.9 hours of I/O time.
- f. This includes 1.6 hours of I/O time. This time is shorter than that in e. because of a different and more efficient broadcast of the data between the host and the 8 clusters.
- g. Each cluster did full calculations for 16 energies for a total of 128 energies. The total time reported was obtained by subtracting the I/O time from the measured time, multiplying the result by 131/128 for normalization to 131 energies and adding the I/O time.
- h. Estimated on the basis of the CRAY X-MP/48 times and the ratio of the speeds of the CRAY 2 and CRAY X-MP/48 for the logarithmic derivative code.
- i. This includes the pro-rated I/O contribution.
- j. All speeds include I/O contribution.
- k. Estimated on the basis of the measured CRAY X-MP/48 speed for the logarithmic derivative code and the relative speeds of the Mark IIIfp and CRAY X-MP/48 for this code.

Table 4: Overall speed of reactive scattering codes on several machines

	Mark IIIfp		CRAY X-MP/48	CRAY 2	CRAY Y-MP/384
	64 processor	128 processors			
Surface function code for J=2 (Mflops)	124	240 ^a	117 ^b	176 ^b	232 ^b
Logarithmic derivative code ^c (Mflops)	48.5 ^d	127 ^{a,d,e}	110 ^b	55.4 ^b	187 ^b
Total main memory of computer (64 bit Mwords)	32	64	8	256	64

- a. Estimated on the basis of the 64 processor performance.
- b. For single processor operation.
- c. For 245 channels. As the number of channels increases, the Mark IIIfp speed increases by a factor not exceeding 1.25, but the speed of the CRAY machines remains approximately constant.
- d. Hypercube configured in clusters of 8 processors.
- e. This speed assumes four-fold increase in the I/O data rate, compared to the 64 processor machine, due to concurrent I/O hardware.

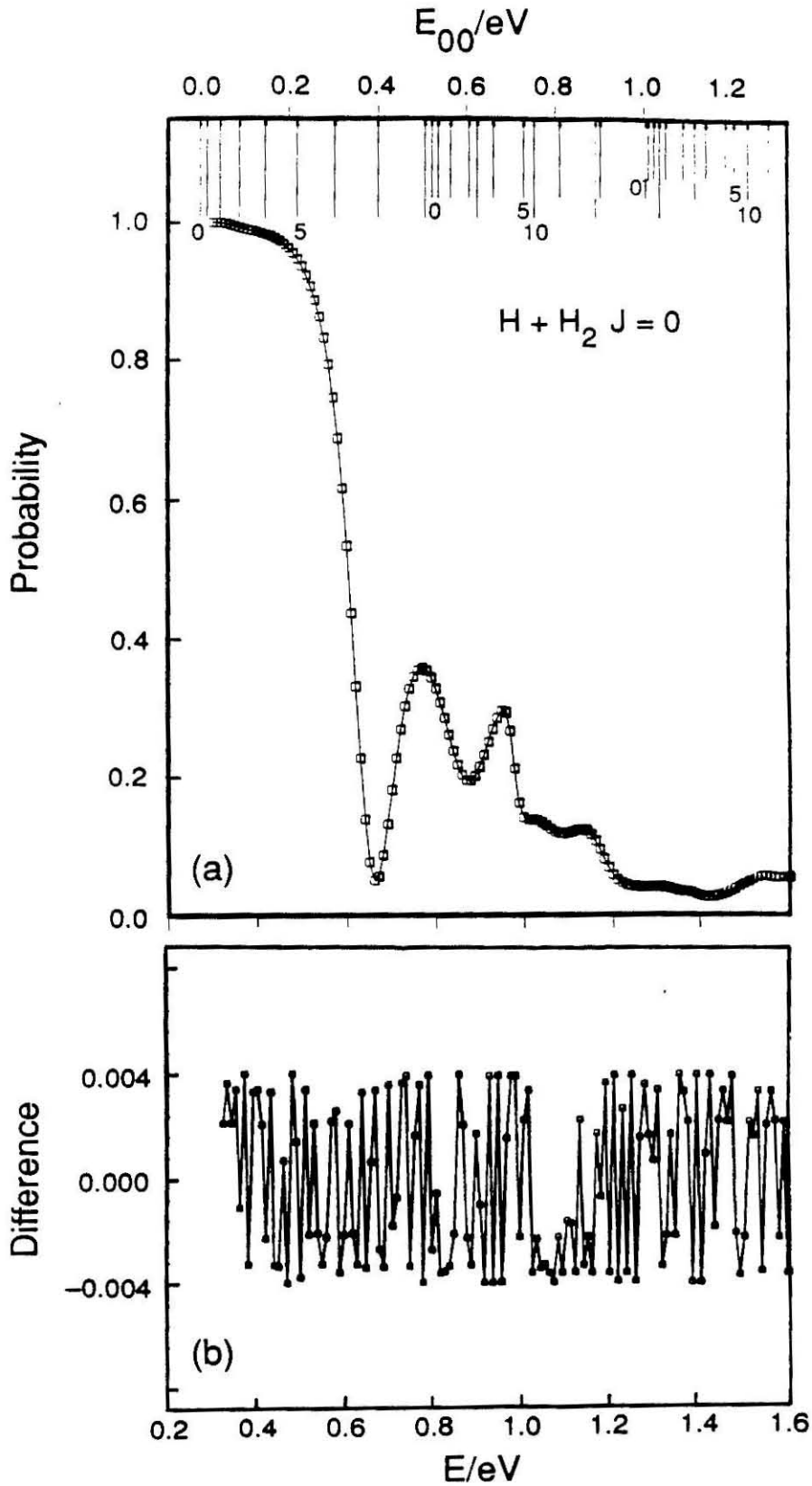


Figure 1

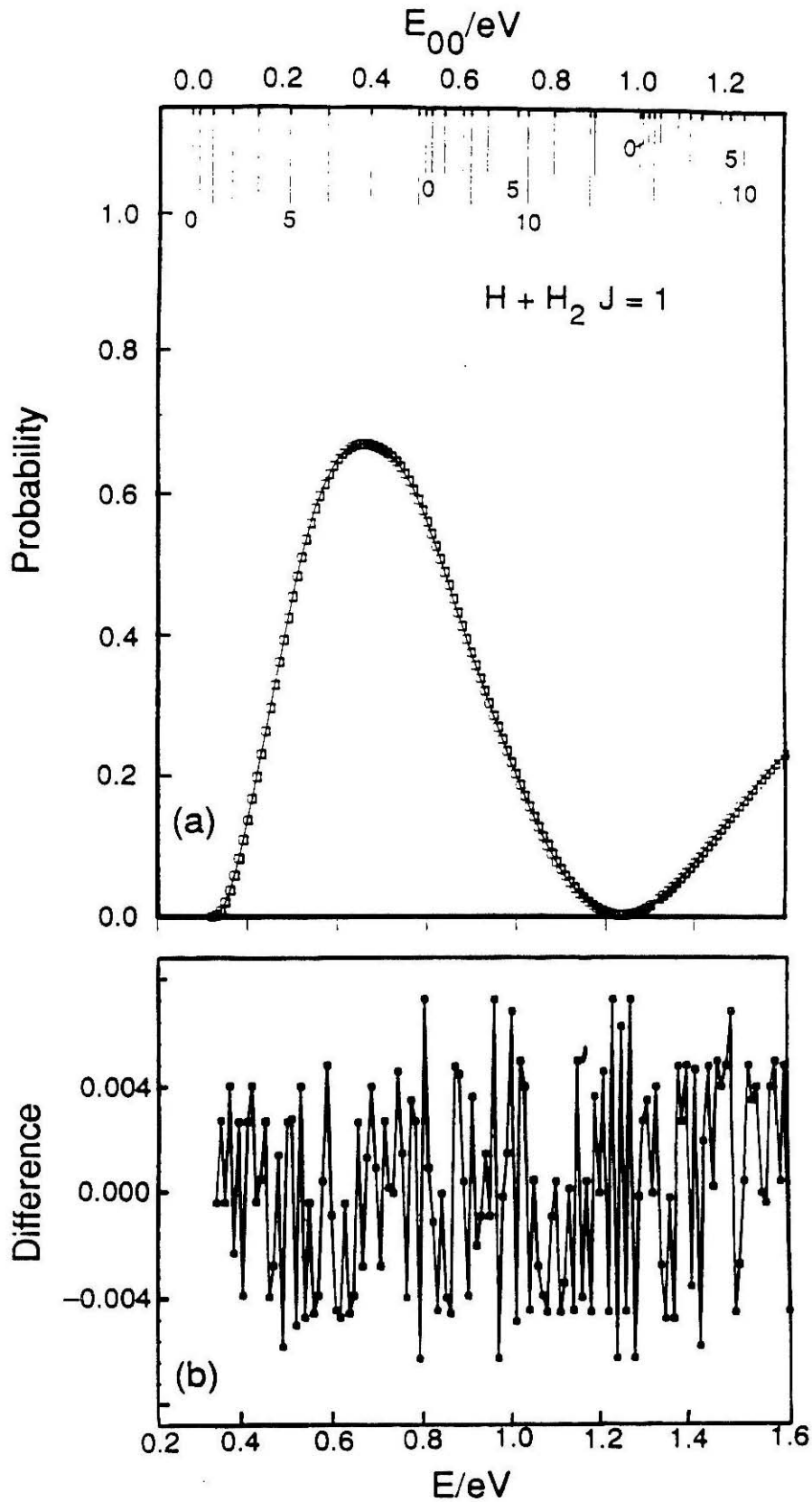


Figure 2

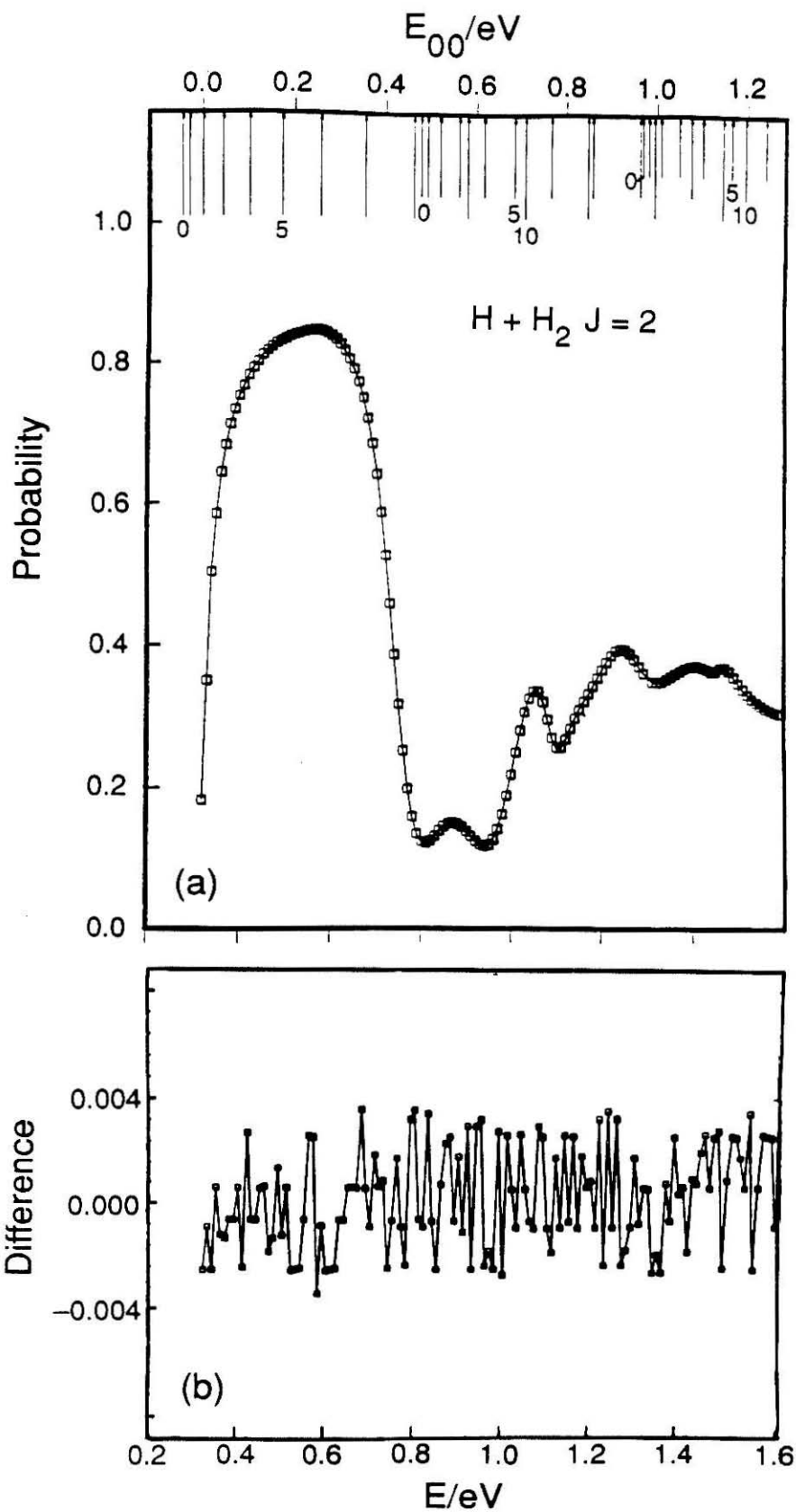


Figure 3

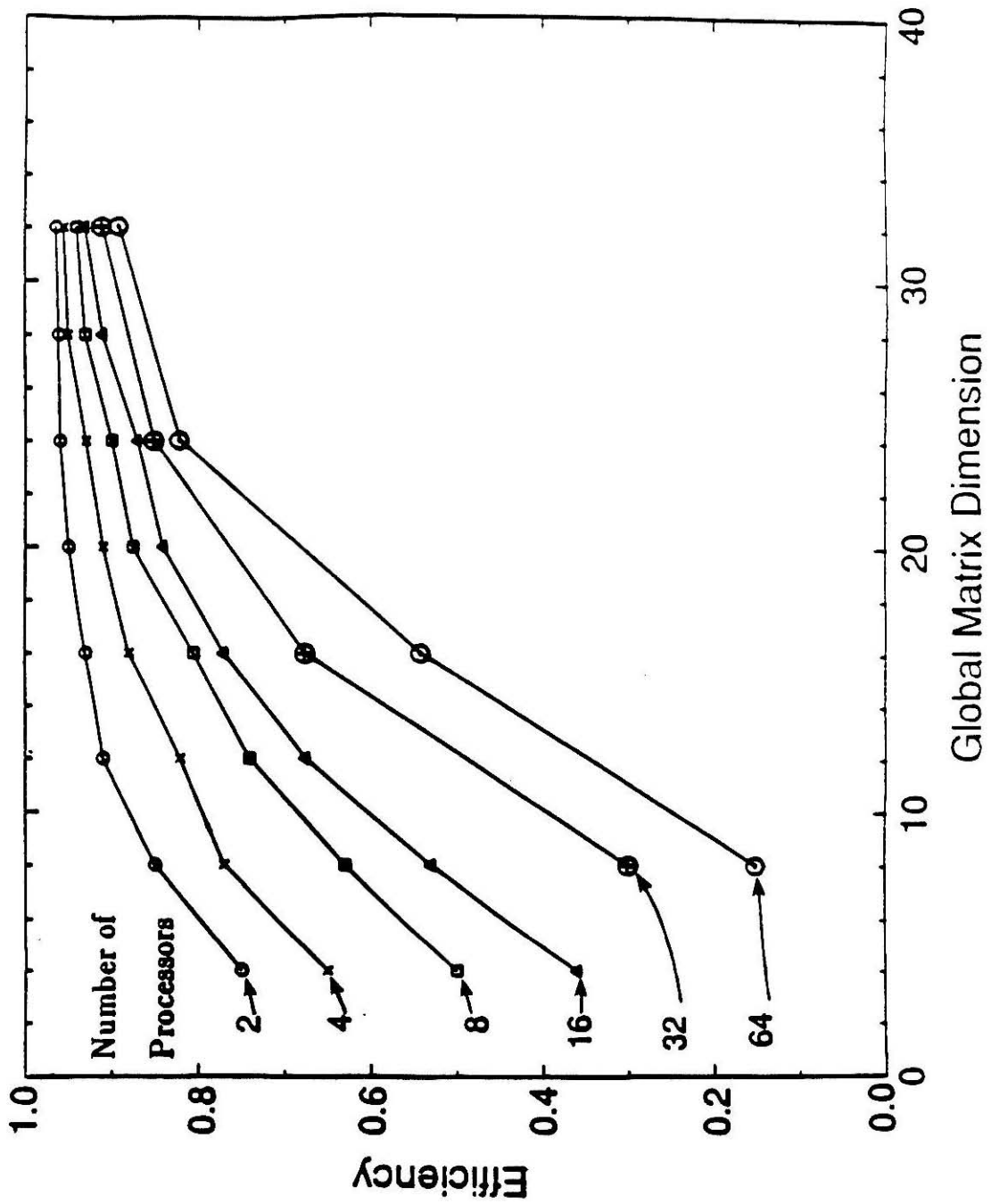


Figure 4

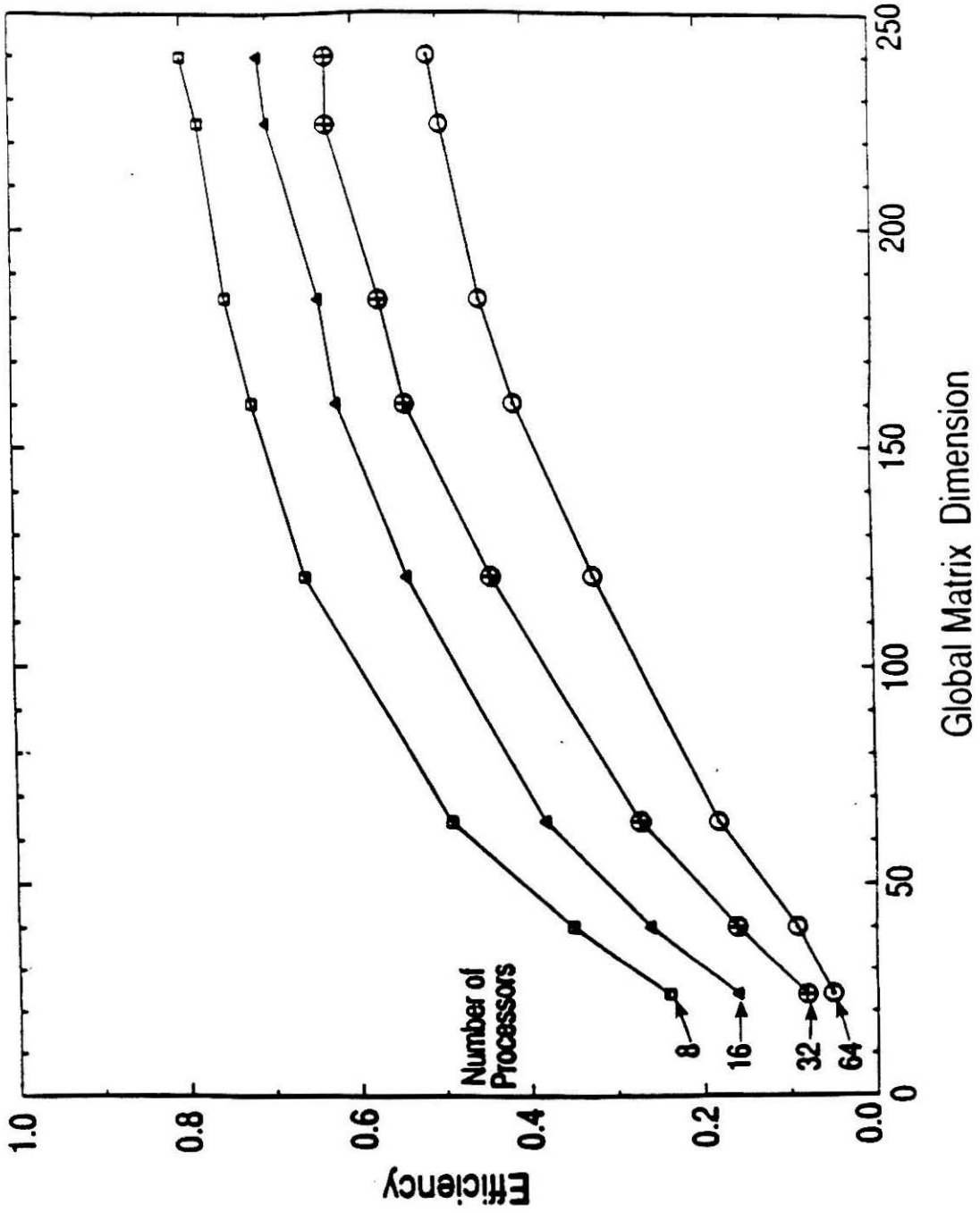


Figure 5

CHAPTER VI

Quantum Chemical Reaction Dynamics on a Highly Parallel Supercomputer

† This paper appeared in *Theor. Chim. Acta* **79**, 225 (1991)

**QUANTUM CHEMICAL REACTION DYNAMICS ON
A HIGHLY PARALLEL SUPERCOMPUTER**

Yi-Shuen Mark Wu ¹ , Steven A. Cuccaro, Paul G. Hipes ² and Aron Kuppermann

Arthur Amos Noyes Laboratory of Chemical Physics

Division of Chemistry and Chemical Engineering ³

California Institute of Technology

Pasadena, CA 91125, USA

(Received September 1990)

ABSTRACT

In this paper we describe the solution of the quantum mechanical equation for the scattering of an atom by a diatomic molecule on a high-performance distributed-memory parallel supercomputer, using the method of symmetrized hyperspherical coordinates and local hyperspherical surface functions. We first cast the problem in a format whose inherent parallelism can be exploited effectively. We next discuss the practical implementation of the parallel programs that were used to solve the problem. The benchmark results and timing obtained from the Caltech/JPL Mark IIIfp hypercube are competitive with the CRAY X-MP, CRAY 2 and CRAY Y-MP supercomputers. These results demonstrate that such highly parallel architectures permit quantum scattering calculations with high efficiency in parallel fashion and should allow us to study larger, more complicated chemical systems. Future extensions to this approach are discussed.

¹ Work performed in partial fulfillment of the requirements for the Ph.D. degree in Chemistry at the California Institute of Technology.

² Current address: 2338 Redwood Road, Scotch Plains, NJ 07076.

³ Contribution number 8209

Key Words: Reactive scattering - Hyperspherical coordinates - Parallel supercomputer

1. INTRODUCTION

Chemistry has long been one of the primary application areas for computers in scientific research. Quantum mechanical reactive scattering calculations, in particular, have consumed vast quantities of computer time on machines of all sizes. Accurate solutions have proved to be difficult and computationally expensive to obtain[1-4]. Such calculations would allow an interplay between theory and experiment which is vital to advance our understanding of the details of chemical reactions at the molecular level. Perhaps more importantly, the existence of accurate benchmark calculations permits the testing of approximate theories which in turn provides physical insights into the chemistry.

The first calculations of accurate quantum mechanical cross sections were reported in 1975 by Schatz and Kuppermann[5,6] and Elkowitz and Wyatt[7] for the simplest chemical reaction $H + H_2 \rightarrow H_2 + H$. After this, there was a lapse of over 10 years before these results were extended to higher energies and other systems. The problem is not only the inherent limitations in the theoretical methods but also due to the lack of sufficiently powerful computers[1-9]. Recently, a variety of efficient methodologies have been developed for carrying out calculations of reaction cross sections. With the current access to the CRAY-type supercomputers, there has been a remarkable surge in the number of publications in this field[10-21]. In particular, the use of symmetrized hyperspherical coordinates (SHC)[22,23] and local hyperspherical surface functions (LHSF)[10,17,18] is a very promising approach[12,24,25]. However, even the fastest available supercomputers are not sufficiently fast to allow the study of chemical reactions involving more than three atoms. Mathematical modelling and understanding the chemistry involved have progressed to a point that only the lack of sufficient computing power is delaying a detailed insight into the nature of many chemical reactions.

The initial route to supercomputing led by the CRAY machines is based on the construction of computers with very fast cycle times. Although this approach has produced very powerful machines, it is generally believed[26-28] that the key to future high performance computation to satisfy our need for both large numbers of CPU cycles and large amounts of fast memory is concurrent processing or the use of several computers tied together through a very high speed network to solve a single problem. The algorithms used and the codes developed on sequential machines must be adapted to parallel computing. Hence, these new parallel algorithms, coupled with the capabilities of parallel supercomputers, permit theoretical studies of a wide variety of chemical reactions.

The considerations above provide motivation for investigating the use of highly parallel computers as a possible way to reduce the computational time for such calculations. We chose the Caltech/JPL Mark IIIfp 64 processor hypercube[26-28], a distributed memory message passing parallel computer, as our test machine. The essential property a calculation must have to be efficiently done on a highly parallel computer is that it be decomposable in such a way that in performing it almost all processors should be computing efficiently almost all of the time, and that the communication time between the processors should represent a small fraction of the computation time. In this paper, we show how quantum mechanical reactive scattering calculations can be structured so as to fulfill these criteria. The performance of this implementation is also examined.

We divide this paper into four additional sections. In section 2 we provide an overview of the methodology and computational requirements for calculating LHSF and for using Johnson's logarithmic derivative method[29,30], modified to include the improvements suggested by Manolopoulos[31], for integrating the resulting coupled channel reactive scattering equations. In section 3 the parallel algorithm is

presented. In section 4 benchmark results of scattering calculations for the $H + H_2$ system total angular momentum $J = 0, 1, 2$ partial waves on the LSTH[32,33] potential energy surface are presented. We emphasize that even though the results we report were obtained for three identical particles, the implementation itself is applicable to general three body system in a parallel fashion. Ongoing and future extensions to this approach are also discussed. The last section contains some concluding remarks.

2. QUANTUM CHEMICAL DYNAMICS

The goal of bimolecular quantum chemical dynamics is to calculate from first principles the reaction cross sections for an atom (or molecule) scattered by another molecule. Most chemical reactions take place as a result of interactions among three or four atoms. The only type of chemical reaction we are likely to be able to solve rigorously in the foreseeable future is a three atom reaction of the type $A + BC \rightarrow AB + C$ or its four atom counterpart. Given the potential energy surface that governs an electronically adiabatic reaction, we use the nuclear motion Schrödinger equation to describe the collision of an atom and a diatomic molecule and the ensuing chemical reaction process.

The Schrödinger equation is a linear, second-order partial differential equation with $3N$ independent variables where N is the number of atoms in the system. One fruitful approach to solve this equation is based on hyperspherical coordinates[10,11,17,18]. The detailed formulation of this approach is discussed elsewhere[10,11,17] and we will present a very brief review of the theory, listing the equations necessary to facilitate the explanation of the parallel algorithms.

For a triatomic system, we label the three atoms A_α , A_β and A_γ . Let (λ, ν, κ) be any cyclic permutation of the indices (α, β, γ) . After removing the motion of

the center of mass, we define as the λ coordinates the mass-scaled[34] internuclear vector \mathbf{r}_λ from A_ν to A_κ , and the mass-scaled position vector \mathbf{R}_λ of A_λ with respect to the center of mass of $A_\nu A_\kappa$ diatom. The symmetrized hyperspherical coordinates[22] are the hyper-radius $\rho = (R_\lambda^2 + r_\lambda^2)^{1/2}$, and a set of 5 angles $\omega_\lambda, \gamma_\lambda, \theta_\lambda, \phi_\lambda$ and ψ_λ , denoted collectively as ζ_λ . The first two of these are in the range 0 to π and are respectively $2 \arctan \frac{r_\lambda}{R_\lambda}$ and the angle between \mathbf{R}_λ and \mathbf{r}_λ . The angles $\theta_\lambda, \phi_\lambda$ are the polar angles of \mathbf{R}_λ in a space-fixed frame and ψ_λ is the tumbling angle of the $\mathbf{R}_\lambda, \mathbf{r}_\lambda$ half-plane around its edge \mathbf{R}_λ . The hamiltonian \hat{H}_λ is the sum of a radial kinetic energy operator in ρ , and the surface hamiltonian \hat{h}_λ , which contains all differential operators in ζ_λ and the electronically adiabatic potential energy function $V(\rho, \omega_\lambda, \gamma_\lambda)$.

$$\hat{H}_\lambda = -\frac{\hbar^2}{2\mu} \left(\frac{\partial^2}{\partial \rho^2} + \frac{5}{\rho} \frac{\partial}{\partial \rho} \right) + \hat{h}_\lambda \quad (1)$$

where

$$\hat{h}_\lambda = \frac{\hat{\Lambda}^2}{2\mu\rho^2} + V(\rho, \omega_\lambda, \gamma_\lambda) \quad (2)$$

and

$$\hat{\Lambda}^2 = -4\hbar^2 \left(\frac{\partial^2}{\partial \omega_\lambda^2} + 2 \cot \omega_\lambda \frac{\partial}{\partial \omega_\lambda} \right) + \frac{\hat{j}_\lambda^2}{\sin^2 \frac{\omega_\lambda}{2}} + \frac{\hat{l}_\lambda^2}{\cos^2 \frac{\omega_\lambda}{2}} \quad (3)$$

\hat{j}_λ is the angular momentum operator corresponding to \mathbf{r}_λ , \hat{l}_λ is that corresponding to \mathbf{R}_λ and $\mu = [m_\alpha m_\beta m_\gamma / (m_\alpha + m_\beta + m_\gamma)]^{1/2}$ is the reduced mass appropriate for the mass-scaled coordinates. \hat{h}_λ depends on ρ parametrically and is therefore the “frozen” hyperradius part of \hat{H}_λ .

The scattering wave function $\Psi^{JM\Pi\Gamma}$ is labelled by the total angular momentum J , its projection M on the laboratory-fixed Z axis, the inversion parity Π with respect to the center of mass of the system and the irreducible representation Γ of the permutation group of the system (P_3 for $H + H_2$) to which the electronuclear wave function, excluding the nuclear spin part[35,36], belongs.

It can be expanded in terms of the LHSF $\Phi^{JM\Pi\Pi}$, defined below, and calculated at the values $\bar{\rho}_q$ of ρ :

$$\Psi_i^{JM\Pi\Pi}(\rho, \zeta_\lambda) = \sum_n b_{ni}^{JM\Pi\Pi}(\rho; \bar{\rho}_q) \Phi_n^{JM\Pi\Pi}(\zeta_\lambda; \bar{\rho}_q) \quad (4)$$

The equation that defines the LHSF $\Phi^{JM\Pi\Pi}$ with associated eigenvalues $\epsilon_n^{JM\Pi\Pi}$ is

$$\hat{h}_\lambda \Phi_n^{JM\Pi\Pi}(\zeta_\lambda; \bar{\rho}_q) = \epsilon_n^{JM\Pi\Pi}(\bar{\rho}_q) \Phi_n^{JM\Pi\Pi}(\zeta_\lambda; \bar{\rho}_q) \quad (5)$$

The domain of the surface function equation is closed and the spectrum is real and discrete. The index i is introduced to permit consideration of a set of many linearly independent solutions of the Schrödinger equation corresponding to distinct initial conditions which are needed to obtain the appropriate scattering matrices.

The LHSF $\Phi_n^{JM\Pi\Pi}(\zeta_\lambda; \bar{\rho}_q)$ and associated energies $\epsilon_n^{JM\Pi\Pi}(\bar{\rho}_q)$ are obtained by using a Rayleigh-Ritz variational approach[17]. The key to the success of the variational approach is finding a set of functions which are numerically inexpensive to calculate and also embody some of the structure of the true surface function. One effective set of functions consists of products of Wigner rotation matrices $D_{M\Omega}^J(\phi_\lambda, \theta_\lambda, \psi_\lambda)$, associated Legendre functions of γ_λ and functions of ω_λ which depend parametrically on $\bar{\rho}_q$ and are obtained from the numerical solution of one-dimensional eigenvalue-eigenfunction differential equations in ω_λ involving a potential related to $V(\bar{\rho}, \omega_\lambda, \gamma_\lambda)$.

The variational method leads to an eigenvalue problem with coefficient and overlap matrices $h^{JM\Pi\Pi}(\bar{\rho}_q)$ and $s^{JM\Pi\Pi}(\bar{\rho}_q)$ and whose elements are 5-dimensional integrals involving the variational basis functions.

The coefficients $b_{ni}^{JM\Pi\Pi}(\rho; \bar{\rho}_q)$ defined by equation (4) satisfy a coupled set of second order differential equations involving an interaction matrix $\mathcal{I}^{JM\Pi\Pi}(\rho; \bar{\rho}_q)$

whose elements are defined by

$$[\mathcal{I}^{J\Pi\Pi}(\rho; \bar{\rho}_q)]_n^{n'} = \left\langle \Phi_n^{JM\Pi\Pi}(\zeta_\lambda; \bar{\rho}_q) \left| V(\rho, \omega_\lambda, \gamma_\lambda) - (\bar{\rho}_q/\rho)^2 V(\bar{\rho}_q, \omega_\lambda, \gamma_\lambda) \right| \Phi_{n'}^{JM\Pi\Pi}(\zeta_\lambda; \bar{\rho}_q) \right\rangle \quad (6)$$

The configuration space ρ, ζ_λ is divided in a set of Q hyperspherical shells $\rho_q \leq \rho \leq \rho_{q+1}$ ($q = 1, 2, \dots, Q$) within each of which we choose a value $\bar{\rho}_q$ used in expansion (4).

When changing from the LHSF set at $\bar{\rho}_q$ to the one at $\bar{\rho}_{q+1}$ neither $\Psi_i^{JM\Pi\Pi}$ nor its derivative with respect to ρ should change. This imposes continuity conditions on the $b_{ni}^{J\Pi\Pi}$ and their ρ -derivatives at $\rho = \rho_{q+1}$, involving the overlap matrix $\mathcal{O}^{J\Pi\Pi}(\bar{\rho}_{q+1}, \bar{\rho}_q)$ between the LHSF evaluated at $\bar{\rho}_q$ and $\bar{\rho}_{q+1}$

$$[\mathcal{O}^{J\Pi\Pi}(\bar{\rho}_{q+1}, \bar{\rho}_q)]_n^{n'} = \left\langle \Phi_n^{JM\Pi\Pi}(\zeta_\lambda; \bar{\rho}_{q+1}) \left| \Phi_{n'}^{JM\Pi\Pi}(\zeta_\lambda; \bar{\rho}_q) \right. \right\rangle \quad (7)$$

The 5-dimensional integrals required to evaluate the elements of $h^{J\Pi\Pi}$, $s^{J\Pi\Pi}$, $\mathcal{I}^{J\Pi\Pi}$ and $\mathcal{O}^{J\Pi\Pi}$ are performed analytically over the three Euler angles ϕ_λ , θ_λ and ψ_λ and by two-dimensional numerical quadratures over γ_λ and ω_λ . These quadratures are the most expensive part of the entire LHSF computation and account for over 90% of the total time needed to calculate the $\Phi_n^{JM\Pi\Pi}$ and the matrices $\mathcal{I}^{J\Pi\Pi}$ and $\mathcal{O}^{J\Pi\Pi}$.

The system of second-order ordinary differential equations in the $b_{ni}^{J\Pi\Pi}$ is integrated as an initial value problem from small values of ρ to large values using Manolopoulos' logarithmic derivative propagator[31]. Matrix inversions account for more than 90% of the time used by this propagator. All aspects of the physics can be extracted from the solutions at large ρ by a constant ρ projection[10,11,37].

3. PARALLEL ALGORITHM

One must first have an idea of what can be gained by parallel processing. Vast speedup can only be achieved for problems that can be grouped into concurrent cooperative subtasks. This, of course, involves an understanding the level of parallelism that a problem manifests. Even with such understanding and of an adequate mapping onto a system of cooperative processors, there still remains the critical issue of how to best implement processor coordination. Further, it is vitally important that the local data in processors be correct in a global sense, i.e., data modifications must be distributed across private memory boundaries. Since quantum reactive scattering calculations are well suited to multiprocessor systems, the parallel structures in which parallelism is achieved is at the processor level rather than at the functional decomposition level. In building a parallel implementation on the hypercube architecture, our main guidelines have been simplicity and utilization of as much of the original sequential code as possible.

The computer used for this work is a 64-processor Mark IIIfp hypercube. It consists of an ensemble of individual processing elements called nodes. The design of the Mark IIIfp hypercube permits as few as one and as many as 256 nodes in the ensemble. It is a leading design for MIMD-type (multiple instruction stream multiple data stream) distributed memory parallel architectures based on message passing[26-28]. Each node consists of two independent Motorola 68020 microprocessors, one for computation and one for I/O, and four megabytes of dynamic local memory with an access speed of 400 nanoseconds. The computation microprocessor has a Motorola 68882 floating-point arithmetic coprocessor, two serial ports, one printer port and 128 kilobytes of static private memory. The I/O microprocessor has 64 kilobytes of static private memory, one serial port and hardware to support the node to node communication within the hypercube. An additional daughter board with a pipe-lined 32-bit floating point unit based on

the Weitek XL series of chips is attached to each node which further contains 128 kilobytes of code cache, 128 kilobytes of static memory and has a nominal peak speed of 16 Mflops. The Crystalline Operating System(CrOS)-channel-addressed synchronous communication provides the library routines to handle communications between nodes[28,38,39]. Program development is done on a Motorola 68020-based Counterpoint workstation that runs on UNIX. It acts as an access controller mechanism to the peripherals for the entire hypercube. This allows the native compilers and linkers of the control processor to be used to construct executable code to run on the nodes of the hypercube. The programs need to provide two parts with one running on the control processor and one running on each hypercube node. It is written in C programming language except for the time-consuming two-dimensional quadratures and matrix inversions, which are optimized in Weitek XL assembly language.

The hypercube is configured as a two dimensional array of processors. The mapping is done using binary Gray codes[28,40] which gives the Cartesian coordinates in processor space and communication channel tags for a processor's nearest neighbors. With a distributed-memory machine like the hypercube, the elements of a large matrix of data must be distributed across the memory of all the processors. This makes it possible to fully utilize the large memory available and facilitates the load-balancing task of keeping most of the processors busy doing useful arithmetic most of the time. The parallelization of scientific codes is frequently based on a large grain size decomposition of the task. To port a sequential code to a hypercube, a method of distributing the global matrix among the processors is the first choice that must be made and it is closely related to the parallel algorithm chosen.

We mapped the matrices into processor space by local decomposition. Let N_r and N_c be the number of processors in the rows and columns of the hypercube configuration, respectively. Element $A(i, j)$ of an $M \times M$ matrix is placed in processor row $P_r = \text{int}(\frac{i \times N_r}{M})$ and column $P_c = \text{int}(\frac{j \times N_c}{M})$, where $\text{int } x$ means the integer part of x . This data decomposition has been found easy to maintain and has provided satisfactory load balancing; it has the further advantage that it does not require matrices of special dimensions.

The parallel code implemented on the hypercube consists of five major steps. Step one constructs, for each value of $\bar{\rho}_q$, a primitive basis set composed of the product of Wigner rotation matrices, associated Legendre functions, and the numerical one-dimensional functions in ω_λ mentioned in Section 2 and obtained by solving the corresponding one-dimensional eigenvalue-eigenvector differential equation using a finite difference method. This requires that a subset of the eigenvalues and eigenvectors of a tridiagonal matrix be found.

A bisection method[41] which accomplishes the eigenvalue computation using the TRIDIB routine from EISPACK[42] was ported to the Mark IIIfp. This implementation of the bisection method allows computation of any number of consecutive eigenvalues specified by their indices. Eigenvectors are obtained using the EISPACK inverse iteration routine TINVIT with modified Gram-Schmidt orthogonalization. Each processor solves independent tridiagonal eigenproblems since the number of eigenvalues desired from each tridiagonal system is small but there are a large number of distinct tridiagonal systems. To achieve load balancing, we distributed subsets of the primitive functions among the processors in such a way that no processor computes greater than one eigenvalue and eigenvector more than any other. These large grain tasks are most easily implemented on MIMD machines; SIMD (single instruction stream multiple data stream) machines would

require more extensive modifications and would be less efficient because of the sequential nature of effective eigenvalue iteration procedures. The one-dimensional bases obtained are then broadcast to all the other nodes.

In step two a large number of two-dimensional quadratures involving the primitive basis functions which are needed for the variational procedure are evaluated. These quadratures are highly parallel procedures requiring no communication overhead once each processor has the necessary subset of functions. Each processor calculates a subset of integrals independently.

Step three assembles these integrals into the real symmetric dense matrices $s^{J\Pi\Pi}(\bar{\rho}_q)$ and $h^{J\Pi\Pi}(\bar{\rho}_q)$ which are distributed over processor space. The entire spectrum of eigenvalues and eigenvectors for the associated variational problem is sought. With the parallel implementation of the Householder method[43], this generalized eigensystem is tridiagonalized and the resulting single tridiagonal matrix is solved in each processor completely with the QR algorithm[44]. The QR implementation is purely sequential since each processor obtains the entire solution to the eigensystem. However, only different subsets of the solution are kept in different processors for the evaluation of the interaction and overlap matrices in step four. This part of the algorithm is not time-consuming and the straightforward sequential approach was chosen. It has the further effect that the resulting solutions are fully distributed, so no communication is required.

Step four evaluates the two-dimensional quadratures needed for the interaction $\mathcal{I}^{J\Pi\Pi}(\rho; \bar{\rho}_q)$ and overlap $\mathcal{O}^{J\Pi\Pi}(\bar{\rho}_{q+1}; \bar{\rho}_q)$ matrices. The same type of algorithms are used as were used in step two. By far, the most expensive part of the sequential version of the surface function calculation is the calculation of the large number of two-dimensional numerical integrals required by steps 2 and 4. These steps are however highly parallel and well suited for the hypercube.

Step five uses Manolopoulos'[31] algorithm to integrate the coupled linear ordinary differential equations. The parallel implementation of this algorithm is discussed elsewhere[29]. The algorithm is dominated by parallel Gauss-Jordan matrix inversion and is I/O intensive, requiring the input of one interaction matrix per integration step. To reduce the I/O overhead a second source of parallelism is exploited. The entire interaction matrix (at all ρ) and overlap matrix (at all $\bar{\rho}_q$) data sets are loaded across the processors and many collision energies are calculated simultaneously. This strategy works because the same set of data is used for each collision energy and because enough main memory is available. Calculation of scattering matrices from the final logarithmic derivative matrices is not computationally intensive, and is done sequentially.

The program steps were all run on the Weitek coprocessor which only supports 32-bit arithmetic. Experimentation has shown that this precision is sufficient for the work reported below. The 64-bit arithmetic hardware needed for larger calculations was installed after the present calculations were completed.

4. RESULTS AND DISCUSSION

Accuracy:

Calculations were performed for the $H+H_2$ system on the LSTH surface[32,33] for partial waves with total angular momentum $J = 0, 1, 2$ and energies up to 1.6 eV. Flux is conserved to better than 1% for $J = 0$, 2.3% for $J = 1$ and 3.6% for $J = 2$ for all open channels over the entire energy range considered.

To illustrate the accuracy of the 32-bit arithmetic calculations, the scattering results from the Mark IIIfp with 64 processors are compared with the results obtained using a CRAY X-MP/48 and a CRAY-2. The differences of the transition probability do not exceed 0.004 in absolute value over the energy range investigated.

Timing and parallel efficiency:

In Tables I and II we present the timing data on the 64 processor Mark IIIfp, a CRAY X-MP/48 and a CRAY 2, for both the surface function code (including calculation of the overlap \mathcal{O}^{JIII} and interaction \mathcal{I}^{JIII} matrices) and the logarithmic derivative propagation code. For the surface function code, the speeds on the first two machines is about the same. The CRAY 2 is 1.43 times faster than the Mark IIIfp and 1.51 times faster than the CRAY X-MP/48 for this code. The reason is that this program is dominated by matrix-vector multiplications which are done in optimized assembly code in all 3 machines. For this particular operation the CRAY-2 is 2.03 times faster than the CRAY X-MP/48 whereas for more memory-intensive operations the CRAY 2 is slower than the CRAY X-MP/48[45]. A slightly larger primitive basis set is required on the Mark IIIfp in order to obtain surface function energies of an accuracy equivalent to that obtained with the CRAY machines. This is due to the lower accuracy of the 32-bit arithmetic of the former with respect to the 64-bit arithmetic of the latter.

The absolute times presented in Table I and II are apt to decrease as the codes are improved and the numerical parameters are further tuned. As a result, they are not well suited for a comparison of the relative effectiveness of different reactive scattering methodologies[10-21]. The relevant information in those tables is, instead, the relative times among different machines as given by the corresponding speeds. These are indicative of the relative effectiveness of these machines for performing the reactive scattering calculations described in this paper.

The efficiency (ε) of the parallel LHSF code was determined using the definition $\varepsilon = \frac{T_1}{(N \times T_N)}$ where T_1 and T_N are respectively the implementation times using a single processor and N processors. The single processor times are obtained from runs performed after removing the overhead of the parallel code,

i.e., after removing the communication calls and some logical statements. Perfect efficiency ($\varepsilon = 1.0$) implies that the N -processor hypercube is N times faster than a single processor. In figure 1 efficiencies for the surface function code (including the calculation of the overlap and interaction matrices) as a function of the size of the primitive basis set are plotted for 2, 4, 8, 16, 32 and 64 processor configurations of the hypercube. The global dimensions of the matrices used are chosen to be integer multiples of the number of processor rows and columns in order to insure load balancing among the processors. Because of the limited size of a single processor memory, the efficiency determination is limited to 32 primitives. As shown in figure 1, the efficiencies increase monotonically and approach unity asymptotically as the size of the calculation increases. Converged results require large enough primitive basis sets so that the efficiency of the surface function code is estimated to be about 0.95 or greater.

The data for the logarithmic derivative code given in Table II for a 245 channel (*i.e.*, LHSF) example show that the Mark IIIfp has a speed about 62% to that of the CRAY 2 but only about 31% of that of the CRAY X-MP/48. This code is dominated by matrix inversions, which are done with optimized assembly code in all three machines. The reason for the slowness of the hypercube with respect to the CRAYs is that the efficiency of the parallel logarithmic derivative code is 0.52. This relatively low value is due to the fact that matrix inversions require a significant amount of inter-processor communication. Figure 2 displays efficiencies of the logarithmic derivative code as a function of the number of channels propagated for different processor configurations, as done previously for the Mark III[29,46] hypercubes. The data can be fit well by an operations count formula developed previously for the matrix inversion part of the code[47]; this formula can be used to extrapolate the data to larger numbers of processors or larger numbers of channels.

It can be seen that for an 8 processor configuration, the code runs with an efficiency of 0.81. This observation suggested that we divide the Mark IIIfp into 8 clusters of 8 processors each and perform calculations for different energies in different clusters. The corresponding timing information is also given in Table II. As can be seen from the last row of this table, the speed of the logarithmic derivative code using this configuration of the 64 processor Mark IIIfp is 48.5 Mflops, which is about 44% of that of the CRAY X-MP/48 and 88% of that of the CRAY 2. As the number of channels increases, the number of processors per cluster may be made larger in order to increase the amount of memory available in each cluster. The corresponding efficiency should continue to be adequate due to the larger matrix dimensions involved.

Ongoing and future extensions:

From the previous discussions it appears that our application is well adapted to the hypercube architecture. However, our systems are experimental and continually evolving in terms of both hardware and software. In the near future, the number of processors of the Mark IIIfp will be increased to 128 and the I/O system will be replaced by high performance CIO (concurrent I/O) hardware. The new Weitek coprocessors installed since the present calculations were done perform 64 bit floating point arithmetic at about the same nominal peak speed as the 32 bit boards. From the data in the present paper it is possible to predict with good reliability the performance of this upgraded version of the Mark IIIfp. Speed measurements on the CRAY Y-MP/864 of the San Diego Supercomputer Center show that it is 2 times faster than the CRAY X-MP/48 for the surface function code and 1.7 times faster for the logarithmic derivative code. In Table III, we summarize the available or predicted speed information for the present codes for the current 64 processor and near future 128 processor Mark IIIfp as well as the CRAY X-MP/48,

CRAY 2 and CRAY Y-MP/864 supercomputers. It can be seen that Mark IIIfp machines are competitive with all of the currently available CRAYs (operating as single processor machines).

From Table I-III, we can find that the design details of the most advanced supercomputers make some better-suited for certain computations than other. The surface function code is most efficient on the hypercube while the logarithmic derivative code will run better on CRAY-type machines. Distributing large computations among several supercomputers will provide the opportunity both to bring to bear greater computing power than is available in any single machine and to use the most suitable machine for each step of the task. In the near future a high performance network will be built which can support host interfaces that operate at 1600 million bits per second (Mbps) and connects multiple supercomputers at the Los Alamos National Laboratory, the California Institute of Technology, the Jet Propulsion Laboratory and the San Diego Supercomputer Center. With such a distributed heterogenous computer, it should be possible to run a single program on the eight processors of the CRAY Y-MP/864 and the 128 processors of the Mark IIIfp hypercube at the same time, with a speedup of 18 times the speed of one CRAY X-MP/48. Quantum scattering calculations on larger, more complicated chemical systems will become feasible at that time.

5. SUMMARY

We have developed and implemented a strategy for performing quantum mechanical reactive scattering calculations on the Mark IIIfp hypercube parallel supercomputer. The results obtained for the $H+H_2$ system $J = 0, 1, 2$ partial waves agree well with those from a CRAY X-MP/48 and a CRAY-2. The high degree of parallelism of the most time-consuming step of the surface function calculation (the

evaluation of two-dimensional numerical quadratures) leads to a high efficiency for that calculation. As a result, the speed of the 64 processor Mark IIIfp for the surface function calculation is about the same as that of the CRAY X-MP/48 and about 0.7 of that of the CRAY 2. When configuring the Mark IIIfp into 8 clusters of 8 processors each, the logarithmic derivative code is about 56% slower than the CRAY X-MP/48 and 12% slower than the CRAY 2. The speed of the 128 processor Mark IIIfp soon to become available should exceed, both for the surface function calculation and the logarithmic derivative calculation, those of the CRAY X-MP/48 and CRAY 2; however, although still comparable to the CRAY Y-MP/864 for the surface function code, it will be 32% slower for the logarithmic derivative code (the CRAYs operating as single processor machines). These results demonstrate the feasibility of performing reactive scattering calculations with high efficiency in parallel fashion. As the number of processors continues to increase and with the gigabit network that is currently been planned, such parallel calculations in systems of greater complexity will become practical in the not too distant future.

ACKNOWLEDGEMENTS

The work described in this paper was supported in part by DOE grant DE-AS03-83ER and Air Force Astronautics Laboratory contract F04611-86-K-0067. The calculations were performed on the 64 processor Mark IIIfp Caltech/JPL hypercube, the CRAY X-MP/48 at JPL, the CRAY X-MP/48 and CRAY Y-MP/864 at the NSF San Diego Supercomputing Center and the CRAY-2 at the Air Force Weapons Laboratory and we thank those institutions for their help. We also thank Dr. B. Lepetit and Prof. Geoffrey Fox for useful discussions.

REFERENCES

- [1] D. G. Truhlar and R. E. Wyatt, *Ann. Rev. Phys. Chem.* 27 (1976) 1.
- [2] G.C. Schatz, in: *Theory of Chemical Reaction Dynamics*, ed. by D. C. Clary, Proceedings of NATO workshop, Orsay, France, 1986, pp. 1.
- [3] B. C. Garrett and D. G. Truhlar, *Ann. Rev. Phys. Chem.* 35 (1984) 159.
- [4] J. M. Bowman, *Adv. Chem. Phys.* 61 (1985) 115.
- [5] G. C. Schatz and A. Kuppermann, *J. Chem. Phys.* 62 (1975) 2502.
- [6] G. C. Schatz and A. Kuppermann, *J. Chem. Phys.* 65 (1976) 4642; 65 (1976) 4668.
- [7] A. B. Elkowitz and R. E. Wyatt, *J. Chem. Phys.* 62 (1975) 2504; 63 (1975) 702.
- [8] R. B. Walker, E. B. Stechel and J. C. Light, *J. Chem. Phys.* 69 (1978) 2922.
- [9] R. B. Bernstein, ed.: *Atom-Molecule Collision Theory*; Plenum: New York, 1979.
- [10] A. Kuppermann and P. G. Hipes, *J. Chem. Phys.* 84 (1986) 5962.
- [11] P. G. Hipes and A. Kuppermann, *Chem. Phys. Lett.* 133 (1987) 1.
- [12] G. A. Parker, R. T Pack, B. J. Archer and R. B. Walker, *Chem. Phys. Lett.* 137 (1987) 564;
R. T Pack and G. A. Parker, *J. Chem. Phys.* 87 (1987) 3888.
- [13] J. Z. H. Zhang and W. H. Miller, *Chem. Phys. Lett.* 140 (1987) 329; 153 (1988) 465; 159 (1989) 130.
- [14] G. C. Schatz, *Chem. Phys. Lett.* 150 (1988) 92.
- [15] J. Z. H. Zhang, D. J. Kouri, K. Haug, D. W. Schwenke, Y. Shima and D. G. Truhlar, *J. Chem. Phys.* 88 (1988) 2492.
- [16] M. Mladenovic, M. Zhao, D. G. Truhlar, D. W. Schwenke, Y. Sun and D. J. Kouri, *Chem. Phys. Lett.* 146 (1988) 358;

- C. H. Yu, D. J. Kouri, M. Zhao and D. G. Truhlar, *Chem. Phys. Lett.* 157 (1989) 491.
- [17] S. A. Cuccharo, P. G. Hipes and A. Kuppermann, *Chem. Phys. Lett.* 154 (1989) 155.
- [18] S. A. Cuccharo, P. G. Hipes and A. Kuppermann, *Chem. Phys. Lett.* 157 (1989) 440.
- [19] F. Webster and J. C. Light, *J. Chem. Phys.* 90 (1989) 300.
- [20] J. Linderberg, S. Padkjaer, Y. Öhrn and B. Vessal, *J. Chem. Phys.* 90 (1989) 6254.
- [21] D. E. Manolopoulos and R. E. Wyatt, *Chem. Phys. Lett.* 159 (1989) 123.
- [22] A. Kuppermann, *Chem. Phys. Lett.* 32 (1975) 374.
- [23] R. T. Ling and A. Kuppermann, in: *Electronic and Atomic Collisions, Abstracts of papers of the 9th International Conference on the Physics of Electronic and Atomic Collisions, Seattle, Washington, 24-30 July 1975, Vol. 1*, J. S. Rusley and R. Geballe, eds. (Univ. Washington Press, Seattle, 1975) pp. 353, 354.
- [24] J. M. Launay and M. Le Dourneuf, *Chem. Phys. Lett.* 163 (1989) 178.
- [25] J. M. Launay and M. Le Dourneuf, *Chem. Phys. Lett.* 169 (1990) 473.
- [26] C. L. Seitz and J. Matisoo, *Phys. Today* 37(5) (1984) 38;
C. L. Seitz, *Comm. of the ACM* 28(1) (1985) 22.
- [27] G. C. Fox and S. W. Otto, *Phys. Today* 37(5) (1984) 50.
- [28] G. C. Fox, M. A. Johnson, G. A. Cyzenga, S. W. Otto, J. K. Salmon and D. W. Walker in: *Solving Problems in Concurrent Processors*; Prentice Hall, New Jersey, 1988.

- [29] P. G. Hipes, T. Mattson, Y-S. Mark Wu and A. Kuppermann, Proceedings of the Third Conference on Hypercube Concurrent Computers and Applications, Pasadena, 1988 (ACM, New York, 1988) pp. 1051-1061.
- [30] B. R. Johnson, J. Compl. Phys. 13 (1973) 445; J. Chem. Phys. 67(1977) 4086; NRCC Workshop, Lawrence Berkeley Laboratory, Report No. LBL 9501, 1979.
- [31] D. E. Manolopoulos, J. Chem. Phys. 85 (1986) 6425.
- [32] B. Liu, J. Chem. Phys. 58 (1973) 1925;
P. Siegbahn and B. Liu, J. Chem. Phys. 68 (1978) 2457.
- [33] D. G. Truhlar and C. J. Horowitz, J. Chem. Phys. 68 (1978) 2468; 71 (1979) 1514 (E).
- [34] L. M. Delves, Nucl. Phys. 9 (1959) 391; 20 (1960) 275.
- [35] B. Lepetit, Z. Peng and A. Kuppermann, "Calculation of Bound Rovibrational States on the First Electronically Excited State of the H_3 System", Chem. Phys. Lett., in press.
- [36] B. Lepetit and A. Kuppermann, "Numerical Study of the Geometric Phase in the $H + H_2$ Reaction", Chem. Phys. Lett., in press.
- [37] D. M. Hood and A. Kuppermann, in: Theory of Chemical Reaction Dynamics, ed. D. C. Clary (Reidel, Dordrecht, 1986) pp. 193-214.
- [38] G. C. Fox, editor, Caltech JPL concurrent computation project Annual report 1983-1984, February 1985.
- [39] G. C. Fox, G. Lyzenga, D. Rogstad and S. Otto, The Caltech concurrent computation program-Project description, Proc. 1985 ASME International Computers in Engineering Conference (1985).
- [40] E. N. Gilbert, Bell System Technical Journal 37 (1958) 815;
J. Salmon, Caltech Concurrent Computation Project Report C³P-51, 1984.

- [41] Ilse C. F. Ipsen and E. R. Jessup, Proceeding of the Second Conference on Hypercube Multiprocessors, Knoxville, Tennessee, 1987;
Ilse C. F. Ipsen and E. R. Jessup, Yale internal report: YALEU/DCS/RB-548;
G. C. Fox, Caltech Concurrent Computation Project Report *C³P-95*, 1984.
- [42] B. T. Smith, Matrix Eigensystem Routine- EISPACK Guide, 2nd ed., Vol. 6 of Lecture Notes in Computer Science (New York: Springer-Verlag) 1976.
- [43] G. C. Fox, Caltech Concurrent Computation Project Report *C³P-98*, 1984;
J. Patterson, Caltech Concurrent Computation Project Report *C³P-56.58*, 1986.
- [44] J. H. Wilkinson and C. Reinsch, in: Linear Algebra, vol.II of Handbook for Automatic Computation (New York: Springer- Verlag) 1971 pp. 227-240.
- [45] W. Pfeiffer, A. Alagar, A. Kamrath, R. H. Leary and J. Rogers, Benchmarking and Optimization of Scientific Codes on the CRAY X-MP, CRAY 2, and SCS-40 Vector Computers, November 1988, San Diego Supercomputer Center Report GA-A19478.
- [46] P. Messina, C. F. Baillie, E. W. Felten, P. G. Hipes, D. W. Walker, R. D. Williams, W. Pfeiffer, A. Alagar, A. Kamrath, R. H. Leary and J. Rogers, Benchmarking Advanced Architecture Computers, Caltech Concurrent Computation Project Report *C³P-712*, 1988.
- [47] P. G. Hipes and A. Kuppermann, Gauss-Jordan Inversion with Pivoting on the Caltech Mark II Hypercube, in Proceeding of the Third Conference on Hypercube Multiprocessors, Pasadena CA., 19-20 January 1988, edited by G. C. Fox, Vol II-Applications (California Institute of Technology, Mail Stop 206-49, Pasadena, CA, 1988) pp. 1621-1634.

FIGURE CAPTIONS

Figure 1 Efficiency of the surface function code (including the calculation of the overlap and interaction matrices) as a function of the global matrix dimension (*i.e.*, the size of the primitive basis set) for 2, 4, 8, 16, 32, and 64 processors. The solid curves are straight line segments connecting the data points for a fixed number of processors and are provided as an aid to examine the trends.

Figure 2 Efficiency of logarithmic derivative code as a function of the global matrix dimension (*i.e.*, the number of channels or LHSF) for 8, 16, 32, and 64 processors. The solid curves are straight line segments connecting the data points for a fixed number of processors and are provided as an aid to examine the trends.

Table I: Performance of the surface function code^a

J	Mark IIIfp ^b 64 processors		CRAY X-MP/48		CRAY 2	
	Time (hr)	Speed (Mflops)	Time (hr)	Speed (Mflops)	Time (hr)	Speed (Mflops)
0	0.71 ^c	100 ^d	0.74 ^e	96 ^f	0.49 ^g	145 ^h
1	2.88 ⁱ	112 ^d	3.04 ^j	106 ^f	2.01 ^k	160 ^h
2	5.60 ^l	124 ^d	5.94 ^m	117 ⁿ	3.96 ^o	176 ^k

- a. This code calculates the surface functions at the 51 values of $\bar{\rho}$ from 2.0 bohr to 12.0 bohr in steps of 0.2 bohr, the corresponding overlap matrices between consecutive values of $\bar{\rho}$ and the propagation matrices in ρ steps of 0.1 bohr. The number of primitives used for each J and described in the remaining footnotes permits us to generate enough LHSF to achieve the accuracy described in the text.
- b. 64 single precision processors.
- c. For $80A_1$, $80A_2$ and $160E$ primitives. This basis is larger than the one described in e. below and is needed to generate the same number of linearly independent surface functions as in e. The reason for this difference is the 32-bit arithmetic of the Mark IIIfp compared to the 64-bit arithmetic of the CRAY X-MP/48.
- d. Estimated on the basis of the absolute measured speed on the CRAY X-MP/48 and the measured relative speeds of the Mark IIIfp with respect to the CRAY X-MP/48.
- e. For $76A_1$, $76A_2$ and $152E$ primitives.
- f. Measured using the hardware-performance monitor of the PERFMON and PERFPRT subroutines.
- g. This time, for the same primitives as described in e. was estimated on the basis of the relative speeds of the CRAY 2 and CRAY X-MP/48 measured for a set of 5 values of $\bar{\rho}$. It is smaller than the time in e. for the reason given in h.
- h. Estimated on the basis of the relative speed of the CRAY 2 with respect to the CRAY X-MP/48 described in g. The reason this speed is 2/3 of the corresponding CRAY X-MP/48 speed is that the dominant parts of the calculation are optimized assembly code matrix-vector multiplications for which the CRAY 2 is 50 % faster than the CRAY X-MP/48. Otherwise, the CRAY 2 is slightly slower than CRAY X-MP/48. See Text.
- i. For $72A_1$, $80A_2$ and $152E$ primitives of even parity and $152A_1$, $160A_2$ and $312E$ primitives of odd parity. These numbers of primitives are larger than the ones given in j. for the reason given in c.
- j. For $64A_1$, $76A_2$ and $140E$ primitives of even parity and $140A_1$, $152A_2$ and $292E$ primitives of odd parity.
- k. Estimated on the basis of the relative speeds of the CRAY X-MP/48 and CRAY 2 and the measured CRAY X-MP/48 times or speeds.
- l. For $216A_1$, $232A_2$ and $448E$ primitives of even parity and $136A_1$, $152A_2$ and $288E$ primitives of odd parity. These numbers are larger than those in o. for the reason given in c.
- m. This time is estimated as in k., since the calculation cannot be done on the CRAY X-MP/48 because of insufficient memory.
- n. Estimated to be the same as in f. since the calculation cannot be done on the CRAY X-MP/48 for the reason given in m.
- o. For $204A_1$, $216A_2$ and $420E$ primitives of even parity and $128A_1$, $140A_2$ and $268E$ primitives of odd parity.

Table II : Performance of the logarithmic derivative code^a

	Mark IIIfp ^b		CRAY X-MP/48	CRAY 2
	64 processor global configuration ^c	8 clusters of 8 processors ^d		
Total time(hrs)	4.8 ^e	3.4 ^{f,g}	1.5	2.9 ^h
Time for 1 energy(min)	2.2 ⁱ	1.6 ⁱ	0.7	1.3
Efficiency	0.52	0.81	—	—
Speed ^j (Mflops)	34.4 ^k	48.5 ^k	110	55.4

- a. Based on a calculation using 245 surface functions and 131 energies, and a logarithmic derivative integration step of 0.01 bohr.
- b. 64 single precision processors.
- c. The calculation for each energy was distributed among all 64 processors.
- d. The hypercube was configured into 8 clusters of 8 processors each. Each cluster did full calculations for 16 energies, for a total of 128 energies. The times reported were multiplied by 131/128 for normalization purposes. All 8 clusters operated simultaneously.
- e. This includes 1.9 hours of I/O time.
- f. This includes 1.6 hours of I/O time. This time is shorter than that in e. because of a different and more efficient broadcast of the data between the host and the 8 clusters.
- g. Each cluster did full calculations for 16 energies for a total of 128 energies. The total time reported was obtained by subtracting the I/O time from the measured time, multiplying the result by 131/128 for normalization to 131 energies and adding the I/O time.
- h. Estimated on the basis of the CRAY X-MP/48 times and the ratio of the speeds of the CRAY 2 and CRAY X-MP/48 for the logarithmic derivative code.
- i. This includes the pro-rated I/O contribution.
- j. All speeds include I/O contribution.
- k. Estimated on the basis of the measured CRAY X-MP/48 speed for the logarithmic derivative code and the relative speeds of the Mark IIIfp and CRAY X-MP/48 for this code.

Table III : Overall speed of reactive scattering codes on several machines

	Mark IIIIfp		CRAY X-MP/48	CRAY 2	CRAY Y-MP/864
	64 processor	128 processors			
Surface function code for J=2 (Mflops)	124	240 ^a	117 ^b	176 ^b	232 ^b
Logarithmic derivative code ^c (Mflops)	48.5 ^d	127 ^{a,d,s}	110 ^b	55.4 ^b	187 ^b
Total main memory of computer(64 bit Mwords)	32	64	8	256	64

- a. Estimated on the basis of the 64 processor performance.
- b. for single processor operation.
- c. For 245 channels. As the number of channels increases, the Mark IIIIfp speed increases by a factor not exceeding 1.25, but the speed of the CRAY machines remains approximately constant.
- d. Hypercube configured in clusters of 8 processors.
- e. This speed assumes four-fold increase in the I/O data rate, compared to the 64 processor machine, due to concurrent I/O hardware.

Table IV : Hypothetical future parallel supercomputer characteristics

	Class A Mark IIIfp	Class B (1991-1995) ^a	Class C (1996-2000) ^a
Sustained speed/node (Mflops)	2	20	200
Memory/node (Mwords)	0.5	4	32
Inter-node communication bandwidth(Mbyte/sec)	1	100	1000
Number of nodes	128	1024	8192
Total sustained speed	256 Mflops	20 Gflops	1.6 Tflops
Total memory	64 Mword	4 Gword	262 Gword
Total I/O rate	128 Mbyte/sec	10 Gbyte/sec	1 Tbyte/sec

a. Time frame within which this machine class is expected to become available.

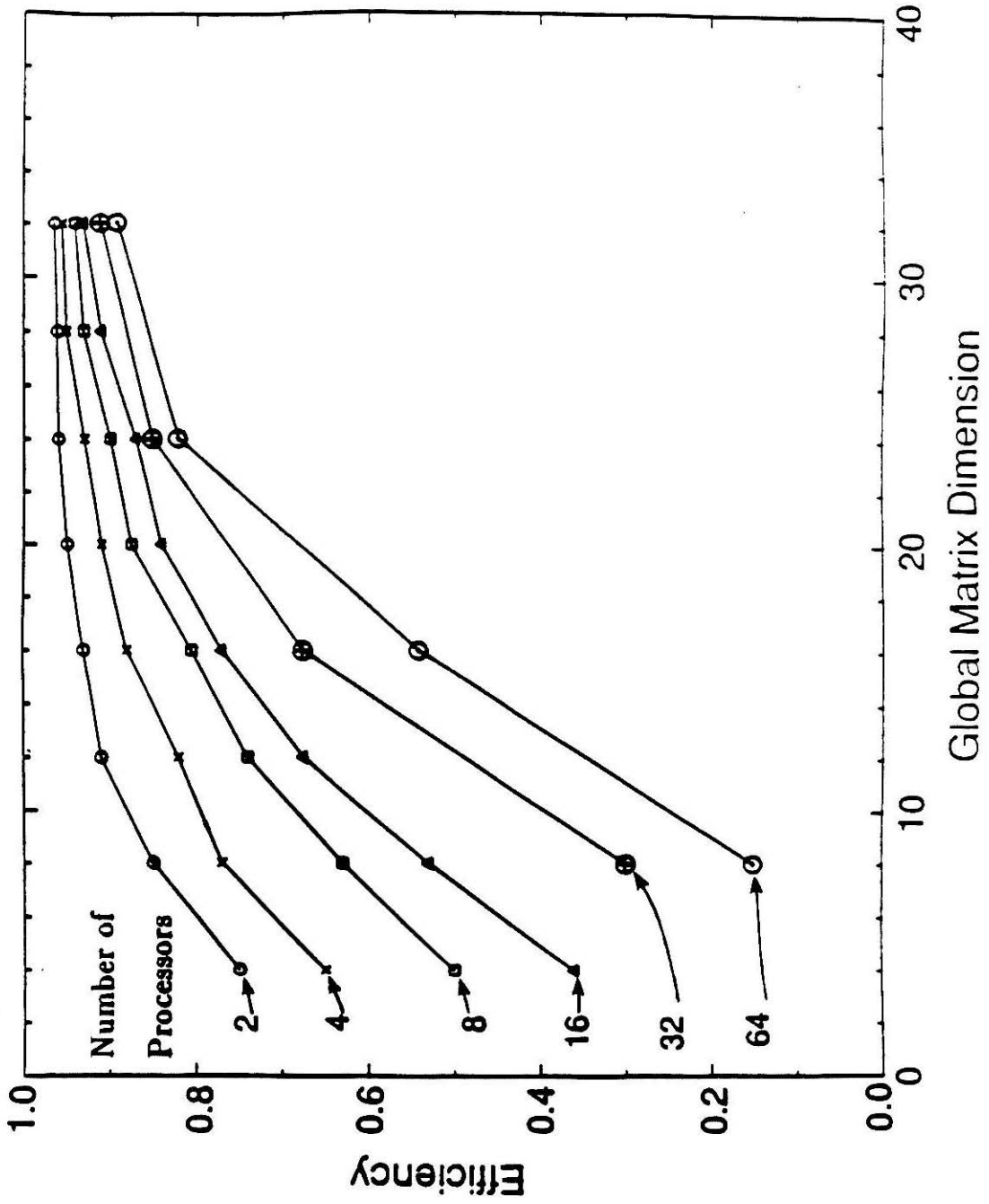


Figure 1

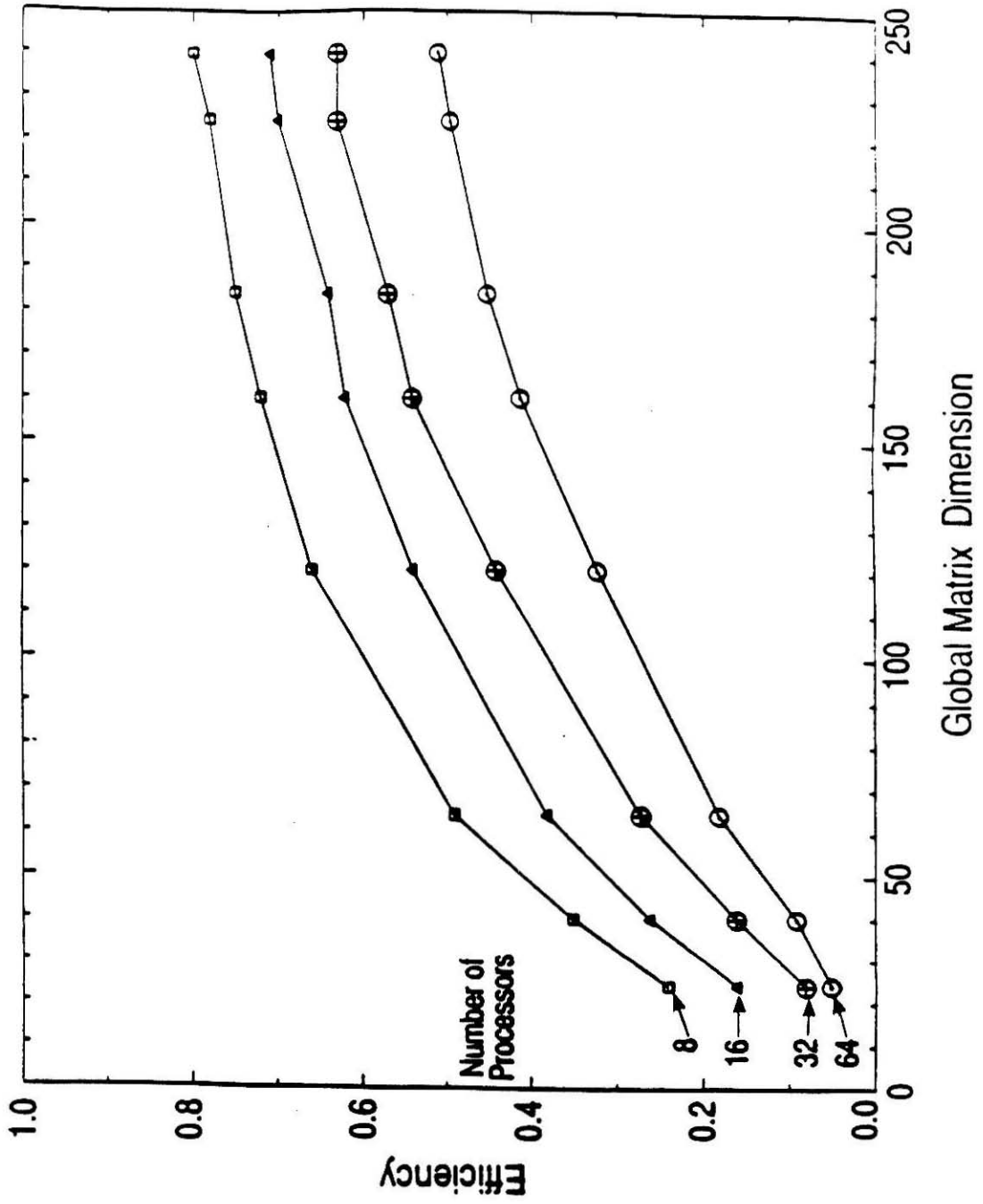


Figure 2

CHAPTER VII

Three-Dimensional Quantum Mechanical Electron-Hydrogen Scattering by the Symmetrized Hyperspherical Coordinate Method. Theory

Three-Dimensional Quantum Mechanical Electron-Hydrogen Scattering by the Symmetrized Hyperspherical Coordinate Method. Theory

Yi-Shuen Mark Wu¹ , Diane M. Hood and Aron Kuppermann

Arthur Amos Noyes Laboratory of Chemical Physics

Division of Chemistry and Chemical Engineering

California Institute of Technology

Pasadena, CA 91125, USA

Abstract

We present an efficient numerical method for obtaining accurate solutions to the Schrödinger equation for the collision of an electron with a hydrogen atom using symmetrized hyperspherical coordinates. The scattering wave functions are expanded in a set of local space-fixed hyperspherical surface functions that are eigenfunctions of a reference hamiltonian. This results in coupled differential equations in the hyperradius variable that are integrated to generate primitive wave functions. These solutions are linearly combined to satisfy the reactance and scattering matrix boundary conditions, from which the integral and differential cross sections are obtained. Symmetry considerations that simplify the calculations are discussed in detail. This formulation permits a very complete description of the electron-hydrogen scattering processes and can be extended to energies above the ionization threshold.

¹ Work performed in partial fulfillment of the requirements for the Ph.D. degree in Chemistry at the California Institute of Technology.

1. Introduction

Studies of collisions of electrons with hydrogen atoms have been of great interest for the past two decades[1]. It is one of the simplest processes in atomic physics and has been extensively studied, both theoretically and experimentally. One of the intriguing aspects of this problem is that agreement between experiment and even the most sophisticated of current theories is not satisfactory, because of the strong correlation between the two electrons[2].

Over the years many theoretical approaches have been made particularly for the electron-hydrogen problem. One of the major difficulties in the past has been the lack of a computationally efficient method for obtaining accurate cross sections. The close-coupling method used by Burke *et al.*[3,4] uses target hydrogen atom eigenfunctions to expand the full wave function. The convergence of this basis set is slow because it does not take the presence of the second electron into account. This method can be modified to include correlation functions[5] and pseudostate functions[6] in the expansion, and fairly converged results have been obtained for energies below the $n = 3$ threshold[7]. However, there is disagreement with the magnitude of the experimental $1s \rightarrow 2s$ cross section.

In the variational approach, the scattering equations are formulated by using a pseudostate basis[8]. The pseudostate basis contains all the open channel exact hydrogen eigenstates, while the higher bound and continuum states are represented by pseudostates chosen to be orthogonal, each of which has an associated effective energy level[9,10]. The primary problem associated with using pseudostates concerns the selection of a pseudostate basis set that will accurately represent the complete set of states. There have been various schemes proposed for this selection such as requiring that the basis set predict the correct value for some atomic parameter such as the static dipole polarizability. However, there is no

guarantee that these types of criteria are appropriate for scattering problems since the atomic parameter may be sensitive to a different radial range of the wave functions than that for the scattering calculation. Another problem is the existence of non-physical resonances below the pseudostate effective energies.

The use of hyperspherical coordinates and of the local hyperspherical surface function formalism in electron-atom scattering problems[11,12] and three-dimensional reactive scattering problems[13-17] has proven to be a successful approach to solving the Schrödinger equation. One of the difficulties in applying this approach is the accurate and efficient calculation of local hyperspherical surface functions, especially for reactive scattering processes.

The two electrons in the electron-hydrogen system do not move independently; indeed they are strongly correlated with each other. Correlation is totally ignored in the simplest versions of the independent electron model[3], but more sophisticated methods attempt to add in short range correlation effects[5]. The utility of hyperspherical coordinates becomes clear because a large part of the electron correlation is contained in the corresponding surface function basis set.

In this paper, we report the development and implementation of a general quantum theory for solving the electron-hydrogen system using symmetrized hyperspherical coordinates. We will set up the general Schrödinger equation for a three particle system in hyperspherical coordinates and discuss features of the potential energy surface. The method used for obtaining the solution of the Schrödinger equation, including the surface function expansion, calculation of potential matrix elements, and the solution of the coupled radial equation will be described.

2. The Space-fixed Schrödinger Equation

For electron-hydrogen scattering below the ionization threshold there are two arrangement channels, $e_1 + \text{H}$ and $e_2 + \text{H}$, where e_1 and e_2 are the two electrons. The third arrangement channel, in which the electrons are close to each other but distant from the proton, does not need to be considered, since it is not a stable one.

Let (λ, ν, κ) be any cyclic permutation of the indices (α, β, γ) . Given a system of three particles A_α, A_β and A_γ with masses m_α, m_β and m_γ , respectively, we define the λ coordinates as $(\mathbf{R}'_\lambda, \mathbf{r}'_\lambda)$ where \mathbf{R}'_λ is the vector from the center of mass of $\nu\kappa$ to λ and \mathbf{r}'_λ is the vector from ν to κ . The Hamiltonian, after removing the center of mass motion, for the three particles in this Jacobi center of mass coordinate system is

$$\hat{H} = -\frac{\hbar^2}{2\mu_{\lambda,\nu\kappa}}\nabla_{\mathbf{R}'_\lambda}^2 - \frac{\hbar^2}{2\mu_{\nu\kappa}}\nabla_{\mathbf{r}'_\lambda}^2 + V'(\mathbf{R}'_\lambda, \mathbf{r}'_\lambda, \gamma_\lambda) \quad (2.1)$$

where $\mu_{\lambda,\nu\kappa} = \frac{m_\lambda(m_\nu+m_\kappa)}{m_\lambda+m_\nu+m_\kappa}$, $\mu_{\nu\kappa} = \frac{m_\nu m_\kappa}{m_\nu+m_\kappa}$ are the reduced masses corresponding to the vectors \mathbf{R}'_λ and \mathbf{r}'_λ . $V'(\mathbf{R}'_\lambda, \mathbf{r}'_\lambda, \gamma_\lambda)$ is the potential energy function describing the interactions of the three particles. The coordinate γ_λ is the angle between \mathbf{R}'_λ and \mathbf{r}'_λ .

The Hamiltonian can be put in a simpler form by the introduction of Delves' mass-scaled coordinates[18], defined as

$$\begin{aligned} \mathbf{R}_\lambda &= a_\lambda \mathbf{R}'_\lambda; \\ \mathbf{r}_\lambda &= a_\lambda^{-1} \mathbf{r}'_\lambda; \\ a_\lambda &= \left(\frac{\mu_{\lambda,\nu\kappa}}{\mu_{\nu\kappa}}\right)^{\frac{1}{4}} \end{aligned} \quad (2.2)$$

The Schrödinger equation in Delves' mass-scaled coordinates is

$$\left[-\frac{\hbar^2}{2\mu}(\nabla_{\mathbf{R}_\lambda}^2 + \nabla_{\mathbf{r}_\lambda}^2) + V(\mathbf{R}_\lambda, \mathbf{r}_\lambda, \gamma_\lambda) - E\right]\Psi(\mathbf{R}_\lambda, \mathbf{r}_\lambda) = 0 \quad (2.3)$$

where

$$\nabla_{\mathbf{R}_\lambda}^2 = \left(\frac{\partial^2}{\partial R_\lambda^2} \right) + \frac{2}{R_\lambda} \left(\frac{\partial}{\partial R_\lambda} \right) - \frac{\hat{L}_{R_\lambda}^2}{\hbar^2 R_\lambda^2} \quad (2.3a)$$

$$\nabla_{\mathbf{r}_\lambda}^2 = \left(\frac{\partial^2}{\partial r_\lambda^2} \right) + \frac{2}{r_\lambda} \left(\frac{\partial}{\partial r_\lambda} \right) - \frac{\hat{L}_{r_\lambda}^2}{\hbar^2 r_\lambda^2} \quad (2.3b)$$

where $\mu = \left(\frac{m_\lambda m_\nu m_\kappa}{m_\lambda + m_\nu + m_\kappa} \right)^{\frac{1}{2}}$ is the single reduced mass for the system of particles and E is the total energy in the center of mass coordinate system.

Let us consider space-fixed axes, by which we mean a system $Oxyz$ whose origin O is the center of mass and whose axes are parallel to a system of laboratory-fixed axes, \mathbf{r}_λ is represented by distance r_λ , azimuth θ_{r_λ} , and polar angle φ_{r_λ} , while \mathbf{R}_λ is represented by R_λ , θ_{R_λ} and φ_{R_λ} . The orbital angular momentum terms $\hat{L}_{R_\lambda}^2$ and $\hat{L}_{r_\lambda}^2$ are expressible in terms of the angles $\theta_{R_\lambda}, \varphi_{R_\lambda}$ and $\theta_{r_\lambda}, \varphi_{r_\lambda}$, respectively. Since the two angular momentum operators describe the same rotation but for different electrons; therefore we will use \hat{l}_1 for \hat{L}_{R_λ} and \hat{l}_2 for \hat{L}_{r_λ} .

3. Symmetrized Hyperspherical Coordinates

The λ symmetrized hyperspherical coordinates for this system are obtained by conversion from the two distance variables R_λ and r_λ to a hyperradius ρ and an additional angle ω_λ [13],

$$\rho = (r_\lambda^2 + R_\lambda^2)^{\frac{1}{2}}; \quad \omega_\lambda = 2 \arctan \frac{r_\lambda}{R_\lambda}; \quad 0 \leq \omega_\lambda \leq \pi. \quad (3.1)$$

The four angular degrees of freedom remain the same. In this coordinate system the Hamiltonian is expressed as

$$\hat{H} = -\frac{\hbar^2}{2\mu} \left(\frac{\partial^2}{\partial \rho^2} + \frac{5}{\rho} \frac{\partial}{\partial \rho} \right) + \frac{\hat{\Lambda}^2}{2\mu\rho^2} + V(\rho, \omega_\lambda, \gamma_\lambda) \quad (3.2)$$

where the Grand Canonical angular momentum operator $\hat{\Lambda}^2$ is

$$\hat{\Lambda}^2 = \hat{L}_{\omega_\lambda}^2 + \frac{\hat{l}_1^2}{\sin^2 \frac{\omega_\lambda}{2}} + \frac{\hat{l}_2^2}{\cos^2 \frac{\omega_\lambda}{2}} \quad (3.3)$$

and the hyperspherical angular momentum operator is

$$\begin{aligned} \hat{L}_{\omega_\lambda}^2 &= -4\hbar^2 \left(\frac{\partial^2}{\partial \omega_\lambda^2} + 2\cot \frac{\partial}{\partial \omega_\lambda} \right) \\ &= -4\hbar^2 \frac{1}{\sin \omega_\lambda} \left(\frac{\partial^2}{\partial \omega_\lambda^2} + 1 \right) \sin \omega_\lambda. \end{aligned} \quad (3.4)$$

The orbital angular momentum operators \hat{l}_1^2 and \hat{l}_2^2 are expressed as

$$\hat{l}_1^2(\theta_{R_\lambda}, \varphi_{R_\lambda}) = -\hbar^2 \left[\frac{\partial^2}{\partial \theta_{R_\lambda}^2} + \cot \theta_{R_\lambda} \frac{\partial}{\partial \theta_{R_\lambda}} + \frac{1}{\sin^2 \theta_{R_\lambda}} \frac{\partial^2}{\partial \varphi_{R_\lambda}^2} \right] \quad (3.5)$$

$$\hat{l}_2^2(\theta_{r_\lambda}, \varphi_{r_\lambda}) = -\hbar^2 \left[\frac{\partial^2}{\partial \theta_{r_\lambda}^2} + \cot \theta_{r_\lambda} \frac{\partial}{\partial \theta_{r_\lambda}} + \frac{1}{\sin^2 \theta_{r_\lambda}} \frac{\partial^2}{\partial \varphi_{r_\lambda}^2} \right]. \quad (3.6)$$

This system has several advantages: The hyperradius ρ is independent of the arrangement channel; the operators for the hyperradius and hyperangles may be separated; and the conversion between different arrangement channels is relatively easy.

4. Potential Energy Function

The potential energy function for the system of two electrons and a proton is the sum of the Coulomb interaction of the three particles:

$$V(R_\lambda, r_\lambda) = -\frac{e^2}{|\mathbf{r}_\lambda|} - \frac{e^2}{|\mathbf{R}_\lambda|} + \frac{e^2}{|\mathbf{r}_\lambda - \mathbf{R}_\lambda|} \quad (4.1)$$

Here the zero of energy is taken to be energy of the configuration for which the three particles are infinitely separated. Since the mass scaling factors are very close to unity, we set $r_\lambda = r'_\lambda$ and $R_\lambda = R'_\lambda$ without loss of accuracy. The error

introduced by this assumption is negligible compared with the desired scattering calculation accuracy, and this can be corrected for if desired by an appropriate perturbation expansion.

In hyperspherical coordinates the potential energy function transforms into

$$V(\rho, \omega_\lambda, \gamma_\lambda) = -\frac{e^2}{\rho} \left(\frac{1}{\cos \frac{\omega_\lambda}{2}} + \frac{1}{\sin \frac{\omega_\lambda}{2}} - \frac{1}{\sqrt{1 - \sin \omega_\lambda \cos \gamma_\lambda}} \right) \quad (4.2)$$

This potential has a simple $1/\rho$ dependence and we might expect the forces involved to be long range and die off slowly.

In order to better visualize the properties of the potential energy function, we obtained contour plots of V for energies both above and below the ionization potential in a system of coordinates $OX_\lambda Y_\lambda Z_\lambda$ [13] defined as

$$\begin{aligned} X_\lambda &= \rho \sin \omega_\lambda \cos \gamma_\lambda; \\ Y_\lambda &= \rho \sin \omega_\lambda \sin \gamma_\lambda; \\ Z_\lambda &= \rho \cos \omega_\lambda. \end{aligned} \quad (4.3)$$

The range of γ_λ is 0 to π , and there is a one-to-one correspondence between points in the $Y_\lambda \geq 0$ half-space of the $OX_\lambda Y_\lambda Z_\lambda$ space and configuration of the system. This mapping of V shows that the hyperspherical surface not only has the same symmetry as the physical problem, but also treats the different arrangement channels evenly.

In Figure 1 we show several contours obtained at $Z_\lambda = 0$ bohr. There is a pointed profusion that reaches to the origin, which corresponds to $Y_\lambda = 0$, $X_\lambda > 0$. This region is due to the high energy of the configuration when the two electrons are very close to one another. Contours obtained by taking $Y_\lambda = 0$ which are perpendicular to Figure 1 are shown in Figure 2. The potential energy surface is symmetric with respect to the $Z_\lambda = 0$ plane, which is due to the two identical

electrons. Thus the three-dimensional internal configuration space is divided into two symmetric arrangement channels.

5. Partial Wave Expansion of the Wave Function

The complete symmetry group of the Hamiltonian is the set of all operators which commute with the Hamiltonian and is organized into operator subgroups which follow naturally from the character of the symmetry operations. Rotational invariance of the Hamiltonian permits us to choose the spatial wave function to belong to an irreducible representation of the subgroup $SO(3)$ of the complete symmetry group of the Hamiltonian. A basis for the invariant subspace corresponding to an irreducible representation is fixed by choosing each function to be an eigenfunction of the operator \hat{J}_z , the operator for the space-fixed Z component of the total angular momentum, which is the vector sum of \hat{l}_1 and \hat{l}_2 , with eigenvalues $M\hbar$, where $M = 0, \pm 1, \pm 2, \dots, \pm J$.

The Hamiltonian of the system is also invariant with respect to exchange of the electrons and to inversion through the center of mass of the system. As a result, solutions to the Schrödinger equation can be found which are simultaneously eigenfunctions of the exchange operator \hat{P}_{12} and the inversion operator $\hat{\mathfrak{S}}$. The Pauli principle requires that the total wave function change sign when the coordinates of the two identical fermion particles are exchanged. Therefore, a singlet ($S = 0$) spin state must be spatially symmetric with respect to exchange and the triplet ($S = 1$) spin state must go with an anti-symmetric spatial wave function.

We therefore expand Ψ in terms of their simultaneous eigenfunctions $\Psi^{JM S \Pi}$,

$$\Psi = \sum_{J=0}^{\infty} \sum_{M=-J}^J C^{JM} \sum_{\Pi=0}^1 \sum_{S=0}^1 \Psi^{JM S \Pi} \quad (5.1)$$

where $\Psi^{JM S \Pi}$ are the solutions of the set of eigenfunction equations

$$\begin{aligned}
 \hat{H}\Psi^{JM S \Pi} &= E\Psi^{JM S \Pi} \\
 \hat{J}^2\Psi^{JM S \Pi} &= J(J+1)\hbar^2\Psi^{JM S \Pi} \\
 \hat{J}_z\Psi^{JM S \Pi} &= M\hbar\Psi^{JM S \Pi} \\
 \hat{P}_{12}\Psi^{JM S \Pi} &= (-1)^S\Psi^{JM S \Pi} \\
 \hat{S}\Psi^{JM S \Pi} &= (-1)^\Pi\Psi^{JM S \Pi}
 \end{aligned} \tag{5.2}$$

6. Expansion of the Partial Waves in Terms of Surface Functions

Motion in the ρ coordinate is almost decoupled from the hyperangular coordinates whose motion is greater than the radial motion. We define local hyperspherical surface functions $\Phi_n^{JM S \Pi}$ to be well behaved solutions to the Schrödinger equation for the five-dimensional hamiltonian defined by equation (3.2), which resulted from omitting from \hat{H} the radial kinetic energy operator. This operator commutes with the same set of operators as the full six-dimensional hamiltonian operator, and therefore we define the surface functions to be simultaneous eigenfunctions of \hat{J}^2 , \hat{J}_z , \hat{P}_{12} and \hat{S} . It depends on ρ only parametrically, and is given explicitly by

$$\hat{h}(\omega_\lambda, 4\text{angles}; \rho) = \frac{\hat{\Lambda}^2}{2\mu\rho^2} + V(\rho, \omega_\lambda, \gamma_\lambda) \tag{6.1}$$

Therefore

$$\hat{h} \Phi_n^{JM S \Pi} = \epsilon_n^{J S \Pi} \Phi_n^{JM S \Pi} \tag{6.2}$$

The index n arises from the quantization of the energies of the surface functions, which follows from the finite bounds on the values of the five hyperangles.

The five-dimensional surface functions $\Phi_n^{JM S \Pi}$ are an excellent basis set for expansion of the six-dimensional scattering wavefunction $\Psi^{JM S \Pi}$, since they

contain much of the effect of the kinetic energy operators and of the potential energy function. The $\Psi_{n'}^{JM S \Pi}$ are therefore expressed as:

$$\Psi_{n'}^{JM S \Pi} = \rho^{-\frac{5}{2}} \sum_n b_n^{J S \Pi} \Phi_n^{JM S \Pi} \quad (6.3)$$

Although n' spans a denumerably infinite but discrete set of surface functions, in practice it must be truncated to a finite number which are needed to obtain appropriate scattering matrices.

To solve for these coefficients, the $\Phi_n^{JM S \Pi}$ are determined at a set of discrete values of $\bar{\rho}$. Substituting equation (6.3) into the Schrödinger equation corresponding to the hamiltonian defined by equation (3.2) and using equation (6.2), the coefficients are found to satisfy

$$\left\{ -\frac{\hbar}{2\mu} \frac{d^2}{d\rho^2} + \frac{15\hbar^2}{8\mu\rho^2} + \left(\frac{\bar{\rho}}{\rho}\right)^2 \epsilon_n^{J S \Pi}(\bar{\rho}) - E \right\} b_n^{JM S \Pi}(\rho; \bar{\rho}) + \sum_{n'} b_{n'}^{J S \Pi}(\rho; \bar{\rho}) [\mathcal{I}^{J S \Pi}]_n^{n'}(\rho; \bar{\rho}) = 0 \quad (6.4)$$

in which the interaction matrix $\mathcal{I}^{J S \Pi}$, which is a measure of the coupling of the surface functions by the potential, or equivalently of the change in the wavefunction as a function of ρ from the values at $\rho = \bar{\rho}$, is defined by

$$[\mathcal{I}^{J S \Pi}]_n^{n'}(\rho; \bar{\rho}) = \langle \Phi_n^{JM S \Pi} | \hat{V}(\rho, \omega_\lambda, \gamma_\lambda; \bar{\rho}) | \Phi_{n'}^{JM S \Pi} \rangle. \quad (6.5)$$

The potential of interaction $\hat{V}(\rho, \omega_\lambda, \gamma_\lambda; \bar{\rho})$ is defined as

$$\hat{V}(\rho, \omega_\lambda, \gamma_\lambda; \bar{\rho}) = V(\rho, \omega_\lambda, \gamma_\lambda) - \left(\frac{\bar{\rho}}{\rho}\right)^2 V(\bar{\rho}, \omega_\lambda, \gamma_\lambda). \quad (6.6)$$

Since we will expand the six-dimensional wave function in terms of a finite number of surface functions, the expansion (6.3) will become inaccurate for sufficiently large value of $|\rho - \bar{\rho}_i|$ (Here we label $\bar{\rho}_i$, with $i = 0$ for the smallest value of $\bar{\rho}$ and increasing with ρ), as some of the coupling is with functions excluded

from the truncated surface function basis. Therefore, the coefficient $b_n^{JS\Pi}(\rho; \bar{\rho})$ are calculated as a function of ρ in a region near $\bar{\rho}_i$ corresponding to a hyperspherical shell. It is then necessary for determination of the scattering wavefunction at all ρ to smoothly match the wavefunction calculated for each shell across the boundary $\rho = \rho_{i,i+1}$ of adjacent hyperapherical shells. This is accomplished by imposing the conditions

$$b_n^{JS\Pi}(\rho_{i,i+1}; \bar{\rho}_{i+1}) = \sum_{n'} b_{n'}^{JS\Pi}(\rho_{i,i+1}; \bar{\rho}_i) [\mathcal{O}^{JS\Pi}]_n^{n'}(\bar{\rho}_{i+1}, \bar{\rho}_i); \quad (6.7)$$

$$\left(\frac{\partial b_n^{JS\Pi}(\rho; \bar{\rho}_{i+1})}{\partial \rho} \right)_{\rho \rightarrow \rho_{i,i+1}^{(+)}} = \sum_{n'} \left(\frac{\partial b_{n'}^{JS\Pi}(\rho; \bar{\rho}_i)}{\partial \rho} \right)_{\rho \rightarrow \rho_{i,i+1}^{(-)}} [\mathcal{O}^{JS\Pi}]_n^{n'}(\bar{\rho}_{i+1}, \bar{\rho}_i); \quad (6.8)$$

in which the overlap matrices $\mathcal{O}^{JS\Pi}$ are defined by

$$[\mathcal{O}^{JS\Pi}]_n^{n'}(\bar{\rho}_{i+1}, \bar{\rho}_i) = \langle \Phi_n^{JM\S\Pi}(4\text{angles}; \bar{\rho}_{i+1}) | \Phi_{n'}^{JM\S\Pi}(4\text{angles}; \bar{\rho}_i) \rangle. \quad (6.9)$$

Equation (6.4) can be put in matrix form

$$-\frac{\hbar^2}{2\mu} \frac{d^2 \mathbf{b}^{JS\Pi}}{d\rho^2} + \mathcal{I}^{JS\Pi} \mathbf{b}^{JS\Pi} + \left[\left(\frac{\bar{\rho}}{\rho} \right)^2 \mathbf{e}^{JS\Pi} + \left(\frac{15\hbar^2}{8\mu\rho^2} - E \right) \mathbf{I} \right] \mathbf{b}^{JS\Pi} = \mathbf{0} \quad (6.10)$$

All the matrices appearing in this equation are square and their dimension equals the number of surface functions used in equation (6.3). To put this equation in more general form we define $\mathbf{U}^{JS\Pi}$:

$$\mathbf{U}^{JS\Pi} = -\frac{2\mu}{\hbar^2} (\mathcal{I}^{JS\Pi} + \left(\frac{\bar{\rho}}{\rho} \right)^2 \mathbf{e}^{JS\Pi} + \left(\frac{15\hbar^2}{8\mu\rho^2} - E \right) \mathbf{I}) \quad (6.11)$$

which gives

$$\frac{d^2 \mathbf{b}^{JS\Pi}}{d\rho^2} + \mathbf{U}^{JS\Pi} \mathbf{b}^{JS\Pi} = \mathbf{0} \quad (6.12)$$

7. Basis Set for Expansion of the Surface Function

The eigenfunctions of \hat{l}_1^2 and \hat{l}_2^2 are spherical harmonics, $Y_{l_1, m_1}(\theta_1, \varphi_1)$ and $Y_{l_2, m_2}(\theta_2, \varphi_2)$. Here we set $\theta_{R\lambda} = \theta_1, \varphi_{R\lambda} = \varphi_1$ and $\theta_{r\lambda} = \theta_2, \varphi_{r\lambda} = \varphi_2$. A set of one-dimensional surface functions, $f^{J\Sigma\Pi^i}_{l_1 l_2}(\omega_\lambda; \rho)$, independent of the orientation of the system in space can be defined by expansion of the surface function in terms of coupled spherical harmonics, $\mathcal{Y}_{l_2 l_1}^{JM}$:

$$\Phi_i^{JMS\Pi} = \sum_{l_2 l_1} \mathcal{Y}_{l_2 l_1}^{JM}(\theta_2, \varphi_2, \theta_1, \varphi_1) f^{J\Sigma\Pi^i}_{l_2 l_1}(\omega_\lambda; \rho) \quad (7.1)$$

where $\mathcal{Y}_{l_2 l_1}^{JM}(\theta_2, \varphi_2, \theta_1, \varphi_1)$ are orthonormal eigenfunctions of the total angular momentum operator \hat{J}^2 and its projection \hat{J}_z , as well as \hat{l}_1^2 and \hat{l}_2^2 :

$$\mathcal{Y}_{l_2 l_1}^{JM}(\theta_2, \varphi_2, \theta_1, \varphi_1) = \sum_{m_1 m_2} C(l_1 l_2 J; m_1 m_2 M) Y_{l_2 m_2}(\theta_2, \varphi_2) Y_{l_1 m_1}(\theta_1, \varphi_1) \quad (7.2)$$

The C's are Clebsch-Gordan coefficients in the notation of Rose[19].

Substitution of this expansion into equation (6.1), multiplication by $\mathcal{Y}_{l_2' l_1'}^{JM}(\theta_2, \varphi_2, \theta_1, \varphi_1)$ and integration over the four angles leads to the equation satisfied by these functions:

$$\begin{aligned} \frac{1}{2\mu\rho^2} (\hat{L}_{\omega_\lambda}^2 + \frac{l_1'(l_1'+1)\hbar^2}{\sin^2 \frac{\omega_\lambda}{2}} + \frac{l_2'(l_2'+1)\hbar^2}{\cos^2 \frac{\omega_\lambda}{2}}) f^{J\Sigma\Pi^i}_{l_2' l_1'}(\omega_\lambda; \rho) \\ + \sum_{l_2 l_1} V^{J\Pi}_{l_2' l_1'}^{l_2 l_1} f^{J\Sigma\Pi^i}_{l_2 l_1}(\omega_\lambda; \rho) = \epsilon_i^{J\Sigma\Pi}(\rho) f^{J\Sigma\Pi^i}_{l_2' l_1'} \end{aligned} \quad (7.3)$$

where the $V^{J\Pi}_{l_2' l_1'}^{l_2 l_1}$ are the surface potential matrix elements

$$V^{J\Pi}_{l_2' l_1'}^{l_2 l_1}(\omega_\lambda; \rho) = \langle \mathcal{Y}_{l_2' l_1'}^{JM} | V(\rho, \omega_\lambda, \gamma_\lambda) | \mathcal{Y}_{l_2 l_1}^{JM} \rangle \quad (7.4)$$

and can be calculated analytically. It is symmetric with respect to $\omega_\lambda \rightarrow \pi - \omega_\lambda$ and $l_2 l_1 \rightarrow l_1 l_2$.

The variational basis set $t_p^{Jl_2l_1}(\omega_\lambda; \rho)$ with associated eigenvalues $\nu_p^{J\Pi l_2l_1}$ that we have chosen to use to expand the surface functions was obtained by neglecting the off-diagonal terms of the potential matrix, such that

$$\left[\frac{1}{2\mu\rho^2} (\hat{L}_{\omega_\lambda}^2 + \frac{l_1(l_1+1)}{\sin^2 \frac{\omega_\lambda}{2}} + \frac{l_2(l_2+1)}{\cos^2 \frac{\omega_\lambda}{2}} + V_{l_2l_1}^{J\Pi l_2l_1}(\omega_\lambda; \rho)) \right] t_p^{Jl_2l_1}(\omega_\lambda; \rho) = \nu_p^{J\Pi l_2l_1}(\rho) t_p^{J\Pi l_2l_1}(\omega_\lambda; \rho) \quad (7.5)$$

We can introduced the function

$$T_p^{Jl_2l_1}(\omega_\lambda; \rho) = \sin\omega_\lambda t_p^{Jl_2l_1}(\omega_\lambda; \rho) \quad (7.6)$$

to force the boundary condition $T_p^{Jl_2l_1}(\omega_\lambda = 0; \rho) = T_p^{Jl_2l_1}(\omega_\lambda = \pi; \rho) = 0$ in order for $t_p^{Jl_2l_1}(\omega_\lambda; \rho)$ to be finite at those values of ω_λ .

Replacement of equation (7.6) into (7.5) leads to the following set of coupled differential equations:

$$-\frac{2\hbar^2}{\mu\rho^2} \frac{d^2}{d\omega_\lambda^2} T_p^{Jl_2l_1}(\omega_\lambda; \rho) + V_{eff}^{Jl_2l_1} T_p^{Jl_2l_1}(\omega_\lambda; \rho) = \nu_p^{J\Pi l_2l_1}(\rho) T_p^{Jl_2l_1}(\rho) T_p^{Jl_2l_1}(\omega_\lambda; \rho) \quad (7.7)$$

where $V_{eff}^{Jl_2l_1}$ is the effective potential defined as

$$V_{eff}^{Jl_2l_1} = -\frac{\hbar^2}{2\mu\rho^2} \left(4 - \frac{l_2(\beta+1)}{\cos^2 \frac{\omega_\lambda}{2}} - \frac{l_1(l_1+1)}{\sin^2 \omega_\lambda} \right) + V_{l_2l_1}^{J\Pi l_2l_1}(\omega_\lambda; \rho) \quad (7.8)$$

The eigenfunctions $T_p^{Jl_2l_1}(\omega_\lambda; \rho)$ are solved numerically using finite difference methods. They must be computed separately at a discrete values $\bar{\rho}_i$ of ρ such that for each $\bar{\rho}_i$, that set is appropriate for a range of values of ρ .

The basis functions $T_p^{Jl_2l_1}(\omega_\lambda; \rho)$ are orthogonal with the same $[l_1 l_2]$

$$\int_0^\pi T_p^{Jl_2l_1}(\omega_\lambda; \rho) T_{p'}^{Jl_2l_1}(\omega_\lambda; \rho) d\omega_\lambda = \delta_p^p, \quad (7.9)$$

If l_1 equals l_2 , the $T_p^{Jl_1}$ functions are either symmetric or antisymmetric, and are obtained in separate calculations. Since the parity Π is always even when

l_1 equals l_2 , if J is even, the singlet basis functions will be symmetric with respect to $\omega_\lambda = \pi/2$, but if J is odd, then it is the triplet basis functions that have this symmetry.

The basis functions in which we expand the surface functions $\Phi_n^{JM S \Pi}$ need to possess appropriate symmetry properties regarding electron exchange and inversion through the proton. To obtain such a property we take linear combination of two simple product functions $\mathcal{Y}_{l_2 l_1}^{JM}(\theta_2, \varphi_2, \theta_1, \varphi_1) t_p^{J l_2 l_1}(\omega_\lambda; \rho)$ and $\mathcal{Y}_{l_1 l_2}^{JM}(\theta_2, \varphi_2, \theta_1, \varphi_1) t_p^{J l_2 l_1}(\pi - \omega_\lambda; \rho)$ according to

$$\begin{aligned} \Theta_{l_2 l_1 p}^{JM S \Pi} = & N_{l_2 l_1} [\mathcal{Y}_{l_2 l_1}^{JM}(\theta_2, \varphi_2, \theta_1, \varphi_1) t_p^{J l_2 l_1}(\omega_\lambda; \rho) \\ & + (-1)^\Lambda \mathcal{Y}_{l_1 l_2}^{JM}(\theta_2, \varphi_2, \theta_1, \varphi_1) t_p^{J l_2 l_1}(\pi - \omega_\lambda; \rho)] \end{aligned} \quad (7.10)$$

where

$$\Lambda = S + J - \Pi \quad (7.11)$$

and $N_{l_2 l_1}$ is a normalization coefficient. For $l_1 = l_2 = l$ only one term is needed:

$$\Theta_{llp}^{JM S \Pi} = \mathcal{Y}_{ll}^{JM}(\theta_2, \varphi_2, \theta_1, \varphi_1) t_p^{J l}(\omega_\lambda; \rho) \quad (7.12)$$

The basis functions must be linearly independent and this leads to a restriction on the values assumed by l_1 and l_2 , because $\Theta_{l_1 l_2 p}^{JM S \Pi}$ differs from $\Theta_{l_2 l_1 p}^{JM S \Pi}$ by at most, a sign change. We therefore expand over pairs $[l_1 l_2]$, for which, $l_1 \leq l_2$

$$\Phi_n^{JM S \Pi} = \sum_{[l_1 l_2] p} a_{l_2 l_1 p}^{J S \Pi n}(\rho) \Theta_{l_2 l_1 p}^{JM S \Pi}(\omega_\lambda, 4\text{angles}; \rho) \quad (7.13)$$

Using the functions defined by equation (7.7) and (7.9), we can transform equation (7.3) into an algebraic eigenvalue-eigenvector equation in $e_n^{J S \Pi}(\rho)$ and $a_{l_2 l_1 p}^{J S \Pi n}$ by multiplying $\sin^2 \omega_\lambda t_p^{J l_2 l_1}(\omega_\lambda; \rho)$ and integrated over $d\omega_\lambda$. Stating the eigenvalue-eigenvector problem in matrix notation we have

$$(\mathbf{V}_0^{J S \Pi} + \mathbf{u}^{J S \Pi}) \mathbf{a}^{J S \Pi} = \mathbf{a}^{J S \Pi} \mathbf{e}^{J S \Pi} \quad (7.14)$$

where we define the diagonal matrices

$$(\mathbf{u}^{\text{JS}\Pi})_{l_2'l_1'p'}^{l_2l_1p} = \delta_{l_2'l_1'p'}^{l_2l_1p} \nu_p^{\text{J}\Pi l_2l_1}(\rho) \quad (7.15)$$

$$(\mathbf{e}^{\text{JS}\Pi})_{n'}^n = \delta_{n'}^n \epsilon_n^{\text{JS}\Pi}(\rho) \quad (7.16)$$

The interaction matrices $\mathbf{V}_0^{\text{JS}\Pi}$ are obtained by a unitary transformation:

$$\begin{bmatrix} \mathbf{V}_0^{\text{J}\Pi, \text{S}=0} & \mathbf{0} \\ \mathbf{0} & \mathbf{V}_0^{\text{J}\Pi, \text{S}=1} \end{bmatrix} = \mathbf{T}^{\text{tr}} \mathbf{V}_0^{\text{J}\Pi} \mathbf{T} \quad (7.17)$$

The matrix $\mathbf{V}_0^{\text{J}\Pi}$ is given as

$$(\mathbf{V}_0^{\text{J}\Pi})_{l_2'l_1'p'}^{l_2l_1p}(\rho) = (1 - \delta_{l_2'l_1'}^{l_2l_1}) \mathbf{V}^{\text{J}\Pi}_{l_2'l_1'p'}^{l_2l_1p} \quad (7.18)$$

which is symmetric and only has elements in off-diagonal blocks.

8. Calculation of Potential Matrix Elements

In order to calculate the surface functions we need to calculate potential functions $V^{\text{J}\Pi}_{l_2'l_1'}(\omega_\lambda; \rho)$ as well as the matrix elements $V^{\text{J}\Pi}_{l_2'l_1'p'}^{l_2l_1p}(\rho)$.

The first two terms of the potential function in equation (4.2), representing electron-nucleus attraction, are independent of the integration variables $(\theta_1, \varphi_1, \theta_2, \varphi_2, \gamma_\lambda)$, and lead to diagonal terms in the potential matrix. The off-diagonal elements in those matrices results from the third term (electron repulsion) term.

It is convenient for the evaluation of the potential energy matrix elements to use products of body-fixed Wigner rotation functions[19] and renormalized Legendre polynomials[20].

$$D_{\Omega l_1}^{JM}(\theta, \varphi, \gamma, \psi) = \sqrt{\frac{2J+1}{8\pi^2}} D_{M\Omega}^J(\varphi, \theta, \psi) \mathcal{P}_{l_1}^\Omega(\gamma) \quad (8.1)$$

The $\mathcal{Y}_{l_2 l_1}^{JM}$ and $D_{\Omega l_1}^{JM}$ are inter-related by the expression[21]

$$\mathcal{Y}_{l_2 l_1}^{JM}(\theta_2, \varphi_2, \theta_1, \varphi_1) = \sum_{\Omega=-J}^J (-1)^{l_1-\Omega} C(Jl_1 l_2; \Omega - \Omega) D_{\Omega l_1}^{JM}(\theta, \varphi, \gamma, \psi) \quad (8.2)$$

where $\theta_2 = \theta$ and $\varphi_2 = \varphi$. Substituting $\mathcal{Y}_{l_2 l_1}^{JM}$ into the potential matrix element expression (7.4), and taking the advantage of the orthonormality of $D_{\Omega l_2}^{JM}$ gives

$$\begin{aligned} V^{J\Pi l_2 l_1'} = & (-1)^{l_1+l_1'} \sum_{\Omega} C(Jl_1' l_2'; \Omega - \Omega) C(Jl_1 l_2; \Omega - \Omega) V_{l_1 l_1'}^{\Omega}(\omega_{\lambda}; \rho) \\ & - \frac{1}{\rho} \delta_{l_1' l_2}^{l_1' l_2'} \left(\frac{1}{\cos \frac{\omega_{\lambda}}{2}} + \frac{1}{\sin \frac{\omega_{\lambda}}{2}} \right) \end{aligned} \quad (8.3)$$

where we have defined a new quantity $V_{l_1 l_1'}^{\Omega}(\omega_{\lambda}; \rho)$ by

$$V_{l_1 l_1'}^{\Omega}(\omega_{\lambda}; \rho) = \frac{1}{\rho} \int_0^{\pi} \mathcal{P}_{l_1'}^{\Omega*}(\gamma) (1 - \sin \omega_{\lambda} \cos \gamma)^{-\frac{1}{2}} \mathcal{P}_{l_1'}^{\Omega}(\gamma) \sin \gamma d\gamma \quad (8.4)$$

In order to compute this integral, we expand the repulsion energy term in a series of Legendre polynomials of $\cos \gamma$ [22].

$$\begin{aligned} (1 - \sin \omega_{\lambda} \cos \gamma)^{-\frac{1}{2}} = & \frac{1}{\cos \frac{\omega_{\lambda}}{2}} \sum_{k=0}^{\infty} P_k(\cos \gamma) \tan^k \frac{\omega_{\lambda}}{2} \quad \text{for } 0 \leq \omega_{\lambda} \leq \frac{\pi}{2} \\ & \frac{1}{\sin \frac{\omega_{\lambda}}{2}} \sum_{k=0}^{\infty} P_k(\cos \gamma) \cot^k \frac{\omega_{\lambda}}{2} \quad \text{for } \frac{\pi}{2} \leq \omega_{\lambda} \leq \pi \end{aligned} \quad (8.5)$$

Using this expression leads to integrals over products of three associated Legendre functions, which can be evaluated analytically.

The final exact expression for $V^{J\Pi l_2 l_1'}$ is found to be the following:

$$\begin{aligned} V^{J\Pi l_2 l_1'} = & (-1)^{l_1+l_1'} \frac{1}{\rho} \sqrt{\frac{2l_1+1}{2l_1'+1}} \sum_m \frac{\tan^m \frac{\omega_{\lambda}'}{2}}{\cos \frac{\omega_{\lambda}'}{2}} C(l_1 m l_1'; 000) \\ & \times \sum_{\Omega} C(Jl_1' l_2'; \Omega - \Omega) C(Jl_1 l_2; \Omega - \Omega) C(l_1 m l_1'; \Omega 0 \Omega) \\ & - \frac{1}{\rho} \delta_{l_2 l_1}^{l_2' l_1'} \left(\frac{1}{\cos \frac{\omega_{\lambda}}{2}} + \frac{1}{\sin \frac{\omega_{\lambda}}{2}} \right). \end{aligned} \quad (8.6)$$

The matrix elements $V^{J\Pi}_{l_2' l_1' p'}(\rho)$ are obtained by trapezoidal rule integration over ω_λ .

9. Solution of Coupled Equations

It is most convenient to solve the coupled equation (6.12) by using logarithmic derivative integration[23]. The unknown function $\mathbf{b}^{J\Pi}(\rho; \bar{\rho})$ to its logarithmic derivative is defined as

$$\mathbf{y}^{J\Pi}(\rho; \bar{\rho}_i) = \mathbf{b}'^{J\Pi}(\rho; \bar{\rho}_i)(\mathbf{b}^{J\Pi}(\rho; \bar{\rho}_i))^{-1} \quad (9.1)$$

We find by differentiation of equation (9.1) and using equation (6.12) that $\mathbf{b}^{J\Pi}(\rho; \bar{\rho}_i)$ satisfies the matrix Ricatti-Bessel equation[24]

$$\mathbf{y}^{J\Pi}(\rho; \bar{\rho}_i) + \mathbf{y}^{2J\Pi}(\rho; \bar{\rho}_i) + \mathbf{U}^{J\Pi}(\rho; \bar{\rho}_i) = 0 \quad (9.2)$$

Similarly, equation (6.7) and (6.8), which interrelate the wavefunction and its derivative in the various surface function basis sets at different $\bar{\rho}$, may be expressed in matrix form as

$$\mathbf{b}^{J\Pi}(\rho; \bar{\rho}_{i+1}) = [\mathcal{O}^{J\Pi}(\bar{\rho}_{i+1}, \bar{\rho}_i)]^{-1} \mathbf{b}^{J\Pi}(\rho; \bar{\rho}_i) \mathcal{O}^{J\Pi}(\bar{\rho}_{i+1}, \bar{\rho}_i) \quad (9.3)$$

$$\mathbf{b}'^{J\Pi}(\rho; \bar{\rho}_{i+1}) = [\mathcal{O}^{J\Pi}(\bar{\rho}_{i+1}, \bar{\rho}_i)]^{-1} \mathbf{b}'^{J\Pi}(\rho; \bar{\rho}_i) \mathcal{O}^{J\Pi}(\bar{\rho}_{i+1}, \bar{\rho}_i) \quad (9.4)$$

Therefore, the logarithmic derivative matrices in different $\bar{\rho}$ basis sets can be related in the same way:

$$\mathbf{y}^{J\Pi}(\rho; \bar{\rho}_{i+1}) = [\mathcal{O}^{J\Pi}(\bar{\rho}_{i+1}, \bar{\rho}_i)]^{-1} \mathbf{y}^{J\Pi}(\rho; \bar{\rho}_i) \mathcal{O}^{J\Pi}(\bar{\rho}_{i+1}, \bar{\rho}_i) \quad (9.5)$$

We use an efficient procedure developed by Johnson[23] to numerically integrate equation (9.2), using the initial condition $\mathbf{y} = 10^{36} \mathbf{I}$. This corresponds to

the initial conditions of $\mathbf{b} = \mathbf{0}, \mathbf{b}' = \mathbf{I}$ at $\rho = \rho_0$, where ρ_0 is a value close to zero. The integration of \mathbf{y} is carried out to a large enough ρ for the electron-hydrogen atom interaction to have become negligible. One then projects the resulting scattering solutions at constant ρ on the asymptotic hydrogen atom wavefunctions from which all aspects of physics can be extracted.

10. Asymptotic Analysis - R and S Matrices

To obtain differential and integral cross sections, it is necessary to use an asymptotic form which corresponds to the physical conditions of a scattering process. Asymptotically in each arrangement channel λ , as $R_\lambda \rightarrow \infty$, the wavefunction of physical interest has the form

$$\Psi_{i'}^{JM S \Pi} \sim_{R_\lambda \rightarrow \infty} \sum_{nl_2 l_1 \lambda} \frac{1}{R_\lambda} U_{nl_2 l_1 \lambda}^{J S \Pi i'}(R_\lambda) \Phi_{nl_2 l_1}^{JM \Pi}(r_\lambda, \Omega) \quad (10.1)$$

where $\Phi_{nl_2 l_1}^{JM \Pi}(r_\lambda, \Omega)$ is the product of $\mathcal{Y}_{l_2 l_1}^{JM}(\theta_2, vb, ta, va)$ and the hydrogen radial function $R_{Nl_1}(r_\lambda)$. In addition, the radial functions $U^{J S \Pi}(R_\lambda)$ behave asymptotically as a combination of Riccati-Bessel functions[24],

$$U_{nl_2 l_1}^{J S \Pi i'}(R_\lambda) \sim_{R_\lambda \rightarrow \infty} \sum_{\bar{n} \bar{l}_1 \bar{l}_2} [J_{\bar{n} \bar{l}_1 \bar{l}_2}^{J S \Pi}(R_\lambda) - \sum_{\hat{n} \hat{l}_1 \hat{l}_2} N_{\hat{n} \hat{l}_1 \hat{l}_2}^{J S \Pi}(R_\lambda) \mathbf{R}^{J S \Pi} \begin{smallmatrix} \bar{n} \bar{l}_1 \bar{l}_2 \\ \hat{n} \hat{l}_1 \hat{l}_2 \end{smallmatrix}] C_{\bar{n} \bar{l}_1 \bar{l}_2}^{J S \Pi i'} \quad (10.2)$$

In matrix form, this equation can be rewritten as

$$\mathbf{U}^{J S \Pi} \sim_{R_\lambda \rightarrow \infty} [\mathbf{J}(\mathbf{R}_\lambda) - \mathbf{N}(\mathbf{R}_\lambda) \mathbf{R}^{J S \Pi}] \mathbf{C}^{J S \Pi} \quad (10.3)$$

where \mathbf{J} and \mathbf{N} are diagonal matrices and $\mathbf{R}^{J S \Pi}$ is the reactance matrix for partial wave J , spin S , and parity Π . The diagonal matrix $\mathbf{C}^{J S \Pi}$ is a square matrix whose row and column is spanned by the quantum number $(nl_1 l_2)$ and is given by

$$C_{nl_1 l_2}(R_\lambda) = \begin{cases} \cos(k_n R_\lambda - l_2 \pi / 2) & \text{for open channels} \\ \exp(-|k_n| R_\lambda) & \text{for closed channels.} \end{cases} \quad (10.4)$$

where k_n is the channel wave number given by

$$k_n = \frac{1}{\hbar} [2\mu(E - E_n)]^{\frac{1}{2}} \quad (10.5)$$

The open channel elements of \mathbf{J} and \mathbf{N} are given by

$$\begin{bmatrix} \mathbf{J}(\mathbf{R}_\lambda) \\ \mathbf{N}(\mathbf{R}_\lambda) \end{bmatrix}_{n\bar{l}_1\bar{l}_2}^{n\bar{l}_1\bar{l}_2} = \delta_{n\bar{l}_1\bar{l}_2} v_n^{-\frac{1}{2}}(k_n R_\lambda) \begin{bmatrix} j_{l_2}(k_n R_\lambda) \\ y_{l_2}(k_n R_\lambda) \end{bmatrix} \quad (10.6)$$

where j_{l_2} and y_{l_2} are spherical Bessel functions[24], v_n is the channel velocity $\hbar |k_n| / \mu$. The closed channel elements of \mathbf{J} and \mathbf{N} are given by

$$\begin{bmatrix} \mathbf{J}(\mathbf{R}_\lambda) \\ \mathbf{N}(\mathbf{R}_\lambda) \end{bmatrix}_{n\bar{l}_1\bar{l}_2}^{n\bar{l}_1\bar{l}_2} = \delta_{n\bar{l}_1\bar{l}_2} v_n^{-\frac{1}{2}}(\kappa_n R_\lambda) \begin{bmatrix} i_{l_2}(\kappa_n R_\lambda) \\ k_{l_2}(\kappa_n R_\lambda) \end{bmatrix} \quad (10.7)$$

where $i_{l_2}(z)$ and $k_{l_2}(z)$ are modified spherical Bessel functions of the first and third kinds, and $\kappa_n = |k_n|$.

The open-open part of the reactance matrix $\mathbf{R}_{\text{oo}}^{\text{JSII}}$ is real and symmetric in an exact calculation. The amount of asymmetry in the actual open-open part of reactance matrix can be used to be a measure of error in the calculation. The open-open part of the scattering matrix $\mathbf{S}_{\text{oo}}^{\text{JSII}}$ is obtained from reactance matrix using the relationship[25]

$$\mathbf{S}_{\text{oo}}^{\text{JSII}} = \frac{\mathbf{I} + i\mathbf{R}_{\text{oo}}^{\text{JSII}}}{\mathbf{I} - i\mathbf{R}_{\text{oo}}^{\text{JSII}}} \quad (10.8)$$

The open-open part of scattering matrix is both symmetric and unitary due to time reversal invariance of the Schrödinger equation[26].

In order to determine $\mathbf{R}_{\text{oo}}^{\text{JSII}}$ we need to project the basis from surface functions to asymptotic solutions. Since the latter is expressed in terms of the distances R_λ and the former in terms of the hyperradius ρ , we must perform a transformation of variables to a common one. This transformation is accomplished by combining equation (7.13), (10.3) and integrate over the full range of the four angles $(\theta_1, \varphi_1, \theta_2, \varphi_2)$, but over ω_λ from 0 to $\pi/2$ only. It is important that this

integration not be carried over the whole range of $\omega_l l$. The reason is that the hydrogen atom bound states, $R_{n l_1}(r_\lambda)$ are defined in one channel only, which can be considered to be separated from the other channel by the $\omega_\lambda = \pi/2$ boundary.

The resulting expression is:

$$\begin{aligned} \rho^{-\frac{5}{2}} b^{J S \Pi i'} = & \sum_{l_2' l_1' p'} a_{l_2' l_1' p'}^{J S \Pi i} \sum_{n l_1 l_2} \sum_{\bar{n} \bar{l}_1 \bar{l}_2} \int F^{J S \Pi n l_1 l_2}_{l_2' l_1' p'}(\omega_\lambda, \gamma; \bar{\rho}) \frac{1}{R_\lambda} [J_{n l_1 l_2}^{\bar{n} \bar{l}_1 \bar{l}_2}(R_\lambda) \\ & - \sum_{\hat{n} \hat{l}_1 \hat{l}_2} N_{n l_1 l_2}^{\hat{n} \hat{l}_1 \hat{l}_2}(R_\lambda) \mathbf{R}^{J S \Pi \bar{n} \bar{l}_1 \bar{l}_2}_{\hat{n} \hat{l}_1 \hat{l}_2}] \sin^2 \omega_\lambda d\omega_\lambda \times C_{\bar{n} \bar{l}_1 \bar{l}_2}^{J S \Pi i'} \end{aligned} \quad (10.9)$$

where we define

$$F^{J S \Pi n l_1 l_2}_{l_2' l_1' p'} = 2 \int \Theta_{l_2' l_1' p'}^{J M S \Pi}(\omega_l l, 4 \text{ angles}; \bar{\rho}) \Phi_{n l_1 l_2}^{J M \Pi}(r_\lambda, 4 \text{ angles}) d(4 \text{ angles}) \quad (10.10)$$

The corresponding expression for the derivative of $\mathbf{b}^{J S \Pi}$ with respect to ρ is:

$$\begin{aligned} \frac{d\mathbf{b}^{J S \Pi}}{d\rho} = & \frac{3}{2\rho} \mathbf{b}^{J S \Pi} + \rho^{\frac{3}{2}} \mathbf{a}^{J S \Pi} \int \frac{\partial F^{J S \Pi}}{\partial \rho} (\mathbf{J} - \mathbf{N} \mathbf{R}^{J S \Pi}) \frac{\sin^2 \omega_\lambda}{\cos \frac{\omega_\lambda}{2}} d\omega_\lambda \mathbf{C}^{J S \Pi} \\ & + \rho^{\frac{3}{2}} \mathbf{a}^{J S \Pi} \int \mathbf{F}^{J S \Pi} \left(\frac{\partial \mathbf{J}}{\partial \rho} - \frac{\partial \mathbf{N}}{\partial \rho} \mathbf{R}^{J S \Pi} \right) \frac{\sin^2 \omega_\lambda}{\cos \frac{\omega_\lambda}{2}} d\omega_\lambda \mathbf{C}^{J S \Pi} \end{aligned} \quad (10.11)$$

In matrix form, equation (10.10) and (10.11) can be rewritten as

$$\mathbf{b}^{J S \Pi} = \rho^{\frac{3}{2}} \mathbf{a}^{J S \Pi} (\mathbf{A}_1^{J S \Pi} - \mathbf{B}_1^{J S \Pi} \mathbf{R}^{J S \Pi}) \mathbf{C}^{J S \Pi} \quad (10.12)$$

$$\frac{d\mathbf{b}^{J S \Pi}}{d\rho} = \frac{3}{2\rho} \mathbf{b}^{J S \Pi} + \rho^{\frac{3}{2}} \mathbf{a}^{J S \Pi} (\mathbf{A}_2^{J S \Pi} - \mathbf{B}_2^{J S \Pi} \mathbf{R}^{J S \Pi}) \mathbf{C}^{J S \Pi} \quad (10.13)$$

where the following matrices are defined

$$\begin{bmatrix} \mathbf{A}_1^{J S \Pi} \\ \mathbf{B}_1^{J S \Pi} \end{bmatrix} = \int \mathbf{F}^{J S \Pi}(\omega_\lambda, \gamma) \begin{bmatrix} \mathbf{J}(\mathbf{R}_\lambda) \\ \mathbf{N}(\mathbf{R}_\lambda) \end{bmatrix} \frac{\sin^2 \omega_\lambda}{\cos \frac{\omega_\lambda}{2}} d\omega_\lambda \quad (10.14)$$

$$\begin{aligned} \begin{bmatrix} \mathbf{A}_2^{J S \Pi} \\ \mathbf{B}_2^{J S \Pi} \end{bmatrix} = & \int \left[\left(\frac{\partial \mathbf{F}^{J S \Pi}(\omega_\lambda, \gamma)}{\partial \rho} \right)_{\omega_\lambda} \begin{bmatrix} \mathbf{J}(\mathbf{R}_\lambda) \\ \mathbf{N}(\mathbf{R}_\lambda) \end{bmatrix} \right. \\ & \left. + \mathbf{F}^{J S \Pi}(\omega_\lambda, \gamma) \begin{bmatrix} \partial \mathbf{J}(\mathbf{R}_\lambda) / \partial \rho \\ \partial \mathbf{N}(\mathbf{R}_\lambda) / \partial \rho \end{bmatrix} \right] \frac{\sin^2 \omega_\lambda}{\cos \frac{\omega_\lambda}{2}} d\omega_\lambda \end{aligned} \quad (10.15)$$

Forming the logarithmic derivative from equation (9.1), we eliminate $\mathbf{C}^{JS\Pi}$ and solve for the R-matrix:

$$\begin{aligned} \mathbf{R}^{JS\Pi} = & \left[\left(\frac{db^{JS\Pi}}{d\rho} b^{JS\Pi-1} - \frac{3}{2\rho} I \right) a^{JS\Pi} B_1^{JS\Pi} - a^{JS\Pi} B_2^{JS\Pi} \right]^{-1} \\ & \times \left[\left(\frac{db^{JS\Pi}}{d\rho} b^{JS\Pi-1} - \frac{3}{2\rho} I \right) a^{JS\Pi} A_1^{JS\Pi} - a^{JS\Pi} A_2^{JS\Pi} \right] \end{aligned} \quad (10.16)$$

The scattering matrix can be calculated from equation (10.8).

11. Asymptotic Analysis - Differential and Integral Cross Sections

In the space-fixed representation, the asymptotic form of the physical scattering wavefunctions are given by:

$$\begin{aligned} \Psi^{\lambda'n'l_1'm'_1} \sim & \sum_{\lambda n l_1 m_1} [\delta_{\lambda n l_1 m_1}^{\lambda'n'l_1'm'_1} e^{ik_{n'}z_\lambda} + f_{\lambda n l_1 m_1}^{\lambda'n'l_1'm'_1}(\theta_1, \varphi_1) \\ & \frac{e^{ik_{\lambda n l_1 m_1} R_\lambda}}{R_\lambda}] \frac{R_{\lambda n l_1 m_1}(r_\lambda)}{r_\lambda} Y_{l_2 m_2}(\theta_2, \varphi_2) \end{aligned} \quad (11.1)$$

The axis of quantization for m'_1 is the direction of the initial wave-number vector k_n which has been chosen to lie along the space-fixed Oz axis. The component of R_λ along that axis is z_λ .

We can define the transition matrix from the open-open sub-block of the scattering matrix as

$$\mathbf{T}^{JS\Pi} = \mathbf{I} - \mathbf{S}_{oo}^{JS\Pi} \quad (11.2)$$

With this definition and equation (10.1) through (10.16), the scattering amplitude can be obtained as the following:

$$\begin{aligned} f_{n l_1 m_1}^{n' l_1' m'_1} = & \sum_{\Pi l_2 l_2'} \left(\frac{v_{n'}}{v_n} \right)^{\frac{1}{2}} \left(\frac{i^{1+l_2'-l_2}}{k_{n'}} \right) e^{i(m'_1-m_1)\varphi} \sqrt{\frac{2l_2'+1}{2}} \mathcal{P}_{l_2}^{m'_1-m_1}(\theta) \\ & \sum_J T_{n l_1 l_2}^{JS\Pi n' l_1' l_2'} C(l_1' l_2' J; m'_1 0 m'_1) C(l_1 l_2 J; m_1 m'_1 - m_1 m'_1) \end{aligned} \quad (11.3)$$

The space-fixed Pauli antisymmetrized differential cross section σ^S is found from the scattering amplitude, and is independent of the angle φ :

$$\begin{aligned}\sigma_{nl_1m_1}^{Sn'l_1'm'_1} &= \frac{v_n}{v_{n'}} |f_{nl_1m_1}^{Sn'l_1'm'_1}(\hat{\mathbf{R}})|^2 \\ &= \frac{1}{2k_{n'}^2} \left| \sum_{\Pi l_2 l_2'} i^{l_2' - l_2} \mathcal{P}_{l_2}^{m'_1 - m_1}(\theta) (2l_2' + 1)^{\frac{1}{2}} T_{oo}^{S\Pi nl_1m_1l_2m_2} \right|^2\end{aligned}\quad (11.3)$$

where $T_{nl_1m_1l_2m_2}^{S\Pi n'l_1'm'_1l_2'm'_2}$ is defined as

$$T_{nl_1m_1l_2m_2}^{S\Pi n'l_1'm'_1l_2'm'_2} = \delta_{m'_2}^0 \sum_J C(l_1'l_2'J; m'_1 0 m'_1) C(l_1l_2J; m_1 m_2 m'_1) T_{nl_1l_2}^{JS\Pi n'l_1'l_2'}\quad (11.4)$$

These functions are zero for $\theta = 0, \pi$ except if $m = 0$, which leads to the selection rule $m'_1 = m_1$ for non-zero scattering in those directions.

To obtain the integral cross section we integrate over $d\hat{\mathbf{R}}$ and can be written

$$\begin{aligned}Q_{nl_1m_1}^{n'l_1'm'_1} &= \frac{\pi}{k_{n'}^2} \sum_{\Pi l_2' l_2''} \sqrt{(2l_2' + 1)(2l_2'' + 1)} i^{l_2' - l_2''} \\ &\quad \times [(T_{oo}^{\Pi n'l_1'm'_1})^\dagger (T_{oo}^{\Pi n'l_1'm'_1})]_{l_2'}^{l_2''}\end{aligned}\quad (11.5)$$

where we have indicated in square brackets the multiplication of a sub-block of T-matrix with its adjont.

The summed and averaged cross section with respect to the magnetic quantum numbers m_1 and m'_2 can be calculated from

$$Q_{nl_1}^{n'l_1'} = \frac{1}{(2l_1' + 1)} \sum_{m_1} \sum_{m'_1} Q_{nl_1m_1}^{n'l_1'm'_1}\quad (11.6)$$

Summary

We have presented the theory using the hyperspherical coordinate formulation for electron-hydrogen elastic and inelastic scattering using local surface functions.

This method can in principle be extended to energies above the ionization threshold by including hyperspherical harmonics in the surface function basis set. This approach is very promising and should lead to a very complete description of the electron-hydrogen scattering processes.

REFERENCES

- [1] U. Fano, *Rep. Prog. Phys.* **46** (1983) 97.
- [2] H. R. J. Walters *Phys. Rep.* **116** (1984) 1.
- [3] P. G. Burke, S. Ormonde, and W. Whitaker, *Proc. Phys. Soc.* **92** (1967) 319.
- [4] P. G. Burke and H. Schey, *Phys. Rev.* **126** (1962) 147.
- [5] P. G. Burke and A. J. Taylor, *Proc. Phys. Soc.* **88** (1966) 549.
- [6] S. Geltman and P. G. Burke, *J. Phys. B* **3** (1970) 1062.
- [7] J. F. Williams, *J. Phys. B* **9** (1976) 1519.
- [8] J. Callaway, *Phys. Rep.* **45** (1978) 89.
- [9] R. K. Nesbet, *Phys. Rev.* **179** (1969) 60.
- [10] R. K. Nesbet and R. S. Oberoi, *Phys. Rev. A* **6** (1972) 855.
- [11] J. Macek, *J. Phys. B* **1** (1968) 831.
- [12] D. M. Hood and A. Kuppermann in: *The Theory of Chemical Reaction Dynamics*, ed. by D. C. Clary (D. Reidel Publishing Co.) p. 193.
- [13] A. Kuppermann, *Chem. Phys. Lett.* **32** (1975) 374;
R. T. Lin and A. Kuppermann, in: *Electronic and Atomic Collisions, Abstracts of Papers of the 9th International Conference on the Physics of Electronic and Atomic Collisions, Seattle, Washington, 24-30 July 1975*, eds. J. S. Risley and R. Geballe (University of Washington Press, Seattle, 1975) pp. 353-354.
- [14] A. Kuppermann and P. G. Hipes, *J. Chem. Phys.* **84** (1986) 5962.
- [15] P. G. Hipes and A. Kuppermann, *Chem. Phys. Lett* **133** (1987) 1.
- [16] S. A. Cuccaro, P. G. Hipes and A. Kuppermann, *Chem. Phys. Lett.* **154** (1989) 155.
- [17] S. A. Cuccaro, P. G. Hipes and A. Kuppermann, *Chem. Phys. Lett.* **157** (1989) 440.
- [18] L. M. Delves. *Nucl. Phys.*, **9** (1959) 3091; **20** (1960) 275.

- [19] M. E. Rose, *Elementary Theory of Angular Momentum*, (Wiley, New York, 1957), Chap. 2.
- [20] H. Klar, *J. Phys. B.* **7** (1974) 1436.
- [21] G. C. Schatz and A. Kuppermann, *J. Chem. Phys.* **65** (1976) 4642.
- [22] R. T. Pack, *J. Chem. Phys.* **60** (1974) 633.
- [23] B. R. Johnson, *J. Compl. Phys.* **13** (1973) 445;
B. R. Johnson, *J. Chem. Phys.* **67** (1977) 4086;
B. R. Johnson, NRCC Workshop, Lawrence Berkeley Laboratory, Report No. LBL 9501 (1979).
- [24] Handbook of Mathematical Functions, edited by M. Abramowitz and I. A. Stegun (National Bureau of Standards, Washington, D. C., 1964).
- [25] N. S. F. Mott and H. S. W. Massey, *The Theory of Atomic Collisions* (Clarendon, Oxford, 1965), 3rd ed., Ch. 14, 15.
- [26] A. M. Lane and R. G. Thomas, *Rev. Mod. Phys.* **30** (1958) 257.

FIGURE CAPTIONS

Figure 1. Potential contours for the electron-hydrogen reaction in the $OX_\lambda Y_\lambda Z_\lambda$ space having spherical coordinates $\rho = (r_\lambda^2 + R_\lambda^2)^{\frac{1}{2}}$, $\omega_\lambda = 2\arctan r_\lambda/R_\lambda$ and γ_λ , for $\gamma_\lambda = 0$ to 180° for $Z_\lambda = 0$ bohr.

Figure 2. Potential contours for the electron-hydrogen reaction for $\gamma_\lambda = 0^\circ$.

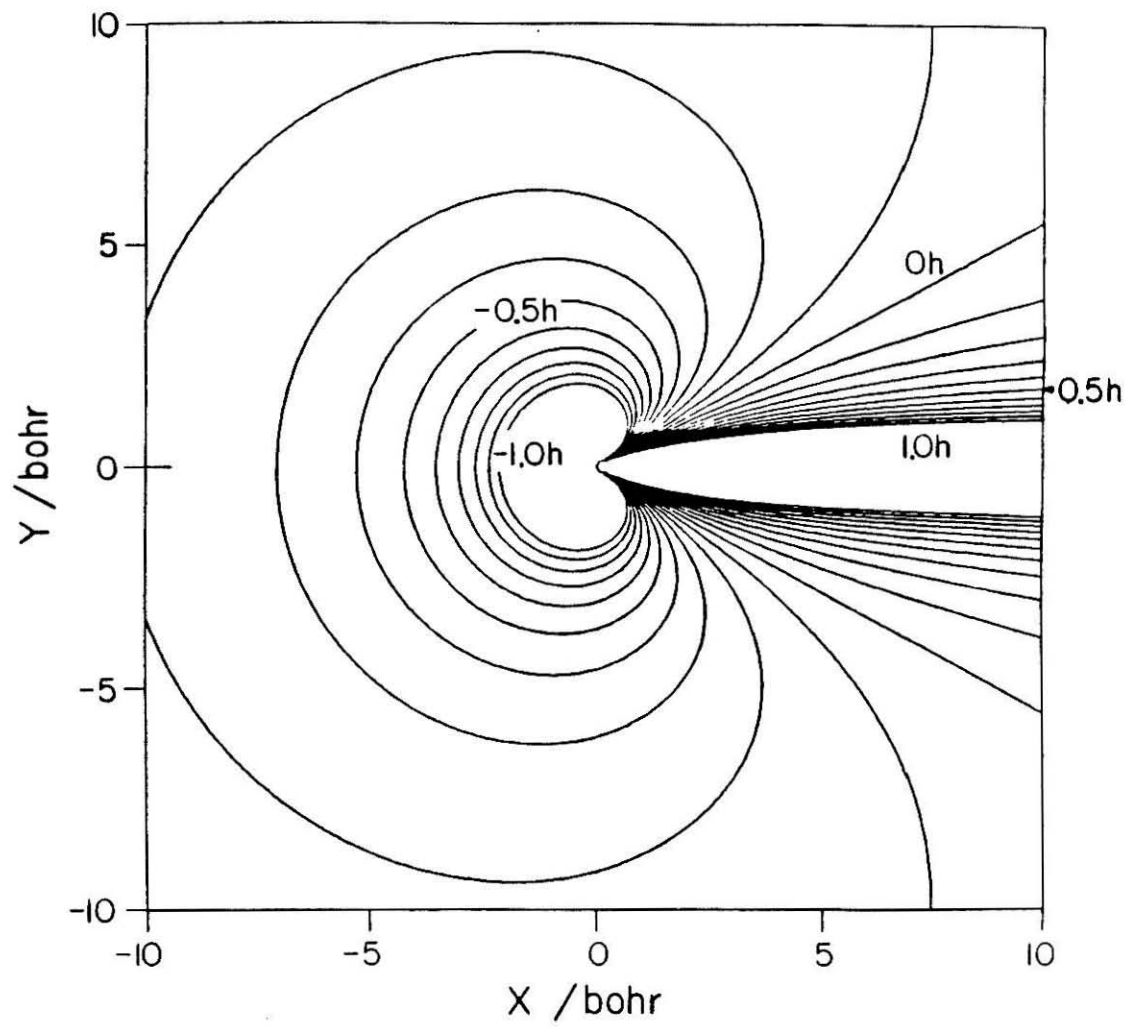


Figure 1

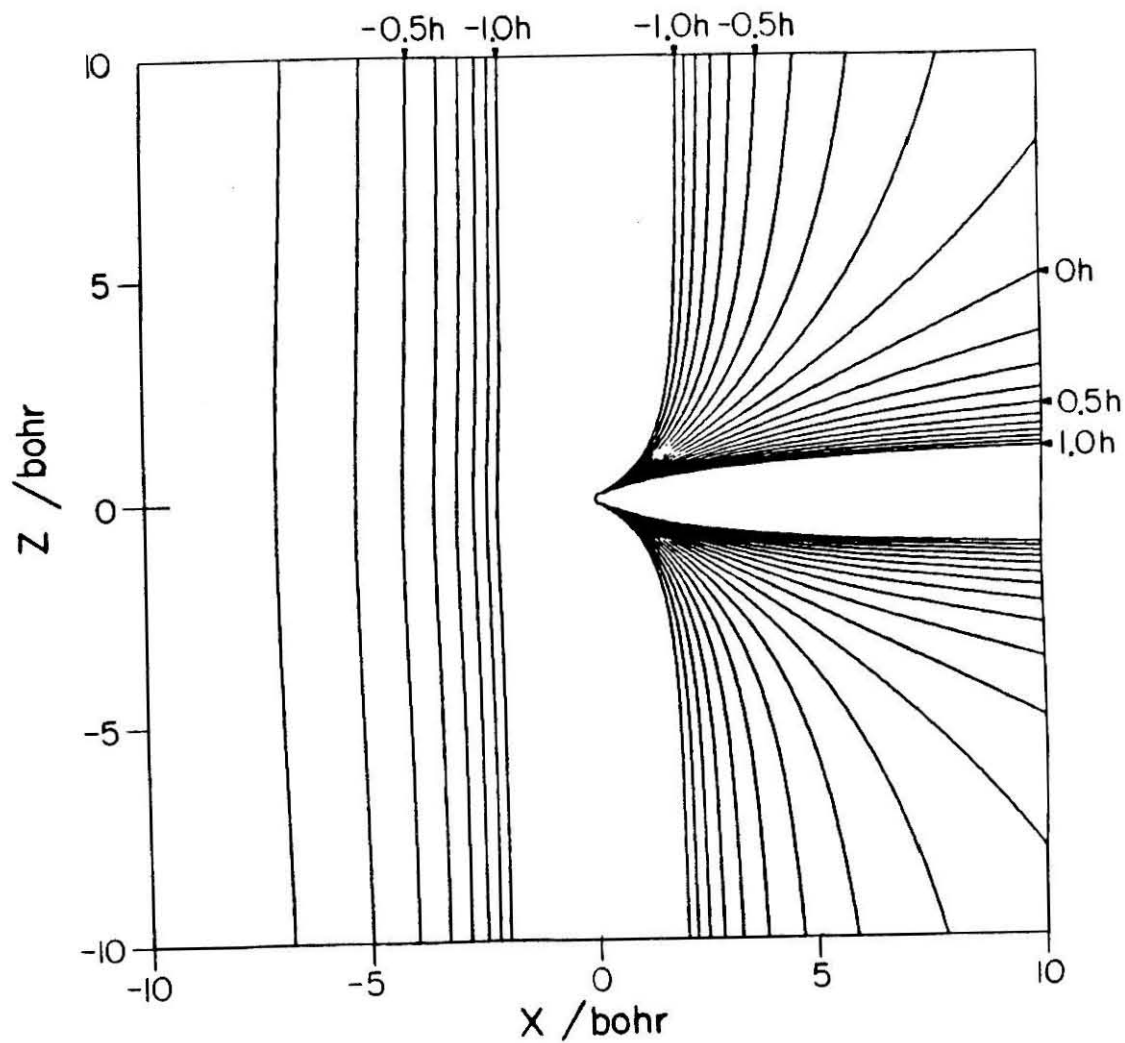


Figure 2

Chapter VIII

Quantum Mechanical Streamlines of Probability Current Density and Tunneling Fractions for Collinear Atom-Diatom Reactions Using Hyperspherical Coordinates

**Quantum Mechanical Streamlines of Probability Current Density
and Tunneling Fractions for Collinear Atom-Diatom Reactions
Using Hyperspherical Coordinates**

Yi-Shuen Mark Wu ¹ and Aron Kuppermann

Arthur Amos Noyes Laboratory of Chemical Physics

Division of Chemistry and Chemical Engineering ²

California Institute of Technology

Pasadena, CA 91125, USA

ABSTRACT

We have developed a procedure to generate physical wave functions from hyperspherical coordinate coupled channel calculations of collinear atom-diatomic molecule collisions. Using the wave functions generated, we calculate the corresponding probability density, probability current density vector fields, and the associate streamlines and tunneling fractions. The streamlines of probability current density provide a pictorial way of obtaining information about scattering processes which is not otherwise obtainable. Special attention is given to the formation of vortices which appear in the streamlines. By examining the variations of the streamlines, one can see what portions of the potential energy surface are most sampled in the reaction and it also helps us to locate the dynamical resonances on the surface. These vortices in the streamlines provide a visual explanation of why the collision cross sections do not agree with the classical expectations. Both the formal and numerical aspects of the present method are discussed in detail. These calculations are very useful in examining various models for chemical reactions and in testing absolute reaction rate theory.

¹ Work performed in partial fulfillment of the requirements for the Ph.D. degree in Chemistry at the California Institute of Technology.

² Contribution number xxxx

1. INTRODUCTION

The emphasis in reactive scattering calculations is usually on quantities which can be observed experimentally, e.g. cross-sections, branching ratios, rate constants, etc. These quantities, which are the results of the chemical reaction after it has occurred, are not all that one wishes to know about chemical reactions. In addition, one would like to know how a chemical reaction occurs.

Classical trajectory[1] calculations allow one to see physically what sort of relative motion leads to chemical reaction and the importance of multiple crossings of the barrier to reaction, which is important for the application of classical transition state theory[2]. However, classical trajectory calculations do not aid in the understanding of the important quantum mechanical effects, such as dynamical resonances and tunneling. The complete characterization of a chemical reaction, which includes the asymptotic observables as well as information about the transition region, is contained in a quantal calculation of the chemical reaction. However, only a small amount of information can be extracted. The additional information can be obtained by using the wavefunction generated in the course of quantum mechanical scattering calculations to determine the corresponding probability density, probability current density vector field and the associated streamlines. By examining the variations of streamlines, one can see which portions of the potential energy surface are most sampled in the reaction as well as locate the resonances on the surface. In addition, one can also extract quantitatively the extent of tunneling. In this manner, streamline calculations demonstrate, in a way which is intuitively clear, the various features of the reaction probability versus energy curve which might provide insight towards new mathematical and physical approximations.

Such calculations have been performed by a number of researchers. Among these, Mortensen and Pitzer[3] presented figures of the collinear $\text{H} + \text{H}_2$ reaction probability density at the total energy of 10 Kcal/mole. Hirschfelder[4] and coworkers use various simple model systems to examine the streamlines of the probability current density vector field. McCullough and Wyatt have made a much more extensive investigation for the collinear $\text{H} + \text{H}_2$ [5] and $\text{F} + \text{H}_2$ [6] reactions and the three-dimensional ($J = 0$) $\text{F} + \text{H}_2$ [7] reaction. From a plot of the flux map they found a vortex formation which they named "the quantum whirlpool effect". Similar observations have been made by Kuppermann, Adams and Truhlar[8].

The mathematics used in streamline calculations is simple, but the scattering wavefunctions generated during the scattering calculations have had serious limitations. The methods previously developed for studying collinear processes are restricted to energies significantly below that of breakup collisions. In addition, they do not efficiently permit us to study for systems in which the central atom is significantly lighter than the end atoms, such as the $\text{I} + \text{HI} \rightarrow \text{IH} + \text{I}$ reaction. With the use of hyperspherical coordinates, developed by Kuppermann, Kaye and Dwyer[9,10], and also by Römelt, Hauke and Manz[11,12] independently, such reactions can now be easily studied.

In this paper, we have developed a formalism to extract the scattering wavefunction from the hyperspherical formulation so that the probability current density field can be calculated. We will briefly review the hyperspherical coordinate method first and outline the theory necessary for this approach. The numerical aspects of its implementation will then be discussed. Finally, applying this method we have computed and displayed streamlines for the collinear $\text{H} + \text{H}_2$ reaction at several values of the total energy which span the energy range where the reaction probabilities have been calculated.

2. Hyperspherical Coordinate in Quantum Mechanical Collinear Reactive Scattering

The detailed formulation of collinear reactive scattering based on hyperspherical coordinates is discussed elsewhere[9,10]. We present a very brief review here for the sake of completeness.

The fundamental idea of the hyperspherical coordinates approach to the collinear reactive atom-diatomic molecule scattering problems is simple. Triatomic exchange reactions are of the type $A + BC \rightarrow AB + C$, with A, B, and C representing atoms confined to move on a laboratory-fixed straight line. The two coordinates necessary to describe the system are the hyperradius ρ and the hyperangle ω , which are defined as

$$\rho = (R_\alpha^2 + r_\alpha^2)^{\frac{1}{2}} \quad (1)$$

$$\omega_\alpha = \tan^{-1}\left(\frac{r_\alpha}{R_\alpha}\right) \quad (2)$$

where R_α, r_α are, respectively, the Delves[13] mass scaled BC internuclear distance and the distance of atom A to the center of mass of the BC molecule.

The nuclear motion Hamiltonian in these coordinates is

$$H(\rho, \omega) = -\frac{\hbar^2}{2\mu} \left[\frac{\partial^2}{\partial \rho^2} + \frac{1}{\rho} \frac{\partial}{\partial \rho} + \frac{1}{\rho^2} \frac{\partial^2}{\partial \omega^2} \right] + V(\rho, \omega). \quad (3)$$

The wavefunction is expanded in terms of the basis set $\phi_i(\omega; \bar{\rho})$, which is obtained by solving equation (3) at a fix value of $\rho = \bar{\rho}$ that cuts through the potential and is given by

$$\Psi_n(\rho, \omega) = \rho^{-\frac{1}{2}} \sum_{n'=0}^N g_{n'n}(\rho; \bar{\rho}) \phi_{n'}(\omega; \bar{\rho}) \quad (4)$$

where the radial wave functions $g_{n'n}(\rho; \bar{\rho})$ are solutions of the differential equation,

$$-\frac{\hbar^2}{2\mu} \frac{d^2 \mathbf{g}(\rho; \bar{\rho})}{d\rho^2} + \mathbf{W}(\rho; \bar{\rho}) \mathbf{g}(\rho; \bar{\rho}) = \mathbf{E}(\rho; \bar{\rho}) \mathbf{g}(\rho; \bar{\rho}). \quad (5)$$

The matrix elements \mathbf{W} and \mathbf{E} are given by the expression

$$\mathbf{W}_{n'n}^n(\rho; \bar{\rho}) = \langle n | V(\rho, \omega) - \frac{\bar{\rho}^2}{\rho^2} V(\omega; \bar{\rho}) | n' \rangle \quad (6)$$

$$\mathbf{E}_{n'n}^n(\rho, \bar{\rho}) = [E + \frac{\hbar^2}{8\mu\rho^2} - E_n(\bar{\rho})] \delta_{n'n}^n, \quad (7)$$

where $|n'\rangle = \phi_{n'}(\omega; \bar{\rho})$, $E_n(\bar{\rho})$ is the eigenvalue of $\phi_n(\omega; \bar{\rho})$, E is the total energy of the system, and $\delta_{n'n}^n$ is the Kronecker symbol.

In solving the differential equation (5), one starts at a value of ρ which is sufficiently small that all eigenvalues E_n are much greater than the total energy E . To a very good approximation, we may take our initial condition to be $\mathbf{g}(\bar{\rho}_0) = \mathbf{0}$, $\mathbf{g}'(\bar{\rho}_0) = \mathbf{I}$ and the differential equation is integrated from $\bar{\rho}_0$ to $\bar{\rho}_{\max}$, where $\bar{\rho}_{\max}$ must be far away from the strong interaction region. At that point, the wavefunctions Ψ_n are numerically projected onto the bound state eigenfunction of the diatomic molecule. From the coefficients of this projection the reaction (\mathbf{R}), scattering (\mathbf{S}), and probability (\mathbf{P}) matrices are determined.

The asymptotic physical scattering wavefunction can be written as

$$\Psi_{\text{phys}}^{\lambda' n'_\lambda} \sim \sum_{\lambda n_\lambda} [\delta_{\lambda n_\lambda}^{\lambda' n'_\lambda} e^{-ik_{\lambda n_\lambda} R_\lambda} + f_{\lambda n_\lambda}^{\lambda' n'_\lambda} e^{ik_{\lambda n_\lambda} R_\lambda}] \phi_{\lambda n_\lambda}(r_\lambda) \quad (8)$$

where r_λ is the internal coordinate of the diatomic molecule in the λ channel, $\lambda' n'_\lambda$ denotes the initial state of the reagents and $k_{\lambda n_\lambda}$ is the wave number of the asymptotic wavefunction for state n of the diatomic molecule defined by

$$k_{\lambda n_\lambda} = \hbar^{-1} [2\mu(E - E_{\lambda n_\lambda})]^{1/2}. \quad (9)$$

The f (scattering amplitude) and S matrix elements are related in the following way

$$f_{\lambda n_\lambda}^{\lambda' n_{\lambda'}} = \left(\frac{v_{\lambda' n_{\lambda'}}}{v_{\lambda n_\lambda}} \right)^{1/2} S_{\lambda n_\lambda}^{\lambda' n_{\lambda'}} \quad (10)$$

where $v_{\lambda n_\lambda}$ is the channel velocity $\hbar |k_{\lambda n_\lambda}| / \mu$.

3. Generating the Physical Wavefunction

In order to study the streamlines of the probability current density, one must obtain adequate wavefunctions at a large number of points along the potential energy surface. A crucial point that should be made here is that the wavefunctions generated in the course of integrating equation (5) do not correspond to the physical wavefunctions we want. In order to maintain the linear independence of the radial wavefunction being integrated, the numerical integrator which was developed by Gordon[14] has to perform some sort of stabilizing transformation to prevent the exponential growth associated with the closed channels. These transformations will alter the wavefunctions during the integration. The stabilizing process used in the hyperspherical coordinate method is the so-called reorthogonalization method developed by Riley and Kuppermann[15]. Therefore, the major difficulties in constructing physical wavefunctions for the calculation of probability current density vector fields are purely numerical in origin. Therefore, to actually generate consistent physical wavefunctiond we need to undo the stabilizing transformations performed on the radial wavefunction.

In principle, any choice of initially linear independent sets of solutions should lead to the same scattering wavefunctions. When we get to the asymptotic region we can form linear combinations of these solution and one of these combinations will be associated to the solution we are interested in. Sometimes this is difficult

to achieve because when we start we do not know exactly how to pick the initial values. However, it is very easy to pick up a linearly independent set of initial values and any set we choose will be in general a random mixture of all solutions. When we integrate toward large ρ , each set will contain some contribution from the most rapidly growing solution. If the small components become insignificant compared to the large component, then those solutions are all essentially the same and taking linear combination of them is useless for constructing the solutions. However, this apparent instability can be completely eliminated by simply back-integrating the solutions.

Since we are interested in the wavefunction in the strong interaction region rather than in the asymptotic region, one can force the wavefunction to be consistent with respect to the beginning of the integration. We first do the scattering calculations with the stabilizing transformation and obtain the \mathbf{S} matrix as accurately as possible. From equation (8), we can use \mathbf{S} matrix to construct the physical wavefunctions along the asymptotic region. Then we start again integrating at large ρ and integrate toward small ρ without performing any stabilizing steps. All the initial starting values we choose have the exact linear combinations associated to the scattering solutions. Therefore, if the integrator worked well, the consistent wavefunction generated in the course of integration will decay to zero or to insignificantly small values near the origin.

Mathematically, the physical wavefunction Ψ_n^{phys} can be calculated by taking the linear combination of the Ψ_n obtained from integrating equation (4). In other words, we want to determine the coefficient matrix \mathbf{W} , where

$$\Psi_n^{\text{phys}}(\rho, \omega) = \sum_{n'=1}^N \Psi_{n'}(\rho, \omega) \mathbf{W}_{n'n}, \quad 1 \leq n \leq N_{\text{open}} \leq N \quad (11)$$

where N is the total number of basis determined and N_{open} is the number of asymptotically open vibrational states. This procedure is discussed in detail in Appendix A.

In a series of calculations performed on the well-studied collinear $\text{H} + \text{H}_2$ reaction, we found in all cases the numerical integrator successfully reached to nonclassical region without difficulties. Another advantage of this method is that the integrator can generate the wavefunction and its first derivatives simultaneously which can be saved for future calculations.

4. Quantum Mechanical Streamline and Tunneling Fraction

The description of the motion of a fluid in hydrodynamics requires a knowledge of the vector field[16]. The vector field describes the direction of motion of a fluid particle and the magnitude of its velocity in that direction at any time t . The fluid particle is a differential element of the fluid. Equivalently, we can use the current density vector field defined by[17]

$$\mathbf{j}^{\lambda n_\lambda} = \frac{\hbar}{2\mu i} [\Psi_{\text{phys}}^{\lambda n_\lambda*} \nabla \Psi_{\text{phys}}^{\lambda n_\lambda} - \Psi_{\text{phys}}^{\lambda n_\lambda} (\nabla \Psi_{\text{phys}}^{\lambda n_\lambda})^*] \quad (12)$$

where $\mathbf{j}^{\lambda n_\lambda}$ is the current density vector and $\Psi^{\lambda n_\lambda}$ is the physical wave function.

The streamlines of $\mathbf{j}^{\lambda n_\lambda}$ are defined as curves in configuration space which at every point $P(R_\lambda, r_\lambda)$ in that space are tangent to the $\mathbf{j}^{\lambda n_\lambda}$ vector at that point. Thus, the equation of motion[18] for the fluid particle analogy to

$$\frac{dR_\lambda}{\mathbf{j}_{\hat{R}_\lambda}^{\lambda n_\lambda}} = \frac{dr_\lambda}{\mathbf{j}_{\hat{r}_\lambda}^{\lambda n_\lambda}} \quad (13)$$

where $\mathbf{j}_{\hat{R}_\lambda}$ and $\mathbf{j}_{\hat{r}_\lambda}$ are the current density vector components for each axis. A streamline is a particular solution to the set of differential equations.

Typical quantum mechanical streamlines and profiles of the component of \mathbf{j} normal to various straight line cuts along the current density field for the collinear $\text{H} + \text{H}_2$ reaction on the LSTH surface[18-20] are displayed, respectively, in Figures 1 and 2. The streamlines are broken up into a series of curve arrows which by definition are everywhere tangent to the probability current density vector $\mathbf{j}^{\lambda n \lambda}$. The length of the arrows are proportional to the magnitude of $\mathbf{j}^{\lambda n \lambda}$ evaluated at its center.

In order to display the relationship between the streamlines and the surface, the streamline plots are superimposed on a contour diagram of the potential energy surface. The solid lines are equipotentials, whose energies in eV, measured with respect to the bottom of the H_2 well, are designated on the plot. The 0.43 eV equipotentials are the two curves labelled E in the figure and correspond to the energy of the calculation. Any classical trajectory at this energy will have to be confined to the region of configuration space between these two equipotentials. The minimum energy path is marked by a dashed line, the saddle point is indicated by a cross.

The streamline plots have some interesting properties which result directly from the principle of conservation expressed by the continuity equation. Because the wavefunction is everywhere single valued and continuous, the streamlines will not cross each other. In addition, by applying the divergence theorem, for any closed contour, C, which encircle the reaction zone, the integral

$$\int_A \nabla \cdot \mathbf{j}^{\lambda n \lambda} dA = \oint_C \mathbf{j}^{\lambda n \lambda} dl = 0 \quad (14)$$

vanishes. A is the area inclosed by the contour C, dl is the boundary line element. This is a consequence that the probability is neither created nor destroyed in the chemical reaction. Therefore, the normal flux of $\mathbf{j}^{\lambda n \lambda}$ through a line segment connecting any two streamlines is independent of the shape of this segment or

where it is placed. It depends only on which two streamlines it connects. In other words, we can say that each streamline carries with it an element of flux.

It is then straightforward to show that for chemical reactions, in which the breakup channel is energetically closed, a given line segment L_{12} which lies in the steep repulsive region of the configuration space at one end and the other end lies in the plateau region, the total flux $Q^{\lambda n_\lambda}$ through L_{12} is equal to

$$J^{\lambda n_\lambda} = \int_{L_{12}} \mathbf{j}^{\lambda n_\lambda} \cdot d\mathbf{l} = P^{\lambda n_\lambda} \cdot Q_{\text{inc}}^{\lambda n_\lambda} \quad (15)$$

where $P^{\lambda n_\lambda}$ is the total reaction probability and $Q_{\text{inc}}^{\lambda n_\lambda}$ is the incident flux.

Thus, we can define the current density profile, \mathbf{J}_n , for a given line L in the configuration space as

$$\mathbf{J}_n = \hat{n} \cdot \mathbf{j}^{\lambda n_\lambda} \quad (16)$$

where the unit vector \hat{n} is normal to the line L and is oriented to the left of that line. A plot of \mathbf{J}_n along a series of lines can reveal a great deal of information about the distribution of the probability current density field.

Equation (13) can be solved by integrating $\frac{dR_\lambda}{dr_\lambda} = \frac{\mathbf{j}_{\hat{R}_\lambda}^{\lambda n_\lambda}}{\mathbf{j}_{\hat{r}_\lambda}^{\lambda n_\lambda}}$ starting at any point in the configuration space or by using a mathematical device called the stream function[21]. The stream function is a natural outcome of the continuity relationship. Consider a function $\Phi(R_\lambda, r_\lambda) = \text{constant}$ such that

$$\mathbf{j}_{\hat{R}_\lambda}^{\lambda n_\lambda} = \frac{\partial \Phi}{\partial r_\lambda} \quad \mathbf{j}_{\hat{r}_\lambda}^{\lambda n_\lambda} = -\frac{\partial \Phi}{\partial R_\lambda}. \quad (17)$$

From the continuity relationship, it follows that

$$\frac{\partial}{\partial R_\lambda} \frac{\partial \Phi}{\partial r_\lambda} - \frac{\partial}{\partial r_\lambda} \frac{\partial \Phi}{\partial R_\lambda} = 0 \quad (18)$$

which shows that Φ always satisfies the principle of continuity; in other words, the existence of Φ implies that the continuity relationship is satisfied and conversely the continuity equation implies the existence of a stream function.

By introducing the value of $\mathbf{j}_{\hat{R}_\lambda}^{\lambda n_\lambda}$ and $\mathbf{j}_{\hat{r}_\lambda}^{\lambda n_\lambda}$ as function of Φ yields the equation for the streamlines in terms of the stream function

$$\frac{\partial \Phi}{\partial R_\lambda} dR_\lambda + \frac{\partial \Phi}{\partial r_\lambda} dr_\lambda = 0 \quad (19)$$

It is the total differential $d\Phi$ (with respect to distance) of $\Phi(R_\lambda, r_\lambda)$. Hence, the equation of any streamline expressed as a function of Φ is given by the equation $d\Phi = 0$, or $\Phi(R_\lambda, r_\lambda) = \text{constant}$. Changing the value of the constant gives different streamlines for the considered flow, but the function $\Phi(R_\lambda, r_\lambda)$ keeps the same analytical form.

Consider the flow pattern as shown by Figure 3. The flux dQ passing through an element dn perpendicular to the streamlines is

$$dQ = \nabla \Phi \cdot dn = d\Phi \quad (20)$$

which is also the total differential of $d\Phi$ with respect to distance. It is deduced that

$$\mathbf{J} = \frac{dQ}{dn} = \frac{d\Phi}{dn} \quad (21)$$

where \mathbf{J} is the current density vector. Therefore, the total flux between two streamlines Φ_1 and Φ_2 is given by their difference

$$\Delta Q = \Phi_2 - \Phi_1. \quad (22)$$

The average value of \mathbf{J} between A and B is

$$J = \frac{\Delta \Phi}{\Delta n} = \frac{\Delta \Phi}{AB}. \quad (23)$$

The streamline representation of \mathbf{J} also provides a method of performing an exact tunneling calculation. We define the tunneling current on a surface as the current that originates in the reactant channel and arrives in the product channel by

traversing a path which at some point goes through a region of configuration space classically inaccessible at that energy. As can be seen from Figure 1, the streamlines cut those classical margins, labeled as E, penetrating into regions of configuration space which are classically inaccessible and carrying with them tunneling flux. Since the streamlines do not cross each other all of the flux which starts to one side of the streamline in the reactant channel must remain on that side throughout the interaction region and the product channel. Let us consider the short-dashed lines of Figure 2. These are limiting streamlines which are each tangent to one of the two E equipotentials. Any other streamline inbetween these never penetrates into the classically forbidden regions of the configuration space, whereas any streamline outside this band necessarily penetrates into such forbidden regions. The total flux carried by the latter streamlines will be defined as the tunneling flux $Q_{\text{tun}}^{\lambda n_\lambda}$, and the ratio of it to the incident total flux $Q_{\text{inc}}^{\lambda n_\lambda}$ will be called the tunneling coefficient $\gamma^{\lambda n_\lambda}$. Therefore,

$$\gamma^{\lambda n_\lambda} = \frac{J_{\text{tun}}^{\lambda n_\lambda}}{J_{\text{inc}}^{\lambda n_\lambda}} = \frac{P_{\text{tun}}^{\lambda n_\lambda}}{P^{\lambda n_\lambda}} \quad (24)$$

The product of $\gamma^{\lambda n_\lambda}$ and the total reaction probability is by definition the tunneling probability $P_{\text{tun}}^{\lambda n_\lambda}$.

The bell-shaped curves of Figure 2 represent the profiles of the component of \mathbf{J} normal to the cuts indicated by the segments of straight lines. The area between those curves and the corresponding straight lines are all equal to one-another and equal to the product of the reaction probability by the incident flux. In addition, the areas under the bell-shaped curves outside of the region between the limiting streamlines are also the same for all cuts and are equal to the tunneling flux.

5. Method of Computation

The physical wave function was obtained from a code developed previously[9,10] by using back-integration. The physical wave functions were in the form of values of Ψ corresponding to grid points of a polar mesh in (R_α, r_α) space. This polar mesh ranged from 200 x 200 points for the low energy range and 400 x 400 points in the high energy range. The stream function is obtained by integrating equation (13) for each mesh point. Off-grid values of Ψ were obtained with a two-dimensional five point Lagrangian interpolation formula.

The streamline plot is simply the contour lines of the stream function. The starting points for the streamlines were selected so that their density along a line, located at the right hand side of the figure, is proportional to the flux distribution across the line. This line was initially selected to have a slope equal to the skew angle of the system. This initial selection of points permits the streamlines to satisfy equation (5). Both the streamlines and the current density profile diagrams are superimposed on contours of the potential energy surface. Usually, there are six potential contours spaced at energy increments of 0.5 eV. The additional contour, E , is inserted amongst these to pictorially separate out the contributions to the current from tunneling.

The current density profile diagrams show the cross sections of flux normal to six lines placed perpendicular to the minimum energy path of the potential energy surface. Thus, we can see immediately the relative distributions of these currents at various positions along the minimum energy path. As we pointed out in section IV, the behavior of the streamlines and the arrows reflect the property of flux conservation. Initially, the lines are grouped close together and the arrows indicate the flow is relatively large. When the flux enters the interaction region where the channel created by the potential widens, the streamlines spread out and there is a corresponding decrease in the lengths of the arrows superimposed on the lines. As

the flux enters the product channel where the potential becomes deep and narrow again the streamlines group back together.

The streamlines isolating the tunneling current are calculated by first producing a general streamline plot then selecting from this plot initial points for streamlines which were approximately tangent to the potential contours labeled as E . The initial position of the streamline was shifted along a line in steps which were successively halved until one or more points on the streamlines satisfied the condition $|V(R_\alpha, r_\alpha) - E| \leq 0.001 eV$ and the remaining points of the streamlines fell within the classically allowed region. This technique isolated the position of the initial points to an interval of ≤ 0.001 bohr. Seven current density profiles are constructed, three in the reactant channel, three in the product channel and one through the saddle point, each of which intersected the two limiting streamlines defining the tunneling current. The initial point and the final point of each line were in a region where the flux was negligible, *i.e.*, far into the inner wall and far out on the plateau of the potential energy surface. From these seven lines, the tunneling coefficient is calculated by using equation IV.11 and IV.13. In practice, the average deviation for the normal currents was better than 0.5 %.

6. SUMMARY

We have developed a general and efficient means of the calculation of probability density, streamline of the probability current density vector field and tunneling fraction for collinear atom-diatomic molecule reactions. This method should be applicable to all such reactions, including heavy-light-heavy systems. It should be also allow to study reactions involving collision-induced dissociation.

APPENDIX A. Determination of the Coefficient Matrix \mathbf{W} .

To simplify the ensuing discussion, we will suppress the coordinate dependencies of the various functions and matrices.

The physical wavefunction Ψ_n^{phys} can be obtained by taking linear combination of the primitive wavefunctions Ψ_n which are available from solving equation (4). The coefficient matrix \mathbf{W} in equation (11) can be expressed in terms of its open and closed parts.

$$\mathbf{W} = \begin{pmatrix} W_{oo} & W_{oc} \\ W_{co} & W_{cc} \end{pmatrix} \quad (\text{A.1})$$

At the asymptotic region[22], the radial wavefunction \mathbf{g} can be written as

$$\mathbf{g} = \mathbf{v}^{1/2}[\mathcal{I}\mathbf{A} - \mathcal{O}\mathbf{B}] \quad (\text{A.2})$$

where the \mathbf{A} and \mathbf{B} are integration constants, \mathbf{v} is a diagonal matrix whose elements are the channel velocity given by

$$\mathbf{v} = \hbar |\mathbf{k}| / \mu \quad (\text{A.3})$$

where \mathbf{k} is the channel wavenumber given by equation (9). \mathcal{I} and \mathcal{O} are the incoming and outgoing waves given by

$$\mathcal{I}_{\lambda n_\lambda}(R_\lambda) = \begin{cases} \exp(-ik_{\lambda n_\lambda} R_\lambda) & \text{for open channels} \\ \exp(|k_{\lambda n_\lambda}| R_\lambda) & \text{for closed channels} \end{cases} \quad (\text{A.4})$$

$$\mathcal{O}_{\lambda n_\lambda}(R_\lambda) = \begin{cases} \exp(ik_{\lambda n_\lambda} R_\lambda) & \text{for open channels} \\ \exp(-|k_{\lambda n_\lambda}| R_\lambda) & \text{for closed channels} \end{cases} \quad (\text{A.5})$$

The scattering matrix \mathbf{S} is defined by the relation

$$\mathbf{S} = \mathbf{B}\mathbf{A}^{-1} \quad (\text{A.6})$$

Equation (A.2) can also be put in the equivalent form

$$\mathbf{g} = \mathbf{v}^{1/2}[\mathcal{S}\mathbf{C} + \mathcal{C}\mathbf{D}] \quad (\text{A.7})$$

where \mathcal{S} and \mathcal{C} are diagonal sine and cosine stationary wave matrices whose diagonal elements are given by

$$\mathcal{S}_{\lambda n_\lambda}(R_\lambda) = \begin{cases} \sin(k_{\lambda n_\lambda} R_\lambda) & \text{for open channels} \\ \exp(-|k_{\lambda n_\lambda}| R_\lambda) & \text{for closed channels} \end{cases} \quad (\text{A.8})$$

$$\mathcal{C}_{\lambda n_\lambda}(R_\lambda) = \begin{cases} \cos(k_{\lambda n_\lambda} R_\lambda) & \text{for open channels} \\ \exp(-|k_{\lambda n_\lambda}| R_\lambda) & \text{for closed channels} \end{cases} \quad (\text{A.9})$$

The reactance matrix \mathbf{R} is defined by the relation

$$\mathbf{R} = \mathbf{D}\mathbf{C}^{-1} \quad (\text{A.10})$$

Substituting equation (A.6) into equation (A.2) and equation (A.10) into equation (A.7), we get

$$\mathbf{g} = \mathbf{v}^{1/2}(\mathcal{I} - \mathcal{O}\mathcal{S})\mathbf{A} \quad (\text{A.11})$$

$$\mathbf{g} = \mathbf{v}^{1/2}(\mathcal{S} - \mathcal{C}\mathbf{R})\mathbf{C} \quad (\text{A.12})$$

These two equations can be related by a matrix \mathfrak{R}

$$(\mathcal{I} - \mathcal{O}\mathcal{S}) = (\mathcal{S} + \mathcal{C}\mathbf{R})\mathfrak{R}. \quad (\text{A.13})$$

The coefficient matrix \mathbf{W} can be obtained by combining equation (10), (11), (A.6), (A.10) and (A.13) which gives

$$\mathbf{W} = \mathbf{C}^{-1}\mathfrak{R}\mathbf{v}^{1/2} \quad (\text{A.14})$$

To evaluate matrix \mathfrak{R} , we break up equation (A.13) into its open and closed parts

$$\left[\begin{pmatrix} \mathcal{S}_o & 0 \\ 0 & \mathcal{S}_c \end{pmatrix} + \begin{pmatrix} \mathcal{C}_o & 0 \\ 0 & \mathcal{C}_c \end{pmatrix} \begin{pmatrix} R_{oo} & R_{oc} \\ R_{co} & R_{cc} \end{pmatrix} \right] \begin{pmatrix} \mathfrak{R}_{oo} & \mathfrak{R}_{oc} \\ \mathfrak{R}_{co} & \mathfrak{R}_{oo} \end{pmatrix} = \begin{pmatrix} \mathcal{I}_o & 0 \\ 0 & \mathcal{I}_c \end{pmatrix} - \begin{pmatrix} \mathcal{O}_o & 0 \\ 0 & \mathcal{O}_c \end{pmatrix} \begin{pmatrix} S_{oo} & S_{oc} \\ S_{co} & S_{cc} \end{pmatrix} \quad (\text{A.15})$$

From equation (A.4), (A.5), (A.8) and (A.9), we have

$$S_c = \mathcal{I}_c \quad (\text{A.16.a})$$

$$C_c = \mathcal{O}_c \quad (\text{A.16.b})$$

$$\mathcal{I}_o = C_o - iS_o \quad (\text{A.16.c})$$

$$\mathcal{O}_o = C_o + iS_o \quad (\text{A.16.d})$$

By substituting equation (A.16) into equation (A.15), we get eight equations

$$\mathfrak{R}_{oo} = -i(I + S_{oo}) \quad (\text{A.17.a})$$

$$R_{oo}\mathfrak{R}_{oo} + R_{oc}\mathfrak{R}_{co} = I - S_{oo} \quad (\text{A.17.b})$$

$$\mathfrak{R}_{oc} = -iS_{oc} \quad (\text{A.17.c})$$

$$R_{oo}\mathfrak{R}_{oc} + R_{oc}\mathfrak{R}_{cc} = -S_{oc} \quad (\text{A.17.d})$$

$$\mathfrak{R}_{co} = 0 \quad (\text{A.17.e})$$

$$R_{co}\mathfrak{R}_{oc} + R_{cc}\mathfrak{R}_{co} = -S_{co} \quad (\text{A.17.f})$$

$$\mathfrak{R}_{cc} = I \quad (\text{A.17.g})$$

$$R_{co}\mathfrak{R}_{oc} + R_{cc}\mathfrak{R}_{cc} = -S_{co} \quad (\text{A.17.h})$$

From equation (A.17.a), (A.17.b) and (A.17.e), we can show

$$\mathfrak{R}_{oo} = -2i(I - iR_{oo})^{-1} \quad (\text{A.18})$$

Combining equation (A.17.c), (A.17.d) and (A.17.g), we can get

$$\mathfrak{R}_{oc} = i(I - iR_{oo})^{-1}R_{oc} \quad (\text{A.19})$$

The entire \mathfrak{R} matrix can be constructed as

$$\mathfrak{R} = \begin{pmatrix} -2i(I - iR_{oo})^{-1} & i(I - iR_{oo})^{-1}R_{oc} \\ 0 & I \end{pmatrix} \quad (\text{A.20})$$

Since we have expressions for the three matrices $\mathbf{v}^{1/2}$, \mathfrak{R} and \mathbf{C}^{-1} , the matrix \mathbf{W} can be constructed from equation (A.14) and thus the physical wavefunction may be obtained from equation (11).

REFERENCES

- [1] R. E. Howard, A. C. Yates and W. A. Lester, Jr. , *J. Chem. Phys.* **66**, 1960 (1977); F. Schnabel and S. Chapman, *Chem. Phys. Lett.* **57**,189 (1978); J. S. Hutchinson and R. E. Wyatt, *J. Chem. Phys.* **70**, 3509 (1977).
- [2] D. G. Truhlar and B. C. Garrett, *Acc. Chem. Res.* **13**, 440 (1980).
- [3] E. Mortensen and K. S. Pitzer, *The Transition State, Chem. Soc. (London)*, Special Publication **16**, 57 (1962).
- [4] J. O. Hirschfelder, A. C. Cristoph, and W. E. Palke, *J. Chem. Phys.* **61**, 5435 (1974); J. O. Hirschfelder, C. J. Goebel, and L. W. Bruch, *J. Chem. Phys.* **61**, 5456 (1974); J. O. Hirschfelder and K. T. Tang, *J. Chem. Phys.* **64**, 760 (1976); **65**, 470 (1976).
- [5] E. A. McCullough and R. E. Wyatt, *J. Chem. Phys.* **54**, 3578 (1971).
- [6] S. L. Lathan, J. F. McNutt, R. E. Wyatt, and M. J. Redmon, *J. Chem. Phys.* **54**, 3578(1971).
- [7] J. F. McNutt and R. E. Wyatt, in: *Potential Energy Surfaces and Dynamics Calculations*, ed. D. G. Truhlar (Plenum Press, New York 1981), pp. 495-517.
- [8] A. Kuppermann, J. T. Adams, and D. G. Truhlar, *8th International Conference on the Physics of Electronic and Atomic Collisions*, 1973, Belgrade, Yugoslavia, pp.149 of Abstracts.
- [9] J. A. Kaye and A. Kuppermann, *Chem. Phys. Lett.* **77**, 573(1981).
- [10] A. Kuppermann, J. A. Kaye, and J. P. Dwyer, *Chem. Phys. Lett.* **74**, 257(1980).
- [11] J. Manz and J. R"omelt, *Chem. Phys. Lett.***81**, 179(1981).
- [12] G. Hauke, J. Manz, and J. R"omelt, *J. Chem. Phys.***73**, 5040(1980); *Chem Phys. Lett.* **74**, 263(1980).
- [13] L. M. Delves, *Nucl. Phys. (a)* **9**, 391 (1959); (b) **20**, 275(1960).

- [14] R. Gordon, *J. Chem. Phys.* **51**, 14(1969).
- [15] M. E. Riley and A. Kuppermann, *Chem. Phys. Lett.* **1**, 537(1968).
- [16] L. M. Milne-Thomson, *Theoretical Hydrodynamics*, (Macmillan, New York, 1968) 5th ed. pp. 5.
- [17] E. Merzbacher, *Quantum Mechanics*, (Wiley, New York, 1961), 2nd ed. , pp. 37.
- [18] B. Liu., *J. Chem. Phys.*, **58**, 1925(1973).
- [19] P. Sieghahn and B. Liu, *J. Chem. Phys.* **68**, 2457(1978).
- [20] D. G. Truhlar and C. J. Horowitz, *J. Chem. Phys.* **68**, 2466(1978).
- [21] James M. Robertson *Hydrodynamics in Theory and Application* (Prentice-Hall, Inc. Englewood Cliffs. N. J.) Sec. 3.3.
- [22] A. Kuppermann, in *Theoretical Chemistry: Advances and Perspectives*, Vol. 6A, ed. D. Henderson (Academic Press, New York, 1981), pp. 79-164.

Figure Captions

[Figure 1.] Plot of streamlines of probability current density for the collision of $\text{H} + \text{H}_2(v = 0)$ at energy 0.47 eV. The arrows point in the direction of the current density vector; the length of the arrows is proportional to the magnitude of the current density vector at its midpoint. The streamlines are superimposed on a contour plot of the potential energy surface, contours are drawn every 0.4 eV from 0.2 eV to 1.8 eV, measured with respect to the bottom of the H_2 well. Contours are also drawn at the energy E of the collision. The minimum energy path is indicated by a dashed line, the saddle point is marked by a cross.

[Figure 2.] Plot of the probability current density profiles at collision energy 0.47 eV. Seven lines normal to the minimum energy path and the magnitude of the current density normal to these lines are drawn. The limiting streamlines are shown by short dashes. The plot is superimposed on a contour plot of the potential energy surface as was used in Figure 1. The magnitude of the currents is proportional to the distance from the line to the corresponding curve.

[Figure 3.] Flux in terms of stream function - notation.

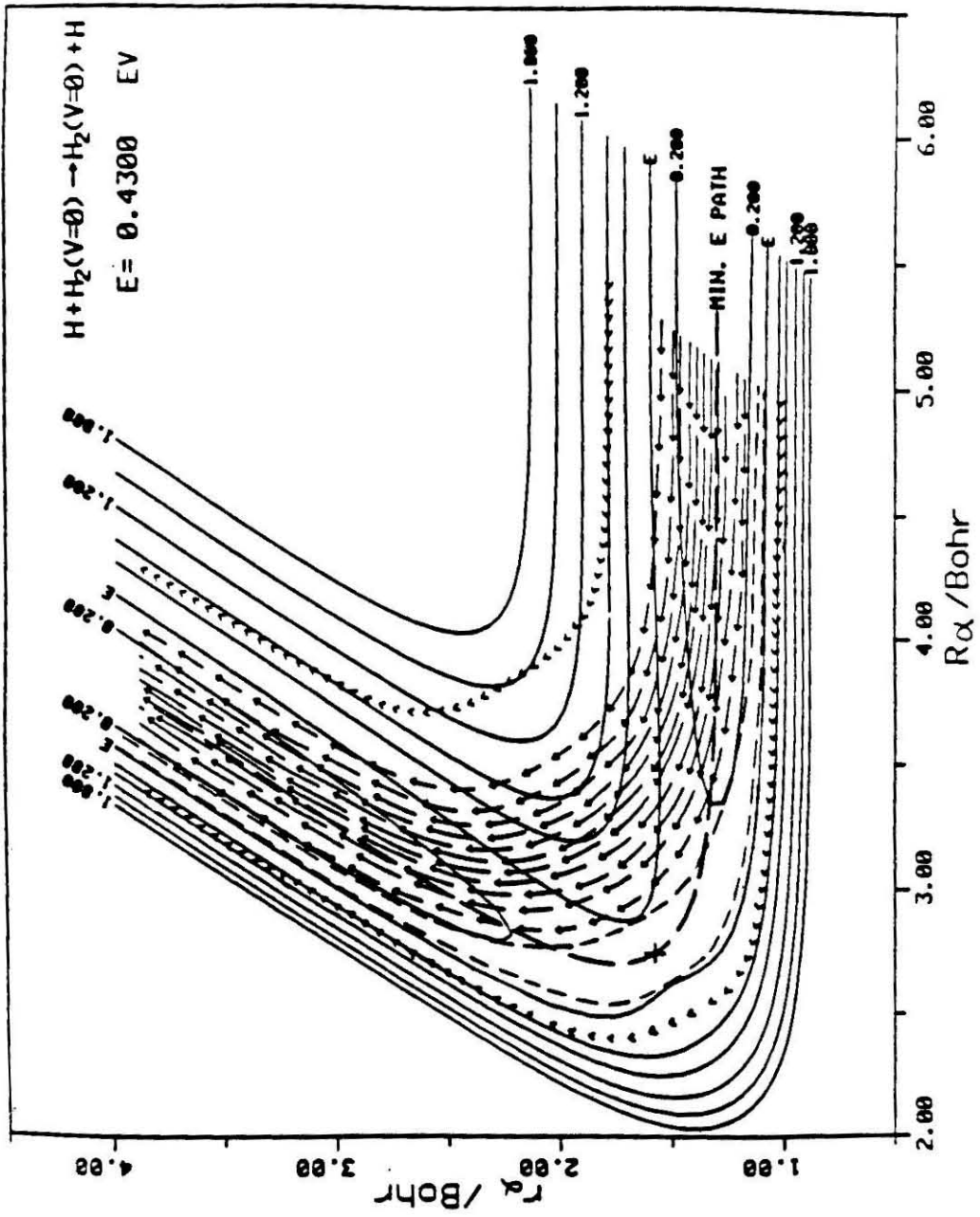


Figure 1

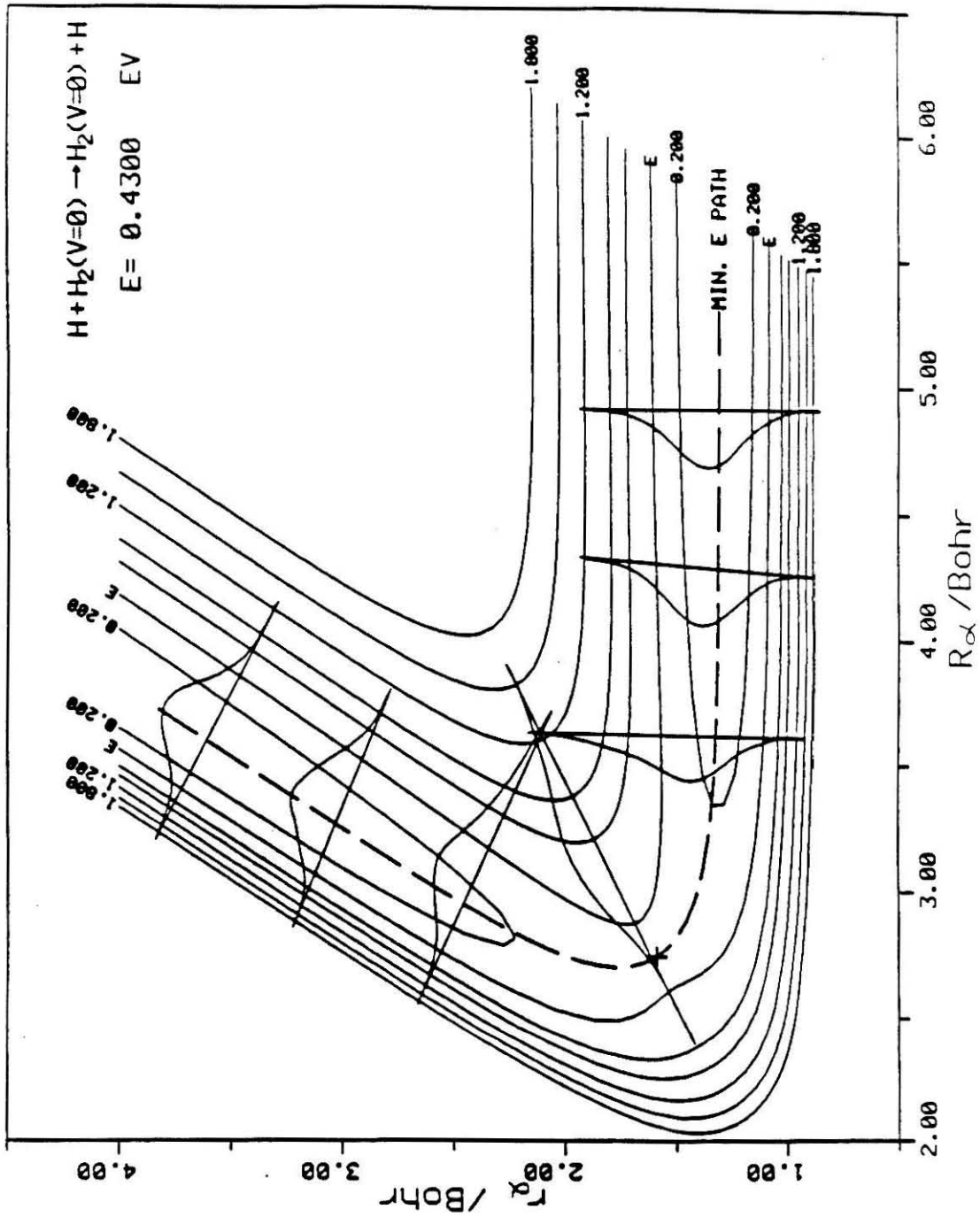


Figure 2

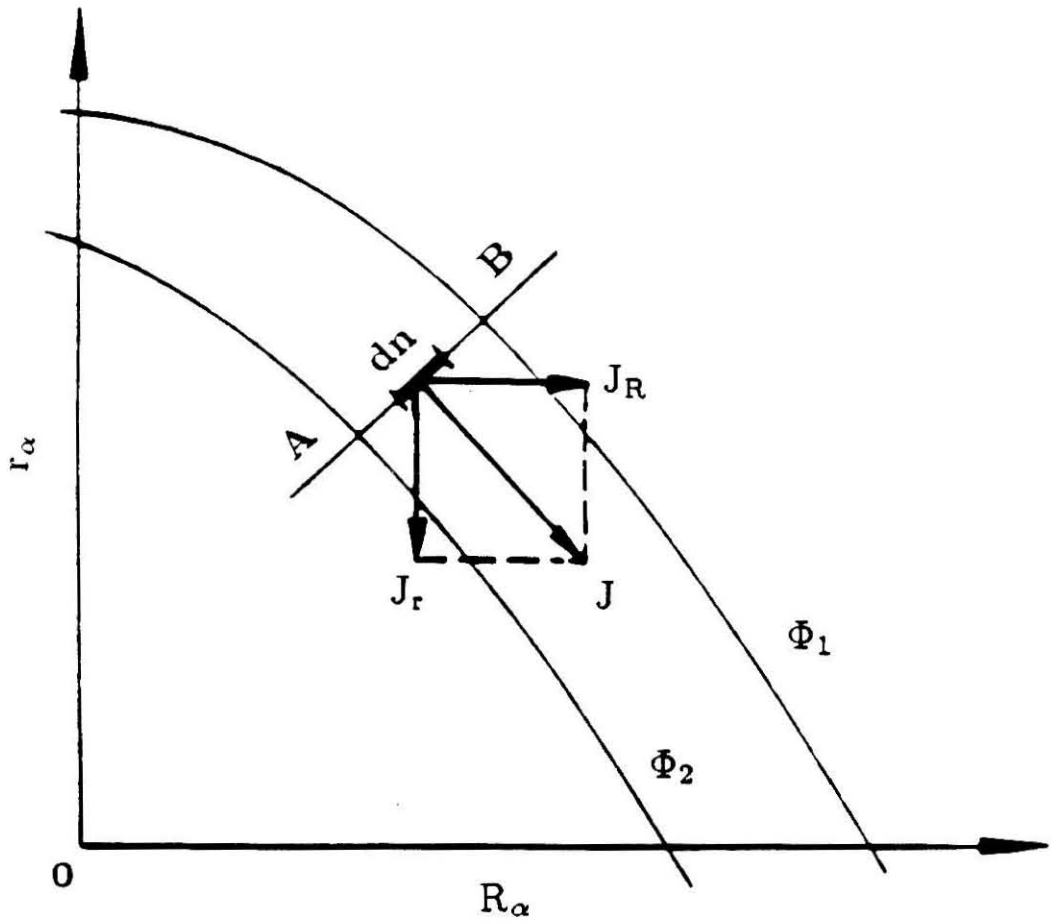
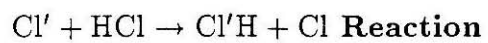


Figure 3

Appendix A

Hyperspherical Study on the Barrier Height Dependence of the Dynamics for the Collinear



**Hyperspherical Study on the Barrier Height
Dependence of the Dynamics for the Collinear
 $\text{Cl}' + \text{HCl} \rightarrow \text{Cl}'\text{H} + \text{Cl}$ Reaction**

Carrie K. Stroud, Yi-Shuen Mark Wu ¹, Jack A. Kaye and Aron Kuppermann

Arthur Amos Noyes Laboratory of Chemical Physics
Division of Chemistry and Chemical Engineering ³
California Institute of Technology
Pasadena, CA 91125, USA

ABSTRACT

Quantum dynamical calculations for the collinear $\text{Cl}' + \text{HCl} \rightarrow \text{Cl}'\text{H} + \text{Cl}$ reaction on low and high barrier potential energy surfaces are presented and discussed within the framework of the hyperspherical coordinate representation. Vibrational excitation of the reactant diatomic was found to decrease the reaction rate for the low barrier surface and increase the reaction rate for the high barrier surface. Quantum mechanical streamline calculations were used for analysis, and discussion of the results is made in terms of the topology of the potential energy surface, in which the skew angle and the barrier height of the system play a leading role in explaining the dynamics of the reaction.

¹ Work performed in partial fulfillment of the requirements for the Ph.D. degree in Chemistry at the California Institute of Technology

³ Contribution number xxx

1. Introduction

The use of hyperspherical coordinates to study the dynamics of heavy-light-heavy (**H-L-H**) reactive triatomic systems[1-18] in the collinear approach has become a powerful method not only for the calculation of transition probabilities, but also for the interpretation of several dynamical phenomena which appear to be characteristic of this kind of reaction. Investigation of the hydrogen atom transfer between two heavy atoms has especially benefitted due to the hyperspherical coordinates ability to accurately represent the small skew angles often encountered in these systems. The collinear light atom transfer reactions exhibit several interesting features: (A) the reaction probabilities oscillate with energy[14]; (B) vibrational adiabaticity is highly favored[19]; (C) in reactive and nonreactive processes vibrationally nonadiabatic transition probabilities tend to be equal; and (D) resonances in the transition probability profiles are present at well-defined energies[20]. All of these features, mainly of quantum nature, have been reviewed recently[21-23].

This paper presents new results for the $\text{Cl}' + \text{HCl}$ [24] reaction emphasizing the effects of vibrational excitation on reaction probabilities, for which little attention has previously been directed. It is observed that the barrier height of the potential energy surface plays a vital role in the final reaction rate upon vibrational excitation. This observation is in itself not surprising, however the outcome is actually opposite of what one intuitively expects. Vibrational excitation ensues an increased reaction rate for a high barrier surface and a decreased reaction rate for a low barrier surface. Other **H-L-H** collinear reactions are expected to exhibit the same behavior since the primary cause for this observation is accredited to the small skew angle.

Quantum mechanical streamline calculations[25-30] provide a great deal of information pertaining to the wavefunction in the interaction region of the potential. Specifically, they are informative on how the reacting system goes from its initial to its final configuration by exhibiting more details of the mechanism of the collision. The streamlines are quantum mechanical analogous to the classical trajectories of a single particle of corresponding reduced mass traveling through the potential surface[25]. Thus they have become a crucial part of the analysis of the sensitivity of the reaction rate to the barrier height for vibrationally excited reactants.

In section 2 we describe the potential energy surfaces we used. In section 3 we briefly discuss the methodology and the selection of the appropriate values of the numerical parameters. In section 4, the interesting feature of the enhancement of the reaction rate on the high barrier surface but inhibition of the reaction rate on the low barrier surface for vibrational excitation reactions is studied with the help of quantum mechanical streamlines. The results are summarized in section 5.

2. Potential Energy Surface

Two different LEPS surfaces[31] were used for both the quantum mechanical and quasiclassical calculations performed on the reactions $CL' + HCl(\nu = 0, 1) \rightarrow Cl'H(\nu') + Cl$. The two potential energy surfaces correspond to those of Smith[32] and have parameters listed in Table 1. Surface A with a barrier height of 6.21 kcal/mole, corresponding to the experimentally determined activation energy[33], is near the upper limit as determined by *ab initio* calculations[34] and a value predicted by calculations correcting for dispersion interactions[34]. In contrast, the barrier of surface B lies near the lower limit[34] and shows much better agreement with quasiclassical trajectory calculations and experimental deactivation

processes[32] $\text{Cl} + \text{H(D)Cl}(\nu = 1) \rightarrow \text{Cl} + \text{H(D)Cl}(\nu = 0)$. Since surfaces A and B have barriers close to the upper and lower limits for this reaction it is reasonable to expect the actual value of the barrier height to lie somewhere inbetween. Both surfaces are shown in Figure 1 and their corresponding minimum energy path profiles are shown in Figure 2. The horizontal lines indicate the vibrational energies of the isolated $\text{HCl}(\nu = 0)$ and $\text{HCl}(\nu = 1)$ molecules.

3. Methodology

The method of hyperspherical coordinates, as described elsewhere[2], was chosen for these calculations because it requires fewer basis functions to achieve convergence of reaction probabilities and is optimum for describing the small skew angle of the $\text{Cl}' + \text{HCl}$ system, which is about 13° . The hyperspherical method differs from other methods mainly in that: (A) one of the coordinates, the hyperradius ρ , is independent of the rearrangement channel, and (B) the reaction is viewed in this formalism as an evolution from small values of ρ , where the particles are close together, to large values of ρ , where the reactants and products channels are separated.

The coupled equations are solved by the usual Gordon propagator[35], together with the reorthogonalization procedure of Riley and Kuppermann[36]. The propagation is made by dividing the configuration space into several sectors defined by discrete values of ρ , and imposing the continuity of the function and of its derivative with respect to ρ at the boundaries $\rho = \rho_i$ between the ρ_{i-1} to ρ_i and ρ_i to ρ_{i+1} regions. The propagation begins at small values of ρ and gradually to large values of ρ where the interaction between the reactants and the products can be neglected. The solutions are then projected onto the asymptotic Jacobi basis from which we get, by standard methods[37], the transition probability.

A total of 16 basis functions (8 symmetric and 8 antisymmetric) were used at energies below that of the first vibrational state while 24 basis functions (12 symmetric and 12 antisymmetric) were used for all energies above that of the first vibrational state. Since fast oscillations in the reaction probability profile are predictable for **H-L-H** system, the standard energy grid was fixed at 0.001 eV, but was reduced where necessary to a minimum of 0.0001 eV in the resonant regions. A total of about 200 and 400 points for the overall energy range provides the proper precision for the plots of reaction probability vs. energy for surfaces A and B respectively. The convergence of the reaction probability with projection distance was examined for $\rho = 26, 28, 30$ bohr and it was found that a projection distance of $\rho = 26$ bohr sufficed for energies below 1.2 eV. The transition probabilities converged to ± 0.001 and flux to ± 0.0001 for all energies on both surfaces. For comparison, quasiclassical trajectory calculations[38], performed with the distance from the Cl' atom to the HCl center of mass, $R_{Cl',HCl}$ at 12 bohr, and terminated when either $R_{Cl',HCl}$ or $R_{Cl,HCl}$, are more than 12 bohr, are presented.

The physical wave functions used for the quantum streamline calculations[30] were obtained by using back-integration from $\rho = 26$ bohr. The physical wave functions were in the form of values corresponding to grid points of a polar mesh. This polar mesh ranged from 200 x 200 points for the low energy range and 400 x 400 points in the high energy range. The streamlines are obtained by taking the contour lines of the stream function which the off-grid values of the function are interpolated with a two-dimensional five point Lagrangian interpolation formula.

4. Results and Discussion

For surfaces A and B both the quantum mechanical and quasiclassical reaction probabilities vs. energy curves are plotted in Figures 3 and 4 for the reactant

vibrational quantum number $\nu = 0, 1$ respectively. The total reaction probability is defined, for a reactant vibrational quantum number ν as

$$P_{\nu}^R = \sum P_{\nu n}^R \quad (1)$$

where the sum is over all possible n , n being the product vibrational quantum number. Figures 5 and 6 show the thermal rate constants calculated from the quantum mechanical probabilities in figures 3 and 4.

With the exception of the resonances the quasiclassical trajectory calculations qualitatively agree with those of the quantum calculations. The $\nu = 0$ transition probabilities appear to oscillate with energy on both surfaces. There is a sudden increase of reactivity just above the energy threshold, followed by a continued decrease leading to a minimum, and afterwards, a slight, smooth and quasi-linear increase until the highest value of the energy range studied is reached. The curves oscillating sinusoidally as a function of E can be interpreted as a two state interference pattern for scattering on the gerade and ungerade vibrationally adiabatic potentials[24] which are shown in Figure 7. The oscillatory behavior of the P_0^R versus energy curves is not of a quantum nature, as it is also present in the quasiclassical trajectory results. The vibrational adiabatic approximation underlying this oscillation is quite valid for both these surfaces since nonadiabatic transitions contribute less than 1 percent to the total reaction probability for the energies considered, although the nonadiabatic effects will become significant for much higher E .

The curious aspect and therefore the focus of this paper is the difference in the curves for the reactive probabilities upon vibrational excitation of the reacting diatomic for the two surfaces. Initially the reaction probability is practically zero but then suddenly becomes extremely high at about 0.05 eV above the opening of the first vibrational state on surface A. However on surface B the

reaction probability curve is significantly greater than zero upon opening of the first vibrational state but with increasing energy exhibits no sudden increase and only begins to slowly rise at about 0.15 eV translational energy. This is further reflected in the Arrhenius plots of thermal rate constants where the vibrational excitation leads to an enhancement of the reaction rate by a factor almost 100 at 200° K and 10 at 500° K on surface A, while for surface B the ground state reaction is faster at all temperatures. An indication that surface A may be more realistic is that the large enhancement of the exchange rate with vibrational excitation has been observed experimentally[33]. The resonances observed on the $\nu = 0, 1$ probability curves have been seen previously for similar surfaces and are discussed elsewhere[24]. Previous studies of this reaction have used a high barrier surface (8.5 kcal/mole)[6,24] and computed reaction rates only for the ground state reagents. This behavior of reaction probability *vs.* energy curves is in marked contrast to that in the H + H₂ reaction[2], which has a relatively high barrier to reaction.

The difference in behavior between surface A and B regarding the effect of vibrational energy can be understood from the quantum mechanical streamlines calculations for a series of energies just above the first vibrational state. Figures 8 and 9 display the streamlines for vibrationally excited transitions for both surfaces at 0.075 eV transitional energy. The streamlines are broken up into a series of curved arrows which by definition are everywhere tangent to the probability current density vector. The length of each arrow is proportional to the magnitude of the probability current density vector evaluated at its center. In order to display the relationship between the streamlines and the surface, the streamline plots are superimposed on a contour diagram of the potential energy surface. The solid lines are equipotentials with energies in eV, measured with respect to the bottom of the HCl well, designated on the plot. The 0.614 eV equipotentials are the curves

labelled E in the figure and correspond to the energy of the calculation. The minimum energy path is marked by a dashed line, and the saddle point is indicated by a cross. Comparing the streamline plots for the two surfaces at identical energies clearly indicates that the flux through surface A is substantially greater than that through surface B.

The corresponding classical picture demonstrates that the higher barrier on surface A actually prohibits the reaction from returning to the reactants channel after crossing the saddle point region whereas the lower barrier of surface B does not. For the vibrationally excited reactants the classical particle begins by oscillating in the reactants channel as it approaches the interaction region of the surfaces. Upon reaching the strong interaction region the particle crosses the barrier near the saddle point and hits the repulsive wall in the products channel. Since the skew angle is so small for this system, upon rebounding from the repulsive wall the particle will approach the dissociation plateau very close to the symmetric stretch coordinate of the saddle point region. On surface A the energy in the interaction region is much higher than it is for surface B, therefore it is a barrier against the classical particle returning to the reactants channel. However, for surface B this barrier is too small to inhibit the particle from again crossing the saddle point region and falling back into the reactants channel. From the paths of the streamlines on surface B obviously only a very few classical trajectories will rebound from the repulsive wall and hit the dissociation plateau deep enough into the products channel to result in a reactive process.

Since many hydrogen transfer reactions of the type studied here are expected to have a barrier to reaction on the order of or smaller than the reagent zero-point energy[39], it seems reasonable that for such reactions, vibrational excitation might be expected to be extremely ineffective in promoting chemical reaction.

The restriction to collinearity is an obvious limitation in assessing the importance of this effect in the three-dimensional world. Approximate three-dimensional quantum mechanical calculations on this system have been reported[40] for ground state reagents and indicate that the oscillations in reaction probabilities with energy persist in three dimensions. Three-dimensional quasi classical trajectory calculations[41] also suggest that such oscillations may be detectable in molecular beam experiments. It is not impossible, therefore, that vibrational inhibition on a low barrier surface might also persist in three dimensions.

5. Summary

In this paper we have presented the results of the dynamical hyperspherical calculations for the reaction $\text{Cl}' + \text{HCl} \rightarrow \text{Cl}'\text{H} + \text{Cl}$ on a low and high barrier potential energy surface, in the collinear configuration approach, together with an analysis and interpretation of them. Vibrational excitation was found to enhance the reaction rate on the high barrier surface but to inhibit it on the low barrier surface. This effect is observed in both quantum mechanical and quasiclassical trajectory calculations. Quantum mechanical streamlines are found to be a valuable tool in helping to understand the dynamics. Since low barriers to reaction are expected for many light atom transfer reactions, especially for reactions involving the heavier halogen atoms, three-dimensional calculations of reaction probabilities would be of great interest.

References

- [1] A. Kuppermann, *Chem. Phys. Lett.* **32** (1975) 374.
- [2] A. Kuppermann, J. A. Kaye, and J. P. Dwyer, *Chem. Phys. Lett.* **74** (1980) 257.
- [3] G. Hauke, J. Manz, and J. Römelt, *J. Chem Phys.* **73** 5040 (1980).
- [4] J. Manz and J. Römelt, *Chem. Phys. Lett.* **76** (1980) 337.
- [5] J. Manz and H. H. R. Schor, *Chem. Phys. Lett.* **107** (1984) 549.; P.L. Gertitishke,
J. Manz, J. Römelt, and H. H. Schor, *J. Chem. Phys.* **83** (1985) 208.
- [6] D. K. Bondi, J. N. L. Connor, B. C. Garrett, and D. G. Truhlar, *J. Chem. Phys.* **78** (1983) 5981.
- [7] D. K. Bondi, J. N. L. Connor, J. Manz and J. Römelt, *Mol. Phys.* **50** (1983) 488.
- [8] J. A. Kaye, Ph.D. Thesis, California Institute of Technology, Pasadena, CA (1982).
- [9] J. A. Kaye and A. Kuppermann, *Chem. Phys. Lett.* **92** (1982) 574.
- [10] N. Abusalbi, D. J. Kouri, V. Lopez, V. K. Babamov, and R. A. Marcus, *Chem. Phys. Lett.* **103** (1984) 458.
- [11] J. A. Kaye and A. Kuppermann, *Chem. Phys. Lett.* **77** (1981) 573.
- [12] J. Manz and J. Römelt, *Chem. Phys. Lett.* **81** (1981) 179.
- [13] C. L. Shoemaker, N. Abusalbi, D. J. Kouri, *J. Phys. Chem.* **87** (1983) 5389.
- [14] C. Hiller, J. Manz, W. H. Miller, and J. Römelt, *J. Chem. Phys.* **78** (1983) 3850.
- [15] J. M. Launay and M. Le Dourneuf, *J. Chem. Phys.* **B 15** (1982) L455.
- [16] B. R. Johnson, *J. Chem. Phys.* **73** (1980) 5051; **79** (1983) 1906, 1916.
- [17] F. T. Smith, *J. Math. Phys.* **3** (1962) 735;

- R. C. Whitten and F. T. Smith, *J. Math. Phys.* **9** (1968) 1103.
- [18] V. Aquilanti, G. Grossi and A. Lagana, *J. Chem. Phys.* **76** (1982) 1587;
G. Grossi, *J. Chem. Phys.* **81** (1984) 3355.
- [19] P. L. Gertitschke, J. Manz, J. Römelt and H. R. R. Schor, *J. Chem. Phys.* **83**
(1985) 205.
- [20] E. Pollak, *Comments At. Mol. Phys.* **15**, **23** and references therein (1984).
- [21] J. Manz, *Comments At. Mol. Phys.* **17** (1985) 91.
- [22] J. Römelt in: NATO ASI Series, Vol. C 170. The Theory of Chemical Reaction
Dynamics, ed. D. C. Clary (Reidel, Dordrecht, 1986) p. 77;
E. Pollak, in: NATO ASI Series, Vol. C 170. The Theory of Chemical Reaction
Dynamics, ed. D. C. Clary (Reidel, Dordrecht, 1986) p. 135.
- [23] G. Schatz, *Ann. Rev. Phys. Chem.* **39** (1988) 317.
- [24] D. K. Bondi and J. N. L. Connor, *Mol. Phys.* **50** (1983) 467.
- [25] J. O. Hirschfelder, A. C. Christoph, and W. E. Palke, *J. Chem. Phys.* **61**
(1974) 5435;
J. O. Hirschfelder, C. J. Goebel, and L. W. Bruch, *J. Chem. Phys.* **61** (1974)
5456;
J. O. Hirschfelder and K. T. Tang, *J. Chem. Phys.* **64** (1976) 760.
- [26] E. A. McCullough and R. E. Wyatt, *J. Chem. Phys.* **54** (1971) 3578.
- [27] S. L. Lathan, J. F. McNutt, R. E. Wyatt and M. J. Redmon, *J. Chem. Phys.*
54 (1971) 3578.
- [28] J. F. McNutt and R. E. Wyatt, in: Potential Energy Surfaces and Dynamics
Calculations, ed. D. G. Truhlar (Plenum Press, New York 1981), p. 495.
- [29] A. Kuppermann, J. T. Adams and D. G. Truhlar, 8th International Conference
on the Physics of Electronic and Atomic Collisions, 1973, Belgrade, Yugoslavia.
p. 149 of Abstracts.

- [30] Y. M. Wu, Ph. D. Thesis, California Institute of Technology, Pasadena CA (1992).
- [31] S. Sato, *J. Chem. Phys.* **23** (1955) 592, 2465.
- [32] I. W. M. Smith, *J. Chem. Soc. Farad. Trans.* **II 71** (1975) 1970.
- [33] F. S. Klein, A. Persky and R. E. Weston, *J. Chem. Phys.* **41** (1964) 1799; **59** (1973) 2775.
- [34] P. Botschwina and W. Meyer, *Chem. Phys. Lett.* **44** (1976) 449.
- [35] R. Gordon, *J. Chem. Phys.* **51** (1969) 14.
- [36] M. E. Riley and A. Kuppermann, *Chem. Phys. Lett.* **1** (1968) 537.
- [37] A. Kuppermann, *Theoretical Aspects of the mechanism of Simple Chemical Reactions*, in the Proceedings of the Summer School on Chemical Photophysics, Les Houches, France, 18-30 June 1979, P. Glorieux, D. Lecler, and R. Vetter, Eds. (Centre de la Recherche Scientifique, Paris, 1979), p. 293.
- [38] R. N. Porter and L. M. Raff, in: Dynamics of molecular collisions, Part B, ed. W. H. Miller (plenum Press, New York, 1976), p. 1;
D. G. Truhlar and J. T. Muckerman, in Atom-Molecule Collision Theory, ed. R. B. Bernstein (plenum Press, New York, 1979), p.505.
- [39] I. Last and M. Baer, *J. Chem. Phys.* **80** (1984) 3246.
- [40] N. Abusalbi, S.-H. Kim, D. J. Kouri, and M. Baer, *Chem. Phys. Lett.* **112** (1984) 502.
- [41] M. Baer and I. Last, *Chem. Phys. Lett.* **119** (1985) 393.

Figure Captions

- Figure 1.** Equipotential contour plot for the $\text{Cl}' - \text{H} - \text{Cl}$ system for the potential energy surface A (top) and B (bottom) described in the text and in Table 1. The solid lines are the contours and are equally spaced in increments of 0.1 eV from 0.1 to 0.8 eV. The dashed lines depict to the minimum energy path. The zero of energy is the bottom of the HCl well. The surface is plotted in the Delves mass-scaled cartesian coordinates system as described in reference [2].
- Figure 2.** Potential along the minimum energy path for potential energy surface A and B as a function of distance along the path, in Delves coordinates, from the saddle point. The horizontal lines indicate the eigenvalues of the isolated $\text{HCl}(\nu = 0)$ and $\text{HCl}(\nu = 1)$ molecules.
- Figure 3.** Reaction probabilities as a function of energy for the $\text{Cl} + \text{HCl}(\nu = 0)$ reaction for potential energy surfaces A (top) and B (bottom). Solid lines are used to indicate total (state-to-all) quantum mechanical (QM) results; dashed lines are used to indicated total quasi-classical trajectory (CL) results.
- Figure 4.** Reaction probabilities as a function of energy for the $\text{Cl} + \text{HCl}(\nu = 1)$ reaction for potential energy surfaces A (top) and B (bottom). Solid lines are used to indicate total (state-to-all) quantum mechanical (QM) results; dashed lines are used to indicated total quasi-classical trajectory (CL) results.
- Figure 5.** Arrhenius plots of quantum mechanical rates k_{ν}^R for reaction computed from the reaction probabilities shown in Figures 3 and 4 for surface A. Solid lines are used for reaction of ground state reagents ($\nu = 0$); dashed lines are used for reaction of vibrationally excited ($\nu = 1$) reagents.
- Figure 6.** Arrhenius plots of quantum mechanical rates k_{ν}^R for reaction computed from the reaction probabilities shown in Figures 3 and 4 for surface B. Solid lines

are used for reaction of ground state reagents ($\nu = 0$); dashed lines are used for reaction of vibrationally excited ($\nu = 1$) reagents.

Figure 7. Eigenvalues $E_n(\rho)$ for surface A (top) and B (bottom) as a function of the propagation coordinate ρ . These curves are pairwise degenerate at large ρ , the symmetric one being always lower than the corresponding antisymmetric one at small ρ . Values of n for the symmetric curves are shown at the top of the figures.

Figure 8. Plot of streamlines of probability current density for the collision at $\text{Cl}' + \text{HCl}(\nu = 1)$ at translational energy $E_{tr} = 0.75$ eV for surface A. The arrows point in the direction of the current density vector; the length of the arrows is proportional to the magnitude of the current density at its midpoint. The streamlines are superimposed on a contour plot of the potential energy surface; contours are drawn every 0.2 eV from 0.2 eV to 0.8 eV, measured with respect to the bottom of the HCl well. Contours are also drawn at the energy E of the collision. The minimum energy path is indicated by a dashed line; the saddle point is marked by a cross. The coordinate system is the Delves mass-scaled cartesian coordinates.

Figure 9. Plot of streamlines of probability current density for the collision at $\text{Cl}' + \text{HCl}(\nu = 1)$ at translational energy $E_{tr} = 0.75$ eV for surface B. The arrows point in the direction of the current density vector; the length of the arrows is proportional to the magnitude of the current density at its midpoint. The streamlines are superimposed on a contour plot of the potential energy surface; contours are drawn every 0.2 eV from 0.2 eV to 0.8 eV, measured with respect to the bottom of the HCl well. Contours are also drawn at the energy E of the collision. The minimum energy path is indicated by a dashed line; the saddle

point is marked by a cross. The coordinate system is the Delves mass-scaled cartesian coordinates.

Table 1: Parameters and properties of LEPS potential energy surfaces A and B^a.

	HCl	Cl ₂
β (bohr ⁻¹)	0.9892	1.0626
R_e (bohr)	2.4060	3.7791
D_e (eV)	4.6258	2.5169
Δ A	0.138	0.138
Δ B	0.185	0.185
Saddle Point Location (bohr)		
A	(2.757, 2.757)	
B	(2.727, 2.727)	
Barrier Height (kcal/mole)		
A	6.21	
B	1.28	

a. Masses used: $m_{Cl} = 34.6974 m_H$.

Cl + HCl

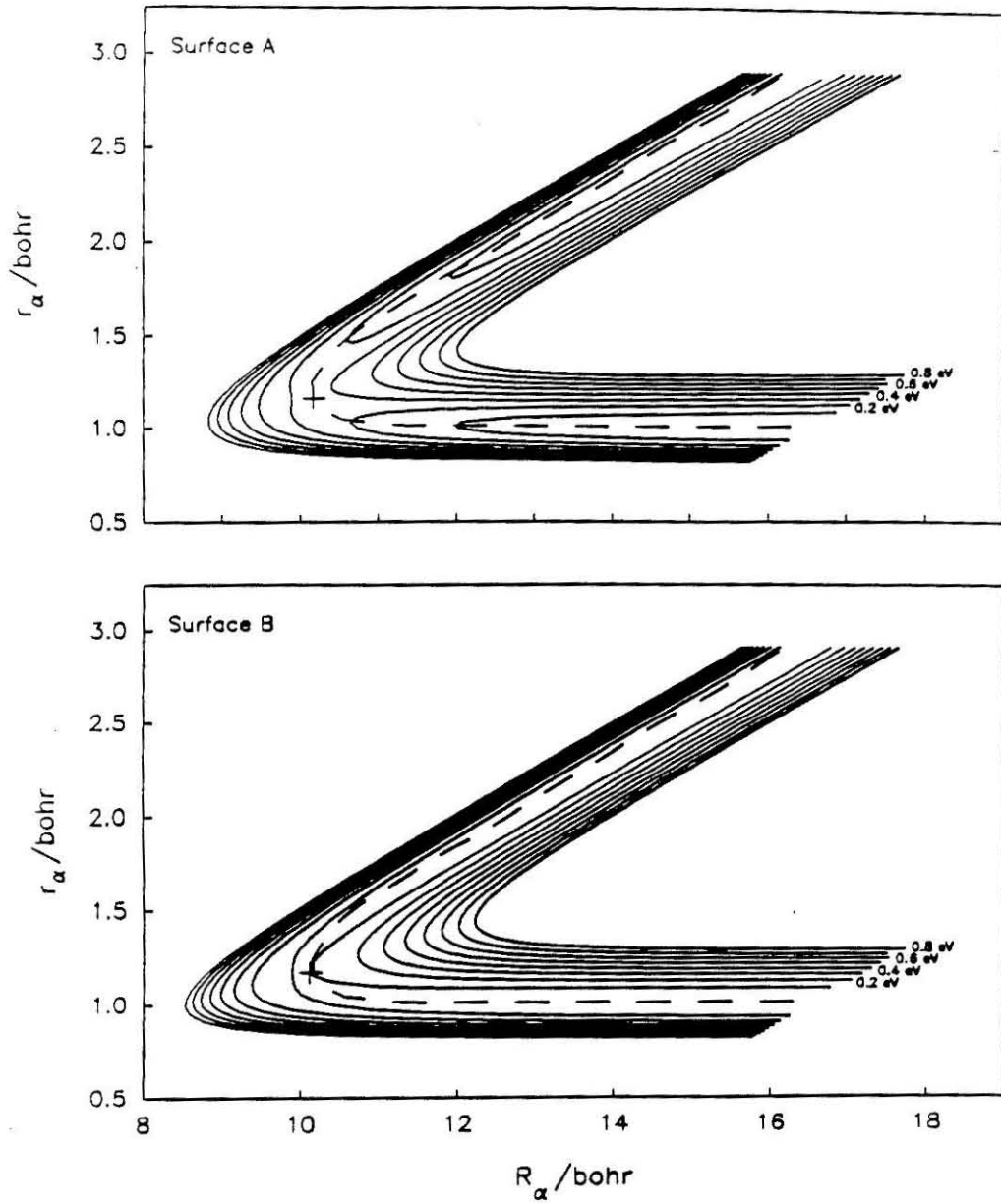


Figure 1.

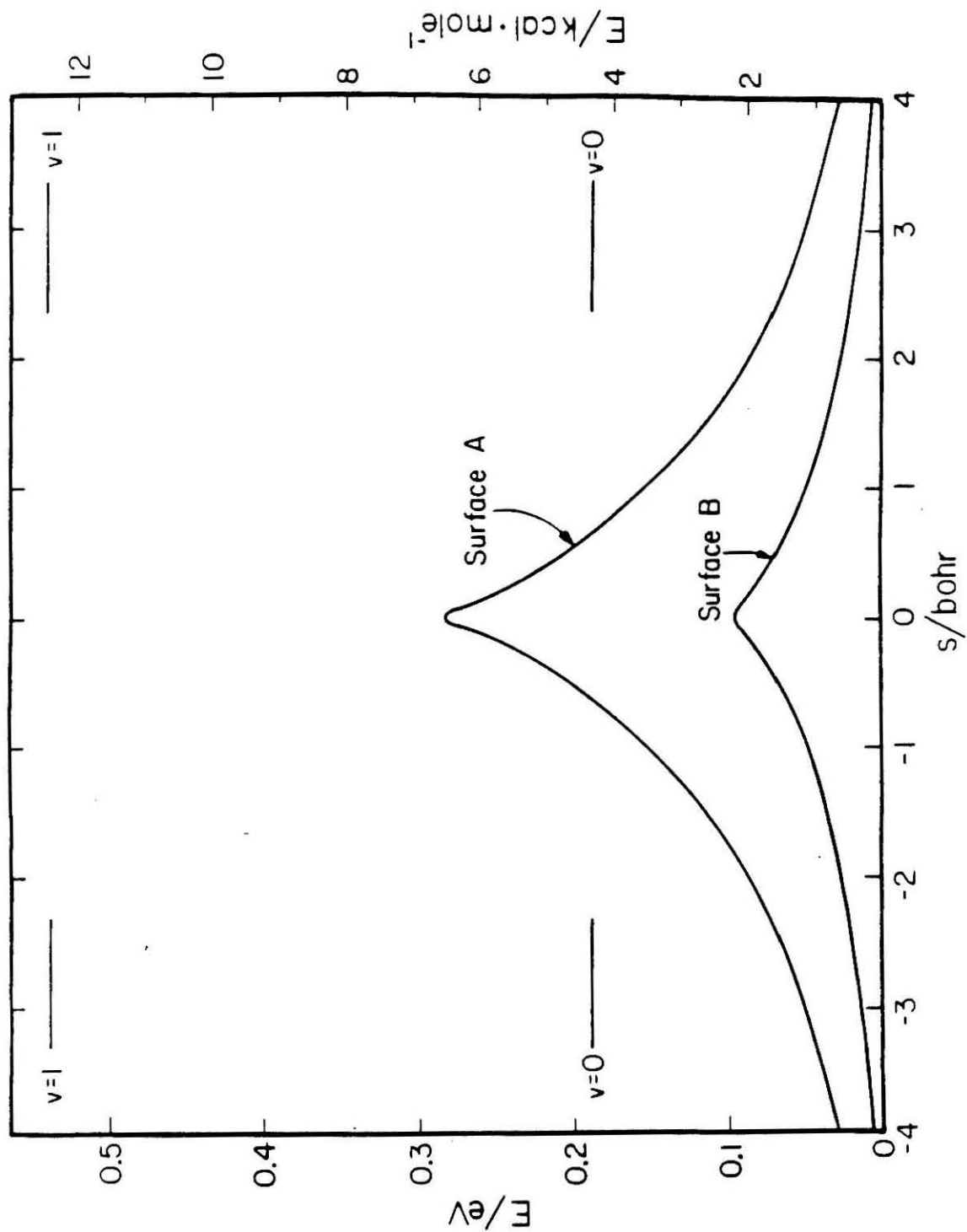
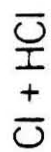
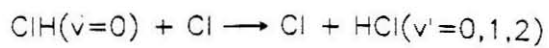


Figure 2.



E / eV

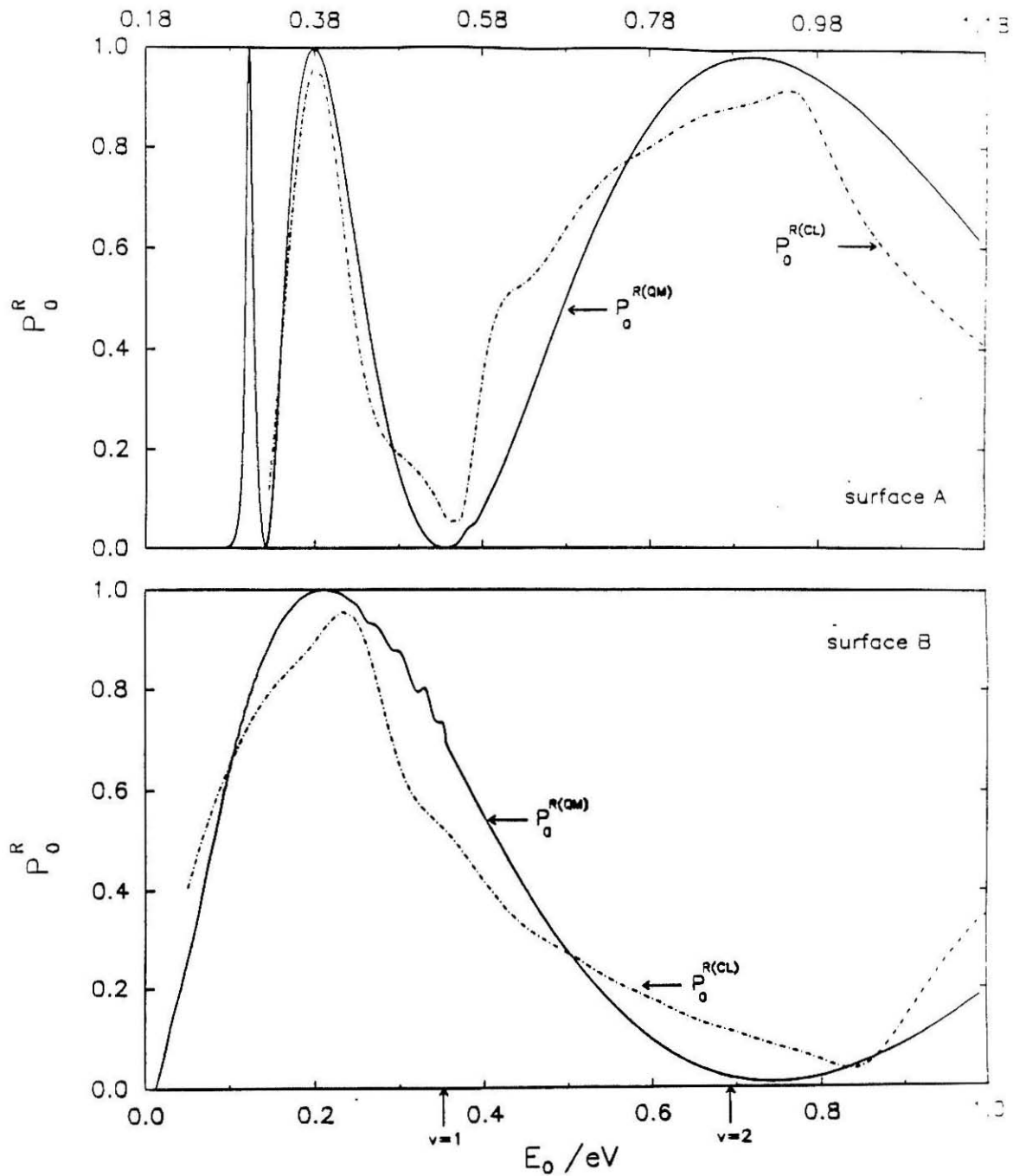
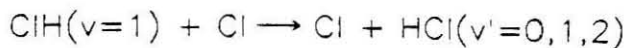


Figure 3.



E / eV

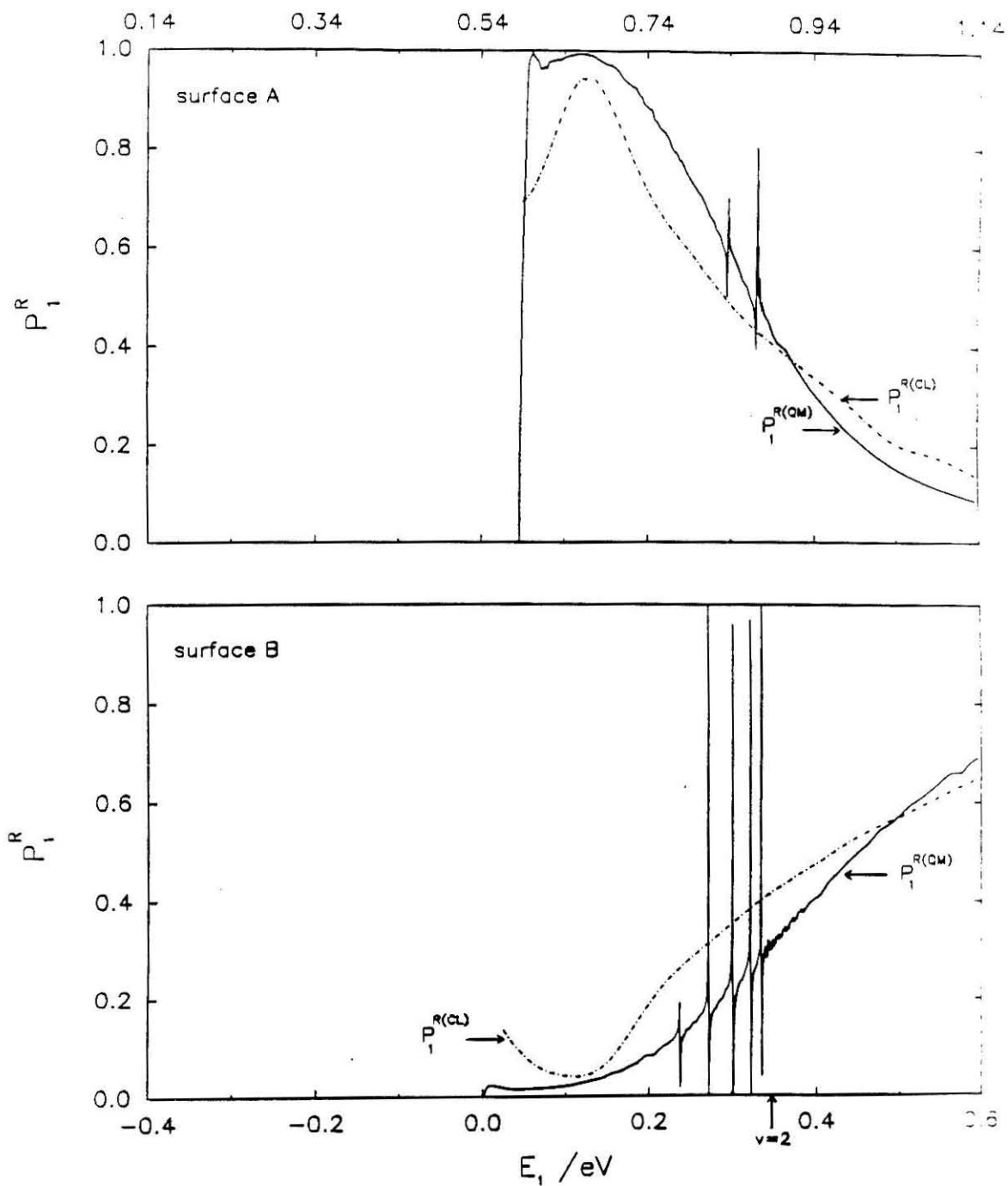


Figure 4.

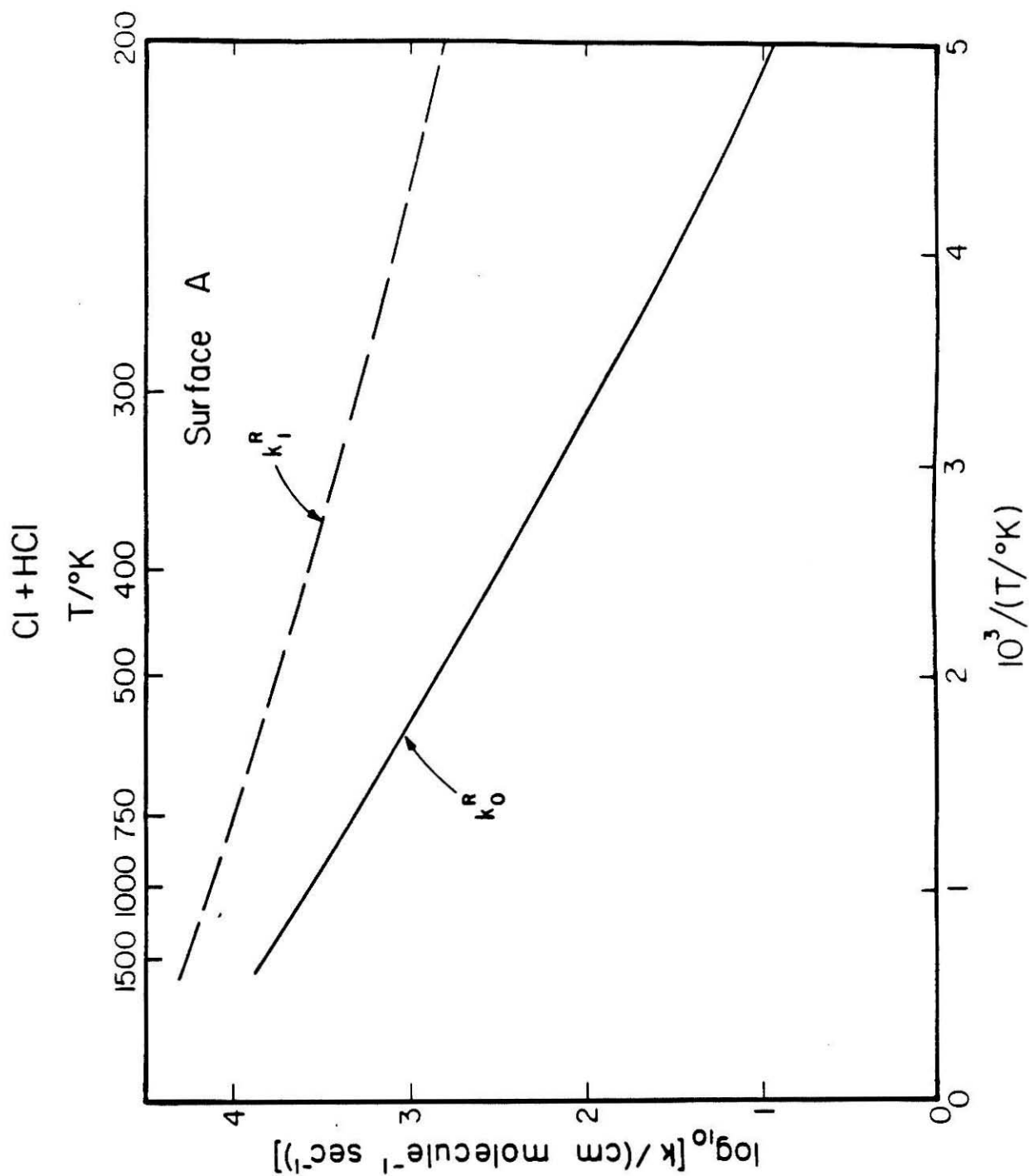


Figure 5.

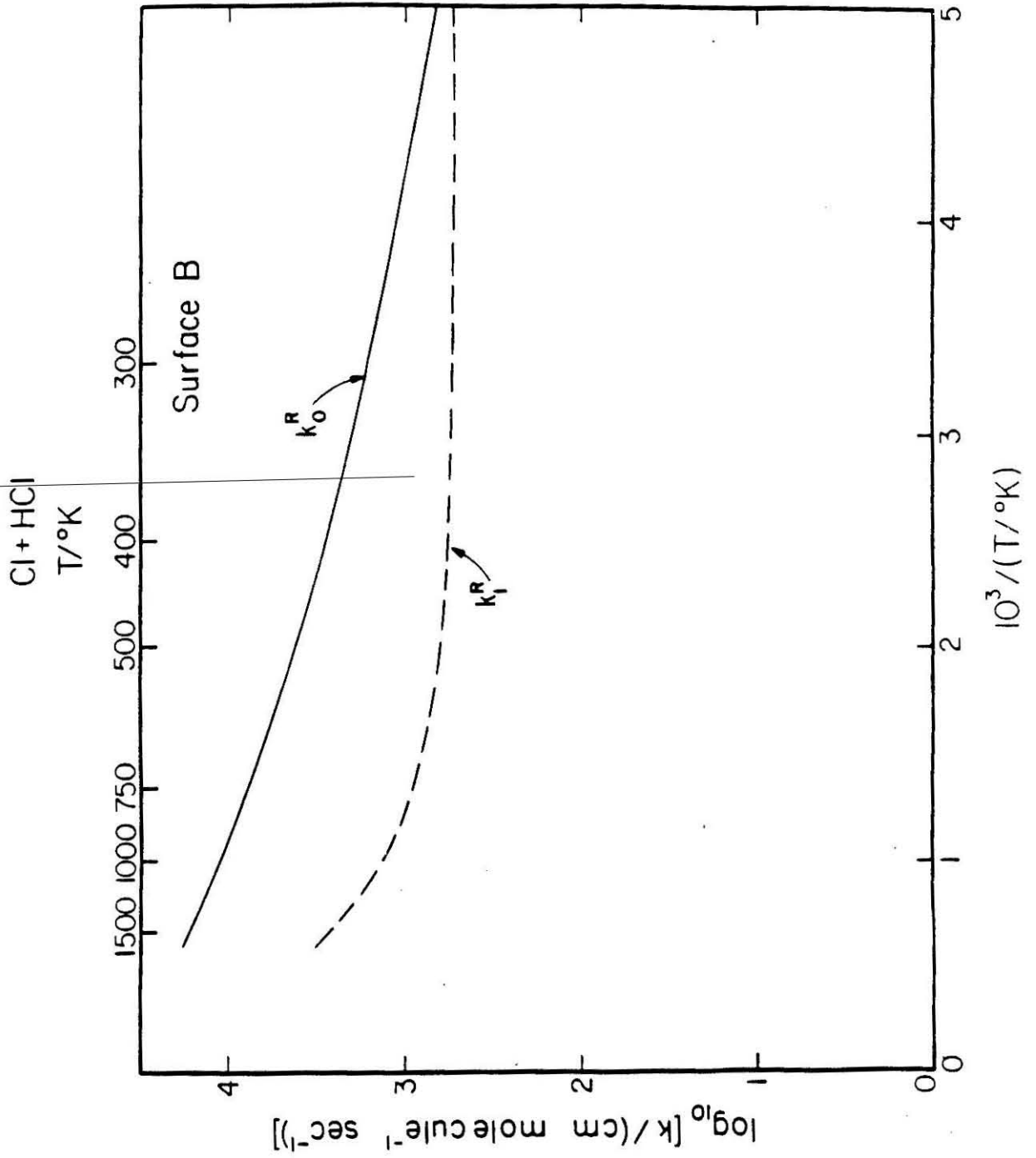


Figure 6.

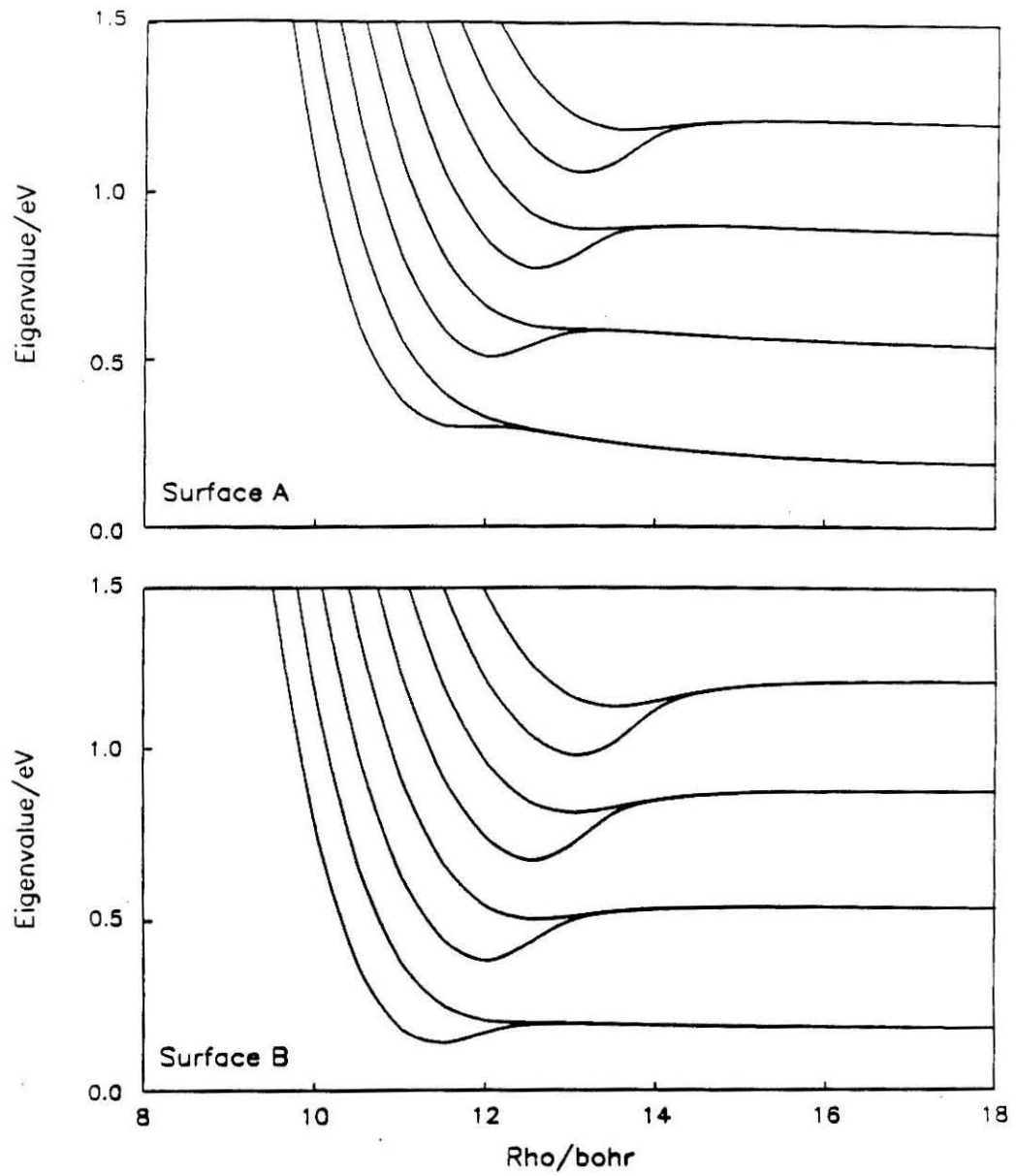


Figure 7.

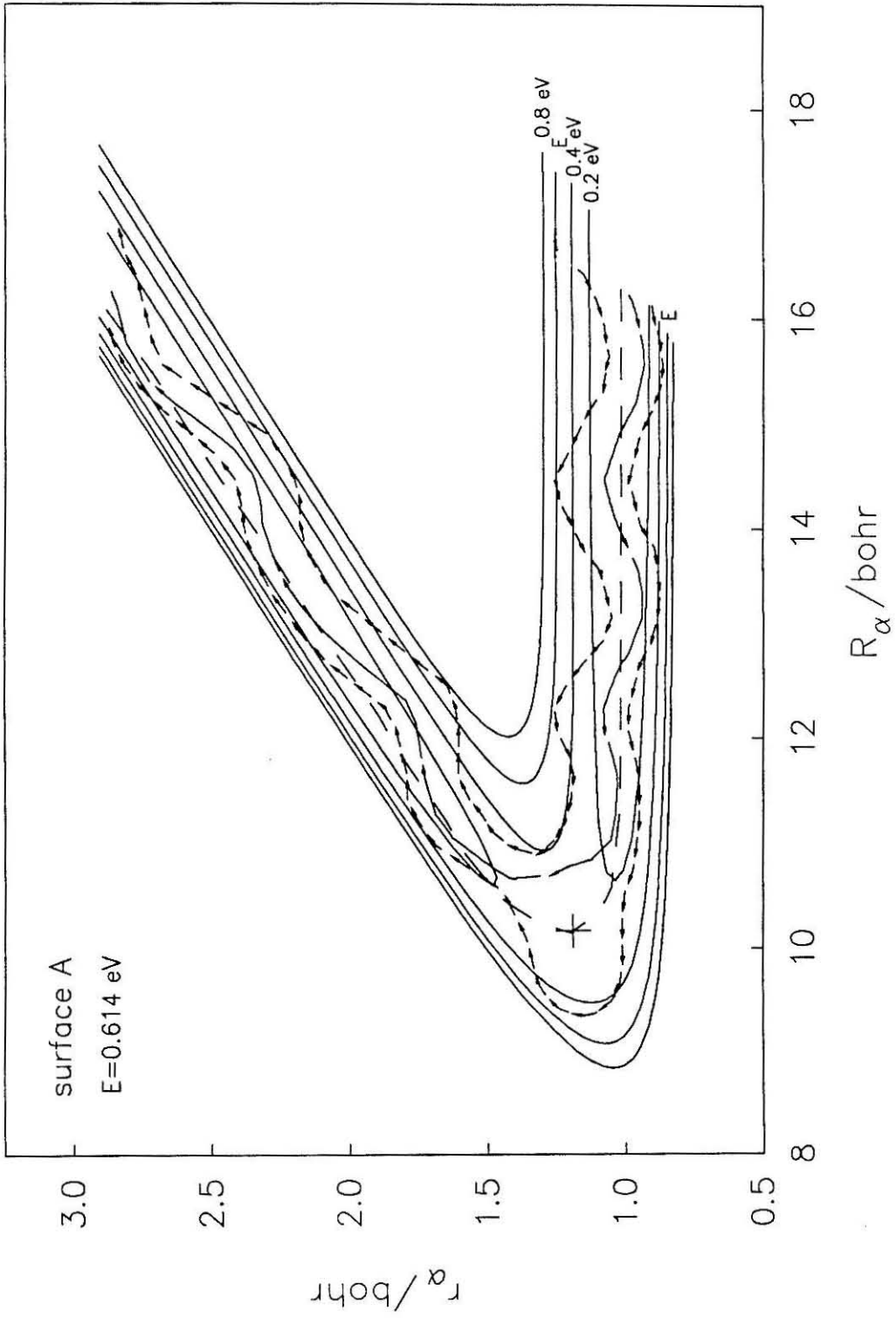


Figure 8

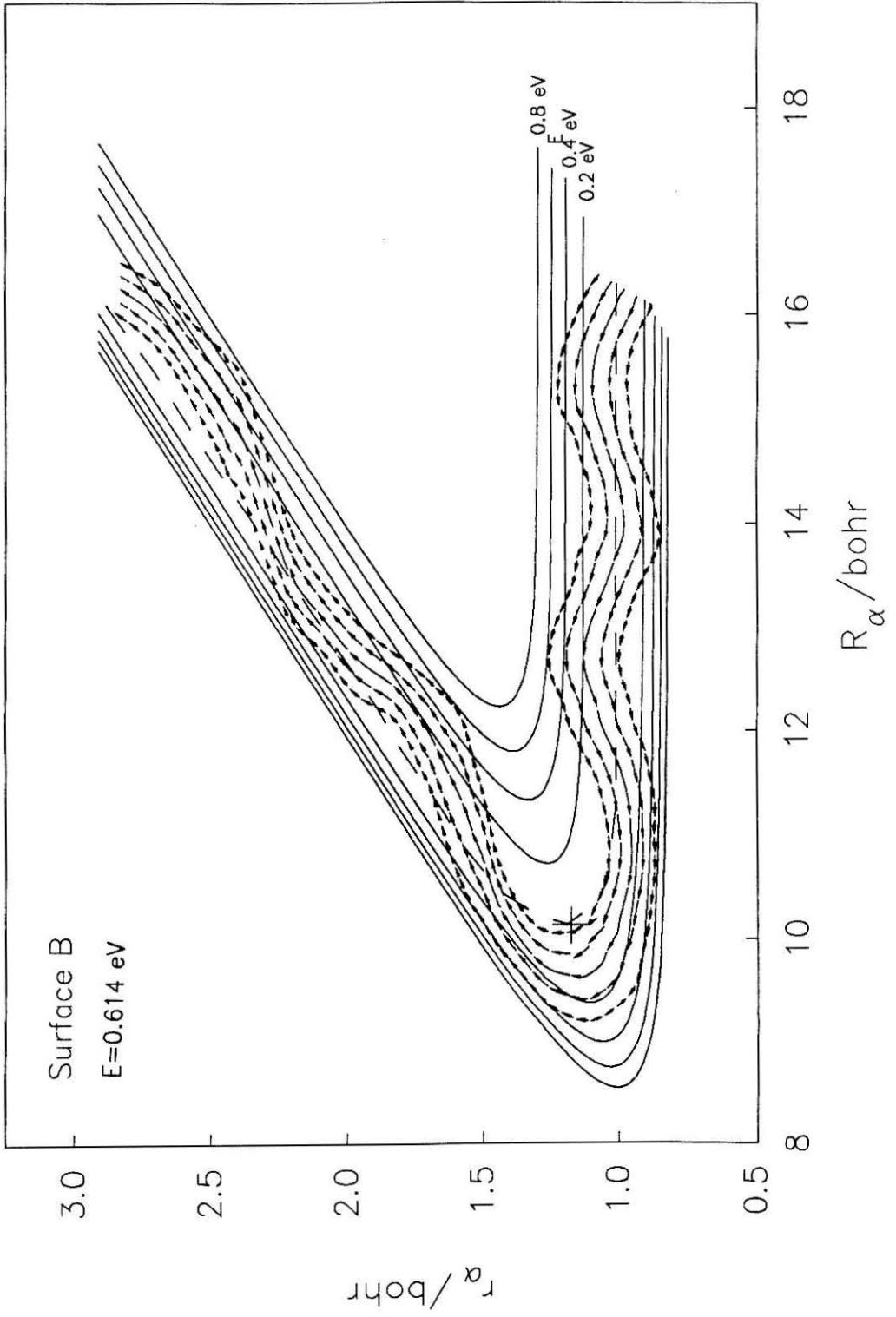


Figure 9

Appendix B

Chemical Reaction Dynamics: Integration of Coupled Sets of Ordinary Differential Equations on the Caltech Hypercube†

† This paper appeared in Proceedings of the Third Conference on Hypercube Concurrent Computers and Applications, Pasadena, 1988 (ACM, New York, 1988) pp. 1051-1061.

Chemical Reaction Dynamics: Integration of Coupled Sets of Ordinary Differential Equations on the Caltech Hypercube

Paul G. Hipes, Tim Mattson^a, Yi-Shuen Mark Wu^b and Aron Kuppermann

Caltech Concurrent Computation Project

206-49, California Institute of Technology

Pasadena, CA 91125, USA

Abstract

Use of the Caltech/JPL hypercube multicomputer to solve problems in chemical dynamics is the subject of this paper. The specific application is quantum mechanical atom diatomic molecule reactive scattering. One methodology for solving this dynamics problem on a sequential computer is based on symmetrized hyperspherical coordinates. We will discuss our strategy for implementing the hyperspherical coordinate methodology on the hypercube. In particular, the performance of a parallel integrator for the special system of ordinary differential equations which arises in this application is discussed.

^a Current address: 50 Kerr Parkway, # 51, Lake Oswego, OR 97035

^b Work performed in partial fulfillment of the requirements for the Ph.D. degree in Chemistry at the California Institute of Technology.

1. Introduction

The physics of systems consisting of a few interacting atoms is governed by a second order linear partial differential equation, the Schrödinger equation. An example of an interesting process involving a few atoms is the reactive scattering of an atom and a diatomic molecule. Accurate numerical solutions to the corresponding Schrödinger equation would provide a quantitative picture which could be compared with experimental results. In such a case, interplay between experiment and theory would permit a detailed understanding of the mechanisms of chemical reactions. Unfortunately, accurate numerical solutions to the Schrödinger equation for reactive scattering problems are very difficult to obtain because of the large number of degree of freedom in the partial differential equation. Currently, supercomputers are used to obtain partial solutions to the Schrödinger equation. That experience leads us to believe that significant progress in *ab initio* chemical dynamics may well rest with the next generation of computers. Parallel computing is an attractive means of increasing the CPU cycles available for our application codes. The combination of a robust efficient algorithm and the performance of parallel computers may permit the simulation of chemical reaction dynamics which are too complicated to solve today.

The outcome of electronically adiabatic bimolecular chemical reactions is governed by the initial quantum states of the reagents and by the potential energy function V which determines the forces at play during the reaction. The molecular level details of such a reaction are embodied in the state-to-state differential cross sections $\sigma_{t \rightarrow t'}(\theta; E_{tr})$ and integral cross sections $Q_{t \rightarrow t'}(E_{tr})$. Here t and t' are sets of quantum numbers which specify the internal state of the reagents and products, respectively, E_{tr} is the kinetic energy of the relative motion of these reagents, and θ the angle between the initial relative velocity vector of the reagents and the final

relative velocity vector of the products. These quantities contain information about the effectiveness of the internal and translational degrees of freedom of the reagents in promoting the reaction, as well as the deposition of the available energy among the degrees of freedom of the products.

There are a number of interesting issues in chemical dynamics of simple gas phase atom diatomic molecule reactions. It is important to perform accurate calculations for several reactions to help establish the relation between reaction cross sections and potential energy surfaces. Such studies will provide insight into the effect of features of the potential energy function on the physics of chemical reactions. Furthermore, the existence of dynamic resonances, which are very sensitive to the shape of the potential energy function, was predicated in approximate models of chemical reactions.^{1,2} It is of major scientific importance to understand theoretically the signature of resonant processes in the real world and to calculate the differential cross sections at resonance energies. Currently it is not possible to thoroughly explore these questions because the numerical calculations are simply too expensive to perform in all but the simplest case.

The calculation of reaction cross sections from an *ab initio* numerical solution of the corresponding Schrödinger equation is very difficult and so far has only been successfully performed for the $\text{H} + \text{H}_2 \rightarrow \text{H}_2 + \text{H}$ reaction over a relatively limited range of total energies.³⁻⁵ For higher energies for which experimental results are available,⁶⁻¹⁰ lack of convergence problems set in. Furthermore, applications to other reactions¹¹ which has less thermoneutral, for which the different arrangement channels are less isolated, or for which the atoms have very different masses, present severe numerical difficulties which have so far not been overcome using the methodology previously developed.

In the last two years we have succeeded in implementing a new computational methodology based on symmetrized hyperspherical coordinates (SHC),¹² which permits accurate calculations on a diversity of chemical reactions over extended energy ranges. This method has been extensively tested for collinear models¹³ and, more recently, for the $J = 0, 1$ angular momentum partial waves of the $\text{H} + \text{H}_2$ exchange reaction.¹⁴⁻¹⁶ In addition to our work with SHC, two new methods, based on an integral equation formalism of reactive scattering have been applied to the $J = 0$ partial wave of this reaction (or an isotopic counterpart)^{17,18} and of the $\text{O} + \text{H}_2$ reaction¹⁹ during the last year. Also, in the past year a methodology based on a different variety of hyperspherical coordinates has been implemented for the $J = 0, 1$ partial waves of some isotopic $\text{H} + \text{H}_2$ reactions,²⁰ as well as a more conventional approach for the $J = 0$ partial wave.²¹

This flurry of activity augurs well for the further development of quantum mechanical reactive scattering, and makes it particularly timely for such calculations to be extended to $J > 1$ in order for experimentally measurable quantities to be calculated for some important elementary chemical reactions, such as $\text{H} + \text{H}_2$, $\text{O} + \text{H}_2$, $\text{Cl} + \text{H}_2$, and $\text{F} + \text{H}_2$ and some of their isotopic counterparts. Such calculations would permit direct comparison with recent experimental results,⁶⁻¹¹ as well as with the results of approximate calculations.²²⁻²⁴

2. Methodology Based on Symmetrized Hyperspherical Coordinates

The methodology to be employed involves the use of symmetrized hyperspherical coordinates (SHC).¹² In summary, the SHC consist of a distance ρ called the hyperradius, and five hyperangles denoted collectively by ω . The former is an overall mass-scaled size parameter. Large values of ρ correspond to separated reagents or products, whereas small ones, of the order of equilibrium interatomic

distances, correspond to reagents or products in close proximity to each other. The five hyperangles ω describe the orientation of the triatomic system in space as well as the ratio of mass-scaled atom-diatom distances to diatom internuclear distances.

The essence of the SHC methodology is the expansion of the scattering wave function in a separable basis set. The basis set is derived from a piece of the Hamiltonian of the system of particle. The full Hamiltonian $\hat{H}(\rho, \omega)$ is defined in a six dimensional configuration space and is the sum of a hyper-radial kinetic energy operator $\hat{T}(\rho)$ and a surface Hamiltonian $\hat{h}(\omega; \rho)$ which contains the hyperangular kinetic energy operator and the potential energy function and depends parametrically on ρ (*i.e.* contains no derivatives with respect to ρ). The local hyperspherical surface functions (LHSF)²⁵ $\Phi_n^{J,M}(\omega; \rho)$ are defined to be the simultaneous eigenfunctions of the surface Hamiltonian $\hat{h}(\omega; \rho)$, the total angular momentum squared operator \hat{J}^2 and the laboratory-fixed Z component of the total angular momentum \hat{J}_Z . The LHSF $\Phi_n^{J,M}(\omega; \bar{\rho}_j)$ are calculated at a discrete set of values of $\bar{\rho}_j$ where $j = 0, 1, 2, \dots$ and which cover the domain of ρ . The scattering wave functions $\Psi^{J,M}(\rho, \omega)$ (defined as the simultaneous eigenfunctions of \hat{H} , \hat{J}^2 , and \hat{J}_Z) are expanded in the LHSF for ρ in some neighborhood of $\bar{\rho}_j$.

$$\Psi^{J,M}(\rho, \omega) = \rho^{-\frac{5}{2}} \sum_{n'}^N f_{n'}(\rho; \bar{\rho}_j) \Phi_{n'}^{J,M}(\omega; \bar{\rho}_j) \quad (1)$$

$$\rho \in (\bar{\rho}_j - \delta, \bar{\rho}_j + \delta)$$

The parameter δ is determined by the gradient of the potential energy function.

The expansion (1) is required to solve the Schrödinger equation. By employing the orthogonality of the LHSF, a set of coupled ordinary differential equations (ODEs) for the coefficients of the expansions as a function of the continuous variable ρ is derived.

$$\sum_{n'}^N \left[\delta_{n'}^n \frac{d^2}{d^2 \rho} + \mathbf{V}_{n,n'}^J(\rho, \bar{\rho}_j) \right] f_{n'}^J(\rho; \bar{\rho}_j) = 0 \quad (2)$$

In equation (2), $\bar{\rho}_j$ is considered a fixed parameter. A distinct set of ODEs exist for each value of this parameter. The system of coupled ODEs which are derived from the Schrödinger equation is referred to in the chemical dynamics literature as the coupled channel Schrödinger equation. The elements of the matrix \mathbf{V}^J in equation (2) involve the total energy E and integrals with integrands which are the product of two LHSF and the potential energy function V . \mathbf{V}^J is called the interaction matrix because it describes the coupling of the LHSF induced by the physics of the system.

The introduction of symmetrized hyperspherical coordinates and the sequential algorithms based on these coordinates are significant advances in chemical dynamics simulations. The previous techniques used different coordinates for different regions of configuration space. Continuity of the solutions at the boundaries between different regions had to be enforced separately. This matching of solutions is the source of numerical problems in the old methods. Hyperspherical coordinates bypass this troublesome problem.

The methodology based on SHC has three distinct phases. The first phase is the calculation of a set of numerical functions, the LHSF. The next phase consists of numerical quadratures using the LHSF. The third phase is the integration of a set of coupled ODEs.

The LHSF have been calculated on sequential machines in a variety of ways. The first successful approach was based on the finite element method,^{14,15} but is very expensive in computer resources. Based on that experience, another variational approach^{16,26} has been implemented and is less expensive than the finite element method. The new approach uses a basis set of global support instead of the local support shape functions of the finite element method. The global basis functions form a rapidly converging expansion of the LHSF and so many fewer

global basis functions are require than local shape functions leading to significant computational savings.

The ODE initial value problem (2) can be integrated with any numerical integrator; however, several special integrators optimized for these problems exists. From the results, a scattering matrix is obtained which contains the experimentally relevant information about the underlying physics of the system. Integration of the set of ODEs has been implemented on the Caltech Mark II and III hypercubes.

3. Logarithmic Derivative Integrator

One sequential algorithm for integrating the special systems of ODEs which occur in chemical dynamics simulations is the logarithmic derivative method of Johnson.²⁷ This is a fourth-order method which enjoys good numerical stability properties and has been used by ourselves and others on sequential computers. It has the appealing feature of requiring only matrix inversion and multiplication, but not matrix eigenvalues and eigenvectors.

The linear algebra tools necessary to write a parallel logarithmic derivative integrator (propagator) for the Caltech hypercube multicomputer are already available. Parallel matrix inversion using the Gauss-Jordan algorithm has been described in another contribution to these proceedings.²⁸ It is efficient and simple to use. Likewise, parallel matrix multiplication has been described and tested for the hypercube by Fox, Otto, and Hey.²⁹

What about the distribution of the matrix onto the hypercube? Both Gauss-Jordan inversion and matrix multiplication use the same data distribution mapping. The data need not be reorganized for the two algorithms. Since the inverter and multiplier are called a large number of times, reorganization of the data might significantly reduce the efficiency of the parallel propagator. In contrast,

the data distribution for inversion by Gaussian elimination is the shuffled-row distribution which is not natural for the matrix multiplication. The shuffled-row data distribution must be used with Gaussian elimination to achieve work load homogeneity.²⁸

The algorithm of Johnson is based on the Ricatti form of the coupled channel Schrödinger equation (2). A matrix \mathbf{f}^J is formed by collecting together solution column vectors f_n^J corresponding to different initial conditions. If the number of different initial conditions is chosen to equal the number of terms in the expansion (1), then \mathbf{f}^J is a square matrix. If the initial conditions are all distinct and nontrivial, then the matrix \mathbf{f}^J is nonsingular. To transform the dependent variables we define the logarithmic derivative matrix (omitting the superscript J)

$$y(\rho; \bar{\rho}_j) = \left[\frac{d}{d\rho} \mathbf{f}(\rho; \bar{\rho}_j) \right] [\mathbf{f}(\rho; \bar{\rho}_j)]^{-1} \quad (3)$$

For the statement of the algorithm, we will suppress the explicit reference to the $\bar{\rho}_j$ in the quantities. The ρ domain is divided into an even number L of equally spaced steps where the constant step size is denoted h . All bold face quantities are N by N real matrices. The algorithm for integrating the logarithmic derivative matrix is

$$\begin{aligned} z_0 &= \mathbf{I} - \mathbf{U}_0 + hy(\rho_0); \\ z_l &= 2\mathbf{I} - \mathbf{U}_l - z_{l-1}^{-1}; \quad l = 1, 2, 3, \dots, L \end{aligned} \quad (4)$$

$$y(\rho_L) = (z_L - \mathbf{I})/h$$

where the input data is

$$\begin{aligned} \mathbf{U}_l &= \begin{cases} \frac{2h^2}{3} \mathbf{V}(\rho_l); & l = 2, 4, 6, \dots, L-2 \\ 8\mathbf{I} - 8[\mathbf{I} + \frac{h^2}{6} \mathbf{V}(\rho_l)]^{-1}; & l = 1, 3, 5, \dots, L-1 \end{cases} \\ \mathbf{U}_0 &= \frac{h^2}{3} \mathbf{V}(\rho_0) \\ \mathbf{U}_L &= \frac{h^2}{3} \mathbf{V}(\rho_L) \end{aligned}$$

The initial value of the logarithmic derivative or z_0 is required to start the

algorithm. For sufficiently small values of ρ , the scattering wave function (1) has a vanishing amplitude implying that the f_n^J are also vanishingly small. As a consequence, for $\bar{\rho}_{j=0}$ we have $z_0^{-1} = 0$ as the initial data for the recursion in (4).

The LHSF form a good basis set for expanding the complete scattering wave function only in a neighborhood of $\bar{\rho}_j$ where the LHSF are calculated. Different sets of LHSF are required for the neighborhoods of different $\bar{\rho}_j$. Different sets of coefficients correspond the same scattering wave function expanded in different sets of LHSF. Matrix multiplication is not required in Johnson's algorithm itself, but is needed to transform the coefficients from the expansion in one set of LHSF to the coefficients corresponding to another set of LHSF:

$$\mathbf{f}(\rho; \bar{\rho}_j) \rightarrow \mathbf{f}(\rho; \bar{\rho}_{j+1}) \quad (5)$$

The transformation is defined by the requirement of continuity of the scattering wave function and its ρ derivative at the boundary between adjacent neighborhoods. This transformation provides the initial logarithmic derivative matrix for a neighborhood $\bar{\rho}_j$ from the final logarithmic derivative matrix of the previous neighborhood $\bar{\rho}_{j-1}$ where $j > 0$.

The logarithmic derivative integrator has been written and tested on the Caltech Mark II and III hypercubes. Its performance is essentially that of parallel Gauss-Jordan matrix inversion which represents the dominant user of CPU cycles. The test problems include the Secrest-Johnson³⁰ model of the nonreactive collision of a helium atom and a hydrogen molecule. The adjective nonreactive means that following each collision the products are the same as the reactants: a helium atom and a hydrogen molecule. The model is simple because the atom and diatomic molecule are confined to a space-fixed straight line. In other words the particles have only one physical dimension to move in. The Secrest-Johnson model is a good test case because the interaction matrix is obtained from a simple function

call so no loading of data from disk drives is required. This model does not use hyperspherical coordinates, but the system of ODEs that must be integrated is of the same structure as equation (2). The efficiency of the logarithmic derivative integrator is shown in the figure 1. The integration used 10^3 steps.

In addition to the Secrest-Johnson problem, the parallel propagator has been applied to a currently interesting chemical dynamics problem: the reactive scattering of $H + H_2$ in three dimensional space. Using the interaction matrix data generated on a Cray X-MP/48, a system of 14 ODEs was integrated on a 4-node Caltech/JPL Mark III hypercube. The results of the parallel propagator were compared to those of a sequential computer and are in satisfactory agreement. The number of $\bar{\rho}_j$ is 100 and the total number of integration step is 10^3 . This test of the parallel propagator brought to light a difficulty with the current Mark III hypercube. The integrator requires an interaction matrix for each step and this data is stored on disk. The movement of data from the disk to the hypercube dominates the entire calculation.

There is a solution to the loss of parallel efficiency due to data movement between the hypercube and disk drive. It is based on the fact that the system of ODEs is solved independently for each collision energy using the same input data. Instead of integrating the logarithmic derivative for each collision energy over the full ρ domain, several logarithmic derivative corresponding to different collision energies could be integrated over a section of the domain using a given part of the data set, increasing the use of the interaction matrix data once its in the hypercube. In fact, hundreds of collision energies are often desired to map out the dynamics as a function of total energy, so this seems a viable means of improving the parallel efficiency of the propagator given external data. This is not yet implemented, but

appears to require only a small modification of the existing algorithm and data structure.

4. Future Work

We are considering a variety of strategies for calculating the LHSF and interaction matrix quadratures on the hypercube. Parallelization of the quadratures can be accomplished by performing a subset of the integrals over the entire domain in each processor. In this case the matrix of integrals is the domain that is decomposed (*i.e.*, the matrix elements are distributed among the processors and each processor is responsible for complete integrals). Another approach is to divide the domain of integration and have each processor do all of the integrals over a part of the domain. The matrix decomposition method of doing the quadratures has been tested and has almost perfect efficiency. Parallel calculation of the LHSF is more difficult because the sequential algorithm is more elaborate. One requirement of the LHSF calculation is a parallel eigensystem solver. It is this facet of the machinery that is currently being implemented. We hope to be performing full reactive scattering calculations on the Mark IIIfp in the near future.

Acknowledgment

It is a pleasure to acknowledge the support of the Department of Energy, grant DE-FG-03-85ER25009.

References

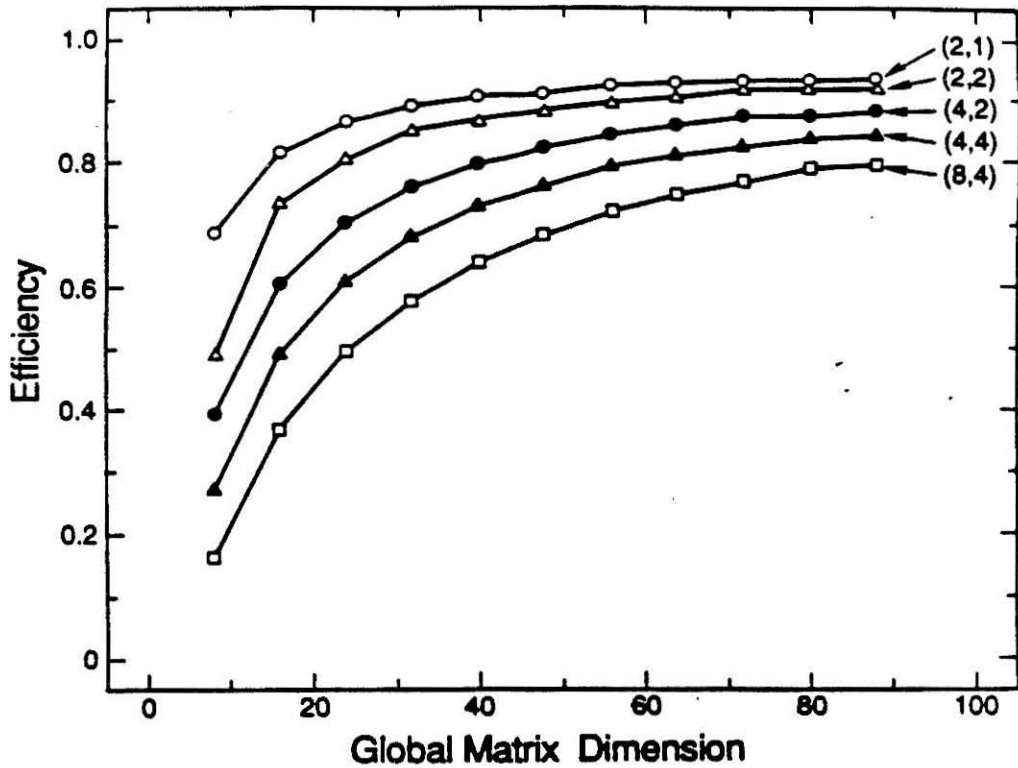
1. A. Kuppermann, in: Potential Energy Surfaces and Dynamics Calculations, editor D. G. Truhlar (plenum Press, New York, 1981), pp. 375-420.
2. B. C. Garrett, D. W. Schwenke, R. T. Skodje, D. Thirumalai, T. C. Thompson, and D. G. Truhlar, in: Resonances in Electron-Molecule Scattering, van der Waal Complexes and Reactive Scattering, edited by D. G. Truhlar, ACS Symposium Series, (American Chemical Society, Washington, D. C., 1987), pp. 375-400.
3. A. B. Elkowitz and R. E. Wyatt, *J. Chem. Phys.* **62**, 2504 (1975).
4. A. Kuppermann and G. C. Schatz, *J. Chem. Phys.* **62**, 2502 (1975); G. C. Schatz and A. Kuppermann, *J. Chem. Phys.* **65**, 4642 (1976); 4668.
5. R. B. Walker, E. B. Stechel, J. C. Light, *J. Chem. Phys.* **69**, 2922 (1978).
6. R. Götting, J. P. Toennies, and M. Vodegal, *Int. J. Chem. Kinet.* **18**, 949 (1986).
7. U. Gerlach-Meyer, K. Kleinermanns, E. Linnebach, and J. Wolfrum, *J. Chem. Phys.* **86**, 3047 (1987).
8. K. Tsukiyama, B. Katz, and R. Bersohn, *J. Chem. Phys.* **84**, 1446 (1986).
9. R. Götting, V. Herreo, J. P. Toennies, and M. Vodegel, *Chem. Phys. Lett.* **137**, 524 (1987).
10. S. A. Buntin, C. F. Giese, and W. R. Gentry, *J. Chem. Phys.* **87**, 1443 (1987).
11. D. M. Neumark, A. M. Wodtke, G. N. Robinson, C. C. Hayden, and Y. T. Lee, *J. Chem. Phys.* **82**, 3045 (1985); D. M. Neumark, A. M. Wodtke, G. N. Robinson, C. C. Hayden, K. Shobatake, R. K. Sparks, T. P. Shafer, and Y. T. Lee, *J. Chem. Phys.* **82**, 3067 (1985).
12. A. Kuppermann, *Chem. Phys. Lett.* **33**, 374 (1975).

13. J. Römelt, in: *The Theory of Chemical Reaction Dynamics*, edited by D. C. Clary, (Kluwer Academic Pub., Hingham, MA, 1987), pp. 77-104.
14. A. Kuppermann and P. G. Hipes, *J. Chem. Phys.* **84**, 5962 (1986).
15. P. G. Hipes and A. Kuppermann, *Chem. Phys. Lett.* **133**, 1 (1987).
16. S. A. Cuccaro and A. Kuppermann, in preparation.
17. J. Z. H. Zhang and W. H. Miller, *Chem. Phys. Lett.* **140**, 329 (1987).
18. K. Haug, D. W. Schwenke, Y. Shima, D. G. Truhlar, J. Zhang, and D. J. Kouri, *J. Phys. Chem.* **90**, 6757 (1986).
19. D. W. Schwenke and D. G. Truhlar, *J. Chem. Phys.* **87**, 1095 (1987).
20. G. A. Parker, R. T. Pack, B. J. Archer, and R. B. Walker, *Chem. Phys. Lett.* **137**, 564 (1987); R. T. Pack and G. A. Parker, *J. Chem. Phys.* **87**, 3888 (1987).
21. F. Webster and J. C. Light, *J. Chem. Phys.* **85**, 4744 (1986).
22. G. C. Schatz, *Chem. Phys. Lett.* **94**, 183 (1983); **108**, 532 (1984).
23. E. Pollak, N. Abusalbi, and D. J. Kouri, *Chem. Phys. Lett.* **113**, 585 (1985).
24. B. C. Garrett and D. G. Truhlar, *J. Chem. Phys.* **84**, 682 (1980); **87**, 4553 (1983).
25. R. T. Ling and A. Kuppermann, in: *Electronic and Atomic Collisions, Abstracts of papers of the 9th International Conference on the Physics of Electronic and Atomic Collisions*, Seattle, Washington, editors, J. S. Riley and R. Geballe (University of Washington Press, Seattle, Washington, 1975), pp. 353-354.
26. D. M. Hood and A. Kuppermann, in: *Theory of Chemical Reaction Dynamics*, editor D. C. Clary (D. Reidel Publishing Co., Boston, 1986), pp. 193-214.

27. B. R. Johnson, *J. Compl. Phys.* **13**, 445 (1973); *J. Chem. Phys.* **67**, 4086 (1977); NRCC Workshop, Lawrence Berkeley Laboratory, Report No. LBL-9501, 1979.
28. P. G. Hipes and A. Kuppermann, "Gauss-Jordan Inversion with Pivoting on the Caltech Mark II Hypercube", 3rd Hypercube Conference, Pasadena, Jan., 1988.
29. G. Fox, A. G. Hey, and S. Otto, *Parallel Computing* **4**, 17 (1987).
30. D. Secrest and B. R. Johnson, *J. Chem. Phys.* **45**, 4556 (1966); see also, D. Rapp and T. E. Sharp, *J. Chem. Phys.* **38**, 2641 (1963).

Figure Caption

Figure 1. Efficiency of the logarithmic derivative integrator on the Mark III hypercube as a function of global matrix dimension for the Secrest-Johnson problem. The ordered pairs associated with each curve give the number of processor rows and the number of processor columns, in that order. The straight line segments between the data points are provided to display the trends and do not represent data.



Efficiency of the logarithmic derivative integrator on the Mark III hypercube as a function of global matrix dimension for the Secrest-Johnson problem. The ordered pairs associated with each curve give the number of processor rows and the number of processor columns, in that order. The straight line segments between the data points are provided to display the trends and do not represent data.

Figure 1